An electro-optical timing diagnostic for pump-probe experiments at the Free-Electron Laser in Hamburg FLASH

DISSERTATION

zur Erlangung des akademischen Grades
Doctor rerum naturalium
(Dr. rer. nat.)
im Fach Physik

eingereicht an der
Fakultät für Mathematik, Informatik und Naturwissenschaften
Universität Hamburg

von

Armin Azima
aus Teheran/Iran

Vorsitzender des Prüfungsausschusses:
Prof. Dr. Günter Sigl

Vorsitzender des Promotionsausschusses:
Prof. Dr. Robert Klanner

Gutachter der Dissertation:

1. *Prof. Dr. Klaus Sengstock*
2. *Prof. Dr. Peter Schmüser*

Gutachter der Disputation:

1. *Prof. Dr. Jörg Rossbach*
2. *Prof. Dr. Wilfried Wurth*
3. *Prof. Dr. Peter Schmüser*

eingereicht am:	02. Juni 2009
Tag der mündlichen Prüfung:	20. Juli 2009

Abstract

Femtosecond pump-probe experiments have extensively been used to follow atomic and molecular motion in time. The very intense extreme ultraviolet XUV light of the Free electron LASer in Hamburg FLASH facility allows to investigate fundamental processes such as direct one or few photon inner shell ionizations. A supplementary Ti:Sapphire near infrared femtosecond laser system allows to perform two-color pump-probe experiments with FLASH involving intense laser fields of hugely different photon energies. Within this work a bunch arrival measurement system has been built, which assists these two-color pump-probe experiments to reduce the temporal jitter of FLASH and to increase the temporal resolution. The diagnostic is based upon an electro-optical detection scheme and measures the relative arrival time between the Ti:Sapphire femtosecond pulse and the electron bunch, which generates the self-amplified by stimulated emission SASE XUV pulse in the undulator section of FLASH. Key feature of the diagnostic is a **150 m** long glass fiber pulse transport line, which inflicts non-linear dispersion. A dispersion control system to compensate for this higher order dispersion has been developed including the control and programming of a spatial light phase modulator. It was possible to transport a **90 fs FWHM** short near infrared femtosecond laser pulse Fourier limited by the dispersion compensated glass fiber. The electro-optical signal induced by the FLASH electron bunch was generated, characterized and optimized. The signal features beside the designated bunch arrival timing capability the additional possibility to measure the longitudinal electron bunch density distribution of an arbitrary bunch of FLASH in a single shot with a temporal resolution of below **100 fs RMS**. Timing and bunch analysis capabilities of the developed diagnostic have been cross-checked with other comparable diagnostics at FLASH like the transversal deflecting cavity structure named LOLA. Finally, the timing diagnostic was part of a series of two-color near-infrared/XUV pump-probe experiments. It was used to correct the measurement delay times of the experiments *a posteriori* and thus compensate for the temporal jitter of FLASH. By this means the temporal resolution of two-color pump-probe experiments at FLASH was improved by more than a factor **4** from **250 fs RMS** or worse to just **60 fs RMS**. A pump-probe experiment performed on a Gallium-Arsenide waver using the FLASH XUV pulse as pump pulse revealed an optical light reflectivity modulation induced by FLASH. The temporal dynamics of this process was investigated in detail due to the jitter corrections of the timing diagnostic. The improved temporal resolution lead to a high degree in the understanding and interpretation of the underlying physical processes of the observed reflectivity modulation. Meanwhile the timing diagnostic advanced to a standard diagnostic, which is regularly utilized by pump-probe experimental groups of the FLASH user facility.

Keywords:
two-color pump-probe experiment, temporal jitter, electro-optical sampling, glass fiber based pulse transportation

Zusammenfassung

Femtosekunden Anrege-Abfrage Experimente werden intensiv genutzt, um die Dynamik innerhalb von Atomen und Molekülen zeitlich zu verfolgen. Der sehr intensive extrem-ultraviolette XUV femtosekunden Lichtpuls des Freie Elektronen LASer FLASH in Hamburg ermöglicht die Untersuchung fundamentaler Prozesse wie Ein- oder Zwei-Photonen-Ionisation der inneren Elektronenschalen. Mit Hilfe eines ergänzenden Titan:Saphir nahinfrarot femtosekunden Lasersystems können zusammen mit dem XUV-Puls Zwei-Farben Anrege- und Abfrageexperimente durchgeführt werden, welche intensive Laserfelder sich stark unterscheidender Photonenenergien benötigen. Im Rahmen dieser Arbeit wurde eine Elektronenpaketankunftszeit Messdiagnostik für den extrem-ultravioletten Freie-Elektronen Laser FLASH in Hamburg entwickelt, welche die besagten Zwei-Farben Anrege- und Abfrageexperimente unterstüzt. Durch die entwickelte Diagnostik können die zeitlichen Ankunftszeitfluktuationen des XUV Pulses, welche durch den zu Grunde liegenden Linearbeschleuniger verursacht werden, aus den gemessenen Daten entfernt werden. Hierdurch wird die zeitliche Auflösung eines Zwei-Farben Anrege- und Abfrageexperiments verbessert. Haupteigenschaft der Ankunftszeitdiagnostik ist ein **150 m** langes Glasfaser basiertes fs-Puls Transportsystem, welches einen nahinfraroten bis zu **90 fs FWHM** kurzen Laserpuls Fourier limitiert transportieren kann. Da die Glasfaser nichtlineare Dispersion verursacht, mußte ein Pulsdispersions-Kontrollsystem entwickelt werden, um diese zunächst nicht bekannte Dispersion höherer Ordnung zu kompensieren. Hierzu wurde unter anderem ein räumlich-spektraler Phasenmodulator angesteuert und ein Pulsdauer-Optimierungs-Alghorithmus entwickelt. Das Ankunftszeitsignal wird mittels einer elektro-optischen Messmethode erzeugt und konnte optimiert und charakterisiert werden. Neben der Haupteigenschaft, die Ankunftszeit des Elektronenpakets zu vermessen, kann mit diesem Signal auch die longitudinale Elektronendichteverteilung eines beliebigen Mikropuls-Elektronenpakets des Linearbeschleunigers mit einer Auflösung von unter **100 fs RMS** vermessen werden. Ankunftszeit und Elektronenpaketform-Analyse Eigenschaften der Diagnostik wurden mit anderen Diagnostiken des Linearbeschleunigers verglichen. Schließlich partizipierte die Ankunftszeitdiagnostik an einer Reihe von Nahinfrarot/XUV Zwei-Farben Anrege- und Abfrageexperimenten und wurde erfolgreich zur Korrektur der auftretenden Ankunftszeitfluktuationen zwischen beiden Lichtpulsen eingesetzt. Durch die Ankunftszeitdiagnostik konnte die Auflösung dieser Anrege-Abfrageexperimente von zunächst **250 fs RMS** oder schlechter auf bis zu **60 fs RMS**, d.h. um mehr als einen Faktor **4** verbessert werden. Ein Anrege-Abfrageexperiment an der Oberfläche eines Gallium-Arsenid Trägers zeigte nach Anregung mit dem intensiven FLASH XUV Puls eine Änderung der Reflektion im visuellen Spektralbereich, welche mit dem optischen Puls abgefragt wurde. Die durch die entwickelte Ankunftszeitdiagnostik deutlich erhöhte zeitliche Meßauflösung ermöglichte ein tieferes Verständnis der physikalischen Vorgänge dieses Effektes. Mittlerweile ist die im Rahmen dieser Arbeit entwickelte Ankunftszeitdiagnostik zu einem Standardwerkzeug der Freie-Elektronen Laser Anwenderanlage FLASH geworden und wird regelmäßig zur Verbesserung zeitaufgelöster Experimente eingesetzt.

Schlagwörter:
Zwei-Farben Anregungs- und Abfrageexperiment, Zeitliche Instabilität, Elektro-optisches Abtasten, Glasfaser basiertes Femtosekundenpuls Transportsystem

Für meinen Sohn Ilya-Marcel

Contents

List of Figures

List of tables

Chapter 1

Introduction

Time resolved measurements of atomic or molecular processes require a high temporal resolution, since typical atomic or molecular time units are in the order of a few 100 as to several 100 fs. These ultra-short timescales became accessible to measurement during the last fifteen years. The instrument of choice to temporally measure dynamic processes in this time range is the *pump-probe technique*. This technique requires a reproducible system, which can be excited and probed multiple times without changing its temporal dynamic. For many systems an even more restrictive requirement must be fulfilled, which is, that each individual in an ensemble of targets must be prepared in the same quantum state. In this case the quantum-mechanical similarity principle guarantees, that each excited individual develops in time in the same way. Hence, it is possible to measure the temporal development of the excited state on different individuals of the prepared ensemble. The pump-probe technique takes advantage of the reproducibility and scans the temporal development in a discrete way time step by time step. The technique uses two pulses,- a pump and a probe pulse -, which interact with the same target but are delayed in time. The first pulse triggers a reaction, which drives the target into an excited state. The second pulse must be able to interact with the excited state and typically probes the relaxation dynamic of this state. The reaction product of the probe reaction or more generally spoken the response of the system on the probe pulse shows characteristic properties, which depend on the delay time between both pulses. From this time dependent response the temporal evolution of the excited state can be derived. If the target is brought back into its initial state or a further target prepared with the same initial state is available, the measurement can be repeated with a different time delay than before.

In this way the complete temporal evolution of the prepared state can be probed in a stroboscopic way time step by time step as if a fast sequence of images of a motion is taken like it is shown in figure 1.1. The temporal resolution of the pump-probe measurement technique is limited by the temporal duration of both pulses and the precision, with which the time delay between both pulses is known.

Typical femtosecond pump-probe experiments initially have been performed in chemistry to probe the reaction kinetic of chemical reactions [WRD93, REF+07]. When this technique came up, the first optical femtosecond lasers were available and a complete class of measurements became accessible, which today is summarized as the femto-chemistry science. The resolution of this measurements were only limited by the duration of the pulses, because both the pump and the probe pulses are derived from the same optical pulse. Hence, there exists no significant temporal jitter influence and thus no additional temporal uncertainty beside the finite pulse durations of the set temporal delay between both pulses at all.

Due to the wavelength restriction of conventional* multi-level lasers to the optical and infrared

*Plasma based X-ray lasers are not considered as *conventional*.

(a) (b)

Figure 1.1: *Two examples of fast measurements in photography.*
(a) A bullet piercing an apple. The photo is sharp and shows one time step of the piercing process. (b) Foto finish of a bicycle race. The photo is blurred since the acquisition time is larger than the motion dynamics of the blurred parts of the photo. The **acquisition time** in photography corresponds with the **pulse duration** of a pump-probe experiment. If the measured process is faster than the acquisition time, the process can not be resolved temporally.

regime, the number of target samples, which are accessible to optical-optical pump-probe measurements is limited. This led to the development of various femtosecond light sources, which deliver ultra-short pulses as pump pulses of much shorter wavelength than the optical lasers [WLP+93, SCH+00]. In this case both pulses are of different wavelength, why this class of experiments is named *two-color pump-probe* experiment. To achieve a femtosecond-precise temporal measurement resolution, these extended ultraviolet (XUV) or ultraviolet (UV) light sources are generated by optical fs-laser pulses, which interact with matter to generate photons of short wavelength. Since the physical processes behind this techniques are not very efficient ($\approx 10^{-6}$) [HKM+02], the first laser driven XUV sources only emitted weak XUV pulses of low photon flux. Thus, the density of the excited targets in the pumped sample created by these sources were small, which decreases the measured pump-probe signal strength. It is possible to get over this drawback by extending the measurement duration and average many events of the same delay time to improve the signal to noise ratio. However, for a lot of experiments this method is not sufficient, since the reaction cross sections requires a higher intensity, which significantly restricts the number of experiments accessible to two-color pump-probe measurements of this type.

The situation has changed dramatically with the invention of free electron based X-ray and XUV lasers (FEL) [DES06, SLA09, DES13]. These light sources provide femtosecond pulses of high photon flux and excellent peak brilliance[†], which outperforms conventional XUV sources or synchrotron radiation sources by many magnitudes in peak brilliance [A+07]. During this work from 2004 to 2008 the only Free Electron Laser in the XUV range in the world was FLASH. FLASH emits coherent SASE[‡]-XUV pulses in the range from 6.5 nm to 45 nm [FEL08]. Experiments, which were made before with laser driven XUV sources were limited by a small peak intensity, which limited the number of possible experiments to only those of large photon interaction cross-section and to linear processes. Only with a high-gain FEL like FLASH experiments involving nonlinear processes and small excitation cross-sections in the XUV regime become accessible and can be performed within minutes or a few hours due to the higher photon flux rate. The high photon flux compensates the small excitation probability and the resulting dilute density of excited targets in the sample.

A significant limitation of the Free Electron XUV laser is the existence of a relatively large tem-

[†]Definition of brilliance: photon flux/(solid angle*area*bandwidth)
[‡]Self Amplified Spontaneous Emission

poral jitter of the XUV pulse, which results from technological limitations of the underlying linear accelerator [SAL+05].The temporal jitter of FLASH with respect to the optical fs-pulse, which is one order of magnitude larger than the XUV pulse duration, decreases the temporal resolution of a two-color pump-probe experiment strongly. To improve this limitation of FLASH in this work a timing tool for FLASH has been constructed [ADS+06]. The timing tool performs an indirect electro-optically based shot-by-shot measurement of the arrival time of the electron bunch, i.e. the source of the XUV pulse, with respect to the optical pump-probe fs-pulse. The temporal information is used *a posteriori* to correct for the temporal jitter of each temporal measurement point, which significantly improves the temporal resolution of a two-color pump-probe experiment at FLASH by at least a factor 4 from 250 fs RMS or worse down to 60 fs RMS [GAB+08]. This temporal resolution improvement has been shown multiple times in various pump-probe experiments [ADR+09, JRS+09]. A similar technique has been developed before at the electron based incoherent X-ray source SPPS at SLAC [CF05]. Within this work this technique for the first time is used in a high-gain SASE FEL emitting coherent XUV pulses.

The developed timing module has become a standard tool at FLASH, which regularly is demanded from users, who plan to perform a two-color pump-probe experiment.

Chapter 2

Theoretical background of electro-optical sampling

Electro-optical sampling is a widely used technique in ultra-fast laser optics and electron bunch analysis. It is based on the interaction between an optical ultra-fast laser pulse and a pulse or a monochromatic wave in the far-infrared or THz-regime. While the basic mathematical treatment remains similar in both spectral regimes, experimentally the pulses are treated completely different. For example, glass elements are opaque at wavelengths larger than $2\,\mu$m. Thus, in THz-science a focussing element must be realized using a reflective focussing mirror or different materials like polyethylene or aluminium oxide.

This chapter provides a theoretical overview to discuss the general interaction processes of fs-laser pulses with matter. The principle and application of the Pockels effect in electro-optical crystals is discussed. The following section is based on reviews found in [DR95], [Agr01a], [Agr01b], [Ste07] and [Win08].

2.1 Interaction of electro-magnetic waves with matter

The propagation of an electro-magnetic wave is described by Maxwell's equations.

$$\nabla \cdot \boldsymbol{D} = \rho, \tag{2.1}$$

$$\nabla \cdot \boldsymbol{B} = 0, \tag{2.2}$$

$$\nabla \times \boldsymbol{E} = -\frac{\partial \boldsymbol{B}}{\partial t}, \tag{2.3}$$

$$\nabla \times \boldsymbol{H} = \boldsymbol{j} + \frac{\partial \boldsymbol{D}}{\partial t}, \tag{2.4}$$

The electric and magnetic field vectors are $\boldsymbol{E}\,[\frac{\mathrm{V}}{\mathrm{m}}]$ and $\boldsymbol{H}\,[\frac{\mathrm{A}}{\mathrm{m}}]$ respectively. The electric displacement density or flux density is $\boldsymbol{D}\,[\frac{\mathrm{As}}{\mathrm{m}^2}]$ and $\boldsymbol{B}\,[\frac{\mathrm{Vs}}{\mathrm{m}^2}]$ is the magnetic flux density. In conventional optics only materials without free charges are used, therefore the current density $\boldsymbol{j}$ and free charges ρ in the following treatment are set to zero. As soon as an electro-magnetic field enters matter the electrons inside align in such a way, that a new field (electric polarization $\boldsymbol{P}$ or magnetization $\boldsymbol{M}$) is generated, which counteracts or increases the external flux:

$$\boldsymbol{P} = \boldsymbol{D} - \varepsilon_0 \boldsymbol{E} = \chi_e \varepsilon_0 \boldsymbol{E} \quad \text{and} \quad \boldsymbol{M} = \boldsymbol{B} - \mu_0 \boldsymbol{H} = \chi_M \mu_0 \boldsymbol{H}, \tag{2.5}$$

where χ_e and χ_M are the electric and magnetic susceptibility tensors. They describe the electro-magnetic material properties including the magnitude and direction with the magnetic field $\boldsymbol{H}$ or

electric field $\boldsymbol{E}$ is modified inside matter. Generally, in all conventional optical media the induced magnetic polarization $\boldsymbol{M}$ is zero. Thus, in order to achieve an equation for only the electric field, it is possible to eliminate $\boldsymbol{B}$. Using equation (2.4) and (2.5), one obtains

$$\nabla \times \boldsymbol{B} = \mu_0 \varepsilon_0 \frac{\partial \boldsymbol{E}}{\partial t} + \mu_0 \frac{\partial \boldsymbol{P}}{\partial t} \quad . \tag{2.6}$$

Applying the curl operator $\nabla\times$ on both sides of equation (2.3) and the mathematical identity $\nabla \times (\nabla \times \boldsymbol{E}) = \nabla(\nabla \cdot \boldsymbol{E}) - \nabla^2 \boldsymbol{E}$ yields

$$\nabla(\nabla \cdot \boldsymbol{E}) - \nabla^2 \boldsymbol{E} = -\frac{\partial}{\partial t} (\nabla \times \boldsymbol{B}) \quad . \tag{2.7}$$

With equation (2.6), one obtains a second order differential equation containing only electric field vector terms:

$$\nabla(\nabla \cdot \boldsymbol{E}) - \nabla^2 \boldsymbol{E} = -\mu_0 \varepsilon_0 \frac{\partial^2 \boldsymbol{E}}{\partial t^2} - \mu_0 \frac{\partial^2 P}{\partial t^2} \tag{2.8}$$

Due to the assumed absence of free charges, $\nabla \cdot \boldsymbol{E} = \rho = 0$ follows. Thus, equation (2.8) reduces to the wave equation for isolating, dielectric materials

$$\nabla^2 \boldsymbol{E} - \frac{1}{c^2} \frac{\partial^2 \boldsymbol{E}}{\partial t^2} = \mu_0 \frac{\partial^2 \boldsymbol{P}}{\partial t^2} \quad . \tag{2.9}$$

For anisotropic materials χ is a tensor and one has to replace $\mu_0 \frac{\partial^2 \boldsymbol{P}}{\partial t^2}$ with $\frac{1}{\varepsilon_0 c^2} \chi_e \frac{\partial^2 \boldsymbol{E}}{\partial t^2}$ according to equation (2.5). Generally, the susceptibility is dependent on the wavelength and intensity of the incident electric field.

For high intensity electric fields, the induced polarization inside a material becomes a nonlinear function of the external field. To investigate the degree of nonlinearity, one can expand the polarization in ascending powers of the electric field:

$$\boldsymbol{P} = \varepsilon_0 (\boldsymbol{\chi}_e^{(0)} + \boldsymbol{\chi}_e^{(1)} \boldsymbol{E} + \boldsymbol{\chi}_e^{(2)} \boldsymbol{E}^2 ...) \boldsymbol{E} \tag{2.10}$$

For a small field all but the first term can be neglected.

The linear susceptibility $\boldsymbol{\chi}_e^0$ induces dispersion on ultrashort pulses and in the case of anisotropic crystals leads to a directional dependence on the speed of light. This is known as birefringence.

The second order susceptibility term $\boldsymbol{\chi}_e^1$ describes how the refraction index depends on the electric field. This is called the linear electro-optic effect or the Pockels effect. Second Harmonic generation is another effect ruled by $\boldsymbol{\chi}_e^1$.

The 3rd order susceptibility $\boldsymbol{\chi}_e^2$ is responsible for the Kerr or quadratic electro-optical effect. The refractive index becomes a function of the intensity ($I \sim \boldsymbol{E}^2$) of the electric field. Assuming a material with inversion symmetry. In this case the second order susceptibility $\boldsymbol{\chi}_e^1$ is zero. For intensities below $10^{16}\,\mathrm{W/cm^2}$ polarization terms higher than third order can be neglected. With the definition equation for the index of refraction $n = \sqrt{\chi_e + 1}$ one obtains

$$n\left(\boldsymbol{E}^2\right) = \sqrt{1 + \boldsymbol{\chi}_e^0 + \boldsymbol{\chi}_e^2 \boldsymbol{E}^2} \tag{2.11}$$

$$= n_0 \sqrt{1 + \frac{\boldsymbol{\chi}_e^2 \boldsymbol{E}^2}{n_0^2}} \tag{2.12}$$

$$\approx n_0 + \frac{1}{2 n_0} \boldsymbol{\chi}_e^2 \boldsymbol{E}^2 \quad . \tag{2.13}$$

And from equation (2.25) follows

$$n(I) = n_0 + n_2 I \tag{2.14}$$

with the linear and nonlinear* indices of refraction n_0 and $n_2 = \sqrt{\frac{\mu_0}{\varepsilon_0}}\frac{1}{2n_0^2}$. This effect is called *optical Kerr effect* and is the basis of non-linear effects like spatial self-focussing (SF) or temporal self-phase modulation (SPM) of intense beams in matter. Third Harmonic generation is another effect ruled by χ_e^2.

2.1.1 Dispersion of ultra-short laser pulses

A solution of (2.9) for a homogeneous medium is a plane wave

$$E(z,t) = E_0 \mathrm{e}^{i(\omega\ t - kz)} \tag{2.15}$$

and any arbitrary linear superposition of plane waves. Inserting (2.15) in (2.9) one obtains, for small intensities ($|E| < 10^5$ V/m), the dispersion relation

$$k = \omega\sqrt{(\chi_e^0(\lambda_0) + 1)\,\epsilon_0\mu_0} = \frac{2\pi n(\lambda_0)}{\lambda_0} = \frac{\omega n(\omega)}{c_0}, \tag{2.16}$$

where c_0 and λ_0 are the velocity of light and the wavelength of the radiation in vacuum, $c = c_0/n$ and $\lambda = \lambda_0/n$, k is the wave number of the plane wave in the medium and $n(\lambda_0) = \sqrt{\chi_e^0(\lambda_0) + 1}$ the index of refraction. For monochromatic light the dispersion is negligible, but in ultrashort physics typically laser pulses with limited bandwidth $\Delta\omega$ around a carrier frequency are used. These pulses can be described by a superposition of plane waves. The most prominent example is the Gaussian laser pulse, where the weighting function, also called spectral field envelope function $\mathcal{E}(\omega)$ has a Gaussian distribution centered around the carrier frequency ω_0:

$$\mathcal{E}(\omega) = \tilde{\mathcal{E}}_0 \exp\left(-\frac{(\omega-\omega_0)^2}{2\sigma_\omega^2}\right) \tag{2.17}$$

The amplitude of the electric field $\tilde{\mathcal{E}}_0$ might be a complex vector, but since it is not dependent of ω and the medium is isotropic, it only contributes a constant phase offset, which can be neglected. Hence, $\tilde{\mathcal{E}}_0$ is supposed to be a real scalar without restriction of any kind.

Thus, writing down the continuous superposition of the non-zero weighted plane waves of a Gaussian laser pulse gives

$$\begin{aligned} E(z,t) &= \frac{1}{\sqrt{2\pi}}\int_{-\infty}^{\infty}\mathcal{E}(\omega)\exp(i(\omega t - k(\omega)z))d\omega \\ &= \frac{1}{\sqrt{2\pi}}\int_{-\infty}^{\infty}\mathcal{E}(\omega)\exp(-i\phi(\omega))\cdot\exp(i\omega t)d\omega \quad . \end{aligned} \tag{2.18}$$

Equation (2.18) is the Fourier transform $\mathcal{F}(\mathcal{E}(\omega))$ of the spectrum of the electric field

$$\tilde{E}(\omega) = \mathcal{E}(\omega)exp(-i\phi(\omega)) \tag{2.19}$$

with the spectral phase function

$$\phi(\omega) = k(\omega)z \quad . \tag{2.20}$$

*This derivation is almost exact. For linear polarized light one can show that $n_2 = 1.5\sqrt{\frac{\mu_0}{\varepsilon_0}}\frac{1}{2n_0^2}$ [Rei04]

In vacuum ($\phi(\omega) = \phi_0 = kz$) (2.18) can be evaluated without further assumptions:

$$\begin{aligned} E(z,t) &= \frac{1}{\sqrt{2}}\int_{-\infty}^{\infty}\mathcal{E}(\omega)\exp(i(\omega t - kz))d\omega \\ &= \exp(i(\omega_0 t - kz))\frac{1}{\sqrt{2}}\int_{-\infty}^{\infty}\tilde{\mathcal{E}}_0\exp\left(-\frac{(\omega-\omega_0)^2}{2\sigma_\omega^2}\right)\exp(i(\omega-\omega_0)t)d(\omega-\omega_0) \\ &= \tilde{\mathcal{E}}_0\sigma_\omega\exp\left(\frac{-\sigma_\omega^2}{2}t^2\right)\exp(i(\omega_0 t - kz)) \\ &= \mathcal{E}_0\exp\left(-\frac{t^2}{2\sigma_\tau^2}\right)\exp(i(\omega_0 t - kz)) \end{aligned} \tag{2.21}$$

with

$$\mathcal{E}_0 = \tilde{\mathcal{E}}_0\sigma_\omega \quad \text{and} \tag{2.22}$$

$$\sigma_\tau = 1/\sigma_\omega \tag{2.23}$$

Equation (2.21) takes the form $\mathcal{E}(t) * \exp(i\omega_0 t)$. This notation is useful for many different types of pulse shapes, as long as the pulse bandwidth is a small fraction of the carrier frequency:

$$\Delta\omega/\omega_0 \ll 1 \tag{2.24}$$

Under this approximation the electric field envelope $\mathcal{E}(t)$ is changing much slower than the rapidly oscillating second part $exp(i\omega_0 t)$. This assumption is generally known as the Slowly Varying Field Envelope Approximation (SVEA). Experimentally, the temporal and spectral intensity profiles $I(t)$ and $S(\omega)$ are easier to measure than the corresponding fields.

$$I(t) = \frac{\varepsilon_0 c}{T_{\text{opt}}}\int_{t-T_{\text{opt}}/2}^{t+T_{\text{opt}}/2} E(t')\cdot E^*(t')\mathrm{d}t' = \frac{\varepsilon_0 c}{2}|\mathcal{E}(t)|^2 \qquad \text{and} \qquad S(\omega) = \frac{\varepsilon_0 c}{2}|\mathcal{E}(\omega)|^2 \tag{2.25}$$

Here $T_{\text{opt}} = 2\pi/\omega_0$ is one optical cycle of the electric field ($T_{\text{opt}} \simeq 2.7\,\text{fs}$ for the fundamental at 800 nm of a typical Ti:Sa laser). For a Gaussian pulse the temporal intensity is

$$I(t) = \frac{\varepsilon_0 c}{2}\mathcal{E}_0^2\exp\left(-\frac{t^2}{\sigma_\tau^2}\right) \quad . \tag{2.26}$$

The Full Width Half Maximum durations (FWHM) of the intensities here are calculated temporally as $T = 2\sqrt{\ln 2}\,\sigma_\tau$ and spectrally as $\Delta\omega = 2\sqrt{\ln 2}\,\sigma_\omega$. The temporal and spectral pulse widths σ_τ and σ_ω respectively are used for the standard deviation of the Gaussian distribution of the electric field in time and frequency domain. The previous definitions for a Gaussian laser pulse allow one to calculate analytically, to a certain degree, the effects of a dispersive medium on a pulse. The phase shift, which a laser pulse acquires traveling through a dispersive material of length z=L, is defined by the wave number $k(\omega)$ in eqn. (2.20). Assuming approximation (2.24) the wave number $k(\omega)$ can be expanded in a Taylor series around ω_0:

$$k(\omega) = k_0 + k'\cdot(\omega-\omega_0) + \frac{1}{2}k''\cdot(\omega-\omega_0)^2 + \ \ldots\ + O(\omega^n) \quad , \tag{2.27}$$

where $k_0 = k(\omega_0) = \omega_0 n(\omega_0)/c$, $k' = \mathrm{d}k/\mathrm{d}\omega|_{\omega=\omega_0}$ and $k'' = \mathrm{d}^2k/\mathrm{d}\omega^2|_{\omega=\omega_0}$.

For simplicity in the following section, dispersion terms higher order than second order shall be disregarded. Inserting (2.27) in equation (2.18) and simplifying in terms of powers of ω one obtains

$$
\begin{aligned}
E(t,L) &= \tilde{\mathcal{E}}_0 \frac{1}{\sqrt{2\pi}} \int_{-\infty}^{\infty} \tilde{\mathcal{E}}_0 \exp\left(-\frac{(\omega-\omega_0)^2}{2\sigma_\omega^2}\right)(\omega-\omega_0)^2 \\
&\quad \cdot\exp[-i(k_0 L + k'L(\omega-\omega_0) + k''L(\omega-\omega_0)^2)]\exp(i\omega t)d\omega \\
&= \tilde{\mathcal{E}}_0 \frac{1}{\sqrt{2\pi}} \int_{-\infty}^{\infty} \exp\left[-\frac{1}{2}\left(\frac{1}{\sigma_\omega^2} + ik''L\right)(\omega-\omega_0)^2\right] \\
&\quad \cdot\exp[-i(k_0 L + k'L(\omega-\omega_0))]\exp(i\omega t)d\omega \qquad (2.28) \\
&= \tilde{\mathcal{E}}_0 \exp(i(\omega_0 t - k_0 L)) \\
&\quad \cdot\frac{1}{\sqrt{2\pi}} \int_{-\infty}^{\infty} \exp\left[\left(-\frac{1}{2}\frac{1}{\sigma_\omega^2} + ik''L\right)(\omega-\omega_0)^2\right] \exp\left[-i(t-k'L)(\omega-\omega_0)\right] d(\omega-\omega_0) \quad .
\end{aligned}
$$

Using

$$
\tilde{\sigma}_\omega^2 \equiv \left(\frac{1}{\sigma_\omega^2} + ik''L\right)^{-1} = \frac{\sigma_\omega^2 - ik''L\sigma_\omega^4}{1 + k''^2 L^2 \sigma_\omega^4}
$$

the Fourier transformation of (2.28) can be evaluated analytically. The result is again a Gaussian pulse, that has been shifted in time by $t - k'L$:

$$
E(t,L) = \tilde{\mathcal{E}}_0 |\tilde{\sigma}_\omega^2| \exp\left[i(\omega_0 t - k_0 L)\right] \exp\left[-\frac{1}{2}\tilde{\sigma}_\omega^2 (t-k'L)^2\right] \qquad (2.29)
$$

After some algebraic manipulations and some definitions one can transform the last expression into the form

$$
E_c(t) = \mathcal{E}_{0c} \exp\left[-\frac{(t-t_g)^2}{2\sigma_{tc}}\right] \exp\left[-i\frac{\alpha}{2}(t-t_g)^2\right] \exp[i\omega_0(t-t_g)]\exp[i\omega_0(t_g - t_{ph})] \qquad (2.30)
$$

with

$$
\begin{aligned}
\mathcal{E}_{0c} &= \frac{\mathcal{E}_0}{\sqrt[4]{1 + \phi_2^2 \sigma_\tau^{-4}}} && (2.31) \\
\sigma_{\tau c} &= \sigma_\tau \sqrt{1 + \phi_2^2 \sigma_\tau^{-4}} && (2.32) \\
\alpha &= -\frac{\phi_2}{\sigma_\tau^4 + \phi_2^2} && (2.33) \\
\phi_2 &= \left.\frac{\mathrm{d}^2\phi}{\mathrm{d}\omega^2}\right|_{\omega=\omega_0} = k''L = \beta && (2.34) \\
t_g &= \left.\frac{\mathrm{d}\phi}{\mathrm{d}\omega}\right|_{\omega=\omega_0} = k'L = \phi_1 && (2.35) \\
t_{ph} &= \frac{k(\omega_0)L}{\omega_0} = \frac{\phi_0}{\omega_0} \quad . && (2.36)
\end{aligned}
$$

From the exponential term $\left(\exp[i\omega_0(t-t_g)]\right)$ one finds, that the whole pulse is delayed by the group delay time, $t_g = k'L$. Thus, one can define a speed for the pulse envelope, which is called group velocity

$$
v_\mathrm{g} = \left.\frac{d\omega}{dk}\right|_{\omega=\omega_0} = 1/k' = L/\phi_1 \quad . \qquad (2.37)
$$

From the term $\exp[i\omega_0(t_g - t_p h)]$ in equation (2.30) follows, that the phase of the carrier frequency is delayed relative to the pulse center by $-t_{ph}$, which defines the carrier phase velocity $v_{ph} = L/t_{ph} = \omega_0/k(\omega_0) = \omega_0 L/\phi_0$. To simplify expression (2.30) further, one can substitute the shifted time by $(t - t_g) \rightarrow t$ and the phase offset of the last exponent by $\omega_0(t_g - t_{ph}) \rightarrow \phi_{off}$ thus resulting with:

$$E_c(t) = \mathcal{E}_{0c}\exp\left[-\frac{t^2}{2\sigma_{tc}} + i\left(-\frac{\alpha}{2}t^2 + \omega_0 t + \phi_{off}\right)\right] \tag{2.38}$$

The envelope of the electric field of the Gaussian pulse has a FWHM duration of $T_c = 2\sqrt{ln2}\sigma_{\tau c}$ and a quadratic time-dependent phase

$$\Phi(t) = -\frac{\alpha}{2}t^2 + \omega_0 t + \phi_{off} \quad . \tag{2.39}$$

The first derivative of the time-dependent phase function is called the *instantaneous* frequency ω_i, which specifies the momentary frequency inside the pulse at time t:

$$\omega_i(t) = \frac{\mathrm{d}\Phi(t)}{\mathrm{d}t} = \omega_0 - \alpha t \quad . \tag{2.40}$$

Thus, the frequencies inside a quadratic chirped pulse are arriving with respect to time according to the proportionality constant α. Hence, the coefficient $\alpha = -\mathrm{d}^2\Phi(t)/\mathrm{d}t^2$ is defined as the *linear chirp parameter* describing the frequency variation during the pulse. With this definition the chirp parameter α is negative for a positively chirped pulse. In a positively chirped pulse the frequency is rising. That is to say, red-shifted frequencies arrive earlier than blue-shifted frequencies. A positive chirp is acquired by a pulse passing through a dispersive material with a refractive index $n(\omega)$ with $\mathrm{d}n/\mathrm{d}\omega > 0$. Materials with $\mathrm{d}n/\mathrm{d}\omega > 0$ are called normal dispersive materials, while materials with $\mathrm{d}n/\mathrm{d}\omega < 0$ are called anomalous dispersive materials. For visible light all optical glasses show normal dispersion.
The refractive index $n(\lambda)$ of optical glasses can be calculated from the Sellmeier equation [SA09]:

$$n^2(\lambda) = 1 + \frac{B_1\lambda^2}{\lambda^2 - C_1} + \frac{B_2\lambda^2}{\lambda^2 - C_2} + \frac{B_3\lambda^2}{\lambda^2 - C_3} \tag{2.41}$$

with the constants $B_{1,2,3}$ and $C_{1,2,3}$. The following relations give the wave number k as a function of $n(\lambda)$ and $n(\omega)$ [DR95]:

$$\begin{aligned} k(\omega) &= \frac{\omega n(\omega)}{c} = \frac{2\pi n(\lambda)}{\lambda} \\ k' &= \frac{\mathrm{d}k}{\mathrm{d}\omega} = \frac{n(\omega)}{c_0} + \frac{\omega}{c_0}\frac{\mathrm{d}n}{\mathrm{d}\omega} = \frac{1}{c_0}\left(n(\lambda) - \lambda\frac{\mathrm{d}n}{\mathrm{d}\lambda}\right) \\ k'' &= \frac{\mathrm{d}^2k}{\mathrm{d}\omega^2} = \frac{2}{c_0}\frac{\mathrm{d}n}{\mathrm{d}\omega} + \frac{\omega}{c_0}\frac{\mathrm{d}^2n}{\mathrm{d}\omega^2} = \frac{\lambda}{2\pi c_0^2}\left(\lambda^2\frac{\mathrm{d}^2n}{\mathrm{d}\lambda^2}\right) \end{aligned} \tag{2.42}$$

2.1.2 Wave propagation in anisotropic crystals

In the previous chapter the special case of isotropic media has been discussed, in which the index of refraction is independent of the incident direction of the light wave. The speed of light in the medium is merely dependent on wavelength. For anisotropic media the index of refraction also depends on the polarization and the angle of incidence of the light. As a result the susceptibility χ becomes a tensor. In this case the induced polarization is not necessarily parallel to the electric field.

Returning to the wave equation (2.9), one can accommodate for anisotropic crystals by substituting the polarization vector $\boldsymbol{P}$ with $P_i = \epsilon_0 \chi_{ij} E_j$ and replace $\mu_0 \frac{\partial^2 \boldsymbol{P}}{\partial t^2}$ with $\frac{1}{\varepsilon_0 c^2} \boldsymbol{\chi} \frac{\partial^2 \boldsymbol{E}}{\partial t^2}$. Thus, one obtains the wave equation for anisotropic materials:

$$\nabla^2 \boldsymbol{E} - \frac{1}{c^2} \frac{\partial^2 \boldsymbol{E}}{\partial t^2} = \frac{1}{\varepsilon_0 c^2} \boldsymbol{\chi}, \frac{\partial^2 \boldsymbol{E}}{\partial t^2} \tag{2.43}$$

The susceptibility tensor $\boldsymbol{\chi}$ is symmetric for non-absorbing crystals and thus can be diagonalized with the non-vanishing eigenvalues also called main-susceptibilities $[\chi_{ii} \equiv \chi_{11}, \chi_{22}, \chi_{33}]$. The axes of a coordinate system, whose choice diagonalizes the susceptibility tensor, are called the principal axes of the crystal. According to (2.16) one obtains the main-indices of refraction from $n_i = \sqrt{1 + \chi_{ii}}$. With the plane-wave solution ansatz from 2.1.1, equation (2.43) becomes

$$\boldsymbol{k} \times (\boldsymbol{k} \times \boldsymbol{E}) + \frac{\omega^2}{c_0^2} \boldsymbol{E} = -\frac{\omega}{c_0^2} \chi_e \boldsymbol{E} \quad . \tag{2.44}$$

The solution of this equation demands, that the coefficient determinant vanishes:

$$\begin{vmatrix} \left(\frac{n_1 \omega}{c_0}\right)^2 - k_y^2 - k_x^2 & k_x k_y & k_x k_z \\ k_y k_x & \left(\frac{n_2 \omega}{c_0}\right)^2 - k_x^2 - k_z^2 & k_y k_z \\ k_z k_x & k_z k_y & \left(\frac{n_3 \omega}{c_0}\right)^2 - k_y^2 - k_x^2 \end{vmatrix} = 0 \tag{2.45}$$

This equation defines a plane in the three-dimensional $\boldsymbol{k}$-space. For the special cases of trigonal, hexagonal and tetragonal crystal lattices only two different main indices of refraction exist and (2.45) can be transformed into

$$\left(k_x^2 + k_y^2 + k_z^2 - n_2^2\right)\left(k_x^2 n_2^2 + k_y^2 n_2^2 + \left(k_z^2 - n_2^2\right) n_3^2\right) = 0 \quad . \tag{2.46}$$

From the second coefficient one obtains

$$\frac{k_x^2}{n_2^2} + \frac{k_y^2}{n_2^2} + \frac{k_z^2}{n_3^2} = 1 \quad , \tag{2.47}$$

which is the equation for an ellipsoid with two different axes. Any wave traveling inside the crystal defines an intersecting ellipse with this index ellipsoid. The length of the two axes of this ellipse (fig. 2.1) equals the indices of refraction n_2 and n_3 for light. The polarization of the incident light can be broke down into polarization components, which are parallel to one of these axes. The material is birefringent, if $n_2 \neq n_3$. For light propagating parallel to the vertical axis, the lengths of the ellipse axes are equal, and the material shows no polarization dependent light speed. This axis is called the optical axis. In general crystals can have up to two non-parallel optical axes. In this case equation (2.47) can be rewritten as

$$\boldsymbol{u} \cdot \boldsymbol{\eta} \cdot \boldsymbol{u} = 1 \tag{2.48}$$

with an arbitrary vector $\boldsymbol{u}$ in $\boldsymbol{k}$-space, and by defining the (electric) impermeability tensor

$$\boldsymbol{\eta} = (\boldsymbol{\chi_e} + \mathbf{1})^{-1} = \boldsymbol{\varepsilon}^{-1} \tag{2.49}$$

as the inverse of the permittivity tensor $\boldsymbol{\varepsilon}$:

$$\boldsymbol{\eta} = \begin{pmatrix} \frac{1}{n_1^2} & 0 & 0 \\ 0 & \frac{1}{n_2^2} & 0 \\ 0 & 0 & \frac{1}{n_3^2} \end{pmatrix} \quad . \tag{2.50}$$

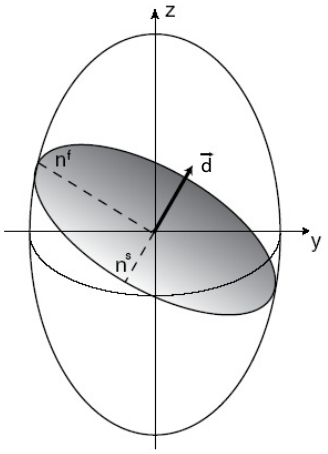

Figure 2.1: *Index ellipsoid and intersecting plane of the main axis of the indices of refraction.* The shaded ellipse is the intersection of the index ellipsoid with the plane normal to the direction of incidence $\boldsymbol{d}$ of the electromagnetic wave. Figure from [Ste07]

The electric impermeability tensor $\boldsymbol{\eta}$ specifies the impenetrability of a material for an electric field or an electro-magnetic wave. The three different eigenvalues λ_i of $\boldsymbol{\eta}$ relate to the main indices of refraction by

$$n_i = \frac{1}{\sqrt{\lambda_i}} \tag{2.51}$$

.

2.1.3 The Pockels effect in GaP and ZnTe

The following section on the electro-optical Pockels effect (EO-effect) is adapted from treatments found in [CSS+05a]. Crystals of the zinc blende structure (e.g. CdTe, GaAs, GaP, ZnS, ZnTe) are composed of two face-centered cubic lattices shifted by one quarter of the spatial diagonal and thus feature a high degree of symmetry. They are isotropic in the absence of an electric field, thus $n_1 = n_2 = n_3 = n_0$. For strong electric fields (E>10^5 V/m) the force of the electro-magnetic field deforms the crystal lattice resulting in an anisotropic crystal. The effect of the anisotropy on the susceptibility $\boldsymbol{\chi_e}$ can be described by a linear dependence on the electric field $\boldsymbol{E}$. In this sense equation (2.10) is interpretable as a Taylor expansion of $\boldsymbol{\chi_e}$ after the electrical field around ($\boldsymbol{E} = 0$) instead of an expansion of the polarization $\boldsymbol{P}$. Given the expression $\boldsymbol{\eta} = (\boldsymbol{\chi_e} + \mathbf{1})^{-1}$ of equation (2.49) it follows, that the electric impermeability $\boldsymbol{\eta}$ also contains terms of higher order in the presence of a strong external electric field and thus can either be expanded using a Taylor-expansion around E = 0:

$$\eta_{ij} = \eta_{ij}(0) + r_{ijk}E_k + s_{ijkl}E_kE_l + \dots \tag{2.52}$$

Here, r_{ijk} are the Pockels coefficients and s_{ijkl} the Kerr coefficients. For gallium phosphide (GaP) and zinc telluride (ZnTe) their order of magnitude is [CSS+05a]:

$$r_{ijk} \approx 10^{-12}\frac{\mathrm{m}}{\mathrm{V}} \qquad\qquad s_{ijkl} \approx 10^{-21}\frac{\mathrm{m}^2}{\mathrm{V}^2}$$

For these crystals, the Kerr effect can be neglected. The impermeability tensor thus becomes:

$$\boldsymbol{\eta}(\boldsymbol{E}) = \epsilon^{-1}\boldsymbol{I} + \boldsymbol{r}\cdot\boldsymbol{E} \tag{2.53}$$

where $\boldsymbol{I}$ is the identity matrix. Inserting this into equation (2.49) yields:

$$\boldsymbol{u}\cdot\boldsymbol{\eta}(\boldsymbol{E})\cdot\boldsymbol{u}=\sum_{i,j=1,2,3}\left(\epsilon^{-1}\delta_{i,j}+\sum_{k=1,2,3}r_{ijk}E_k\right)u_iu_j=1 \tag{2.54}$$

As the tensor $\boldsymbol{\eta}$ is symmetric ($r_{ijk}=r_{jik}$), it is common convention to simplify the tensor by introducing the following nomenclature to contract the indices [CSS05b]:

$(1,1)\rightarrow 1$	$r_{11k}\rightarrow r_{1k}$
$(2,2)\rightarrow 2$	$r_{22k}\rightarrow r_{2k}$
$(3,3)\rightarrow 3$	$r_{33k}\rightarrow r_{3k}$
$(2,3)\rightarrow 4$	$r_{23k}=r_{32k}\rightarrow r_{4k}$
$(1,3)\rightarrow 5$	$r_{13k}=r_{31k}\rightarrow r_{5k}$
$(1,2)\rightarrow 6$	$r_{12k}=r_{21k}\rightarrow r_{6k}$

(2.55)

The symmetry of a crystal restricts the number of independent elements of the matrix of electro-optical coefficients $\{r_{ijk}\}$. As a consequence, the matrix of electro-optical coefficients has only one independent entry ($r_{41}=r_{52}=r_{63}$).

With this information one can now calculate the equation for the electro-optically induced index ellipsoid in the same way as it was presented before in the linear case. Equation (2.48) assumes the following form:

$$\frac{1}{n_0^2}(k_1^2+k_2^2+k_3^2)+2r_{41}(E_1k_2k_3+E_2k_3k_1+E_3k_1k_2)=1 \tag{2.56}$$

The principle refraction indices are obtained when $\boldsymbol{\eta}(\boldsymbol{E})$ is diagonalized by performing a principle axis transformation. The crystals used in the following EO experiments are cut in the (110)-plane (Fig. 2.2 a)).

For theoretical discussion the nature of the external electric field of the EO experiments discussed in this thesis is assumed to be a linear polarized electric wave spectrally located in the THz-regime. The field strength is larger than 10^6 V/m. Due to these facts in the following the external electric field, which induces the presently discussed electro-optical effect, shall be referred to as the *THz-radiation* with wave-vector $\boldsymbol{k_{THz}}$.

To maximize the retardation between the orthogonal polarization components of the optical pulse due to the induced birefringence of the strong electric field of this THz-radiation, the propagation vectors of both radiation pulses propagate along the normal of the cut plane (110), thus their electric field vectors are within this plane. A new coordinate system (X,Y) is defined in this plane with

$$X=\frac{1}{\sqrt{2}}\begin{pmatrix}-1\\1\\0\end{pmatrix}\quad\text{and}\quad Y=\begin{pmatrix}0\\0\\1\end{pmatrix}\quad. \tag{2.57}$$

Detailed calculation on the main axis transformation of the index ellipsoid of (2.56) are found in [CSS$^+$05a]. From the calculated eigenvalues of $\boldsymbol{\eta}(\boldsymbol{E})$ along with (2.51) and the approximation $r_{41}E_{\mathrm{THz}}\ll 1/n_0^2$, the main indices of refraction of a zinc-blende type crystal in the presence of a strong electrical field are

$$\begin{aligned}
n_1 &= n_0+\tfrac{n_0^3r_{41}E_{\mathrm{THz}}}{4}\left(\sin\alpha+\sqrt{1+3\cos^2\alpha}\right)\\
n_2 &= n_0+\tfrac{n_0^3r_{41}E_{\mathrm{THz}}}{4}\left(\sin\alpha-\sqrt{1+3\cos^2\alpha}\right)\\
n_3 &= n_0-\tfrac{n_0^3r_{41}E_{\mathrm{THz}}}{2}\sin\alpha
\end{aligned}$$

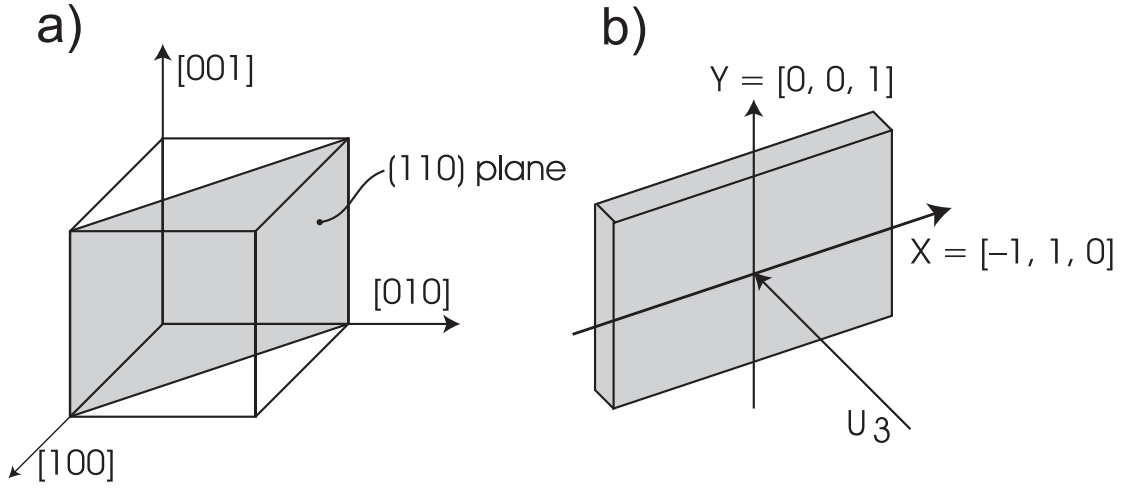

Figure 2.2: *(110)-cut plane and eigenvectors.*
a) The crystals used were cut along the (110)-plane which is shaded. b) The coordinate system (X,Y). The direction of incidence of the THz radiation and the laser pulse are parallel to the vector $\boldsymbol{U}_3$ (b). (Fig. from [CSS+05a])

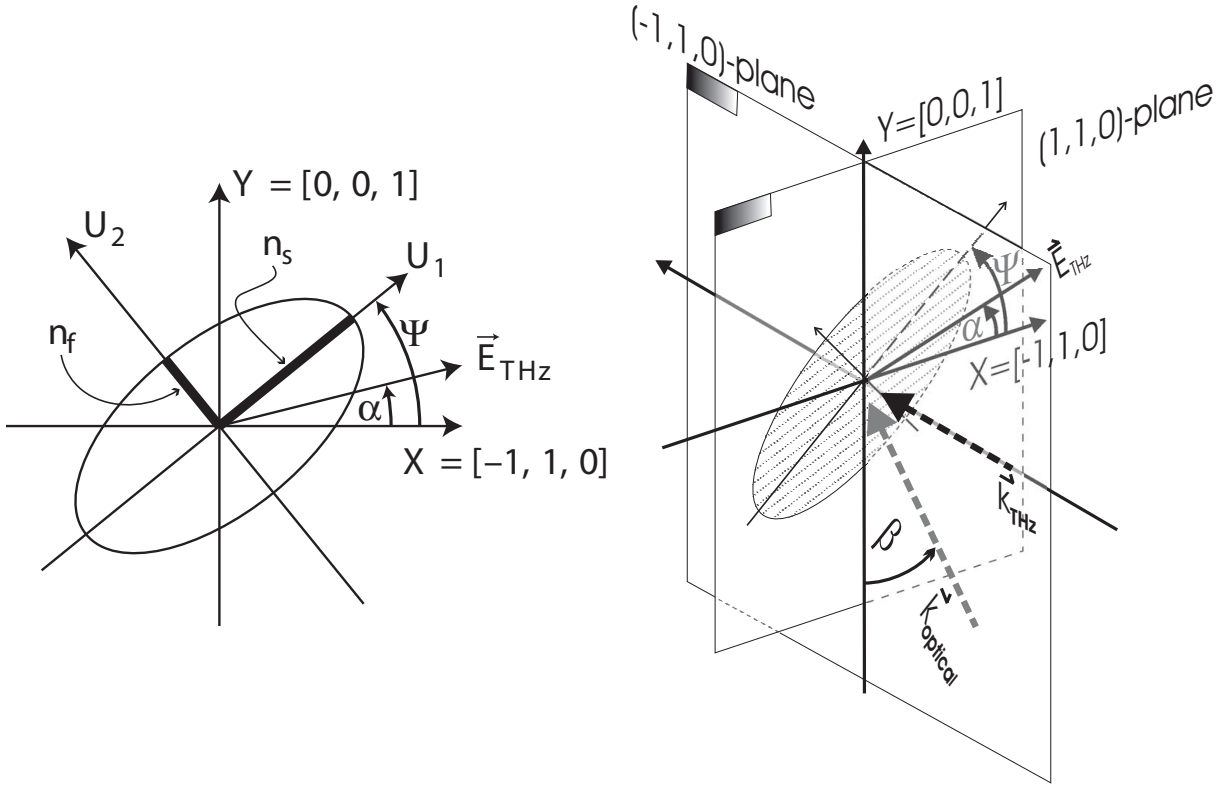

Figure 2.3: *Refractive index ellipsoid of uniaxial EO-crystals within a strong electric field.*
The THz radiation is parallel to the normal of the (110) plane defined by the unit vector $\boldsymbol{U}_3 = (-1/\sqrt{2}, -1/\sqrt{2}, 0)$. An optical propagation vector parallel to the (-110)-plane can include an azimuth angle $\beta \neq 90°$ with the plane (110). If the optical pulse is p-polarized, its electric field vector is still in the cut-plane (110) and the phase retardation of (2.101) is still maximal. The electric field vector $\boldsymbol{E}_{\mathrm{THz}}$ encloses an angle α with respect to the X=[-110]-axis of the crystal. The angle between the long half axis of the ellipse and the X axis is defined by $\psi(\alpha)$. (Fig. adapted from [CSS+05a])

with the normalized eigenvectors

$$\boldsymbol{U}_1 = \frac{1}{2}\sqrt{1+\frac{\sin\alpha}{\sqrt{1+3\cos^2\alpha}}}\begin{pmatrix} -1 \\ 1 \\ \frac{2\sqrt{2}\cos\alpha}{\sqrt{1+3\cos^2\alpha}+\sin\alpha} \end{pmatrix} \qquad \boldsymbol{U}_2 = \frac{1}{2}\sqrt{1+\frac{\sin\alpha}{\sqrt{1+3\cos^2\alpha}}}\begin{pmatrix} 1 \\ -1 \\ \frac{2\sqrt{2}\cos\alpha}{\sqrt{1+3\cos^2\alpha}-\sin\alpha} \end{pmatrix} .$$

$$\boldsymbol{U}_3 = \frac{1}{\sqrt{2}}\begin{pmatrix} -1 \\ -1 \\ 0 \end{pmatrix}$$

The eigenvectors $\boldsymbol{U}_1$ and $\boldsymbol{U}_2$ are perpendicular to each other and $\boldsymbol{U}_1$ encloses an angle ψ with the X-axis, i.e. the [-110] axis (see fig. 2.3). This angle can be evaluated by using the scalar product of $< \boldsymbol{U}_1, \boldsymbol{X} >$ and applying the relation $\cos(2\psi) = 2\cos^2\psi - 1$ to yield

$$\cos 2\psi = \frac{\sin\alpha}{\sqrt{1+3\cos^2\alpha}} \quad . \tag{2.58}$$

The third principal axis is perpendicular to the (110) crystal plane and parallel to the propagation of the THz-radiation.
The index ellipse shown in figure 2.3 is taken from the intersection between the main axis transformed index ellipsoid and the (110)-plane of the crystal. The Ti:Sa laser beam of angular frequency ω may be incident on the EO crystal along the eigenvector $\boldsymbol{U}_3$, or it can tilt to include an angle β with respect to the y-axis (0,0,1). If $\beta \neq 0$ the beam must be p-polarized with respect to the (110)-plane. This keeps the electric vector $\boldsymbol{E}_{\text{laser}}$ completely within the (110) plane and maximizes the applied phase shift. In this case, for a crystal of thickness d, the two components of $\boldsymbol{E}_{\text{laser}}$ along the principal axes $\boldsymbol{U}_1$ and $\boldsymbol{U}_2$ receive a relative phase shift of

$$\Gamma(\alpha) = \frac{\omega d}{c}(n_1 - n_2) = \frac{\omega d}{2c} n_0^3 r_{41} E_{\text{THz}} \sqrt{1+3\cos^2\alpha} \quad . \tag{2.59}$$

In the following this phase shift Γ will be referred to as the *phase retardation* or *phase retardation parameter*. It is proportional to the electric field strength E_{THz} of the external field and depends on the angle α between the field vector and the X-axis. The dependence of ψ and Γ on the angle α is shown in figure 2.4. The maximal phase change is obtained for $\alpha = 0 \Rightarrow \psi = \pi/4$. The main refractive indices and the relative phase shift are plotted in figure 2.4 as a function of the angle α between the electric vector $\boldsymbol{E}_{\text{THz}}$ of the THz field and the X-axis. The larger index corresponds to a slower speed of the light, the smaller index to a faster speed. Hence, it is customary to designate the refractive indices also by $n_{\text{s}} = n_1$, $n_{\text{f}} = n_2$.

2.2 Interaction of THz- and optical pulses with GaP and ZnTe crystals

So far the Pockels effect within an electro-optical crystal under the influence of a constant electric field has been discussed. However, the situation changes, if the electro-optical crystal is exposed to the electric field of the electron bunch of a linear accelerator. In this case the electric field shows a pulse like behavior. The nature of this pulsed behavior shall be discussed at first. Once the field dynamic of a relativistic electron bunch is understood, a detailed discussion on the frequency dependent Pockels effect will be presented. The understanding of this frequency dependence is important in the discussion of electro-optically based sampling techniques, which are used to characterize the electron bunch induced electric pulse temporally and spectrally.

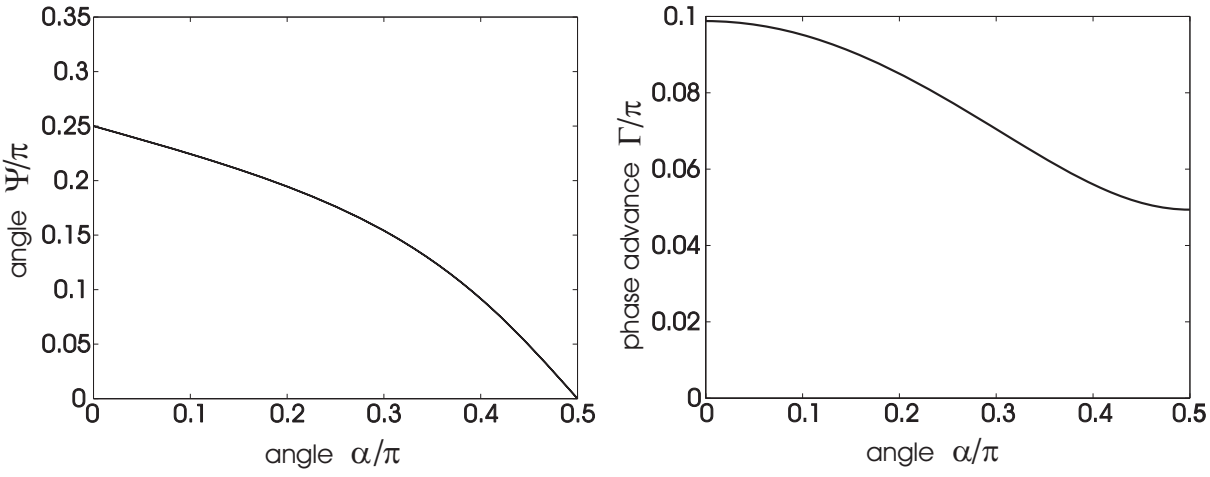

(a) (b)

Figure 2.4: *Calculated angle $\psi(\alpha)$ and the corresponding retardation $\Gamma(\alpha)$*
(a) This figure plots the angle ψ between the first principal axis of the refractive index ellipsoid and the X axis as a function of the angle α between the electric vector $\boldsymbol{E}_{\mathrm{THz}}$ of the THz field and the X axis. (b) The retardation parameter Γ, i.e. the relative phase shift between the two orthogonal components of the laser field $\boldsymbol{E}_{\mathrm{laser}}$, plotted as a function of α. The phase retardation curve is computed for a ZnTe crystal of d=500 μm thickness and a THz field $E_a = 10^6$ V/m. (Fig. from [Ste07])

2.2.1 The Coulomb field of relativistic electron bunches

The electric field $\boldsymbol{E}$ of an electron resting at $\boldsymbol{r} = (0, 0, 0)$ is defined by Coulomb's law:

$$\boldsymbol{E}(\boldsymbol{r}) = \frac{q}{4\pi\varepsilon_0 r^2}\frac{\boldsymbol{r}}{r} \tag{2.60}$$

where the permittivity of free space is ε_0 and the electron charge is $q = -e$. For accelerated electrons moving with a speed close to the speed of light $v \approx c$ in z-direction, the electromagnetic field needs to be Lorenz transformed to the laboratory frame. The components of $\boldsymbol{E}$ are [Jac99]:

$$\begin{aligned} E_x &= \frac{q\gamma}{4\pi\varepsilon_0}\cdot\frac{x}{(x^2+y^2+\gamma^2(z-vt)^2)^{3/2}} \\ E_y &= \frac{q\gamma}{4\pi\varepsilon_0}\cdot\frac{y}{(x^2+y^2+\gamma^2(z-vt)^2)^{3/2}} \\ E_z &= \frac{q\gamma}{4\pi\varepsilon_0}\cdot\frac{z-vt}{(x^2+y^2+\gamma^2(z-vt)^2)^{3/2}} \end{aligned} \tag{2.61}$$

with the relativistic Lorenz factor $\gamma = \frac{1}{\sqrt{1-(v/c)^2}}$. Switching to a cylindrical coordinate system (r, z, φ) with $r = \sqrt{x^2+y^2}$ and $\varphi = \arctan(y/x)$, the electric field of the moving electron in the laboratory system becomes

$$E_r(r,t) = \frac{q\gamma}{4\pi\varepsilon_0}\cdot\frac{r}{(r^2+\gamma^2v^2t^2)^{3/2}} \tag{2.62}$$

$$E_z(r,t) = -\frac{q\gamma}{4\pi\varepsilon_0}\cdot\frac{vt}{(r^2+\gamma^2v^2t^2)^{3/2}} \quad . \tag{2.63}$$

The assumptions in here are, that at time $t = 0$ the electron shall be at $(0, 0, 0)$ and the observer is resting at $(r, 0, 0)$ transversally to the electron and in close vicinity (several [mm] away). Hence the

transversal component $E_\varphi(r,t) = E_y(x,0,z,t)$ is zero. At time $t = 0$ the radial component amounts to $E_r(r,0) = \gamma \cdot E_{r,v=0}$, i.e. the electric field is enlarged by the γ-factor relative to the field of a stationary electron.

The time interval $\Delta t'_e = \frac{r}{v}$ is a characteristic time interval within the context of the analysis of the temporal dynamic of the electric field as the electron bunch passes the point of observation. This time interval is noted within the inertial system of the electron bunch. In the laboratory system this time interval is reduced by the Lorentz factor and is $\Delta t_e = \frac{r}{\gamma v}$. At the two characteristic times $\pm\Delta t_e$ before and after the electron bunch passes the point of observation at $(r,0,0)$, the electric field components are calculated from equations ((2.62),(2.63)) to

$$E_r(r,\Delta t_e) = \frac{q\gamma}{4\pi\varepsilon_0} \cdot \frac{r}{(r^2+1)^{3/2}} \tag{2.64}$$

$$E_z(r,\Delta t_e) = -\frac{q}{4\pi\varepsilon_0} \cdot \frac{r}{(r^2+1)^{3/2}} = \frac{1}{\gamma} \cdot E_r(r,\Delta t) \quad . \tag{2.65}$$

Hence, the longitudinal component is reduced by the Lorenz factor in comparison to the radial component. From this follows, that the observed field in the laboratory system is longitudinally contracted. It forms a flat disc with an opening angle of $2/\gamma$ perpendicular to the direction of movement of the electron [Jac99].

The frequency components $|\tilde{E}_r(r,\omega)|$ of this field detected by an observer at $z = 0$ at a distance r from the electron trajectory, can be calculated using the Fourier transform $\mathcal{F}$ of the radial electric field:

$$\tilde{E}_r(r,\omega) = \mathcal{F}\{E_r(r,t)\} = \frac{1}{\sqrt{2\pi}} \int_{-\infty}^{\infty} E_r(r,t)\exp(-i\omega t)\mathrm{d}t \tag{2.66}$$

$$E_r(r,t) = \mathcal{F}^{-1}\{\tilde{E}_r(r,\omega)\} = \frac{1}{\sqrt{2\pi}} \int_{-\infty}^{\infty} \tilde{E}_r(r,\omega)\exp(i\omega t)\mathrm{d}\omega$$

The Fourier transform is found to be [Jac99, CSS05b]:

$$\tilde{E}_r(r,\omega) = \frac{q\omega}{(2\pi)^{3/2}\varepsilon_0\beta\gamma c^3} K_1\left(\frac{\omega}{\beta\gamma c} r\right) \tag{2.67}$$

The function K_1 is a modified Bessel function. Assuming an electron bunch with an infinitesimally small radius and a longitudinal electron distribution $Q(t)$ moving along the z-axis the radial field becomes:

$$E_{r,Q}(r,t) = (E_r * Q)(r,t) \tag{2.68}$$

$$= \int_{-\infty}^{\infty} E_r(r,t-s)Q(t)\mathrm{d}s \tag{2.69}$$

and the corresponding frequency components $|\tilde{E}_{r,Q}(\omega)|$ are:

$$\tilde{E}_{r,Q}(\omega) = \mathcal{F}\{(E_r * Q)(t)\} \tag{2.70}$$

$$= \mathcal{F}\{E_r(t)\} \cdot \mathcal{F}\{Q(t)\} \tag{2.71}$$

Figure 2.5 shows the radial electric field created by the simulated charge distribution of a bunch at FLASH [Doh] at a distance of r=5 mm from the axis (a) and also the corresponding Fourier

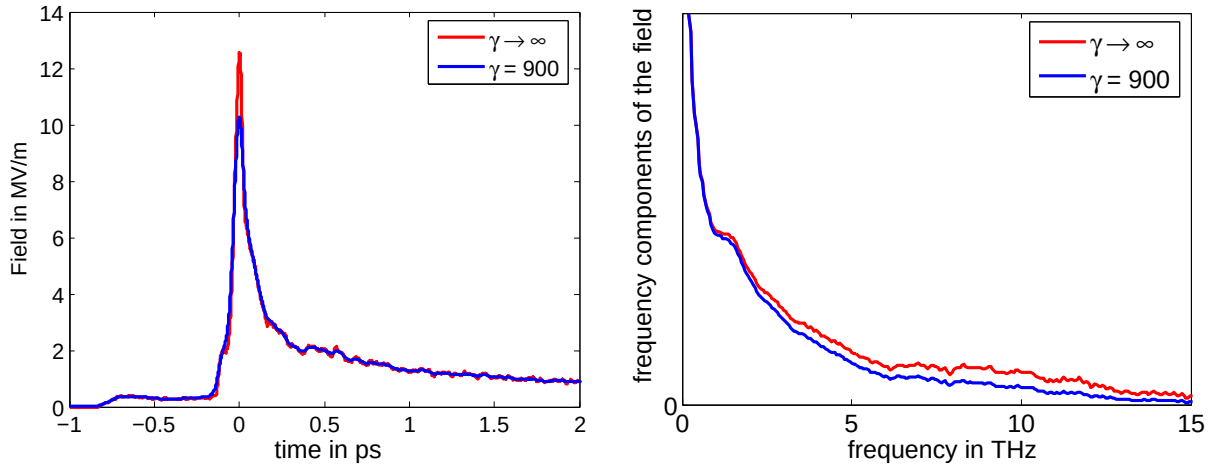

(a) (b)

Figure 2.5: *Simulated electric field distribution for a 450 MeV bunch at FLASH.*
a) The radial electric field of a simulated electron bunch of 450 MeV kinetic energy after the last accelerating module at a distance of $r = 5$ mm (blue curve). The total charge is 500 pC.
b) Fourier transform of the electric field at a distance $r = 5$ mm (blue curve). The red curves show the electric field of the simulated charge distribution for $\gamma \rightarrow \infty$ in time and frequency domain. (Figure from [Ste07])

transform (b). The electron bunch is treated as a 1D electron distribution. This assumption is reasonable, since the transverse size of the real electron bunch is between 150-350 µm FWHM [BFR+01] and thus much smaller than the radial distance from the observation point. The total charge is 500 pC and the particle energy is 450 MeV. The small opening angle of $2/\gamma$ leads to a slight temporal broadening of the electric field pulse at a distance r=5 mm, which results in a reduction of the high frequency parts of the electric field [Ste07]. It is obvious, that the carrier frequency of the pulse is zero, which differs from typical optical laser pulses. The reason is, that the pulse like field behavior is a direct consequence of the relativistic speed of the electron bunch. All that happens as the electron bunch passes by a transversal point of observation in a certain distance to the electron bunch is, that a sudden increase followed by a rapid decrease of the radial electric field is observed. The electron bunch does not emit radiation, since the streamlines of the electric field are not divided from the electron bunch. But as the frequency spectrum of this pulse is located in the lower THz regime, this special electric pulse can be compared with an equivalent THz pulse as emitted from a laser based THz source like in [Jam03]. The field amplitude is proportional in strength to the longitudinal electron bunch density distribution, which owns a pulse like distribution in space. No intermediate electric field sign switch could appear, which explains the lack of a non-zero carrier frequency.

Due to the nonlinear compression of the electron bunches at FLASH (cf. 3.1.1.3), the bunches at the end of the accelerator have a sharp spike with a full width at half maximum (FWHM) duration in the order of 70-110 fs [Röh08] in their longitudinal charge distribution followed by a slow ps-decay (fig. 2.5). This spike leads to frequency components of 10 THz and above [Ste07].

2.2.2 The frequency dependent Pockels effect

Equation (2.101) describes the phase shift between the ordinary and the extra-ordinary wave of a polarized optical light wave within an electro-optical crystal, which is exposed to a strong, homo-

geneous but temporally constant electric field. However, the electric field of the electron bunch of a linear accelerator is pulsed and consists of Fourier components from zero up to several THz (section 2.5). If this THz pulse enters an EO-crystal, it interacts with the crystal lattice, which could result in resonance phenomena, so called transversal (TO) or longitudinal (LO) lattice oscillations. These resonances strongly modulate the complex index of refraction n_{THz} and electro-optical coefficient r_{41}. These effects induce a frequency dependence of the electro-optical phase retardation $\Gamma(t)$ of an electro-magnetic wave inside an electro-optical crystal.

2.2.2.1 Refractive index of GaP and ZnTe in the THz regime

For the electro-optic crystals ZnTe and GaP a good description of n_{THz} in the THz regime is obtained by restricting the frequency sum of the electro-optical response to the lowest transverse-optical (TO) lattice oscillation [CSS+05a]. Accordingly the refractive index can be derived from

$$n_{\mathrm{THz}}(f) = n(f) + i\kappa(f) = \sqrt{\varepsilon(f)} \tag{2.72}$$

where

$$\varepsilon(f) = \varepsilon_{el} + \frac{S_0 f_0^2}{f_0^2 - f^2 - i\Gamma_0 f} \quad . \tag{2.73}$$

For the electro-optical crystal materials Gallium-Phosphide (GaP) and Zinc-Telluride (ZnTe) a measured data set of the refractive index in the THz regime is shown in the corresponding plots of fig. 2.6. Fitting (2.73) to the most recent measurements found in [GZM+99] for ZnTe and of [WZ97] for GaP, one finds the following set of parameters to model the index of refraction for GaP and ZnTe in the THz regime.

$$\boxed{\mathrm{n_{THz}\{ZnTe\}}: \ \varepsilon_{el} = 7.40 \pm 8\%\,, \ f_0 = 5.3 \pm 0.6\%\ \mathrm{THz}\,, \ S_0 = 2.7 \pm 18\%\,, \ \Gamma_0 = 0.09\ \mathrm{THz}} \tag{2.74}$$

$$\boxed{\mathrm{n_{THz}\{GaP\}}: \ \varepsilon_{el} = 8.7\,, \ f_0 = 10.98\,\mathrm{T}Hz\,, \ S_0 = 1.8\,, \ \Gamma_0 = 0.02\ \mathrm{THz}} \tag{2.75}$$

The current measured data situation for ZnTe is sparse, which is reflected by the provided error ranges for the parameters calculated from the spread of the literature parameter values from different sources as provided in [CSS+08]. For GaP the estimated errors are smaller, since more precise data sets exist. For GaP the average parameter errors are estimated to be just a few percent [CSS05b].

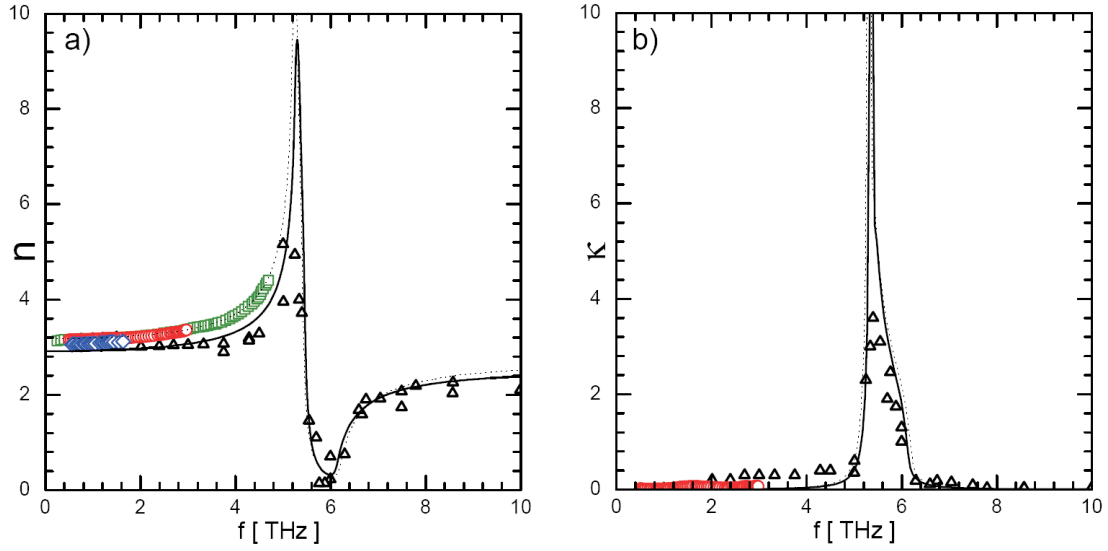

(a) ZnTe

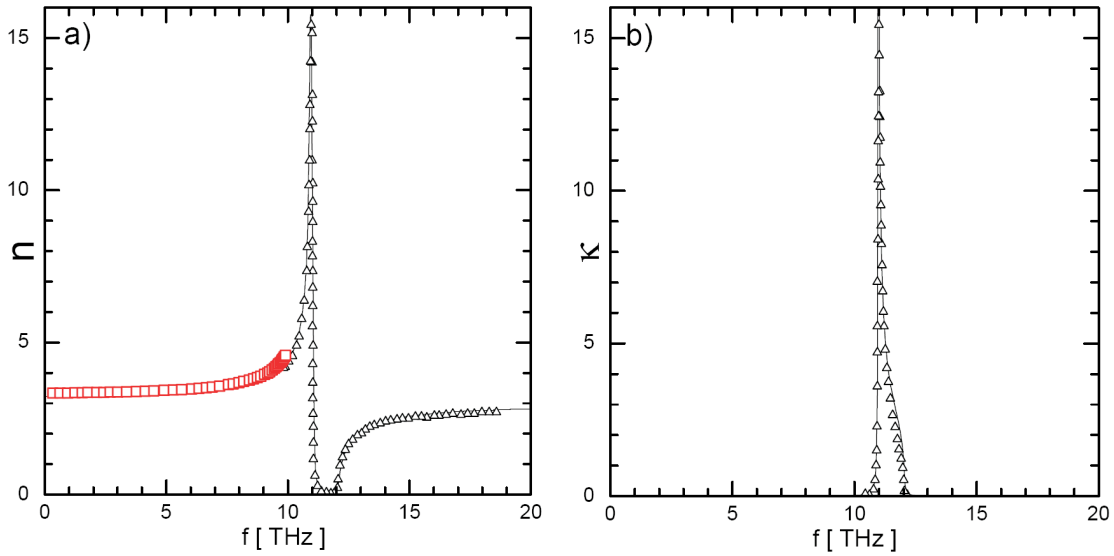

(b) GaP

Figure 2.6: *Various measurements of the real and imaginary part of the refractive index n_{THz} of ZnTe (upper) and GaP (lower) and numerical fits according to equation* (2.73).
The first transverse oscillation TO of the crystal creates a non-zero imaginary part of the index of refraction corresponding to absorption of electro-magnetic waves of the corresponding frequencies. Experimental data shown for ZnTe: Measurement points squares (□) from [[GZM+99]], open triangles (△) from ref. [War91], diamonds (⋄) from [HHMT73] and the circles ∘ from [SWJ01],
and for GaP: Measurement points △ from [KS60] and □ from [WZ97]. The resonance freq. of the first TO for GaP is at 10.98 THz and for ZnTe at 5.31 THz.
When using a GaP crystal, higher frequency from the THz field are accepted in the process of electro-optical sampling and thus the EO signal can map faster temporal structures of the THz signal. Details are found in the text. (Fig. adapted from [CSS+05a])

2.2.2.2 Electro-optical coefficient of GaP and ZnTe in the THz regime

The frequency dependence of the electro-optical coefficient r_{41} of equation (2.101) is governed by the first TO resonance in a way very similar to the index of refraction (compare fig. 2.7). A theoretical model describing measured data is found in [FH66]:

$$r_{41}(f) = d_E \left(1 + \frac{C f_0^2}{f_0^2 - f^2 - i\Gamma_0 f}\right) \tag{2.76}$$

with the following parameters for ZnTe and GaP [CSS+08]:

$$\boxed{\mathrm{r_{41}\{ZnTe\}}: \; d_E = 4.25 \cdot 10^{-12}\ \mathrm{m/V}\,, \; C = -0.07\,, \; f_0 = 5.3\ \mathrm{THz}\,, \; \Gamma_0 = 0.09\ \mathrm{THz}} \tag{2.77}$$

$$\boxed{\mathrm{r_{41}\{GaP\}}: \; d_E = 1 \cdot 10^{-12}\ \mathrm{m/V}\,, \; C = -0.53\,, \; f_0 = 10.98\ \mathrm{THz}\,, \; \Gamma_0 = 0.02\ \mathrm{THz}} \tag{2.78}$$

Differences between GaP and ZnTe are found in the amplitude d_E of the electro-optical coefficient and the frequency f_0 and width Γ_0 of the TO resonance of the index of refraction. The first characterizes the strength of the electro-optical retardation an electro-optical material induces, when it is applied to an electric field. The latter influences the temporal response of the electro-optical retardation to an external time dependent electro-magnetic field. It should be noted, that like in the

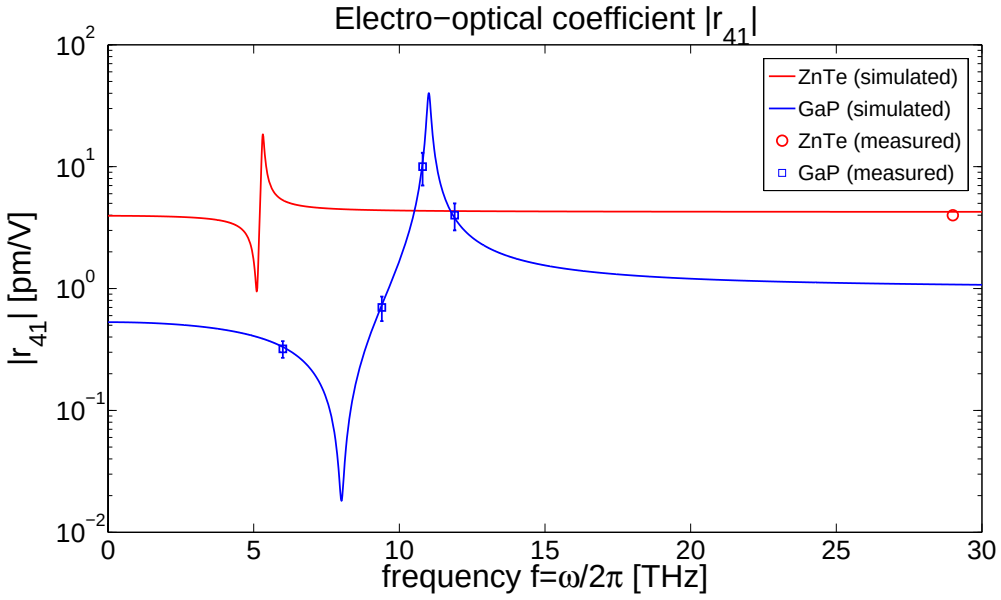

Figure 2.7: *Modulus of the electro-optical coefficient r_{41} of GaP and ZnTe*
Calculated curves and measured data of the electro-optical coefficient $\|r_{41}\|$ of GaP (red) and ZnTe (blue) according to formula (2.76) and the provided parameters in (2.77) and (2.78). The □ are data on GaP taken from [FH66]. The ∘ data point for ZnTe is from [TA71].

case of the index of refraction before the available measured data on r_{41} for ZnTe is different, than it is in the case for GaP, very sparse. The only existing measured data for the absolute value of r_{41} is located in the range of 30 THz, 100 THz and 900 THz [CSS+08], where it amounts to 4-5 pm/V at this frequency regime. Thus the average parameter errors are comparable to those of the index of refraction in the order of $\sim 10\%$ for ZnTe and $\sim 1\%$ for GaP.

Despite of this sparse data situation the use of equation (2.76) is justified by the observation, that r_{41} is affected by the same lattice oscillations as the dielectric function, which had been demonstrated in [FH66]. Due to the low piezoelectric constant of ZnTe [SJ66, BJS63], the value of the constant

C is expected to be small, so the unknown low-frequency value of r_{41} should not differ appreciably from the values measured at high frequency [CSS+08]. For the plot of fig. 2.7 the value of $C = 0.07$ has been taken from ref. [LHS+99b].

2.2.2.3 Phase velocity mismatch between THz and NIR pulse in GaP and ZnTe

To achieve ideal electro-optical sampling conditions, the THz wave and the laser pulse should propagate at the same speed through the crystal. However, the phase and group velocities of a THz wave and a NIR pulse of a certain carrier frequency are matched only within a small THz frequency range [WZ97]. The pulse speed v_g is characterized by the refractive indices of the material and the pulse wavelengths. A Ti:Sa laser pulse propagates with the group velocity

$$v_g = \frac{c}{n}\left(1 + \frac{\lambda}{n}\frac{\mathrm{d}n}{\mathrm{d}\lambda}\right) = \frac{c}{\left(n + f\frac{\mathrm{d}n}{\mathrm{d}f}\right)} \quad . \tag{2.79}$$

The index of refraction in the optical regime follows from the parametrization found in [Mar64] for ZnTe to be

$$n(\lambda) = \sqrt{4.27 + \frac{2.01\lambda^2}{\lambda^2 - 0.00903279}} \quad , \tag{2.80}$$

and for GaP found in[PPY76] to be

$$n(\lambda) = \sqrt{2.670 + \frac{6.40\lambda^2}{\lambda^2 - 0.00903279}} \quad . \tag{2.81}$$

The index of refraction in the THz-regime is defined by equations (2.72), (2.73) and the parameters provided in equations (2.74) and (2.75) respectively. The phase and group velocities in the THz range of ZnTe and GaP are shown in figure 2.8 as a function of frequency. For comparison the optical group velocity at $\lambda = 0.8$ μm is plotted. Note that $v_g = 0.309\,c$ for ZnTe and $v_g = 0.280\,c$ for GaP. At reduced THz frequencies a THz wave propagates with a higher phase velocity than the laser pulse. There is a growing mismatch between the THz phase velocity and the optical group velocity while approaching the lattice resonance of 5.3 THz in ZnTe and 11 THz in GaP [CSS+05a]. This effect is known as phase-slippage. It can be calculated for each monochromatic THz wave separately by

$$\begin{aligned} \Delta\Phi_{slip} &= \frac{\omega_{THz}}{2\pi} \cdot \Delta t_{slip} \\ &= \frac{\omega_{THz}}{2\pi} \cdot \left(v_{g,NIR} - v_{ph,THz}\right) \cdot d \quad . \end{aligned} \tag{2.82}$$

2.2.2.4 Electro-optical response function

It is customary to characterize the electro-optic efficiency by a response function which depends on the THz frequency f and the crystal thickness d. This function also accounts for all previously mentioned effects, including phase-slippage, the frequency dependency of the index of refraction and the electro-optical coefficient in the THz regime:

$$\begin{aligned} G(f,d) &= \frac{2}{1 + n(f) + i\kappa(f)} \frac{r_{41}(f)}{d} \int_0^d \int_{-\infty}^{\infty} \exp[i(kz - 2\pi f t]\delta(z - v_g t)\,\mathrm{d}t\,\mathrm{d}z \\ &= \frac{2}{1 + n(f) + i\kappa(f)} \frac{r_{41}(f)}{d} \int_0^d \exp\left[i\,2\pi f\, z\left(\frac{1}{v_{\mathrm{ph}}(f)} - \frac{1}{v_g}\right)\right]\mathrm{d}z \quad , \end{aligned} \tag{2.83}$$

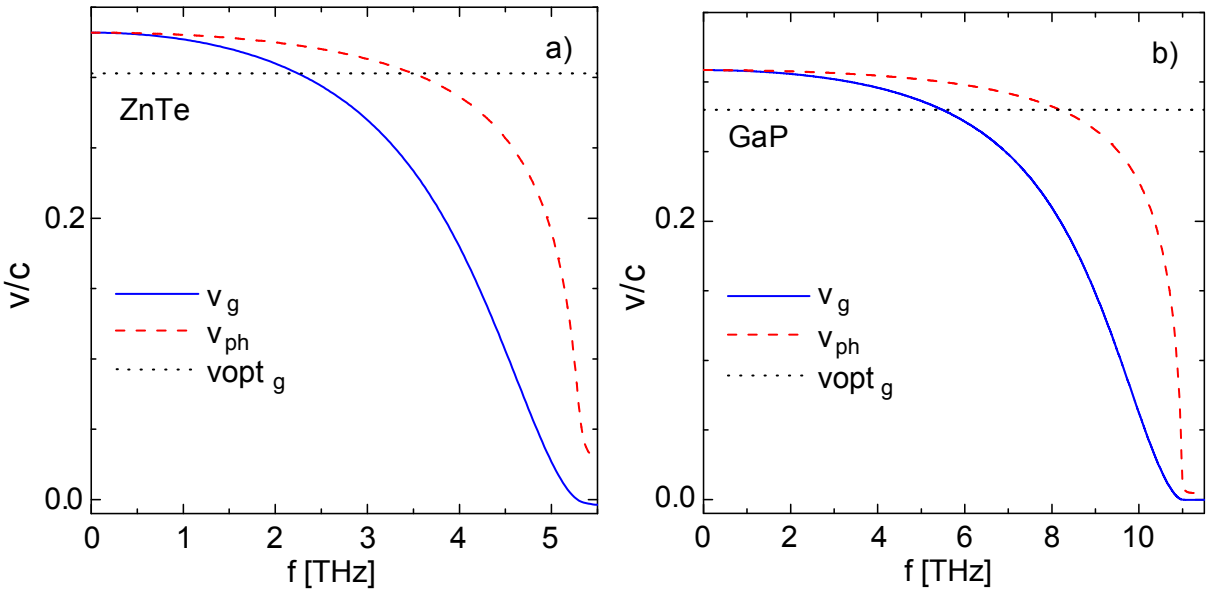

Figure 2.8: *Phase velocity of ZnTe (a) and GaP (b) in the THz range.*
The velocities have been divided by c and have been plotted up to the frequency of the TO resonance of each crystal and thus the frequency scales are different. The group velocity of optical radiation at 0.8 µm is shown as a dotted line. For the sake of completeness the group velocity of a short THz pulse with a non-zero carrier frequency is plotted either. However, for the THz pulse of the electron bunch at FLASH the carrier frequency is zero. (Fig. from [CSS+05a])

where $v_{\mathrm{ph}}(f)$ is the phase velocity and v_{g} is the group velocity of the NIR laser wavelength λ_0. The factor

$$A_{trans}(f) = \frac{2}{1 + n(f) + i\kappa(f)} \tag{2.84}$$

is the frequency-dependent transmission coefficient for the transition of the THz electric field from vacuum into the EO crystal. For a homogeneous crystal the last integral can be evaluated further, such that

$$G(f,d) = \frac{r_{41}c}{(1+n_{\mathrm{THz}})\pi f\,\Delta n}\left[\exp\left(i2\pi f d\frac{\Delta n}{c}\right) - 1\right] \tag{2.85}$$

where the index difference $\Delta n = n_{\mathrm{THz}} - c/v_{\mathrm{g}}$. Some authors do not consider the EO coefficient $r_{41}(f)$ in the definition of the response function. In this thesis the response function shall include all three effects, thus it can also be referred to as the effective response function, while the response function excluding r_{41} shall be defined as refractive response function for now.

Both types of EO response functions of ZnTe are shown in fig. 2.9 for different crystal thicknesses from 100 µm to 1 mm with and without considering the electro-optical coefficient r_{41}.

The corresponding pair of EO response functions of GaP is shown in fig. 2.10 for different crystal thicknesses from 100 µm to 1 mm. The response functions of GaP and ZnTe generally differ in amplitude (response strength) and in the highest accepted frequency of non-zero response. The differences regarding the amplitude result from the difference of the absolute value of the electro-optical coefficient r_{41}. It is 6 times larger for ZnTe than for GaP. Within the frequency regime smaller than the frequency of the transverse-optical resonance, one finds, that the minimum of the modulus of the electro-optical coefficient r_{41} of GaP is found at 7.8 THz (compare fig. 2.7). This minimum of r_{41} shifts the cut frequency of the refractive response function from 11 THz to an effective cut frequency of 7.8 THz. Additionally, this minimum explains the differences between the effective response function and the refractive response function of GaP and ZnTe respectively.

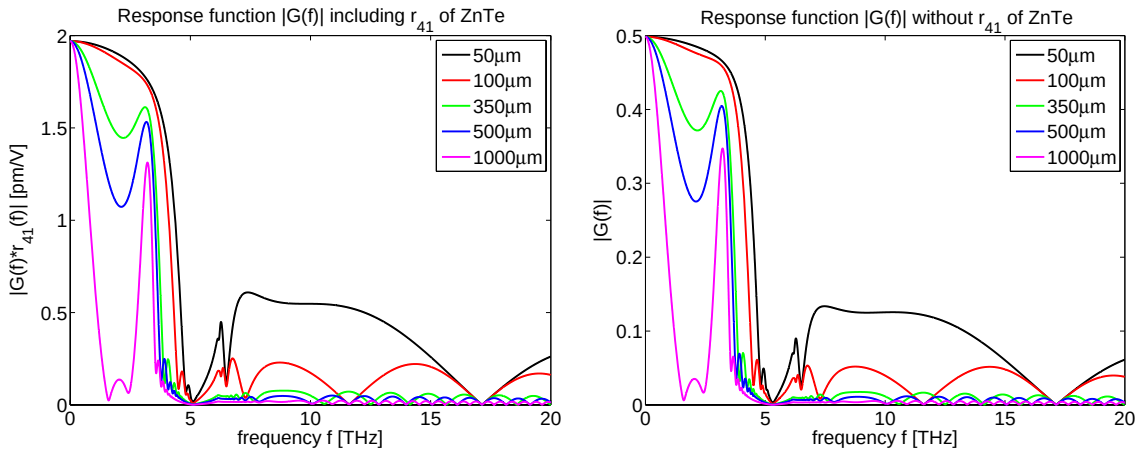

(a) (b)

Figure 2.9: *Response function of ZnTe.*
(a) effective EO response function of ZnTe for crystal thickness of 50 µm, 100 µm, 350 µm and 1000 µm. (b) The refractive response function G/r_{41}. In opposite to the GaP crystal, the electro-optical coefficient r_{41} has no strong influence on the response function of ZnTe. The reason is, that the real part of r_{41} is only negative in a small region between 5.0 and 5.3 THz in opposite to GaP. There the region of negative real part ranges from the zero point at 7.5 Thz until the TO resonance at 11 THz. For frequencies smaller than the resonance the absolute value of r_{41} of ZnTe is 6 times larger than for GaP. Hence, ZnTe suits better than GaP as an electro-optical detector of THz signals composed of Fourier components below 5.3 THz.

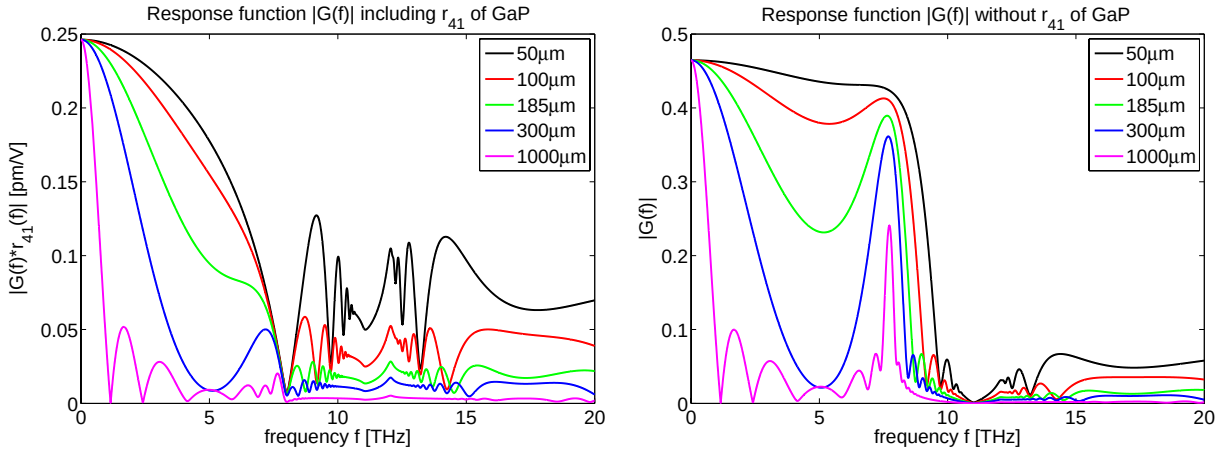

(a) (b)

Figure 2.10: *Response function of GaP.*
(a) effective EO response function $G(\omega)$ of GaP for a crystal thickness of 50 µm, 100 µm, 185 µm, 300 µm and 1000 µm. (b) The response function G/r_{41}. For thin crystals the frequency bandwidth of electro-optical acceptance of GaP is twice as large as for ZnTe, thus outperforms ZnTe as an EO detector of THz signals faster than ≈200 fs.

For ZnTe the calculated differences between the refractive and effective response functions are small (fig. 2.9). But in the case of GaP these differences can not be neglected as demonstrated in fig. 2.10. The reason is, that for ZnTe the minimum of r_{41} is located only 0.3 THz away from the transverse oscillation at 5.0 THz and ends at 5.3 THz. The corresponding region of minimum to maximum of

the transverse lattice resonance of GaP is broader and ranges from 7.8 THz for 3.5 THz up to the TO resonance at 11 THz. Hence, the minimum of the effective response function of GaP is shifted by 3.2 THz to lower frequencies, while for ZnTe the corresponding minima between the two types of response functions are almost found at the same frequency. The physical reason for the smaller influence on the total crystal response in the case of ZnTe is, that the transverse lattice resonance of ZnTe is sharper compared to the resonance width of GaP.

The minima below the transverse lattice resonance in the response functions result from the fact, that the phase slippage between the laser pulse and THz waves of these frequencies over the full crystal thickness is a multiple of 2π [Ste07]. Therefore, the phase retardation Γ caused by the positive half cycle of the THz wave is compensated by a phase retardation of equal amplitude but of opposite sign caused by the negative half cycle. These response minima physically result in a sharp loss of some frequencies of the reconstructed THz pulse Γ_t, which leads to oscillations in the time domain of the electro-optical signal. This shows, that the high THz frequencies can only be reached in sufficient thin crystals. The lattice resonance sets an upper limit of about 5.3 THz to the accessible frequency range for ZnTe, but using GaP instead extends this range.

A fairly thin crystal of GaP ($d \leq 100$ µm) should be used to exploit this capability (fig. 2.10). When the crystal is thicker, for example $d = 350$ µm, the response minimum already appears at 4 THz. For thicker crystals GaP is inferior to ZnTe, which features a much larger EO coefficient r_{41}. Figures 2.9 and 2.10 suggest using a $d \approx 200 - 300$ µm thick ZnTe crystal as a compromise between high-frequency response and signal amplitude. For GaP the thickness should be about 100 µm to detect signals with frequencies up to 7.5 THz, where $|r_{41}(f)|$ for GaP approaches zero. However, due to the small value of r_{41} of GaP the EO signal amplitude is quite low. For crystals thicker than about 200 µm the absolute value of the response function approaches zero due to the velocity mismatch at frequencies lower than 7.5 THz. A small EO signal amplitude is then an unavoidable consequence. For the electro-optical detector used in this thesis a GaP crystal of about 180 µm was chosen, which is a compromise between a lower cut-off frequency and a higher signal amplitude with respect to the frequency range, which the THz pulse of the electron bunch features (compare fig. 2.5(a)).

The total phase retardation $\Gamma(t)$, which an electro-optical crystal under the influence of an external THz field is inducing on an optical wave, can be computed from the EO response function by

$$\Gamma(t) = \frac{2\pi}{\lambda_0} n_0^3 \, d \cdot \mathcal{F}_t^{-1}(E_{THz}(f) G(d, f)) \quad , \tag{2.86}$$

where n_0 is the frequency independent index of refraction of the crystal at the carrier wavelength λ_0 of the optical pulse and d the crystal thickness. The time dependent retardation $\Gamma(t)$ depends on the dynamic amplitude of the electric field of the THz pulse. When the THz pulse consists of frequency components below the first TO lattice resonance, the temporal structure of Γ follows almost proportional that of the THz field. However, the electro-optical replica can never be a perfect temporal copy of the THz-pulse due to the frequency dependency of the electro-optical crystal. A few examples shall demonstrate this fact.

2.2.2.5 Simulation examples of the expected electro-optical retardation at FLASH

Equations (2.85) and (2.86) provide the opportunity to simulate the electro-optical retardation function Γ(t) for various settings of the electrical field and the electro-optical crystal. The simulation code that was used was originally applied by B. Steffen and has proven to reproduce measured EO signals reasonably. Figure 2.11 a) through d) demonstrate various examples of the retardation function, which are expected for different electro-optical conditions. The figure series compares the expected retardation of one fixed set of physical parameters as the width (set to 30 fs RMS) and the total charge (set to 500 pC) of the electron bunch with a variation of the electron bunch shape as well

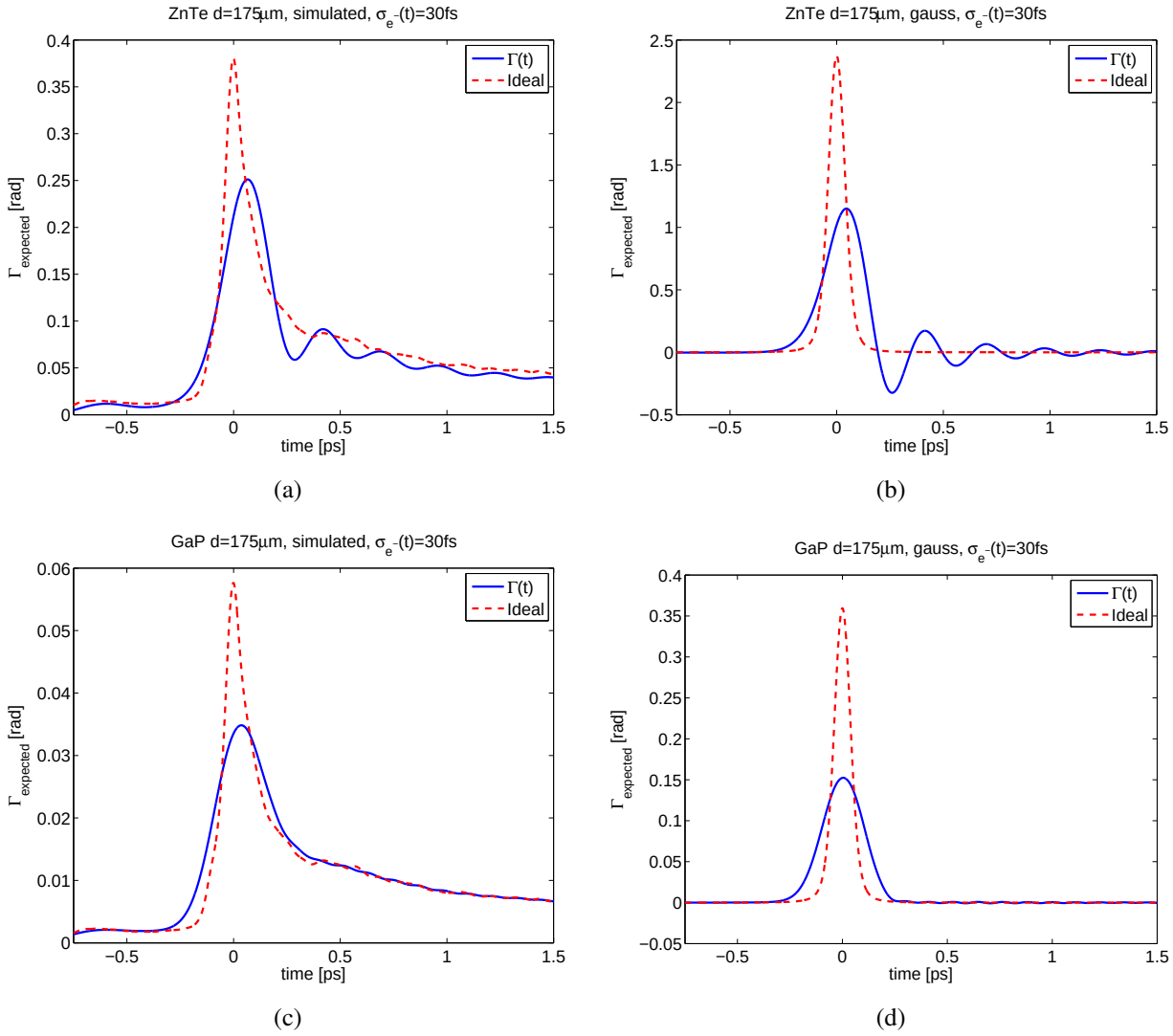

Figure 2.11: (a),(c) The retardation $\Gamma(t)$ assuming the simulated electron bunch density distribution of fig 2.5. (b),(d) Retardation from a Gaussian distributed electron bunch. Total charge q_e=500 pC, distance from crystal set to an arbitrary value of 8 mm. The width σ_e(t) of the simulated spike and of the Gaussian peak is 30 fs RMS. The dashed curves plot an ideal electro-optical retardation disregarding the frequency dependency of Γ.

as of the EO crystal materials. The distance of the crystal from the electron bunch center was set to an arbitrary value of 8 mm. In the plot series the EO retardation signal of a Gaussian distributed electron bunch and of the simulated electron bunch distribution from fig. 2.5 is presented. Both electron bunch density distributions have been simulated with a GaP and a ZnTe crystal of equal thickness of 175 μm. This is the thickness of the GaP crystal, which is used in the measurements discussed in this thesis.

The plots shows, that the Gaussian distributed electron bunch in general creates a 5-7 times larger EO signal than the simulated charge density distribution of equal total charge. The reason is, that for the simulated FLASH density distribution most of the electric charge is smeared out in a 1-2 ps long tail. Only about 5-10% of the complete charge is in the 30 fs RMS narrow spike, whereas for the Gaussian electron bunch 60% is located within the FWHM range of the Gaussian main peak. The simulations indicate further, that in general for ZnTe the phase signal is up to 6 times larger than for GaP as is expected from the larger value of the electro-optical coefficient r_{41} of ZnTe.

However, for ZnTe extra modulations behind the main peak become apparent, which reduces the accuracy to which the electron bunch longitudinal density distribution is being reproduced. All four plots are completed by a dashed curve, which is calculated using equation (2.101), but disregarding the frequency dependencies of the EO crystal. Thus, the dashed curves are perfect replicas of the assumed electron bunch density distribution, but plotted in units of the retardation Γ.

2.3 Detection principles of the electro-optical retardation

Up to now the frequency dependent and independent Pockels effect have been discussed without answering the question, how the retardation, which an electric field induces inside an electro-optical crystal, is actually measured. This section deals this topic. First, a few methods to transform the retardation into a detectable signal are discussed. In the second section various techniques of encoding a temporally changing retardation on a laser pulse are presented.

In chapter 2.1.3 the Pockels effect of an electro-optical crystals of the Zinc-Blende structure was introduced. Particularly equation (2.87)

$$\Gamma(\alpha) = \frac{\omega d}{c}(n_1 - n_2) = \frac{\omega d}{2c} n_0^3 r_{41} E_{\mathrm{THz}} \sqrt{1 + 3\cos^2\alpha} \tag{2.87}$$

(compare with fig. 2.3) was derived, from which one calculates the phase shift between the polarization component parallel and perpendicular to the main axes U_1 and U_2 of the index ellipsoid, while the crystal is under the influence of an external linear polarized electric field. Once a polarized laser pulse travels through the crystal and an electric field is active, the polarization of the laser behind the EO crystal becomes elliptical. With a set of waveplates and a polarizer the polarization modulation is transformed into a modulation of intensity. By this means **the electro-optical effect** inside an electro-optical crystal, which for example is located close to an electron beam of an accelerator, **is made detectable** by an intensity sensitive detector. A principle detection scheme of this purpose is provided in figure 2.12

To understand this scheme a polarization analysis of the full system is necessary.

2.3.1 Jones calculus

The polarization modulation of polarized light traveling through a birefringent optic can be calculated from Jones law. According to [Men01] the Jones matrices of any optical element, which introduces a phase shift of Φ between the s- and p- polarization component evaluated in the principal axis system of the corresponding refractive index ellipsoid, can be written as

$$G(\Phi) = \begin{pmatrix} \exp(-i\Phi) & 0 \\ 0 & \exp(+i\Phi) \end{pmatrix} \quad . \tag{2.88}$$

This generalized Jones matrix describes the polarization modulation of an electrical field vector **E** behind the birefringent element. In this mathematical model and with the coordinate system defined as in fig. 2.3 the electrical field vector of a p-polarized (horizontal, parallel x-axis) or s-polarized (vertical, parallel y-axis) laser is described by 2.2 the electrical field vector

$$\boldsymbol{E_h} = |E| \begin{pmatrix} 1 \\ 0 \end{pmatrix} \qquad \text{and} \qquad \boldsymbol{E_v} = |E| \begin{pmatrix} 0 \\ 1 \end{pmatrix}. \tag{2.89}$$

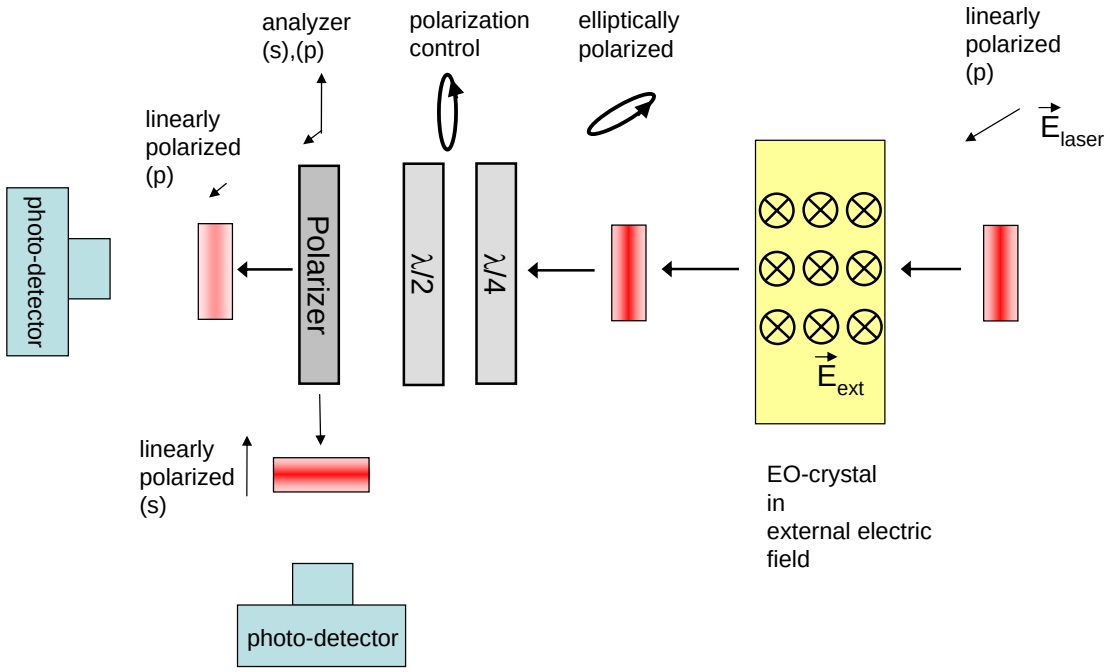

Figure 2.12: *Basic scheme of an electro-optical signal detection*
From right to left: The linearly polarized light enters the electro-optically active crystal. The polarization after the crystal is elliptical. With a set of waveplates one can control the polarization to improve the signal quality. The polarizer splits the s- and p-component of the elliptical polarization into two separate beams. Photo-detectors in the beam paths detect the intensity modulation of each branch.

Since matrix G is noted in the main axis system of the refractive index ellipsoid of the component, any electrical field vector denoted in the laboratory system first must be rotated into the main axis system of the element before the matrix can be applied on it. The rotation matrix looks like

$$\boldsymbol{R}(\phi) = \begin{pmatrix} \cos\phi & -\sin\phi \\ \sin\phi & \cos\phi \end{pmatrix}. \tag{2.90}$$

Hence, the polarization modulation induced by a birefringent component G of an arbitrary polarization $\boldsymbol{E_0}$ is calculated from

$$\boldsymbol{E} = \tilde{\boldsymbol{G}} \cdot \boldsymbol{E_0}$$

with $\tilde{\boldsymbol{G}}$ equals [Mat]

$$\begin{aligned} \tilde{\boldsymbol{G}} &= \boldsymbol{R}(-\phi) \cdot \boldsymbol{G}(\Phi) \cdot \boldsymbol{R}(\phi) && (2.91)\\ &= \begin{pmatrix} \cos(-\phi) & -\sin(-\phi) \\ \sin(-\phi) & \cos(-\phi) \end{pmatrix} \cdot \begin{pmatrix} \exp(-i\Phi) & 0 \\ 0 & \exp(+i\Phi) \end{pmatrix} \cdot \begin{pmatrix} \cos(\phi) & -\sin(\phi) \\ \sin(\phi) & \cos(\phi) \end{pmatrix} && (2.92)\\ &= \begin{pmatrix} \cos[\Phi] - i\cos[2\phi]\sin[\Phi] & i\sin[2\phi]\sin[\Phi] \\ i\sin[2\phi]\sin[\Phi] & \cos[\Phi] + i\cos[2\phi]\sin[\Phi] \end{pmatrix}. && (2.93) \end{aligned}$$

The matrix $\tilde{\boldsymbol{G}}$ is the representation of the Jones matrix $\boldsymbol{G}$ of the optical element in the coordinate system of the optical laser pulse. The Jones matrices of a quarter- and half-wave plate each with fast axis in horizontal direction are described by

$$\boldsymbol{Q} = \exp(+i\pi/4)\begin{pmatrix} 1 & 0 \\ 0 & -i \end{pmatrix} \qquad \boldsymbol{H} = \exp(+i\pi/2)\begin{pmatrix} -1 & 0 \\ 0 & 1 \end{pmatrix}. \tag{2.94}$$

The EO crystal exposed to a strong electrical field acquires indices $n_s(\alpha) = n_1(\alpha), n_f(\alpha) = n_2(\alpha)$ works like a waveplate with variable phase shift. Thus, the EO crystal can be transformed into any kind of waveplate like for example a quarter- or a half-waveplate depending on the crystal length and the strength of the external field. A commonly used optical element, which bases on this effect is a Pockels cell, in which the birefringence quickly can be switched on and off to provide dynamical control of the polarization of a laser pulse.

From the Jones matrix of the EO crystal

$$\boldsymbol{EO}(\alpha) = \begin{pmatrix} \exp(-in_s(\alpha)\omega d/c) & 0 \\ 0 & \exp(-in_f(\alpha)\omega d/c) \end{pmatrix} \tag{2.95}$$

and from equation (2.101) the amount of the electro-optical phase shift Φ_{EO} is derived by

$$\boldsymbol{EO}(\alpha) = \begin{pmatrix} \exp(-i\Gamma(\alpha)/2) & 0 \\ 0 & \exp(+i\Gamma(\alpha)/2 \end{pmatrix} \cdot e^{-\iota\varphi} \tag{2.96}$$

with $\Phi_{EO} = \Gamma/2$.

Since only the relative phase shift Γ between the ordinary and the extra-ordinary polarization component affects the polarization modulation, the overall phase factor $\exp(-i\varphi)$ can be omitted. Because the principal axis system of an EO crystal exposed to an external electrical field is rotated (see fig. 2.3, the corresponding rotation matrix $\boldsymbol{R}(\phi)$ is provided through $\boldsymbol{R}(\Psi(\alpha))$ with angle $\Psi(\alpha)$ as defined in equation (2.58). The effective matrix $\tilde{\boldsymbol{G}}_{\boldsymbol{EO}}$ of the EO-crystal follows from (2.93):

$$\tilde{\boldsymbol{G}}_{\boldsymbol{EO}} = \begin{pmatrix} 1 & 0 \\ 0 & 1 \end{pmatrix} \cdot \cos(\Gamma/2) + i \sin(\Gamma/2) \begin{pmatrix} -\cos(2\Psi) & \sin(2\Psi) \\ \sin(2\Psi) & \cos(2\Psi) \end{pmatrix} \tag{2.97}$$

The polarizer at the end of the chain of optics is mathematically represented by the matrix operation $\begin{pmatrix} 1 & 0 \end{pmatrix} \cdot$ or $\begin{pmatrix} 0 & 1 \end{pmatrix} \cdot$ respectively, whether the p- or s-component of the electrical field is observed.

2.3.2 Special electro-optical detection schemes

To fully simulate the system of polarizing elements as shown in fig. 2.12 the corresponding Jones matrices of all birefringent components in the path of the laser beam between EO-crystal and detector have to be multiplied according to their succession. The rotation of the half wave plate and quarter wave plate of their optical fast axis shall be measured by angle θ and ϕ. Hence the Jones matrix of the complete system S of fig. 2.12 is mathematically described by

$$S(\Psi(\alpha), \Gamma, \phi, \theta) = \tilde{\boldsymbol{Q}}(\phi) \cdot \tilde{\boldsymbol{H}}(\theta) \cdot \tilde{\boldsymbol{G}}_{\boldsymbol{EO}}(\Psi, \Gamma) \quad . \tag{2.98}$$

(Angle θ, ϕ and $\Psi(\alpha)$ as defined before in the text.) Due to the complexity of the matrix components of $\boldsymbol{S}$, they will not be shown here.

However, under certain assumptions the matrix components can be simplified and discussed in detail. One distinguishes the following three different assumption schemes: *Crossed polarizer setup*, *Balanced detection setup* and a mixture of both called *Near crossed polarizer setup*. All three schemes are variations of the basic principle to transform the electro-optical phase shift Γ into a detectable intensity signal. They vary in the way the polarization of the laser pulse behind the EO crystal is controlled. The polarization control is carried out by the quarter- and half-wave plate behind the EO crystal of figure 2.12. All three schemes have advantages and disadvantages. The decision for a detection scheme depends on the expected signal and the used intensity detector as will be shown.

A basic assumption frequently used in the following discussion for all three schemes is, that the external electric field points into the x-direction, i.e. the (-1,1,0)-axis of the crystal as defined in fig. 2.2 and fig. 2.3. In this case the EO-effect is maximized and angle Ψ is calculated from equation (2.58)

$$\psi(\alpha) = \arccos\left(\frac{1}{2}\frac{\sin\alpha}{\sqrt{1+3\cos^2\alpha}}\right) \tag{2.99}$$

to be

$$\Psi_{(\Gamma,max)} = \Psi(\alpha = 0) = \pi/4 \quad . \tag{2.100}$$

Accordingly the maximal retardation Γ follows from (2.101):

$$\Gamma_{max} = \frac{\omega d}{2c} n_0^3 r_{41} E_{\mathrm{THz}} \tag{2.101}$$

2.3.2.1 Crossed polarizer detection

The easiest of the three schemes is found, if a horizontally polarized beam enters the EO crystal and the vertical polarized component behind the EO-crystal is analyzed with one intensity sensitive detector. Thus, the intensity detector is placed into the crossed polarization brunch. In this scheme the vertical polarization component E_v is calculated from

$$E_v = \begin{pmatrix} 0 & 1 \end{pmatrix} \cdot S(\Psi(\alpha), \phi, \theta) \cdot |E_{laser}| \begin{pmatrix} 1 \\ 0 \end{pmatrix} \tag{2.102}$$

In this scheme the half- and quarter wave plates are set neutral, hence, $\theta = \phi = 0$. Under these assumptions the electrical field behind the s-component of the polarizer is calculated to be

$$E_v(\Gamma, \Psi(\alpha)) = -\frac{1+i}{\sqrt{2}} \sin(\Gamma/2) \sin(2\Psi(\alpha)). \tag{2.103}$$

The intensity on the detector is calculated from eq. (2.25)

$$I_v = \frac{\varepsilon_0 c}{2}|E_v|^2 = \frac{\varepsilon_0 c}{2} \cdot |E_0|^2 \sin(\Gamma/2)^2 \sin(2\Psi)^2 \tag{2.104}$$

$$= I_0 \cdot \sin(\Gamma/2)^2 \sin(2\Psi)^2. \tag{2.105}$$

In the case of maximal EO effect ($\Psi = \pi/4$)) one obtains

$$I_{EO,crossed} = I_v = I_0 \cdot \sin(\Gamma/2)^2 \quad . \tag{2.106}$$

Hence, for small Γ the EO signal intensity is proportional to $\sim \Gamma^2$.

Two effects in reality are modifying the ideal case of crossed polarization modulation. First, the polarization of the laser wave, the wave-plates birefringence and the polarizer contrast ration are not perfect. Thus, a small background leakage even for fully crossed polarization settings will always be observed by the detector. For the electro-optical setup used in this thesis an intensity dependent background offset of $+s_{bg} * I_0$ with $s_{bg} = 0.0024$ is observed, which is in agreement with a value of $s_{bg} = 0.003$ found from [Ste07]. Second, the EO crystal even without external field is slightly birefringent. The birefringence originates from mechanical stress applied to the crystal during its manufacturing. The effect of the inherent birefringence will be discussed later.

2.3.2.2 Balanced detection

The second scheme differs from the crossed polarizer setup by the setting of the quarter waveplate behind the EO crystal and the use of an additional intensity detector in the second brunch behind the polarizer. The quarter wave plate's fast optical axis is rotated by $\phi = 45°$. The half waveplate is again set neutral, i.e. $\theta = 0°$. Thus, the wave behind the two plates is circularly polarized. Without electric field the observed intensity in either bunch is $I_{h,v} = 1/2 \cdot I_0$. Thus, the background intensity even in the ideal case is half of the full intensity. Using again the maximal EO effect assumption, i.e. $\Psi = \pi/4$ and the balanced detection settings, which are defined by QWP angle $\phi = 45°$ and HWP angle $\theta = 0°$ one can calculate the electric field $E_{v,h}$ of either brunch from equation (2.98):

$$E_v = -1\frac{1}{\sqrt{2}} \cdot (\cos(\Gamma) + \sin(\Gamma)) * |E_0| \qquad E_h = -i\frac{1}{\sqrt{2}} \cdot (\cos(\Gamma) - \sin(\Gamma)) * |E_0| \quad , \tag{2.107}$$

and the intensity of either polarization component using $I_0 = \frac{\varepsilon_0 c}{2} \cdot |E_0|^2$ becomes

$$I_{v,h} = I_0 \cdot \frac{1}{2}(1 \pm \sin(\Gamma)) \quad . \tag{2.108}$$

Thus, the zero EO signal intensity $I_0/2$ of each detector is in-/decreased by the same full intensity fraction $I_0/2 \cdot \sin(\Gamma)$, which depends on the strength of the EO effect. The difference of both signals is background free

$$I_{EO,balanced} = I_v - I_h = I_0 \cdot \sin(\Gamma) \tag{2.109}$$

and is proportional to $\sin(\Gamma)$ and not to its square. Hence, for small Γ the EO signal intensity is proportional to $\sim \Gamma$ and thus larger than in the case of the crossed polarizer scheme. For example, if an EO signal, which gives rise to a peak phase retardation of $\Gamma = 10°$ as simulated for a typical EO signal at FLASH presented in fig. 2.11 is measured with a balanced detection setup, the detected intensity signal would be about *6 times larger* than if the same signal is measured with a crossed polarizer setup. However, to benefit from the larger EO signal, two intensity sensitive detectors, which can sustain the large background intensity without damage or saturation effects are needed for this scheme. Detectors of this type are not always available. Especially intensity sensitive detectors with single shot capabilities and a dynamic range large enough to cover the bright background have not been available during this work.

2.3.2.3 Near crossed polarizer scheme

A compromise between both schemes is the *near crossed polarizer scheme*, which in a sense is a mixture of both schemes. This scheme takes up to a certain limit advantage of the linear dependency of the EO signal from the phase retardation as in the case of the balanced detection scheme, but tries to overcome the problem of a too strong background. And the scheme works with one detector only. This scheme is an improvement of the crossed polarizer scheme, thus the intensity detector is placed as it was in the crossed polarization scheme. The difference to this scheme is, that the half-waveplate is not fixed to zero anymore. Instead, the two wave-plates simultaneously are used to find an optimal setup for the polarization behind the EO crystal and to minimize the background and maximize the EO signal intensity subject to the phase retardation (see fig 2.13(a)). This has to be done properly or the electro-optical phase retardation could even be compensated and no signal is detectable (see fig. 2.13(b)).

For each combination of $\phi \neq 0$ and $\theta \neq 0$ some background intensity light is leaking through the polarizer. Even for zero background intensity a small offset remains, which originates from leakage of the polarizer and electronic noise of the detector. If the detector were perfect and linear over the

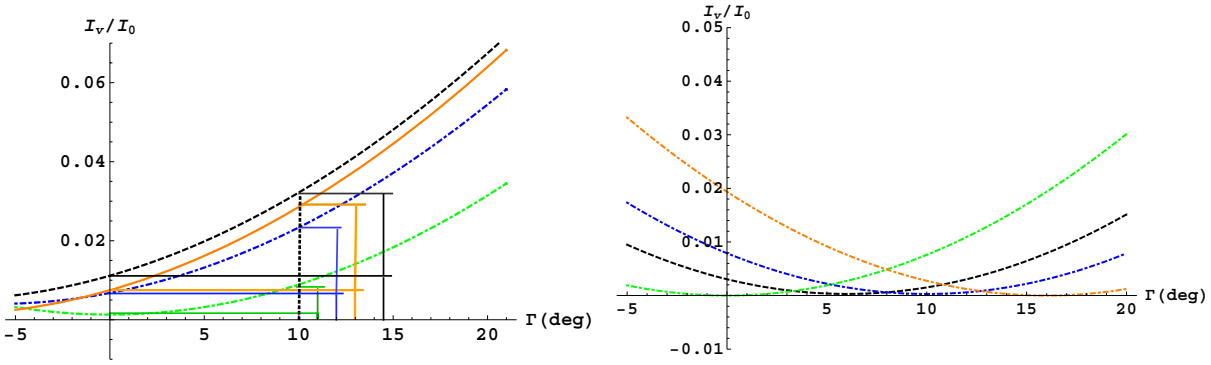

(a) (b)

Figure 2.13: *Detected signal amplitude subject to the settings of the quarter- and half-wave plate.* (a) This figure describes the influence of the electro-optical signal amplitude including a realistic noise offset of 0.0013 for various settings of the quarter-waveplate angle QWP⇔ ϕ and half-waveplate angle HWP⇔ θ and for a theoretical retardation of $\Gamma = 10°$. Dashed line (black), $\theta = -4.5°$, $\phi = -4°$. Dot-dashed line (blue), $\theta = 0°$, $\phi = -3°$. Dot-dashed line (green), $\theta = 0°$, $\phi = 0°$. Solid line (orange), $\theta = -2.25°$, $\phi = -4.5°$. The orange line shows the optimal situation. (b) For some inadequate waveplate angle combinations, the detected EO amplitude is zero, since the electro-optical phase retardation is compensated by the phase-retardation of the waveplates. Dashed line (black), $\theta = 2°$, $\phi = 3$. Dot-dashed line (blue), $\theta = 2°$, $\phi = 5$. Dot-dashed line (green), $\theta = 0°$, $\phi = 0$. Dot-dashed line (orange), $\theta = 4°$, $\phi = 8°$.

full intensity range of the maximum laser intensity I_0, the background for all possible waveplate settings could be easily subtracted applying a background measurement without EO signal before and subtract it for all EO measurement of the same waveplate settings as the background measurement. However, imperfections of the crystal or for small intensities, noise of the detector reduces the signal-to-noise ratio of the intensity amplitude of the EO phase retardation. The noise amplitude strongly depends on the type of intensity detector and must be measured for each setup individually.

Fig. 2.13(a) visualizes the relation between background and signal amplitude. For the black dashed curve the EO phase retardation dependence at $\Gamma = 10°$ is utmost linear, but the signal background is the largest. The blue dashed curve provides a smaller background and thus a smaller noise level, but the EO signal amplitude at $\Gamma = 10°$ is smaller than for the black curve. The solid orange line shows the optimal case with small background intensity and maximal signal amplitude. The green dashed curve represents the fully crossed polarizer setting. Due to the quadratic dependence of the signal amplitude from the phase retardation, the measured amplitude is smaller compared to the orange curve, but the background is smaller as well. However, due to the noise offset at zero background intensity, which also exists in the fully crossed polarizer case, the signal to noise ratio is still worse compared to the orange solid curve.

Thus depending on the noise level of the used detector, it is possible to find an optimal value for the quarter and half waveplate settings, which maximizes the EO signal amplitude while keeping the noise level, which depends on the background level as small as possible.

A quantitative analysis is achieved using eq. (2.98) with variable settings of half-wave plate angle θ and quarter-waveplate angle ϕ. With the symbolic computation program MATHEMATICA the following formula for the intensity detected by the single detector used as in the crossed-polarizer

setup is calculated:

$$I(\theta,\phi,\Gamma) = I_0 \cdot \frac{1}{2}\mathrm{Abs}\left(-(\cos[2\theta] + i\cos[2(\theta-\phi)])\sin\left[\frac{\Gamma}{2}\right] + \right) \left(\cos\left[\frac{\Gamma}{2}\right](i\sin[2\theta] + \sin[2(\theta-\phi)])\right)^2 \tag{2.110}$$

Notice, that this equation is not simultaneously invertible in θ and ϕ. Hence, for the near crossed polarization method it is in general not possible to directly transform an intensity amplitude signal into a phase retardation. This inversion is only possible, if one of both waveplates is set to zero. With expression (2.110) the signal to noise ratio of the EO signal can be calculated by

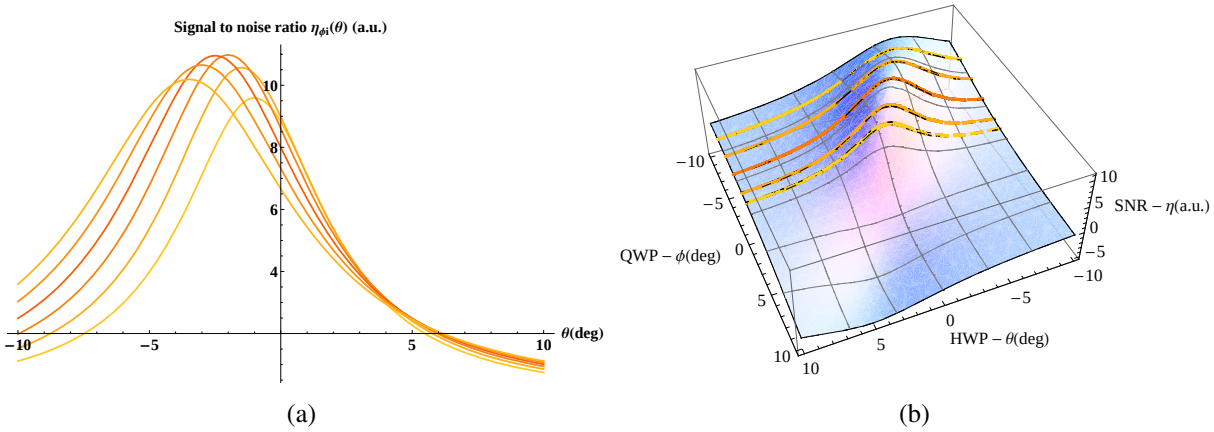

(a) (b)

Figure 2.14: *Optimization of signal to noise ratio of a detected EO signal.*
Several plots of the signal to noise ratio $\eta(\theta,\phi,\Gamma = 10°, a = 0.1, b = 0.0013)$ for different values of the quarter wave plate from -2° to -7° around the calculated optimum of $\phi_{max} = -4.4°$ are plotted versus the angular setting θ of the halfwave plate.

$$\eta(\theta,\phi,\Gamma) = \frac{I(\theta,\phi,\Gamma) - I(\theta,\phi,0)}{I_\sigma(\theta,\phi)} \quad . \tag{2.111}$$

This formula defines the ratio of the EO signal $I(\Gamma) - I_0(\theta,\phi)$ to the noise level $I_\sigma(\theta,\phi)$, which is in general proportional to the background intensity and shows a zero intensity offset, thus

$$I_\sigma = a \cdot I_0(\theta,\phi) + b \quad . \tag{2.112}$$

Reasonable values for a and b are between [0.07 - 0.1] and [0.001 - 0.005] respectively. For the detector used in this thesis the parameter values $a = 0.1, b = 0.0013$ have been measured by a background noise analysis measurement. With this parametrization for the noise amplitude an optimal set of values for the settings of the quarter- and half-wave plate angles ϕ and θ can be calculated by solving the extremal conditions

$$\left(\frac{\partial\eta}{\partial\theta}, \frac{\partial\eta}{\partial\phi}\right) = (0,0) \quad . \tag{2.113}$$

Since these pair of equations is because of the complexity of the equations (2.110) and (2.111) not analytically solvable, a numerical optimization analysis has been performed. The optimal settings for the waveplates have been calculated to

$$(HWP, QWP)_{max} = (\theta,\phi)_{max} = (-2.2, -4.4) \quad . \tag{2.114}$$

For a large range of tested values of ($\Gamma < 20°, 0 < a < 0.2, 0 < b < 0.01$) similar solutions for the optimal value of θ and ϕ have been found numerically. All of these solutions follow the relation

$$\phi_{opt} = 2\theta_{opt} \quad . \tag{2.115}$$

An explanation might be, that for small angular deviations of the half- and quarter wave plate from their neutral position, it is possible to compensate some background intensity induced by the half-waveplate with the quarter waveplate.

An analysis of the EO signal to noise ratio close to the optimum is presented in fig. 2.14.

2.4 Temporal analysis of an electro-optical signal

So far the physical principles behind the EO effect and measurement methods, by which an electro-optical signal is converted into an easily detectable intensity modulation, have been presented. In its application as a temporal detector of the longitudinal electron bunch density distribution, special techniques are necessary, by which any kind of temporal information can be extracted out of the electro-optical modulation of the optical laser pulse.
The simplest technique is the *Electro-Optical Sampling* method (EOS). An optical fs-pulse is shifted

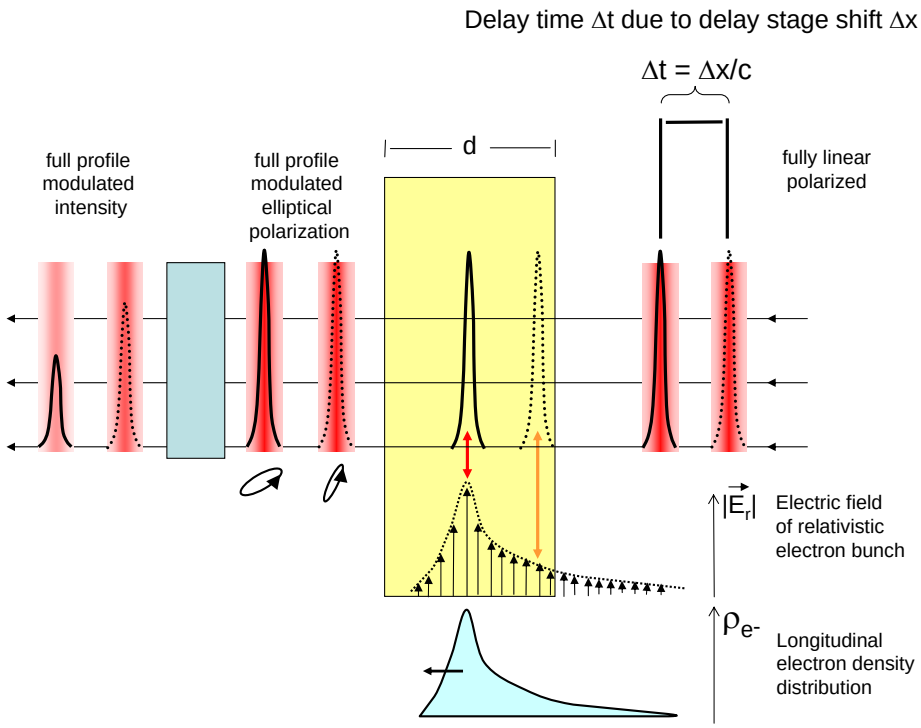

Figure 2.15: *The electro-optical sampling method.*
An optical delay stage shifts the optical pulse in time. For each shot one temporal measurement point is obtained.

in arrival time by means of a mechanical two-mirror delay stage before the electro-optical crystal. Except for the delay stage the detection setup is similar to the one shown in fig. 2.12. The two detectors are fast photodiodes typically used in a balanced detection scheme. The phase retardation, which affects on the optical pulse inside the electro-optical crystal, depends on the relative arrival time of the optical pulse with respect to the electron-bunch at the EO crystal. Assuming stable conditions from bunch to bunch, the temporal properties of the electron bunch are slowly scanned

slice-by-slice. The delay stage shifts the optical pulse in small time steps and a detector measures the intensity variations of the electro-optically modulated laser pulse as the optical pulse moves in time along the electron bunch. Since the full optical laser pulse is modulated, this technique already works with a weak optical pulse of several *pJ* per pulse. This technique is frequently used to analyze stable laser driven THz-sources like in [WZ95, LHS+99a]. However, inside a linear accelerator the assumption of a stable arrival time from bunch to bunch is not fulfilled, which makes it impossible to use EOS technique to temporally scan the electron bunch stepwise.

2.4.1 The spatial decoding technique

To overcome this drawback variations of the electro-optical sampling exist, which provide a complete single-shot temporal density distribution measurement of the electron bunch. One of this various single-shot electro-optical detection techniques bases on a detection scheme introduced by Heinz [HSW+00], who applied this scheme first to analyze stable laser driven THz sources temporally. This scheme is called *spatial decoding*.

In this scheme, the optical laser pulse, typically a 800nm Ti:Sa near infrared (NIR) laser pulse, traverses the electro-optical crystal under an angle of $\alpha \approx 45^o$ relative to the normal of the crystal surface. The electron bunch passes by the crystal in a distance of several mm. Fig. 2.16 shows a side

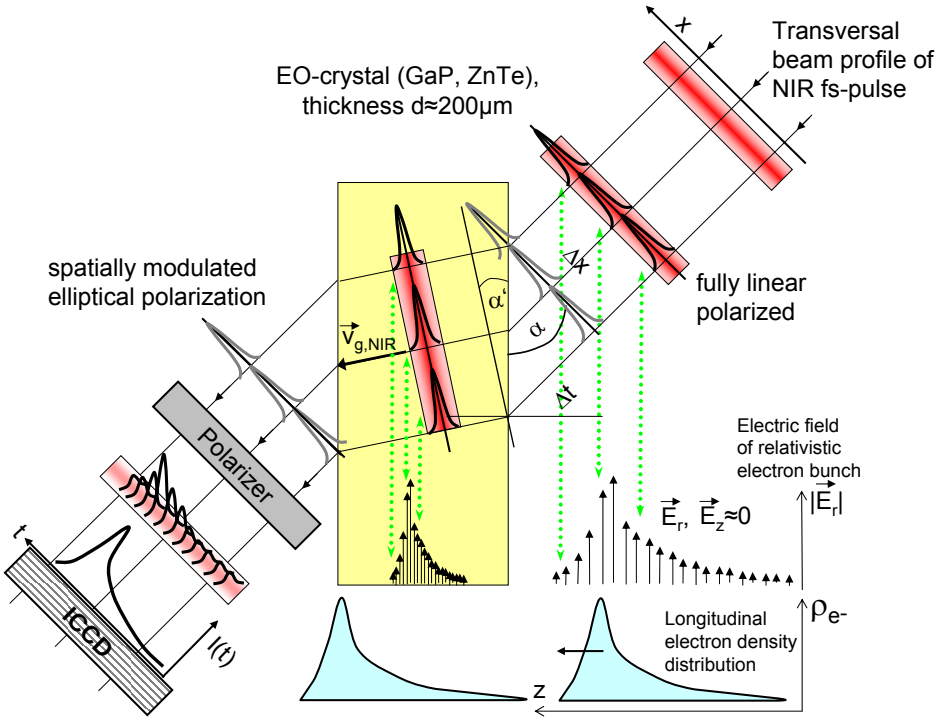

Figure 2.16: *The time-to-space mapping in detail.*
The temporal structure of the electron-bunch THz-radiation is mapped into the transversal beam-profile. A Fourier limited NIR laser pulse acts as a δ-function in the sense of a convolution of the THz field with the laser pulse.

view of the geometrical relations. Due to the angle of incidence α, different sections of the transversal beam profile arrive at the crystal at different times indicated by the green arrows. In the figure the upper part arrive earlier than the lower part of the laser beam. Hence, the angle of incidence maps the spatial coordinate along the transversal beam profile on a temporal variable, which measures the

time of arrival of each corresponding transversal position. In this sense different spatial segments of the transversal beam profile are delayed proportional to their individual transversal position.

Let v_p and v_g be defined as the phase and group velocities of a monochromatic wave and a polychromatic pulse respectively. The indices of refraction $n = c/v_p$ of GaP and ZnTe for the 800 nm NIR pulse are 3.18 and 2.85 respectively. The group indices of refraction $n_g = c/v_g$ of GaP is 3.57 for the NIR pulse and 3.305 for the THz pulse. The group index of refraction of ZnTe is 3.24 for the NIR pulse and 3.01 for the THz pulse. All values calculated using the equations explained in section 2.2.2.3 and 2.2.2.1.

Each of the transversal profile segments correspond to a different time element of the temporal distribution of the equivalent THz pulse (refer to section 2.2.1). According to the present electric field, which affects a transversal profile segment, the polarization is modulated by the Pockels effect. However compared with the simple electro-optical sampling scheme, not the complete electron bunch is modulated. Instead, only a small fraction of the complete transversal beam profile is rotated in polarization. Thus, assuming a polarization rotation of equal strength and similar optical pulse energy for both detection techniques the spatial decoding scheme generates a smaller EO signal than the scanning EO sampling technique. After passing the EO crystal, the spatially varying polarization modulation is transformed into an intensity modulation by a cubic polarizer (contrast ratio 1:5000). The signal is detected by means of the near crossed or crossed polarizer scheme. Thus, the laser background together with the negative copy of the EO signal is divided from the signal. The time axis calibration depends on the imaging system, which transports the signal to a spatial intensity detector. Both topics will be discussed in the following sections.

Apart from the spatial decoding technique, there exist two more decoding techniques for electro-optical single bunch analysis, namely the *spectral decoding scheme* [W+02] and the *temporal decoding scheme* [Jam03].

The spectral decoding scheme is limited in temporal resolution. The reason is based on the limited bandwidth of the chirped and stretched optical laser pulse, which is used to encode the EO signal inside spectrally. According to [EO-06a] this limitation can be calculated by $\tau_{lim} = 2.6\sqrt{T_c T_0}$, where T_c and T_0 are the FWHM of the chirped and transform limited optical pulse durations. For example, if a TiSa laser provides a bandwidth limited pulse duration of 20 fs and is chirped to 1 ps, the limitation is τ_{lim} =370 fs.

The temporal decoding scheme does not suffer of this physical limitation. However, to build a temporal decoding setup, the achievable pulse energy of a Ti:Sa oscillator is not sufficient and a laser pulse amplifier is needed. The amplifier must be localized closely to the EO-crystal, which due to technical reasons is not possible near to the TEO detection site within the linear accelerator. Mostly because of these reasons the spatial decoding scheme is used for the TEO diagnostic.

At FLASH both methods are presently in use to monitor the longitudinal electron bunch trace online. An interesting discussion of the advantages and drawbacks of these methods can be found in [Ste07].

2.4.1.1 Electro-optical time-to-space mapping in detail

In this section more detailed characteristics of the time-to-space mapping shall be discussed. What are the temporal properties of the spatially encoded signal and how does the electro-optical signal depend on the temporal shape of the optical laser pulse ? These are important questions to optimize the signal quality and understand the nature of the signal.

From the response function model explained in section 2.2.2.4, the EO signal is a convolution of the effective crystal response depending on the electrical field emitted by the electron bunch (2.85).

$$\Gamma(t) = \frac{2\pi}{\lambda_0} \cdot n_0^3 \cdot d \int_{-\infty}^{\infty} r_{41}(\omega) G(\omega) E_r(\omega) e^{-i\omega t} d\omega \tag{2.116}$$

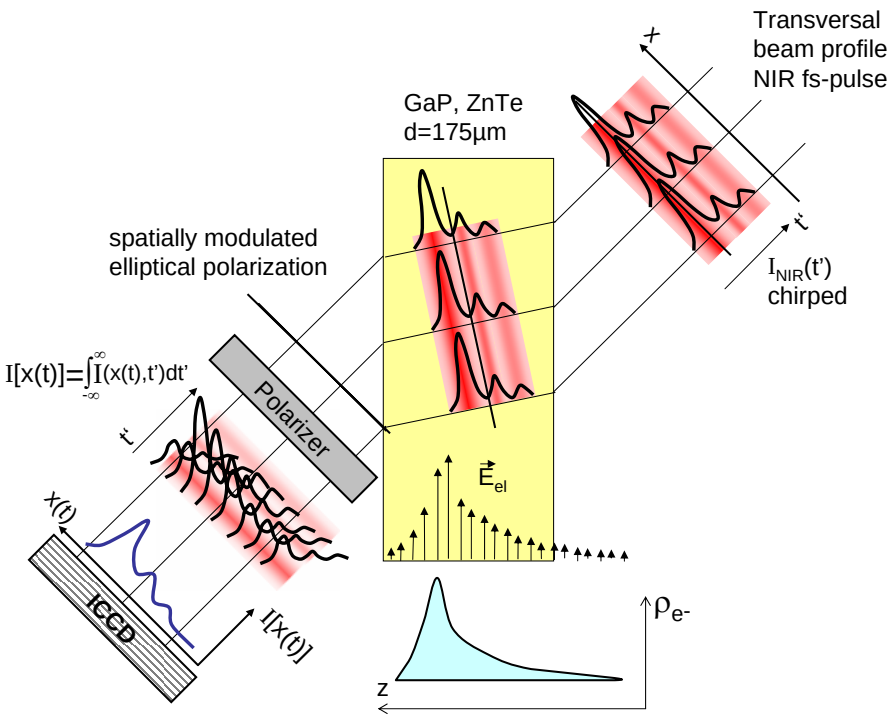

Figure 2.17: *Time-to-space mapping in detail - laser chirped case*
Since the EO-signal follows from a convolution of the optical pulse with the temporal trend of the THz-radiation, a chirped and stretched pulse modifies the detected EO signal.

The electrical field behind the crystal follows from (2.95):

$$\boldsymbol{E_{NIR}}(t) = \begin{pmatrix} \exp(-i\Gamma(t)/2) & 0 \\ 0 & \exp(+i\Gamma(t)/2) \end{pmatrix} \cdot \boldsymbol{E_{NIR,0}} \tag{2.117}$$

Applying the transformation techniques of section 2.3.2 the polarization modulation is transformed into an intensity modulation.

$$\boldsymbol{I_{EO}}(t) = \left| S\left(t, \theta, \phi, \Psi(\alpha)\right) \boldsymbol{E_{NIR,0}} \right|^2 \tag{2.118}$$

2.4.1.2 Arrival time extraction from a spatially encoded EO signal

Finally a short discussion about the dependency of the spatially encoded signal on the relative arrival time between the electron bunch and the optical laser pulse is presented. In fig. 2.18 the relation of the transversal signal position and the relative arrival time between both pulses is shown. First let us assume, that the laser pulse and the electron bunch arrive simultaneously at the crystal. In this case, the intersection of the laser pulse with the crystal is localized at the vertical center of the crystal and matches with the center of the laser pulse transversal profile. In the figure the intersection is marked by a blue spot. The Pockels effect modulates only a small fraction of the laser pulse profile in the center of the profile. If the laser pulse is delayed relative to the electron bunch, the intersection of the laser pulse disk moves along the crystal upwards. Viewed antiparallel to the $\boldsymbol{k}$-vector of the laser pulse, the polarization modulation moves to the right. It moves into the opposite direction, if the electron bunch is delayed. Thus, any temporal fluctuation between both pulses is transformed into a spatial position shift of the intensity modulation, which can be recorded by a spatially resolving intensity sensitive detector like a CCD or a photo diode array. This technique provides not only

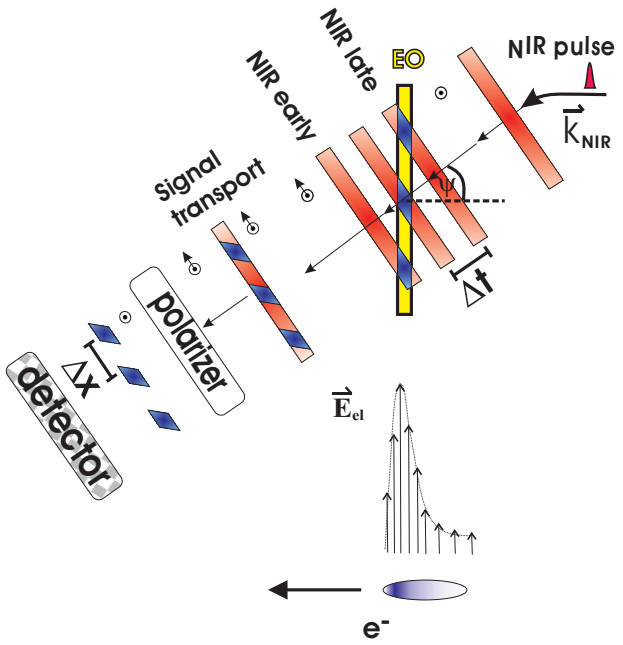

Figure 2.18: *Time-to-space mapping in detail - relative arrival time fluctuations*
This figure demonstrates the relation between the temporal arrival time of the optical pulse and the electron bunch and the spatial position of the signal within the transversal beam profile of the pulse.

a single-shot temporal electron bunch profile detector. It can also be used as a bunch arrival time detector. Fig. 2.18 emphasizes the time-to-space mapping with focus on the arrival time detection possibility. The exact timing information os extracted from the measured bunch profile due to a fit of the peak of the EO signal. Further details on the arrival time extraction are presented in section 4.5. The calibration relation between the time coordinate and the transversal spatial coordinate is discussed in the following section.

2.4.1.3 Imaging of the spatially encoded signal

According to simulation in fig. 2.11 the polarization Γ is in the order of a few degree. Thus, an intensified camera is needed to detect the small intensity modulation. The signal itself is a small spot of 100-200 μm in diameter localized along the transversal NIR beam profile and must be transported without loss of spatial information due to diffraction from the crystal to the detector as shown in fig. 2.18. Thus, the tilted crystal surface representing the object plane is imaged by a Kepler telescope on the intensified CCD camera photocathode (see fig. 2.19).

A simulation with ZEMAX [Moo07] presented in fig. 2.20 visualizes the light transport from the crystal surface to the detector using a two-lens Kepler telescope. The 2D color encoded intensity profiles starting from the object plane to the focal plane demonstrate, how the small signal would increasingly be blurred by diffraction, if the polarization modulated beam profile has propagated without being imaged.

The distances of the lenses and their focal lengths are chosen, so that the image of the complete crystal fits on the CCD chip without clipping taking the objective of the CCD camera into account. Figure 2.22 provides a detailed overview of the geometrical relations between the created EO signal on the crystal surface and the detected EO signal by the CCD camera.

To understand the influence of the tilted object and image plane on the detected signal one needs to analyze the principal imaging of a tilted plane by a Kepler telescope. An analysis with the

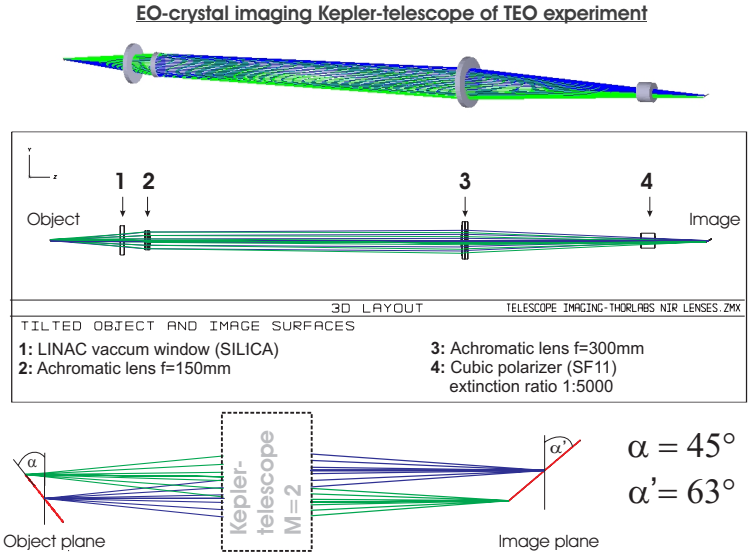

Figure 2.19: ZEMAX model of the TEO signal imaging Kepler telescope.

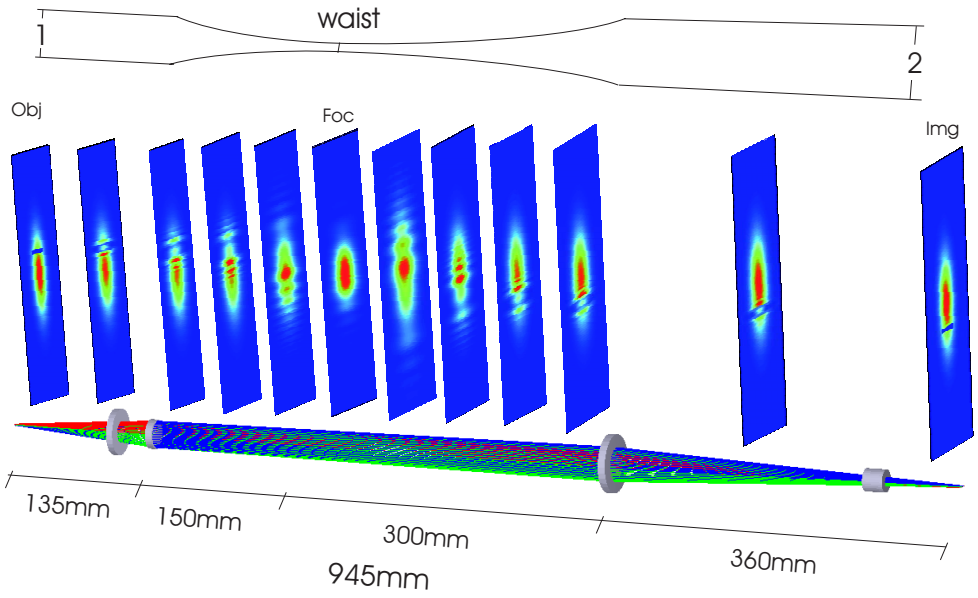

Figure 2.20: *ZEMAX physical propagation simulation of the TEO signal transport by the Kepler telescope.*
The TEO signal is simulated by a rectangular plate centered in the beam object plane of 100 μm thickness, which creates a rectangular intensity modulation in the transversal beam profile. The laser beam profile is cylindrical with 1 mm × 0.15 mm FWHM diameter, alike the NIR laser beam in the TEO experiment. The transversal beam profiles are not true to scale, since the Gaussian beam traversing the telescope has an intermediate focus of 90 μm diameter and the beam would not be visible in the used scale.

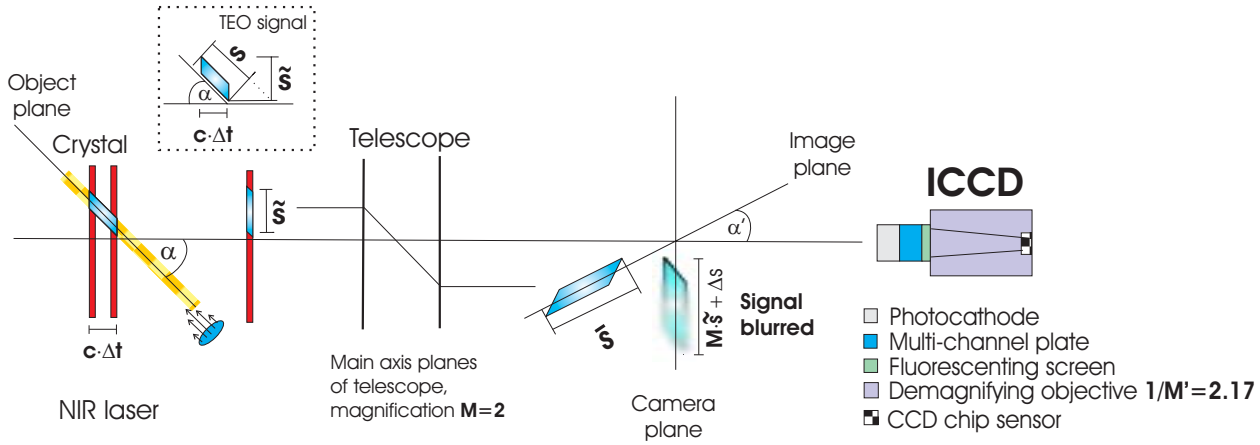

Figure 2.21: *Geometrical relations regarding the imaging TEO signal transport.*
Important variables are the effective width of the signal in the time domain (Δt) and projected on the crystal surface (s) and on the laser beam profile ($\tilde{s}$). For reasons of better understanding the crystal is rotated by angle α=45 degree of the incident laser beam on the crystal surface compared with the real geometrical conditions.

ABCD-matrix formalism leads to

$$b = M^2 \cdot (f_1 - g) + f_2 \tag{2.119}$$

for the connection of object distance g, the distance of the image b and the magnification $M = \frac{f_1}{f_2}$ of the telescope. The formula is in good agreement with the distances calculated by ZEMAX. Thus, any parallelepiped will be transformed into another magnified parallelepiped as shown in fig. 2.22.

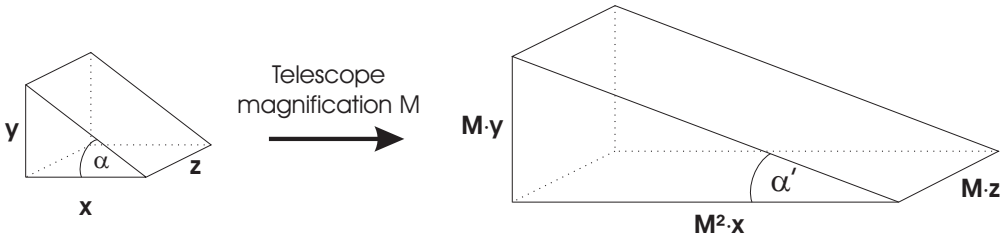

Figure 2.22: *Imaging of a titled plane by a Kepler telescope.*

From this figure directly follows eqn. (2.120) to calculate the optimal angle between the tilted image plane and the optical axis α':

$$\alpha' = \tan^{-1}(\frac{1}{M} \cdot \tan(\alpha)) \tag{2.120}$$

For α=45^0, M=2 one finds 26.6^0, which is in good agreement with the value of 26.0^0 for the corresponding angle of the telescope used in the TEO setup as calculated by ZEMAX. This considerations imply, that it is necessary to rotate the detector by (90^0-α') to match the detector plane with the tilted image plane and provide a clear image of the complete crystal surface. However, due to geometrical restrictions of the experimental station inside the accelerator tunnel, it is not possible to rotate the camera by the calculated large angle of 63.4^0 for the used TEO telescope. A detailed analysis of the imaging deviations due to the tilted object plane has shown, that there are no strong influences on the temporal resolution of the TEO detector. This analysis is presented in appendix A.2.

The temporal coordinate follows from eqn. (2.121), which introduces a factor $\sqrt{(}2)$ for $\Psi = 45^o$ between Δx and Δt. The detection time window is defined by the vertical beam size of the optical laser of 1-2 mm FWHM at the crystal. It can be reduced to increase the signal strength.

$$\Delta t = \frac{\Delta x}{c \cdot \sin(\Psi)} \tag{2.121}$$

Chapter 3

Experimental environment

3.1 The free-electron laser FLASH

The Free electron LASer in Hamburg (FLASH) facility became operational in August 2005. It represents a milestone on the road map of intense short wavelength radiation generation [A+07]. FLASH is a powerful source of extremely bright and ultrashort coherent XUV light. Showing a peak brilliance of up to 10^{30} photons/(s mrad^2 mm^2) per 0.1 % bandwidth, FLASH outperforms 3rd generation synchrotron light sources by a factor of 10^6 in peak brilliance [A+02]. The extreme ultraviolet XUV FEL light allows to explore fundamental processes such as direct one or few photon inner shell ionizations, as well as two-color pump-probe experiments involving intense laser fields of hugely different photon energies.

The driving mechanism of a free electron laser is the collective interaction of electrons with the electromagnetic field in the undulator. FLASH is a self amplified by stimulated emission (SASE) FEL that produces XUV radiation during a single-pass of an electron beam through a long periodic magnetic undulator. When the electron beam enters the undulator, the interaction between the elec-

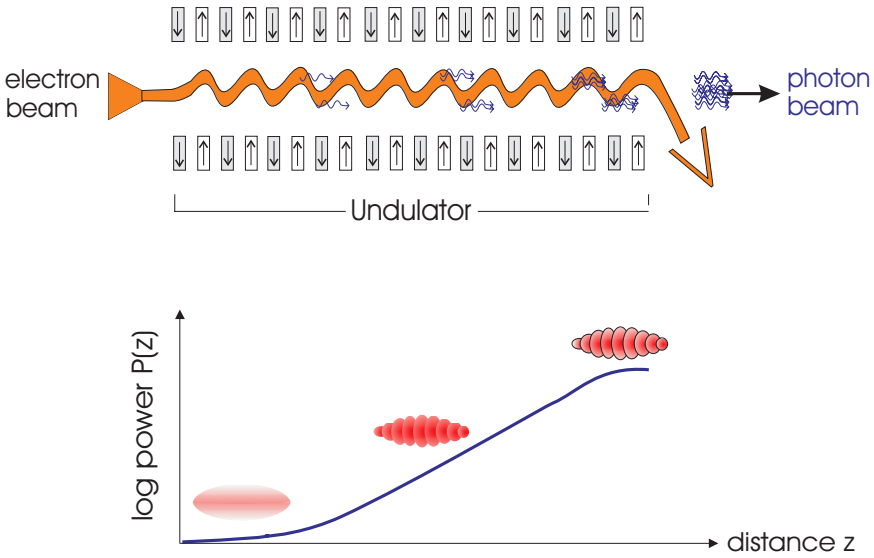

Figure 3.1: *A schematic diagram of a single-pass FEL operating in SASE mode*
Top: The lasing starts from shot noise and grows exponentially. Bottom: The micro-bunching evolves during the amplification process. Saturation is reached, if all lasing electron are divided into micro-bunches with a period equal to the lasing wavelength (figure from [A+02]).

trons oscillating in the undulator and the radiation that they produce, leads to a periodic longitudinal density modulation (micro-bunching) with a period equal to the undulator resonance wavelength equal to the radiation wavelength. The radiation emitted by the micro bunches is in phase and adds coherently leading to an increase in the photon intensity, which further enhances the micro bunching. The amplification process in SASE FELs starts from the shot noise in the electron beam and develops exponentially with the undulator length. The amplification process is schematically depicted in figure 3.1.

An intensity gain in excess of 10^7 with respect to the spontaneous radiation emitted at the beginning of the undulator is obtained in the saturation regime. At this level the shot noise of the electron beam is amplified up to the point, at which complete micro-bunching is achieved and almost all electrons in the lasing spike of FLASH radiate in phase producing powerful, coherent radiation.

3.1.1 The linear accelerator

The linear accelerator of FLASH is the heart of the XUV pulse free-electron laser at DESY. It accelerates electron bunches to highly relativistic energies and guarantees the strict electron bunch shape parameters regarding emittance and bunch compression, which are required to emit SASE light inside an undulator section at the end of the accelerator. An overview of the FLASH linear accelerator is provided in figure 3.2

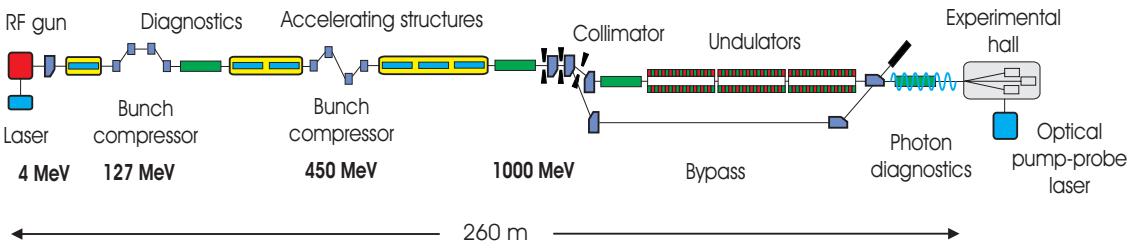

Figure 3.2: *Overview of FLASH*
From left to right: Injection gun with ps-laser system and electron cathode, accelerating modules including two bunch compression stages, bunch diagnostic sections, energy collimator and undulator section, beam dump splitting the electron bunch from the XUV pulse, XUV diagnostic section and transport beam lines and the experimental section.

3.1.1.1 Injection gun

The electron bunch is emitted from a Cs_2Te cathode by a Nd-YLF 11 ps FWHM, 262 nm laser [WKT05] pulse due to the photo-electric effect. The electrons are created within a high accelerating field (40 MV/m on the cathode). The gun cavity is powered by a standard 10 MW klystron. A static magnetic solenoid field is superimposed and provides transverse focusing in order to preserve a small beam cross section. The electron bunch leaves the gun with an energy of 4 MeV per electron, with a bunch length of 10 ps FWHM and a modest peak current of 50 A. A performance measurement of the gun is presented in [AA+04]. It is then injected into first accelerating module ACC1 [BFR+01].

3.1.1.2 Accelerator modules

At FLASH currently 6 accelerating modules accelerate the electron bunch up to relativistic energies (380 MeV - 1 GeV), which are necessary to generate coherent XUV radiation inside the undulator

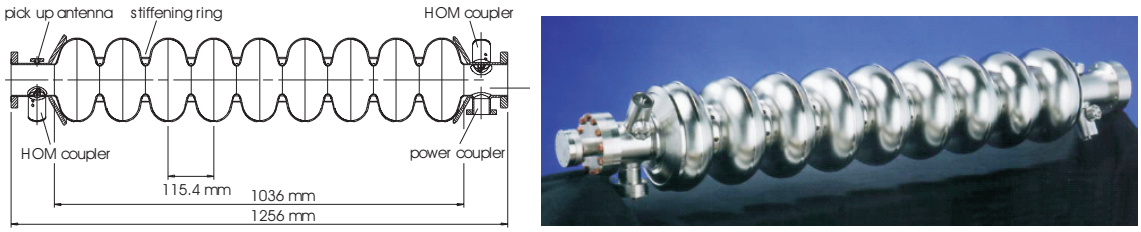

Figure 3.3: *Cross-section and side-view of the Niobium cell accelerator cavities of FLASH.* (Figure adapted from [Aun00])
The standing accelerating wave created from a high power klystron is injected over a waveguide. The pick-up antenna measures the field. Resonant higher-order modes (HOM) induced by the electron bunch are removed by HOM output couplers.

section at the end of the linear accelerator. Each accelerator module contains 8 accelerating standing wave cavities aligned in a row. Each cavity is 1.038 m long [Aun00] and consists of 9 niobium cells. During passage of the electron bunch through a cavity from one cell to the next, the polarity of the longitudinal electric field changes in such a way, that the electron bunch is continuously accelerated and never decelerated.

This resonator mode of operation is referred to as the π- mode with 180° phase difference between adjacent cells. The cell length L is determined by the condition that the electric field has to be inverted in the time $t = L/c = \frac{1}{2 \cdot f}$ a relativistic particle needs to travel from one cell to the next. The optimum RF phase setting, where the electron has the maximum possible energy gain, is usually referred to as *on-crest* acceleration, for all other phases the electron gains less energy (*off-crest acceleration*) or even loses energy (*deceleration*). The fundamental TM_{010} mode of the accelerating electric field has a frequency of 1.3 GHz and the electric field is parallel to the z-axis. The cavity is made from solid niobium, which becomes super-conducting below 9.5 K. The cavity is bath-cooled by superfluid helium at 2 K. The fundamental advantage of super-conducting cavities is their extremely low surface resistance at 2 K leading to RF losses, which are 5 to 6 orders of magnitude lower than in copper cavities. The low RF losses allow to achieve a high resonator quality factor of $Q_0 \geq 10^10$ of the unloaded cavity. By this means a 1 MHz pulse repetition rate within a bunch train of up to 800 micro bunches becomes feasible, since the accelerating field remains stable over the full bunch train. The bunch train repetition rate is 5 Hz. This timing scheme is referred to as *burst mode*-timing scheme (fig. 3.4). Each module is equipped with 8 super-conducting 9-cell Niobium cavities. Each cavity has a frequency tuner, a coaxial RF power coupler, a pickup probe and two higher-order mode (HOM) couplers. A side view of the TTF cavity with the beam tube sections and the coupler ports is shown in figure 3.3. The cells have a spherical contour near their equator for low multipacting sensitivity and a large iris radius to reduce wake-field effects [Aun00].

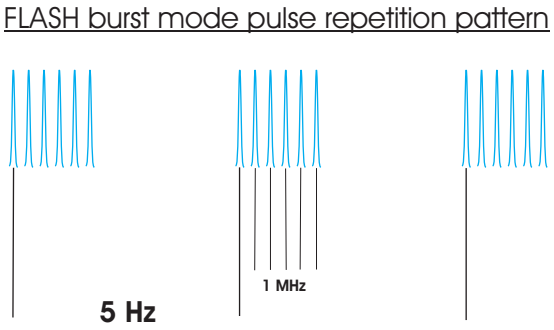

Figure 3.4: *The FLASH specific pulse repetition pattern* A burst of pulses with a repetition rate of 1 MHz is separated from the next burst, which is delayed by 200 ms relative to the burst before. This specific pulse repetition mode is referred to as *burst mode*.

The accelerating gradients vary between 12 MV/m and 25 MV/m for electron energies between 380 MeV to 1 GeV. The photo injector and the accelerating modules are powered by high-power

klystrons of 5 MW and 10 MW output power. A pick-up antenna measures the field inside the cavity. The sum of the measured complex field amplitudes of all cavities in ACC1 are added vectorially with a digital signal processor. The vector sum is used to regulate phase and amplitude of the klystrons and by these means control the phase and amplitude of the cavities.

3.1.1.3 Bunch compression

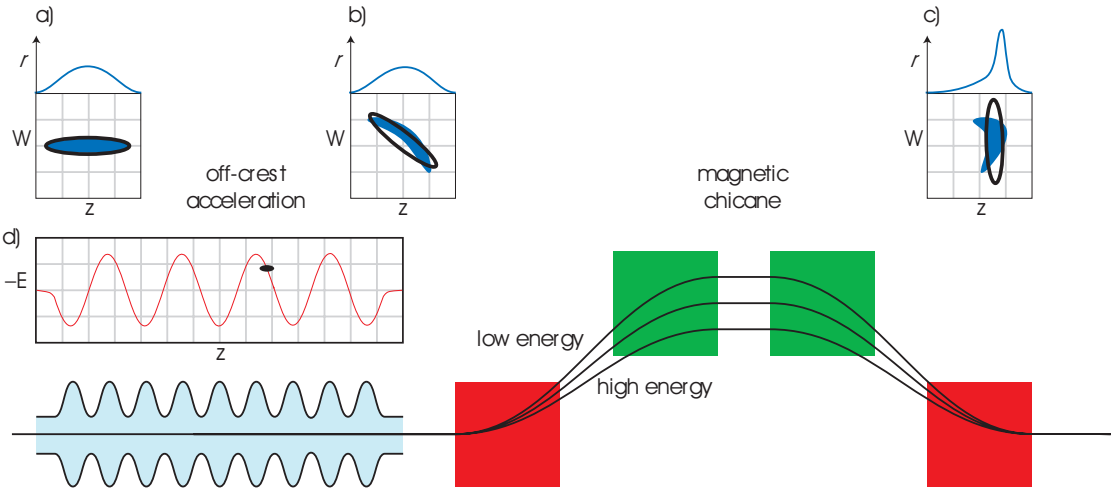

Figure 3.5: *Schematic drawing of a bunch compressor* (figure adapted from [Isc03]).
The off-crest acceleration introduces a correlated energy spread. The phase space is sheared by the magnetic chicane. Symbols: δW: energy gain of a particle, η: particle energy relative to reference particle, ζ: relative longitudinal position inside the bunch, ρ: longitudinal charge density, E: electric field.

The high gain FEL requires a high peak current of several kA of the electron bunch inside the undulators. This bunch requirement can not be realized by the injection gun, since the strong space-charge effects would blow-up the bunch before it reaches the undulators. Two techniques are used to prevent this effect. First, the 1 nC electron bunch is created by a 11 ps FWHM long optical pulse, which leads to only 50 A of peak current. Second, the electron bunch is accelerated to relativistic energies suddenly after the laser pulse hits the photocathode. For relativistic energies the transverse magnetic forces compensate the repulsive electric forces. And second, to reach the demanded high peak currents, the electron bunch needs to be longitudinally compressed. The compression is accomplished in a magnetic chicane. Electrons of higher momentum are kicked less than electrons of smaller momentum. Thus, electrons of higher momentum localized at the tail of the bunch travel along a shorter trajectory through the chicane and can catch up with the electrons in the head of the bunch. Hence, a longitudinal negative energy chirp has to be applied before the bunch can be compressed. This energy chirp is applied by the first acceleration module in the following way. The 10 ps long electron bunch corresponds to 4.7° of the phase of the 1.3 GHz sinusoidal accelerating field. If the bunch passes the accelerating module delayed by 8° off crest, a nonlinear chirp of correct sign is impressed on the electron bunch. A C-type magnetic chicane compresses the bunch as explained in figure 3.5. The inlay plot 3.5 a) shows the intra bunch energy distribution as a function of the longitudinal electron bunch rest frame coordinate ζ before the acceleration. Figure 3.5 b) shows the energy chirp after the off-crest acceleration inside ACC1 as depicted in the inlay 3.5 d) is applied. Figure 3.5 c) shows the particle distribution behind the magnetic chicane. The peak current is increased. The black ellipse shows linear compression, the blue shape the effects of non-linear

compression.

The sinusoidal time dependence of the accelerating field leads to a nonlinear chirp, which after passing through the chicane results in a compressed bunch shape with a narrow peak of (<100 fs FWHM) and a long bunch tail of (≈2 ps) instead of a pure Gaussian peak. To reduce this unwanted non-linearity the energy chirp is introduced in two stages. A first chirp is applied on the long bunch after ACC1 (E_{kin} = 125 MeV). A second smaller chirp is applied by two more accelerating modules (E_{kin} = 380 MeV) between the first and secondary bunch compressor. As the bunch has already been compressed by the first bunch compressor, the nonlinearity of the chirp applied to the bunch by the following two accelerating modules is decreased. Also other distorting effects like coherent synchrotron radiation are reduced by distributing the compression among two bunch compressors at different energies [SAL+05].

The compression section is one of the most critical parts of the machine with regards to timing jitter. Any variation in the energy chirp is converted inside the first bunch compressor directly into timing jitter. This implies tight requirements on the stability of the amplitude and phase stability of the RF fields inside the accelerating cavities. In a single-stage bunch compression scheme, the timing jitter introduced by the bunch compressors can be expressed in the form [SAL+05]:

$$\sigma_t^2 \approx \left(\frac{R_{56}}{c}\frac{\sigma_a}{A}\right)^2 + \left(\frac{C-1}{C}\right)^2 \left(\frac{\sigma_\phi}{\omega_{rf}}\right)^2 + \left(\frac{1}{C}\right)^2 \sigma_{in}^2 \tag{3.1}$$

Here the radius of the first bending magnet of the compressor chicane R_{56} is approximately 160 mm for FLASH (and 100 mm for the XFEL), C is the compression factor (between 20 and 100), ω_{rf} the angular frequency of the accelerating RF. The amplitude fluctuations σ_a/A lead to a jitter (RMS) of 3 to 5 ps per percent and the phase fluctuations σ_ϕ/ω_{rf} to an additional jitter of 2 psperpercent. The best energy stability presently achievable was measured to be $2.8 \cdot 10^{-4}$ [SAL+05], which results in an arrival time jitter of 180 fs RMS. The incoming arrival time jitter due to arrival time fluctuations of the photocathode laser pulse, which are on the order of about 100 fs RMS is damped by the compression factor $C \approx 20$ of the first bunch compressor and are thus negligible.

3.1.2 Electron bunch diagnostic

Since the built up TEO diagnostic is primarily a detector of the linear accelerator electron bunch, it is of importance to compare its performance with other electron bunch detectors. In particular with detectors, which are also installed in the linear accelerator of FLASH and can detect the same electron bunch as TEO. A few of these diagnostics will be shortly introduced.

3.1.2.1 Transverse deflecting structure (TDS)

At FLASH a high resolution longitudinal electron bunch density detector is installed named TDS also known as LOLA detector *. It bases upon a transverse deflecting traveling wave structure and a phosphorous screen. The RF transverse deflecting cavity operating at 2.856 GHz≡ 11/51 of the FLASH fundamental of 1.3 GHz frequency [ABEK02] is used to sweep the beam transverse to the direction of propagation, as shown in fig. 3.6. The structure is operated at the zero-crossing phase of the field, where the time derivative is maximum, so that a strong correlation between longitudinal z-coordinate and transverse position is given. Measurement of the beam size downstream on a profile monitor is used to measure the bunch length. It is possible to deliver a large amount of

*Since it was at first developed at SLAC (Stanford Linear Accelerator) and there has been known under the name LOLA IV

power to such a device to give the beam an extremely strong kick and thereby obtain good bunch length resolution [ABEK02]. The LOLA detector at FLASH can reach a time resolution of 15 fs

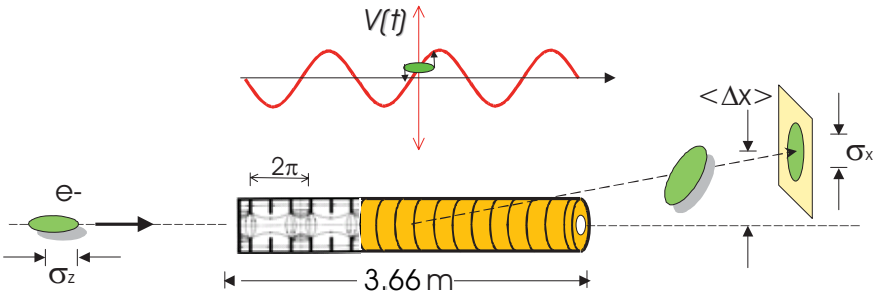

Figure 3.6: *Principle of the transverse deflecting cavity structure LOLA.*
The electron bunch passes the cavity near the zero field crossing of the sinusoidal standing wave inside the cavity structure. The electric field induces a transverse kick, which streaks the longitudinal distributed electrons in vertical direction. A fluorescent screen visualizes the streaked electron bunch. The vertical $< \Delta x >$ kick is of the order of 2-3 cm (figure adapted from [ABEK02]).

RMS [FEL05]. To achieve this high resolution, the electron beam optics must be optimized to yield the smallest possible beam spot on the view screen. For the beam optics used during standard accelerator operation the beam size is bigger and therefore the resolution is limited to about 27 fs RMS [Röh08].

3.2 The optical pump-probe laser system at FLASH

To provide the possibility to perform two-color pump-probe experiments with the XUV high power fs-pulse emitted by the free-electron laser, a separate optical fs-laser system is established close to the experimental stations in the FLASH experimental hall. The system is synchronized by a phase-locking loop control system to the RF frequency of the master oscillator of FLASH. The laser system provides various modes of operation to suit the individual needs of user groups and to match the complex timing structure of the FEL. To provide as well high pulse repetition rates comparable to the FEL inter bunch train repetition rate of 1 MHz and also high pulse intensities from about several GW up to one TW, two different laser amplifier systems are installed. The GW laser system is able to emit NIR pulses at 800 nm with 120 fs FWHM pulse duration and 20 μJ pulse energy, The pulse repetition rate is up to 1 MHz in a burst mode, which matches the burst mode pulse pattern of FLASH. The TW laser system emits an NIR pulse with 5 Hz repetition rate at 800 nm but with up to 25 mJ per pulse. A part of 2 mJ can be transported to the pump-probe experimental stations without being scrambled due to non-linear effects in air or transmissive optics. The pulse duration is 120 fs FWHM as well. Both laser sources use the same Ti:sapphire oscillator as seeding source.

3.2.1 Titanium-Sapphire oscillator

The used oscillator is a conventional passive Kerr lens modelocked Titanium:Sapphire (Ti:Sa) oscillator, which emits optical pulses at a carrier frequency of 800 nm (375 THz) in the near infrared (NIR) spectral range. The oscillator works at a repetition rate of 108.3 MHz, which is 1/12 of the 1.3 GHz frequency, at which the accelerator modules of FLASH are working. With a pulse energy of 4 nJ the emitted power of the oscillator is 450 mW. Within the oscillator a short prism compressor

compensates for the dispersion of the Ti:Sa crystal. Between the two prisms a several mm wide vertical slit is placed. By changing the size of the slit, more or less of the spatially dispersed bandwidth is transmitted. With this technique the bandwidth of the oscillator is tunable within a range of 13 nm FWHM to 26 nm FWHM. A schematic overview of the oscillator is provided in fig. 3.7. The Ti:Sa oscillator is electronically synchronized with the FEL master oscillator.

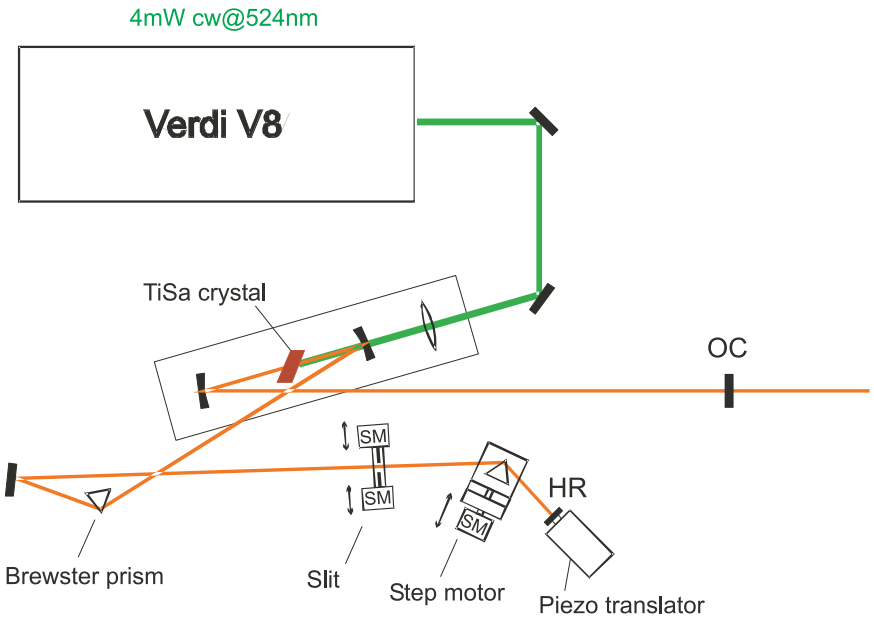

Figure 3.7: *Ti:Sa oscillator design of the FLASH pump-probe laser system.*
The bandwidth selection slit is located between two brewster prisms, where the spectrum is spatially dispersed. The coarse timing synchronization is performed with a step motor, which moves the second prism more or less into the beam and thus changes the optical path length. The step motor is used to compensate for slow drifts. Fast temporal fluctuations are compensated by the stacked Piezo longitudinal translator, on which the high reflecting end mirror of the oscillator resonator is mounted.

3.2.2 Amplifier section

The GW power amplification of the Ti:Sa laser is performed with an OPCPA (optical-parametric chirped pulse amplification) amplifier (see fig. 3.8). The parametric amplification process is necessary due to the high repetition rate of 1 MHz. The pump-laser of this amplifier system is a replica of the photocathode laser of the FLASH injection gun [WKT05].

The TW power amplifier uses a commercially available chirped pulse amplifier system named HIDRA by the laser manufacturer Coherent. In a first stage it amplifies a temporally stretched oscillator pulse in a regenerative amplifier. This amplifier consists of a Nd-YAG laser pulse pumped Ti:Sa crystal, which is placed inside a resonator. The oscillator pulse performs up to 30 round trips inside the resonator and is amplified by stimulated emission inside the Ti:Sa crystal in each pass from 4 nJ up to a final power of 1 mJ per pulse. The preamplified mJ-pulse is finally amplified in pumped Ti:Sa crystal based multi-pass booster section up to 25 mJ. A grating compressor recompresses the amplified pulse.

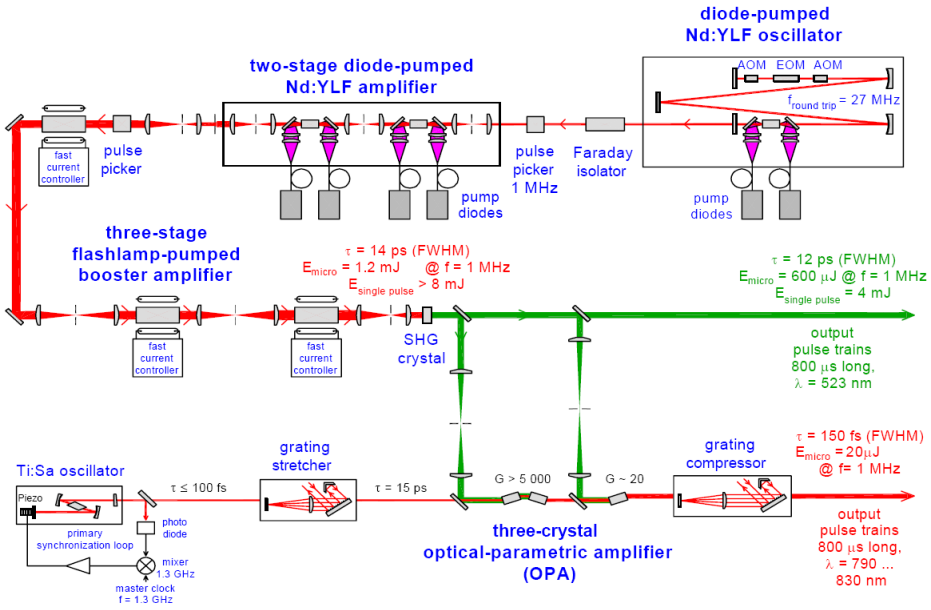

Figure 3.8: *OPCPA 1MHz amplifier of pump-probe laser system.*
The amplified pulse energy is 20μJ. The system operates in burst mode with 1MHz@5Hz repetition rate. The Nd-Ylf oscillator emits pulses with 15 ps FWHM duration. The oscillator is active mode-locked and synchronized by two acusto-optical and one electro-optical modulators. Two OPA amplifier crystals are used in collinear geometry.

3.3 The synchronization system at FLASH

Multiple systems at FLASH must operate synchronized with the linear accelerator. The electronic synchronization is realized by electronic triggers, which are distributed along the whole accelerator facility and which can be shifted in time electronically. Other systems like electronic oscillators or klystrons, which generate a periodic electrical field need a different approach. These system are directly locked to the fundamental 1.3 GHz frequency generated by the master oscillator to stabilize the output frequency in phase and amplitude. For example the radio frequency (RF) output of the klystrons, which generate the accelerating field of the cavity cell structures of the linear accelerator or the repetition rate of a mode-locked Ti:sapphire oscillator.

Figure 3.9 summarizes all timing modules at FLASH, which contribute temporal jitter to the relative arrival time jitter between the XUV and the NIR pulses at the location of a two-color pump-probe experiment. Most of the jitter values have been measured, however numbers with a ** are estimated numbers. The sources of the jitter measurements are found at following places:

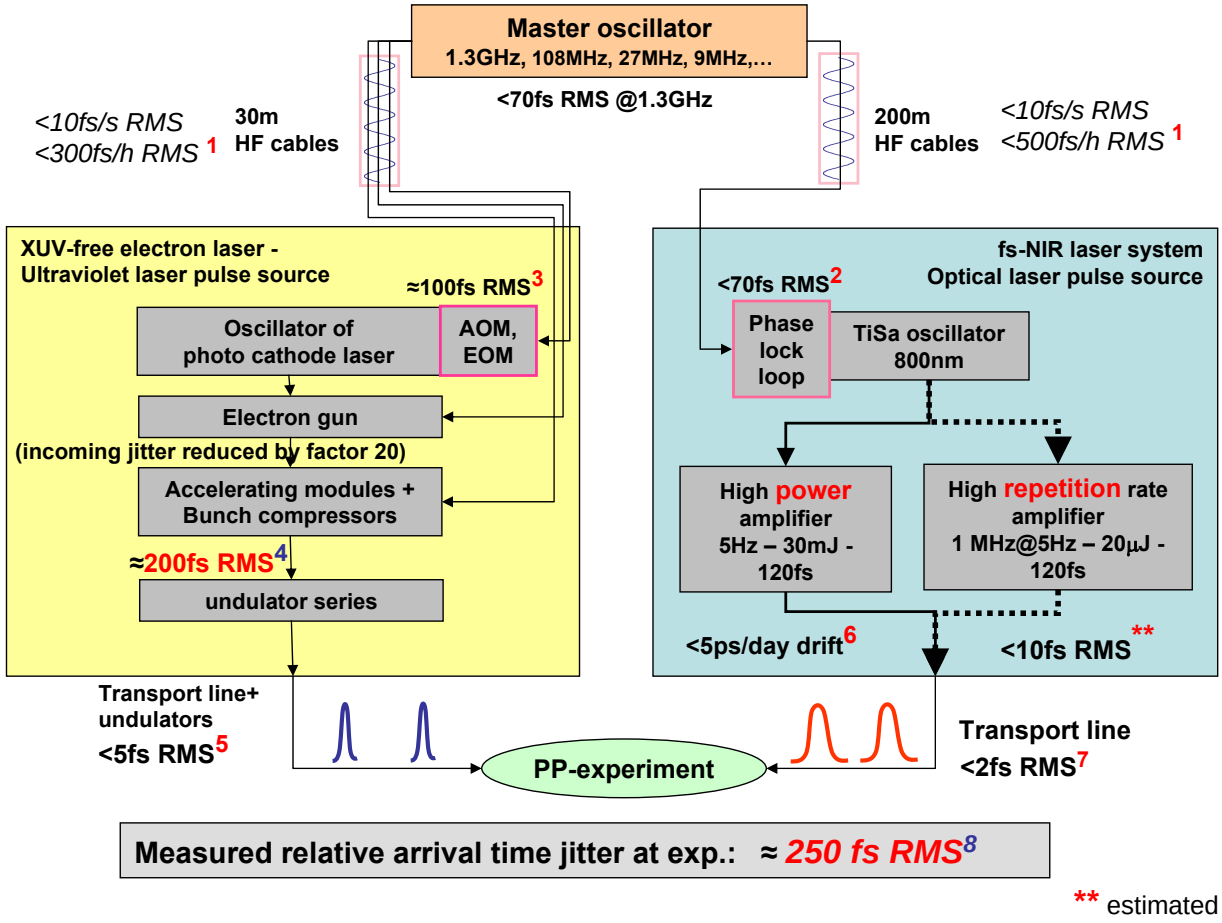

Figure 3.9: *Synchronization at FLASH with jitter sources.*
RF distribution system and synchronization of synchronized lasers and subsystems of the FLASH linear accelerator.

[1]: Jitter created in the RF transport cables. The signal traveling time fluctuations on a second and few minutes time scale are below 10 fs RMS, but on a time scale of minutes to hours the traveling time fluctuates up to 500 fs RMS [Lud]
[2]: jitter induced by the RF synchronization of the Ti:Sa oscillator by a phase lock loop, see figure 3.10.
[3]: Temporal jitter of the gun photo-cathode laser, see [WKT05].
[4]: Main temporal jitter induced by the amplitude and phase instabilities of ACC1, which convert into a temporal jitter in the first bunch compressor, see section 3.1.1.3.
[5]: Temporal jitter induced due to a variation of the longitudinal location of the SASE emitting center of the electron bunch inside the undulators plus the temporal jitter induced by the XUV mirror beamline measured in [Fru].
[6]: Temporal jitter inside a regenerative amplifier <10 fs RMS, see [MKT+00]. Temporal drift <5 ps/day [Due].
[7]: Temporal jitter induced by the optical pulse transport line, measured by a fast SHG cross correlator between a pulse reflected from the end of the transport line and an oscillator pulse [Syn].
[8]: A direct measurement of the relative jitter between the optical NIR pulse and the XUV pulse at the pump-probe experiment, see [MCW+08].

From the numbers one finds, that the major jitter contributions results from the ACC1 instability and from the RF synchronization of the optical laser pulse oscillator. Since the individual jitter numbers are added up quadratically, all small jitter values can be neglected relative to the total jitter at the pump-probe experiment.

3.3.1 Phase locking loop

The Ti:sapphire oscillator, which generates the NIR fs-pulses for the TEO experiment, is synchronized by a phase locking loop (PLL) control system to the master oscillator of the linear accelerator of FLASH. The master oscillator provides frequency waves, which are lower harmonics of the fundamental frequency of the accelerating field inside the accelerating structures of the linear accelerator of FLASH. These RF frequencies are distributed by thermally stabilized coaxial cables along the linear accelerator. The fundamental frequency is 1.3 GHz. Some subharmonics generated by the master oscillator are 108 MHz (1/12), 81 MHz (1/16), 27 MHz (1/48) and 9 (MHz). All frequencies are phase locked to the fundamental. The PLL uses the fundamental and the 1/12th subharmonic to lock the Ti:sapphire oscillator. The phase jitter of the fundamental at the exit of the transport cable accumulates to less than 10 fs RMS temporal jitter.

The PLL is based on the following principle: The back reflecting mirror of the oscillator can be moved to shorten or lengthen the optical path length of the oscillator cavity. The oscillator works at a repetition rate of 108 MHz, which exactly matches with the 1/12th harmonic of the fundamental frequency of FLASH. A deviation of the position of the back-reflecting mirror of less than a micrometer is enough to accumulate an arrival time shift of the optical pulse of a few 10 ns within one second. An analysis of the Fourier transform of the pulse repetition train reveals, that an arrival time modulation of the oscillator pulses corresponds to a phase offset modulation of the Fourier components. A photo diode signal of the oscillator output measures the oscillator pulse train in time. A photo diode converts the oscillator pulse train electronic pulses. These harmonics of the pulse train, which frequency match with the reference waves of the FLASH master oscillator can be filtered electronically with a bandpass filter and used to lock the laser oscillator by comparing the phase offsets between the reference wave(s) and the corresponding Fourier components of the pulse train. The PLL electronic used during this work continuously compares the phase offset of the Fourier components at 108 MHz and the fundamental at 1.3 GHz. It corrects the Piezo length to keep the phase offset differences between the harmonics of the oscillator and the reference waves of FLASH at zero. Thus, the optical laser is kept phase locked and thus arrival time stabilized to FLASH. The PLL electronics, which control the Piezo motor of the resonator back reflector of the oscillator was developed by the Max Born institute (Berlin, Germany).

The stability of the synchronization system has been measured with an "in-loop" measurement using a phase noise spectrum analyzer and as reference the FLASH fundamental frequency at 1.3 GHz. The results are shown in fig. 3.10. The phase noise of the Ti:Sa oscillator accumulates to an average jitter of 60 fs RMS within 1 ms. A specific phase noise measurement within the spectral regime above 1 MHz has shown, that within a corresponding temporal interval of 1 µs the temporal jitter is smaller than 10 fs RMS [Loe], which is better than the jitter of 26 fs RMS found from the shown measurement in fig. 3.10. The differences result from the noise offset of the used photo diodes of each measurement.

For the TEO detector this high frequency regime starting at 1 MHz is of large importance as will be explained in the next chapter.

The use of two frequencies allows to introduce an electronically tuned temporal delay of the Ti:Sa pulse, which is useful to find the temporal overlap between the Ti:Sa pulse and the elec-

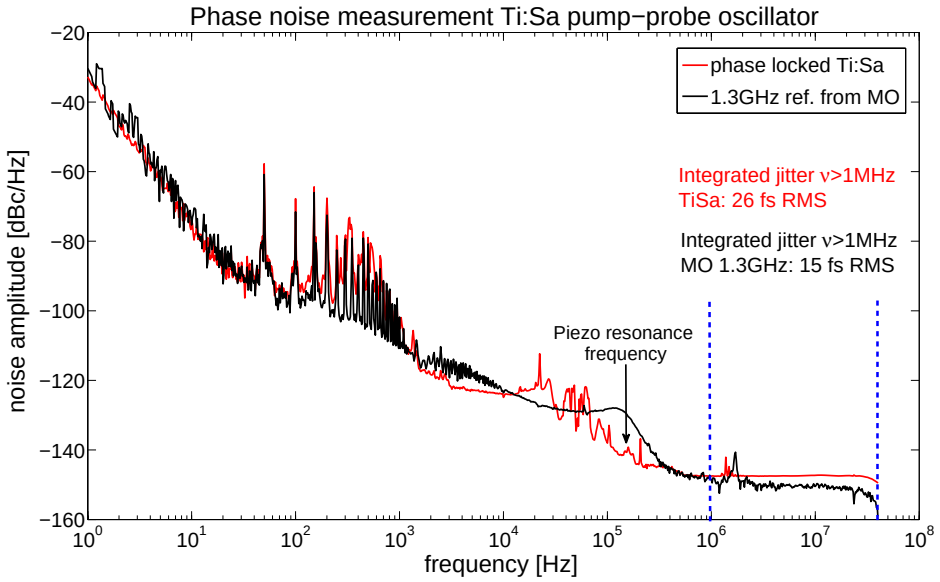

Figure 3.10: *Phase noise measurement of the Ti:Sa oscillator in loop versus the fundamental reference frequency 1.3 GHz of FLASH.*
Red curve: The Ti:Sa oscillator shows an in-loop RMS jitter of only 60 fs, if measured relative to the fundamental reference frequency at 1.3 GHz.
Black curve: To compare the reference fundamental frequency at 1.3 GHz, this reference has been measured relative to a reference frequency derived from the internal clock of the phase noise analyzer.

tron bunch as explained in the following: The PLL electronic compares the phase offsets of two frequencies, i.e. the fundamental frequency at 1.3 GHz and the 12 times smaller frequency at the oscillator repetition rate of 108 MHz. Both offsets are regulated to zero. It follows, that there exist 12 possible phase offset settings of the 108 MHz frequency, which all fulfill the zero difference phase condition for both frequencies simultaneously. These positions are called *buckets*. These buckets or phase/time steps can be used to stepwise shift the optical pulse over a time range, which corresponds to one round trip of the Ti:Sa oscillator pulse in its cavity. Thus, the bucket step is $\Delta t_{bucket} = 1/108 * 12 = 770\,\text{ps}$.

3.4 The experimental area of FLASH

This section shall introduce the major components necessary to perform experiments with the XUV pulse of FLASH in the experimental area. An overview of the experimental environment is provided in figure 3.11 and in [TAB+09]. In the figure the following points of interests are marked:
(1) The optical laser system has been discussed in section 3.2.
(2) A fast streak camera with a specified resolution of 2 ps measuring the relative arrival time of the optical NIR pulse and a pulse, which results from synchrotron radiation emitted during the bending and splitting of the electron bunch from the XUV pulse by a strong dipole magnet after the undulator section of the FEL linear accelerator.
(3) The XUV beamlines are evacuated to 10^{-9} mbar. The XUV mirrors of the beamlines are carbon coated.
(4) A monochromator grating to reduce the XUV spectrum. Details are found in [Wel07].
(5) The optical laser beamlines are evacuated and transport the optical pulse to one of the experi-

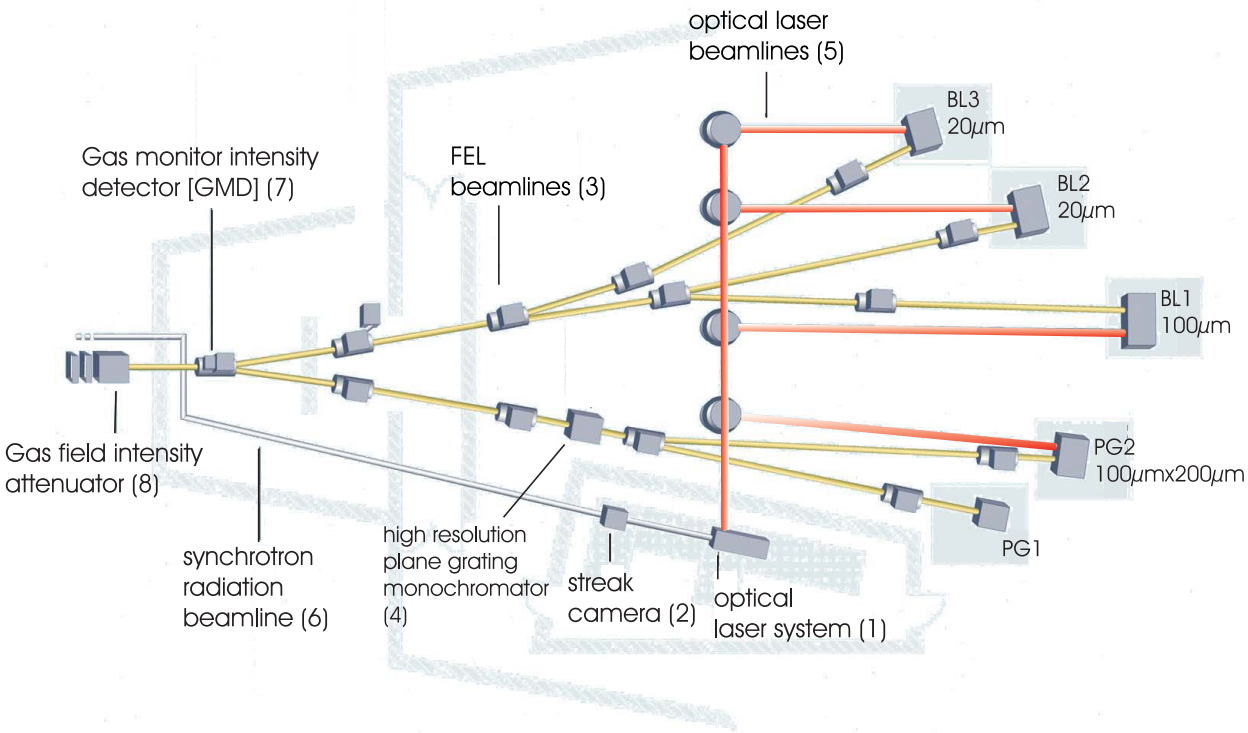

Figure 3.11: *Overview of the experimental hall of the FLASH facility.*
The optical laser beam transport lines distribute the optical fs-laser pulse to the experimental stations of the individual XUV beamlines of FLASH. Only one pump-probe experiment at the same time can be performed.

mental stations.
(6) The synchrotron radiation beamline for the timing streak camera.
(7) A gas monitor detector, which measures the energy of each XUV pulse shot-by-shot [Ric03].
(8) A gas attenuator to reduce the XUV pulse energy by means of gas absorption in a controlled, non-invasive way.

Chapter 4

Experimental setup and characterization of the electro-optical timing system

The relative arrival time jitter Δt_{jitter} of an optical pulse and a XUV pulse at the location of the pump-probe experiment during this work was between 150-350 fs RMS (see sections 5.3.1, 6.5.1.1 and in [MCW+08]). The pulse durations are in the range of 10 fs-50 fs FWHM $\Leftrightarrow$ 4 fs-12fs RMS for the XUV and 120 fs FWHM $\Leftrightarrow$ 50 fs RMS for the optical pulse. Thus the distribution width of the temporal jitter was larger than the pulse duration of the interacting two pulses. Hence, without any further efforts the temporal resolution of two-color pump-probe experiments at FLASH would be limited by the jitter and not by the pulse durations as it ideally should be. This emphasizes the necessity to install an online single-shot timing system at FLASH, with which the uncertainty on the relative temporal pulse arrival time during a two-color pump-probe experiment is reduced and the experiments temporal resolution will be improved.

Requests on the timing system are the capability to measure the arrival time of each XUV pulse with respect to the optical pump-probe laser pulse in a noninvasive way on a sub 100 fs timescale to significantly improve the two-color pump-probe temporal resolution. Within the framework of this thesis a diagnostic capable to perform the task to measure the arrival time of one arbitrary electron bunch of each bunch train has been developed. In the following this diagnostic is called Timing by Electro-Optical sampling (TEO). The timing measurement scheme is presented in figure 4.1. The diagnostic measures the relative arrival time between an NIR laser pulse from the pump-probe seed oscillator and the electron bunch of FLASH in the linear accelerator right before the undulator section. The diagnostic utilizes the non-invasive electro-optical spatial decoding measurement technique (see section 2.4.1) and does not influence the electron bunch. The XUV pulse emitted by the electron bunch can be used in a pump-probe experiment without any restriction.

The idea of the TEO diagnostic is that the indirectly measured relative arrival time between the electron bunch and the pump-probe oscillator seed pulse as well as the relative arrival time between the XUV pulse and the optical pump-probe pulse at the location of the two-color pump-probe experiment at the end of the FEL is almost equal. Under these assumption, the retrieved arrival time data by the TEO diagnostic is used a posteriori inside the two-color pump-probe experiment to correct for the temporal jitter as will be shown in chapter 6. In this sense, the problem to measure the relative arrival time is shifted from an optical-XUV pulse correlation to an optical-electron bunch correlation.

Let τ_{NIR,e^-} be the relative arrival time between electron bunch and NIR pulse in the linear accelerator as measured by the TEO diagnostic. And let $\tau_{NIR,\gamma}$ be the actual relative arrival time between XUV pulse and NIR pulse inside a pump-probe experiment (compare fig. 4.1). With this definitions the present performance of the TEO diagnostic is such, that the temporal uncertainty between the measured and the actual relative arrival times σ_{TEO}=τ_{NIR,e^-}-$\tau_{NIR,\gamma}$ is smaller than 60 fs RMS, which

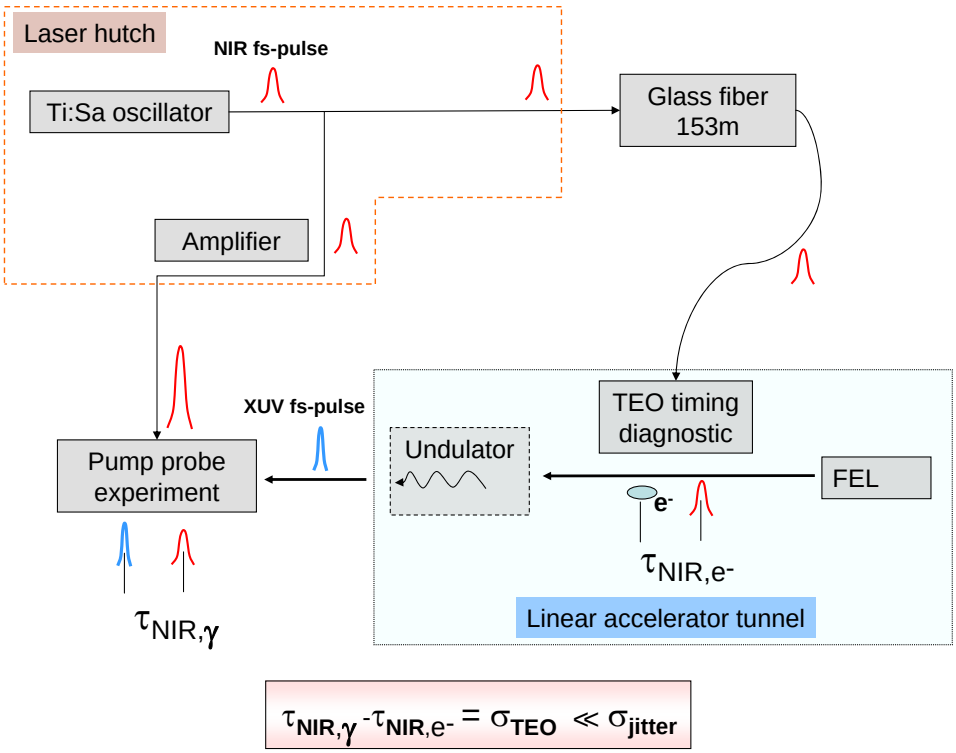

Figure 4.1: *Principle of the two-color pump-probe timing diagnostic at FLASH.*
The optical NIR pulse, which is simultaneously used either for the arrival time measurement or the two-color pump-probe experiment are emitted by the same oscillator. This improves the temporal resolution of the timing diagnostic (see main text). The arrival time detection is carried out shot-by-shot and is fully parasitic without influence on the XUV pulse. The detected electron bunch/optical relative arrival time is used as a measure of the XUV/optical relative arrival time.

is 3 to 6 times smaller than the temporal jitter of the linear accelerator as will be shown in chapter 6. Previous experiments with a similar detection technique at SPPS in Stanford/USA have shown a minimal arrival time error of about 65 fs RMS [CF05].

Figure 4.1 shows, that the two optical fs-pulses to either clock the arrival time or to perform the two-color pump-probe experiment are emitted by the same oscillator. This is The most significant feature of the TEO timing diagnostic. The opposite method to use separate oscillators for each of both fs-pulses independently would require to synchronize both oscillators to FLASH separately. This would introduce one more jitter source in the order of 70-100 fs RMS compared to the single oscillator setup. Hence, the decision to use only one oscillator guarantees a high temporal correlation between the timing detection NIR fs-pulse and the pump-probe NIR fs-pulse. However this decision creates the problem to transport the optical pulse over 150 m to the timing diagnostic inside the linear accelerator, which is because of stability and geometrical reasons only possible using an optical glass fiber. This transporting glass fiber leads to further problems discussed in the following section.

At this point it is worth to mention, that there exists a large difference between the optical path lengths on the one hand from the oscillator to the location of the TEO diagnostic and on the other hand from the oscillator to the pump-probe experiment. This difference is that large, that the optical pump-probe fs-pulse and the optical TEO fs-pulse can not be one and the same. The optical travel time through the 153 m long transportation glass fibre is 750 ns and thus much larger than the travel time of only 100 ns from the oscillator to the pump-probe experiment. Thus, the effective temporal

difference between the event time of the pump-probe experiment and the event time of the electro-optical cross-correlation, i.e. the event time of the jitter measurement, amounts to 650 ns. With a temporal inter pulse spacing of the Ti:Sa oscillator of 9.3 ns, one finds, that **70** pulses of the Ti:Sa oscillator pulse train are in between the TEO fs-pulse and the optical pump-probe fs-pulse. **Any temporal jitter between these both pulses would deteriorate the resolution of TEO !**
Fortunately this effective traveling time difference is shorter than the time any mechanical disturbance means and shorter than the 3.2 µs long life time of the excited electronic state of the Titanium:Sapphire crystal active medium of the oscillator. The accumulated phase noise jitter of the synchronized oscillator within a time interval smaller than 1 µs is smaller than 10 fs RMS* (see fig. 3.10). Because this noise is much smaller than the Ti:Sa pulse duration of 50 fs RMS according to fig. 3.10, no significant temporal jitter between the optical pump-probe pulse and the TEO femtosecond laser pulse is possible.

Hence, despite of the fact that not the same optical NIR pulse is used for the TEO arrival time measurement and the two-color pump-probe experiment simultaneously, the used *consecutive pulses*-scheme is temporally equivalent to the ideal situation, in which exactly the same optical oscillator pulse would be used for both purposes. This is a major reason for the feasibility of the fiber based indirect temporal jitter diagnostic discussed in this work !

4.1 The optical pulse transport system

The following section will concentrate on the fiber based pulse transportation system of the TEO timing diagnostic and its technical realization.

As explained before the purpose of the TEO diagnostic is to cross-correlate an optical ultrashort fs-laser pulse with the electron bunch of FLASH. One would ideally place the fs-pulse generating optical laser system as close as possible to the location of the cross-correlation. But the oscillator of this laser system resides in the experimental hall at the end of the accelerator nearby the user experiments and there is a 150 m span between the TEO system and the laser amplifier. Using two separate oscillators would introduce an additional jitter source (see previous section 4). A high temporal synchronization between the optical TEO pulse and the optical pump-probe pulse is only achieved, if both of them are emitted by the same oscillator. The challenge is to transport the broadband Ti:Sa pulse over 150 m without changing its temporal properties.

The classical way to let the pulse simply propagate from the experimental hall inside a vacuum beam tube and back into the accelerator was not possible, since the TEO diagnostic was planned after all sections of FLASH had been built. Implementing another optical beam line afterwards to transport the optical fs-pulse to the TEO timing station in the accelerator area was prevented by FLASH specific geometrical reasons connected with the fact that the XUV beamline of FLASH crosses the storage ring of the synchrotron radiation light source PETRA [PET]. A more realistic option is to carry the optical pulse via a glass fiber from the experimental hall to the location of the FEL electron bunch cross-correlation.

In summary, the problem consists of deliver of an ultrashort near-infrared laser pulse of about 20 nm bandwidth temporally fourier limited and polarization maintained about 150 m through a highly dispersive glass fiber.

A schematic overview of the fiber based pulse transporting system is shown in figure 4.2. The only difference to fig. 4.1 is the additional dispersion control system. The schematic overview starts with the Ti:Sa oscillator, which works at a repetition rate of 108.3 MHz. Using a system of Pockels cells one pulse is selected from the oscillator pulse train. This pulse is first amplified and

*Measurement limited by the ground floor noise level of the photo-diode.

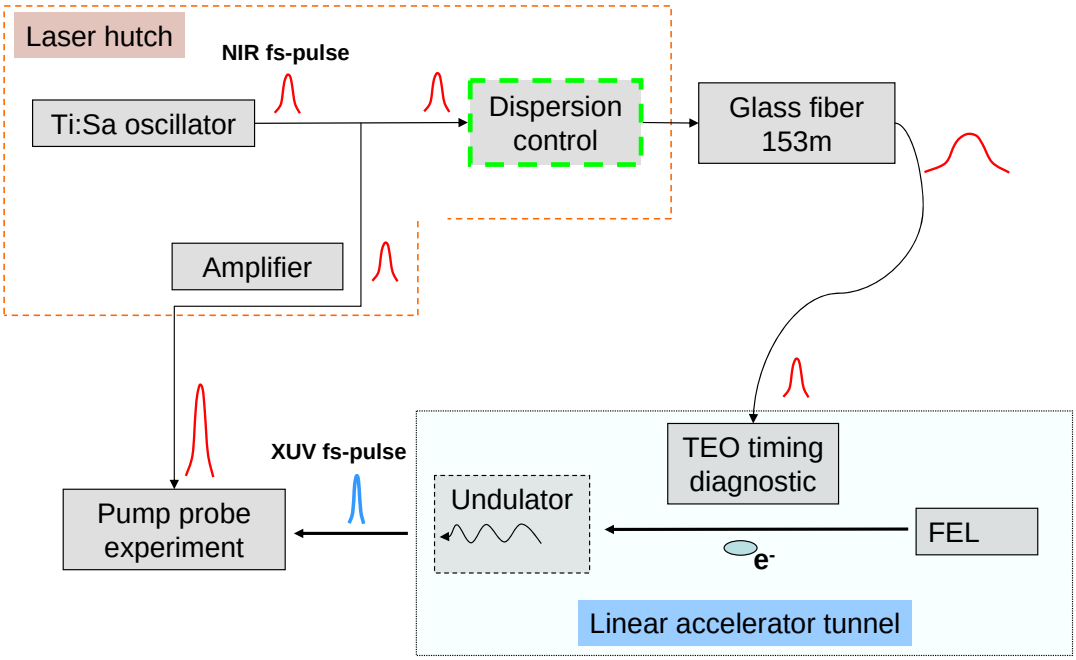

Figure 4.2: *TEO fs-pulse transportation system*
The pump-probe and EO cross-correlation pulse are emitted from the same oscillator. The TEO pulse is transported via a glass fiber. Before entering the glass fiber the pulse propagates through an optical system to compensate for the pulse distorting effects, which originate from the fiber dispersion and microphonics. The dashed line surrounds all elements, which are located in the laser hutch situated in the FLASH experimental hall about 150 m away from the electron bunch-optical correlation experiment.

then transported through vacuum beam tubes to the pump-probe experiment at the end of the linear accelerator in the experimental hall. The rest of the fs-pulse train including the specific optical fs-pulse, which is used to perform the electro-optical arrival time measurement, is coupled into a glass fiber, which leads to the TEO setup in the FLASH tunnel.

The dispersion of the fiber is pre-compensated by a complex dispersion control system before the pulse is injected into the fiber. This is performed by a set of dispersive optical components like a grating and a prism compressor as well as a spatial light modulator (SLM). The complete dispersion control system will be explained in detail in the next section.

After traveling through the 150 m long glass fiber the pulse is temporally Fourier limited and ready to be used for the electro-optical cross-correlation within an electro-optical crystal placed next to the electron beam.

4.1.1 Polarization maintaining single-mode fiber

The transport of the optical fs-pulse is performed with a single mode fiber to maintain the beam profile quality and prevent spectral distortions due to interference between different transverse modes (mode dispersion), which are created inside a multi-mode fiber. Another problem, which must be prevented, is polarization mode coupling. A circular core single mode fiber shows only slightly different phase constants

$$\beta_{x,y} = \frac{2\pi n_{x,y}}{\lambda_0} \tag{4.1}$$

for the two orthogonal polarization states of the propagating transverse LP_{01} mode. Both orthogonal modes show similar propagation properties and thus energy transfer between both polarization states is possible, which is called *polarization coupling*. The physical reasons for this energy transfer are continuous twists or stochastic vibrations inside the fiber. To be precise, polarization coupling occurs only if the power spectrum of such perturbations is comparable with a spatial frequency equal to $(\beta_x - \beta_y)$. Since such a power spectrum exhibits a low-pass behavior and is damped, the larger the difference $(\beta_x - \beta_y)$, the higher the probability of avoiding polarization coupling [Can]. Hence, during the manufacturing process of the fiber one creates an artificial increase of the birefringence to enlarge this phase constant difference and hinder energy transfer between different polarization modes. This can be realized by an introduction of an asymmetric stress distribution from a non-circular cladding cross-section or by placing rods of another material within the fiber cladding (examples shown in fig. 4.3).

4.1.2 Effects of the single-mode fiber on the fs-pulse

Spectral dispersion one generated using a glass fiber to carry a broadband near infrared femtosecond pulse leads to a temporal pulse distortion generally including a pulse broadening (see section 2.1.1). During the development of the TEO experiment the only commercially available fibers capable to deliver a 800 nm Ti:Sa pule with zero spectral dispersion were photonic fibers[†], which at that time could only been manufactured with a length of a few meters. Non-photonic glass zero dispersion fibers were only available for the telecom spectral range at 1550 nm but not for 800 nm.

We have chosen a non-photonic polarization maintaining single mode fiber for the transportation of the TEO fs-pulse, which is not dispersion compensated. Regarding the spectral dispersion problematic one can compare this fiber with a dispersive bulk glass optic of about 150 m thickness, since the influence of the glass fiber dispersion on the Ti:Sa fs-pulse temporal distribution is the same! Typical glass species mainly inflict second order (Group Velocity Dispersion, GVD) and third Order dispersion (TOD) on a fs-pulse. However, for the particular glass fiber used in the TEO setup (FS-PM-4611 from 3M optical components) no data sheet was available, which could specify the exact amount of dispersion. Thus the dispersion, which includes the possibility of nonlinear contributions, of the used fiber to transport the beam was unknown and must be measured. Results of this measurement are shown in section 4.1.7.2.

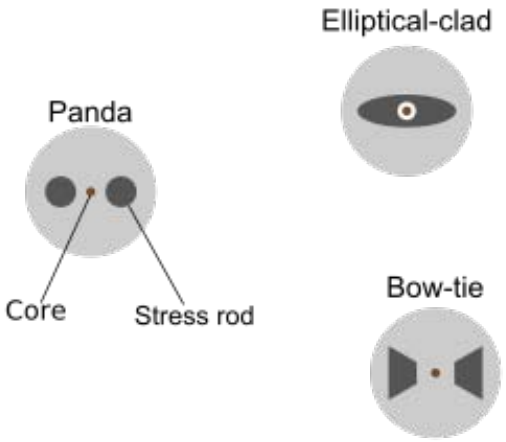

Figure 4.3: *Polarization maintaining single-mode fiber variations.*
Various ways to apply an artificial stress and to create a linear polarization maintaining fiber. According to manufacturer specifications in the present TEO setup a fiber using the "Oval-Inner Clad" variation is used.

Despite the lack of precise fiber parameters, a simulation of the pulse propagation under the assumption[*] that the single mode fiber core is made out of SQ1 (silica quartz glass), was performed using LabII [SHSF]. LabII is a Labview based temporal pulse propagation code to estimate the dispersion parameters. The simulation result is shown in fig. 4.5.

In addition to spectral dispersion, a pulse traveling inside a single-mode fiber is also affected by micro-phonics and nonlinear modulations. Phonons are continuously excited within a fiber due to vibration or sound waves from the environment around the fiber or just due to thermal excitation. These micro-vibrations locally change the index of refraction, which modulates the optical path length inside the fiber. Arrival time fluctuations on the order of a few tens of femtoseconds with frequencies of up to several hundreds of Hz are observed [LSC+07].

Unwanted nonlinear effects like Raman scattering or the optical Kerr effect arising from the intensity dependence of the susceptibility $\chi(I(t))$ (compare section 2.1), could appear at high intensities These effects could create new frequencies or inflict self-phase modulation on the pulse, which would temporally distort the pulse and must be avoided by keeping the intensity inside the fiber below 10^2 GW/cm^2 [Agr01b].

[†]A photonic fiber is a fiber, in which the fiber core is surrounded by a glass lattice of periodically arranged a few μm small hollow spaces forming for example a honeycomb structure.

[*]declaration of manufacturer

Summarized the problems, which are connected with a optical fs-pulse transport via a more than 150 m long glass fiber in the near infrared regime can be divided into the following subjects:

1. Linear dispersion
2. Non-linear dispersion
3. Fiber length fluctuations
4. Non-linear effects

All of these problems require an answer to solve them simultaneously. This is realized by a fiber control system, which consists out of special optical components each solving one of the enlisted problems. In detail these components are the following enumerated with respect to its corresponding problem:

1. a grating compressor compensates linear dispersion
2. a spatial light modulator compensates non-linear dispersion
3. a fiber feedback cross-correlation system compensates fiber length fluctuations
4. a highly linear dispersive glass rod prevents non-linear effects in the glass fiber.

The complete dispersion control system is plotted in the overview scheme of figure 4.4.

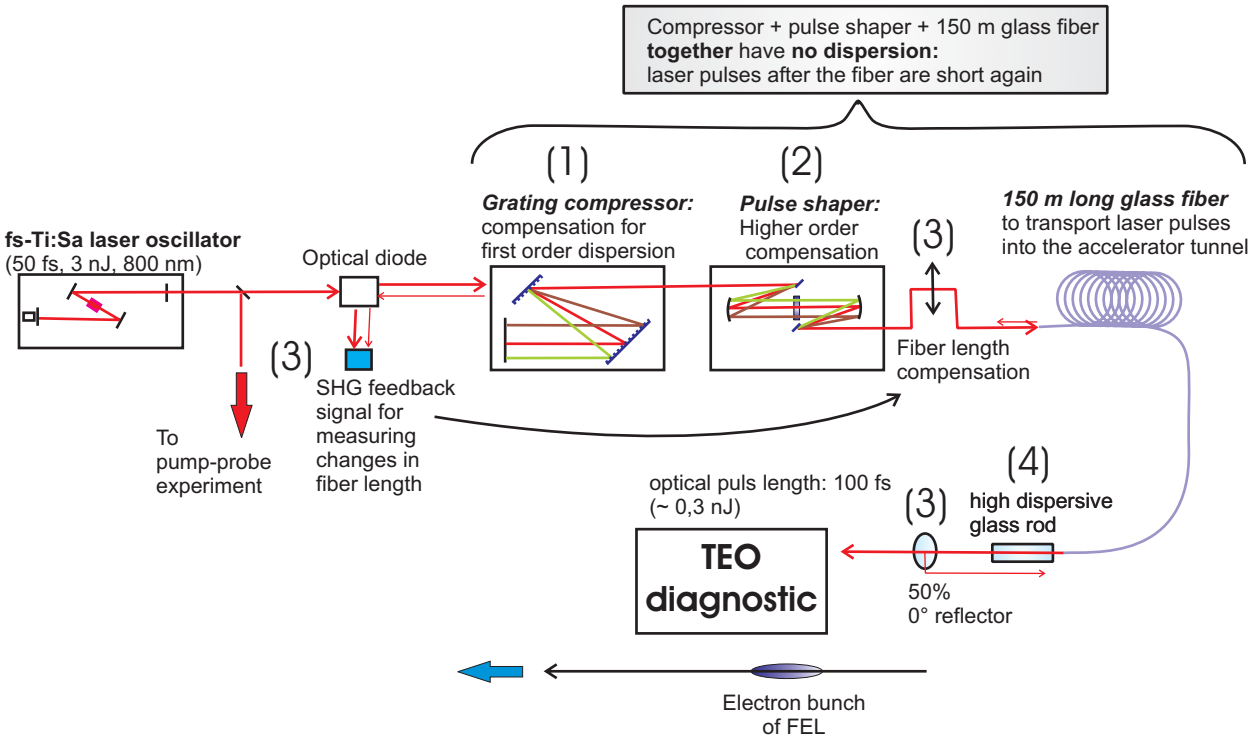

Figure 4.4: *TEO dispersion control system*
This scheme shows the dispersion control system to carry the near infrared fs-pulse Fourier limited and temporally stabilized through the 150 m long polarization maintaining glass fiber. The enumerated components are explained in the text.

All of these individual special optical components and their effect will be explained in the following sections.

4.1.3 Grating compressor

To recompress the strong pulse broadening of the fiber due to linear, second order dispersion as demonstrated in fig. 4.5, one has to use a double grating compressor. The principle of a grating compressor is to create an artificial modulation on the optical path length of the individual frequencies of an ultrashort fs-pulse. As a result this applies a linear chirp on the pulse due to geometrical dispersion. The geometry of the compressor governs the shape and the sign of the frequency chirp that is induces on the pulse. Without any additional focussing optic the chirp is negative similar to the chirp an anomalous dispersive material would apply. A detailed geometrical discussion is found in [Tre69]. Here only the result of this discussion is provided. From the optical path length modulation $\Delta L(\omega)$ (compare fig. 4.7) of the compressor one obtains, by multiplication with the wave number $k(\omega)$, the spectral phase function $\varphi(\omega)$ of an optical fs-pulse after the compressor:

$$\varphi(\omega) = 2 \cdot \left(\frac{\omega}{c} \cdot l \cdot \frac{1 + \cos(\alpha - \beta(\omega))}{\cos(\beta(\omega))} - \frac{q 2\pi l}{d} \tan\beta(\omega) \right) \quad . \tag{4.2}$$

$\beta(\omega)$ is the angle of diffraction, $\alpha(\omega)$ is the angle of incidence, l is the transversal grating distance and d is the lattice parameter. The geometrical relations are shown in fig. 4.7.

The 2nd and 3rd order coefficients of a Taylor expansion of (4.2) around the center carrier frequency ω_0 correspond to the GVD and TOD of the compressor.

GVD:

$$\varphi_2(\omega) = -\frac{8cdl\pi^2}{(-(2c\pi - d\omega - d\omega\sin[\alpha])(2c\pi + d\omega - d\omega\sin[\alpha]))^{3/2}} \tag{4.3}$$

TOD:

$$\begin{aligned} \varphi_3(\omega) \quad = \quad & -\frac{3cd^2l\pi^2\left(-16c^2d\pi^2\omega - 3d^3\omega^3 + \left(48c^2d\pi^2\omega - 4d^3\omega^3\right)\cos[2\alpha] + 64c^3\pi^3\sin[\alpha] - \cdots\right)}{(-(2c\pi - d\omega - d\omega\sin[\alpha])(2c\pi + d\omega - d\omega\sin[\alpha]))^{7/2}} \\ & \frac{\left(\cdots - d^2\omega^2\left(d\omega\cos[4\alpha] + 48c\pi\cos[\alpha]^2\sin[\alpha]\right)\right)}{(-(2c\pi - d\omega - d\omega\sin[\alpha])(2c\pi + d\omega - d\omega\sin[\alpha]))^{7/2}} \end{aligned} \tag{4.4}$$

From equation (4.3) follows, that the second order geometrical dispersion of a double grating compressor depends on the transverse distance l (see fig. 4.7). Thus, this equation can be used to estimate the length of a grating compressor, which compensates the GVD of the pulse transported within a single-mode fiber [refer to section 4.1.2]. Inserting this length and the rest of the relevant parameters

$$l = 1236.4\,\text{mm}; \quad d^{-1} = 1500\,1/\text{mm}; \quad c = 3 \cdot 10^8\,\text{m/s}; \quad \alpha = 65°;$$

into equations (4.3) and (4.4), one obtains a geometrically induced GVD and TOD of the compressor of

$$\begin{aligned} \varphi_2 &= -5.77 * 10^6\,\text{fs}^2 \qquad \text{LabII: } -5.53 * 10^6\,\text{fs}^2 \\ \varphi_3 &= -0.01018 * 10^9\,\text{fs}^3 \qquad \text{LabII: } -0.00968 * 10^9\,\text{fs}^3 \end{aligned}$$

The calculated values are in good agreement with those found by a simulation with LabII, in which the compressor optimally compensates for the material dispersion. The geometrical dispersion would stretch the 60 fs FWHM oscillator pulse up to 256 ps FWHM just like the fiber. However, the sign of the (GVD induced) chirp is opposite to that of the fiber. Thus both dispersion compensate each other regardless, if the pulse first propagates through the fiber and then through the compressor or vice versa. Hence, in the TEO setup the compressor is placed in a laser lab before the fiber, which is easy to access, instead of being placed after the fiber in the restricted access accelerator tunnel.

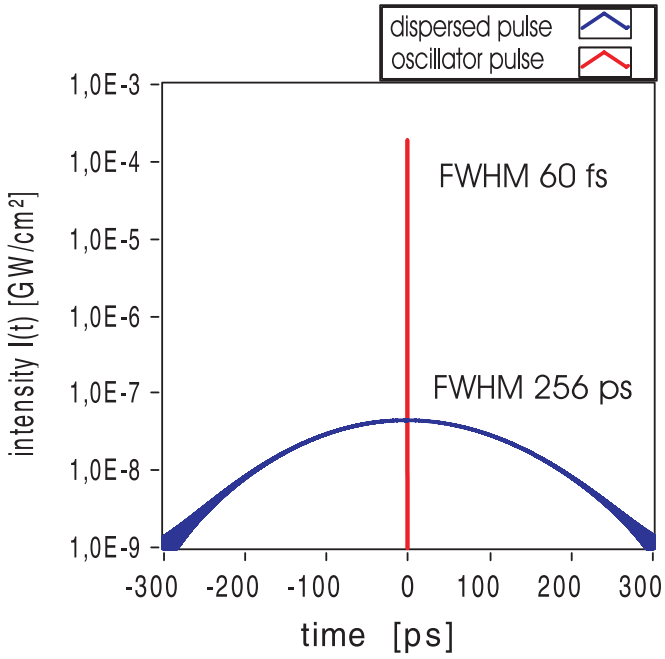

Figure 4.5: *Logarithmic plot of the simulated pulse dispersion due to the fiber.*
The fiber length is measured from a pulse travel time measurement to be 153 ± 3 m. The pulse duration of the Ti:Sa pulse measured from a FROG measurement [REF:optical laser] is 60 ± 5fs FWHM. The simulation gives rise to a GVD of $5.53 \cdot 10^6$ fs^2 and TOD of $0.46 \cdot 10^7$ fs^3. The effect of the TOD is too small with respect to the broadening due to the GVD, thus no typical oscillations are visible.

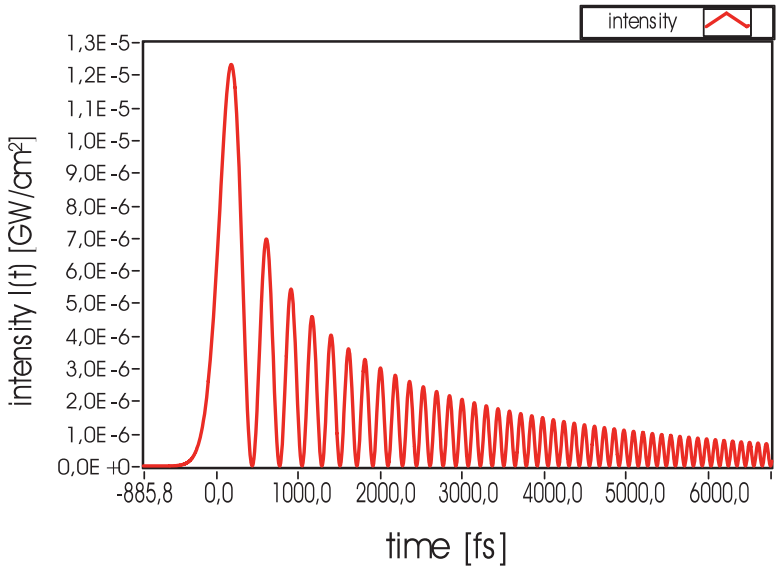

Figure 4.6: *Simulated TiSa pulse after compressor and glass fiber.*
Although the GVD is zero behind fiber and compressor, a large amount of TOD remains giving rise to heavy oscillations.
Simulation parameters: Transverse distance of gratings: 1236.6 mm; Gratings periodicity: 1500/mm; length of SQ1-fiber material: 153 m; spectral width: 15.7 nm ⇔ 60 fs FWHM Fourier limited; total TOD after fiber and compressor: $1.39 * 10^7$ fs^3

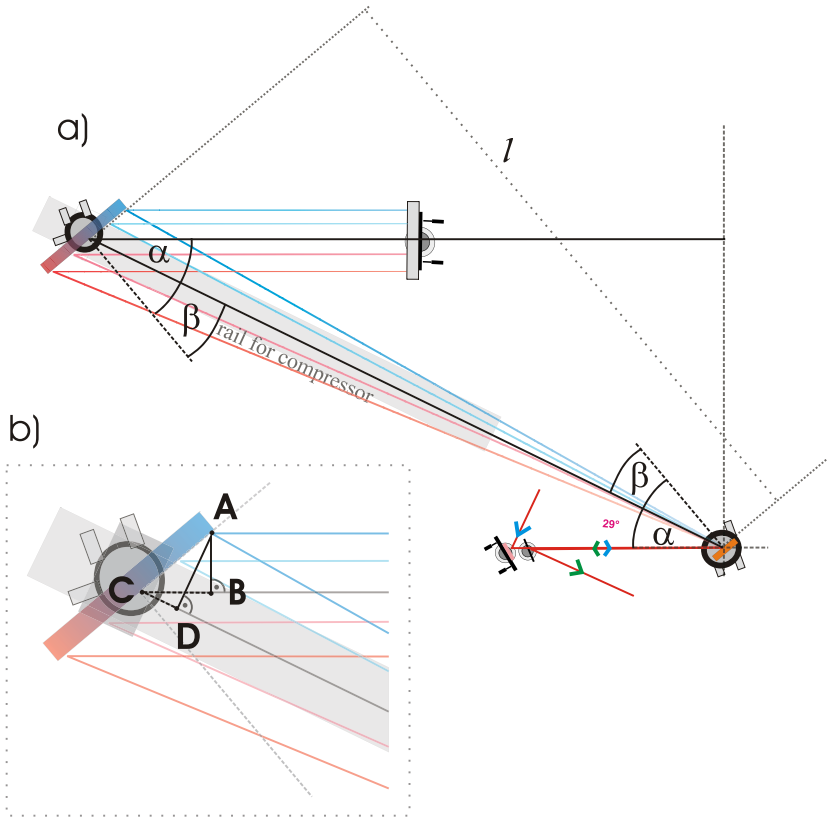

Figure 4.7: *Principle of the two-grating compressor of the TEO fiber transportation setup*
a) Geometrical relationships within the grating compressor used to compensate for the second order dispersion of the pulse transported by a single-mode fiber.
b) Zoom of the second grating. The nonlinear optical path length difference $\Delta L(\omega) = \overline{BC} - \overline{CD}$ creates an artificial linear chirp of negative sign.

4.1.4 Spatial light modulator

Double grating compressors can only compensate for second order normal dispersion and a small amount of third order dispersion. If a larger amount of second order dispersion (GVD> 10^4 fs^2) is to be compensated, a grating compressor will even inflict additional non-negligible geometric third order dispersion. Thus, to transport the pulse dispersion compensated through the 150 m long fiber a well aligned and designed grating compressor must be used. But additionally a device to compensate for an unknown large amount of nonlinear third order and perhaps higher orders of dispersion (TOD(Compressor + Fiber) $\approx 1.5{\cdot}10^7$ fs^3) is needed. The effect of this amount of third order dispersion on the 60 fs FWHM pulse from the used Ti:Sa oscillator is demonstrated in fig. 4.6. The pulse starts to oscillate due to interference between shorter and longer wavelengths of the pulse, which leads to local beats[†][Tre] inside the fs-pulse. A possible device, with which these portions of nonlinear dispersion can be compensated for is the spatial light modulator (SLM) 640-12 from JenOptic.

The idea of this device is to individually control the spectral phase and/or amplitude of each spectral component of a fs-pulse. An arbitrary phase or spectral modulation, with which a fs-pulse can be temporally modulated can be applied with an SLM. In the TEO setup it is used as a phase modulator. This device consists of a liquid crystal matrix of 640 individual liquid crystal (LC) elements of thickness d_{LC}=9 μm sandwiched between two glass plates each of thickness d_{glass}=1.5 mm. Every element has a width of w_{cell} =97 µm and is separated from its neighbor cell by a gap w_{gap}=3 µm. Each LC-element is able to change its index of refraction independently. The gap

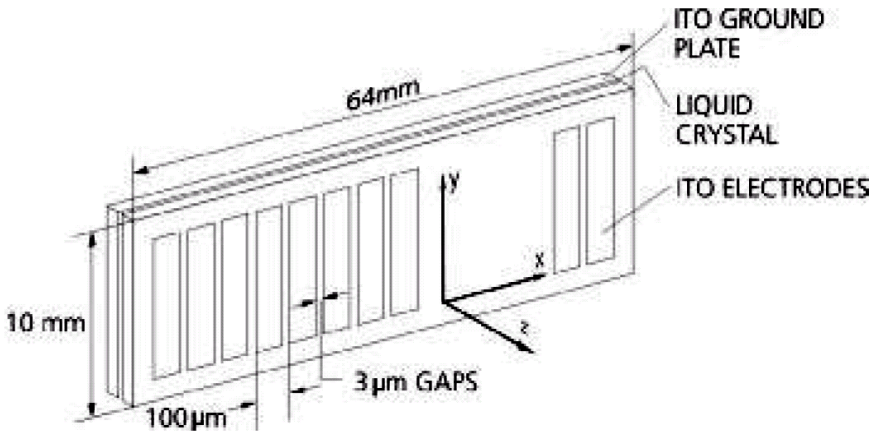

Figure 4.8: *Liquid crystal matrix of the spatial light modulator SLM 640/12 consisting of 640 liquid crystal cells.* (Fig. adapted from [Jen03].)

refractive index can not be controlled actively, but connects the refractive index of two adjacent cells in a steady way. The physical background behind the tunable index of refraction is, that liquid crystals are long chains of organic molecules, which show anisotropic dielectric properties (achirality). A special group of these class of organic crystals are lyotropic crystals, which form combined with a solvent a nematic fluid. Within this fluid the chopstick shaped molecules are oriented parallel to a defined direction. An electric field can change the orientation by switching all molecules simultaneously. Due to the anisotropy of each molecule the reoriented cell becomes birefringent (typically uniaxial). Thus, for a certain electric field strength and polarization parallel to the extra-ordinary axis of the liquid crystal, the light wave passing through the cell is shifted in phase according to equation (4.5) [Jen03]. The electric field is created by applying a constant voltage U between two

[†]Schwebungen

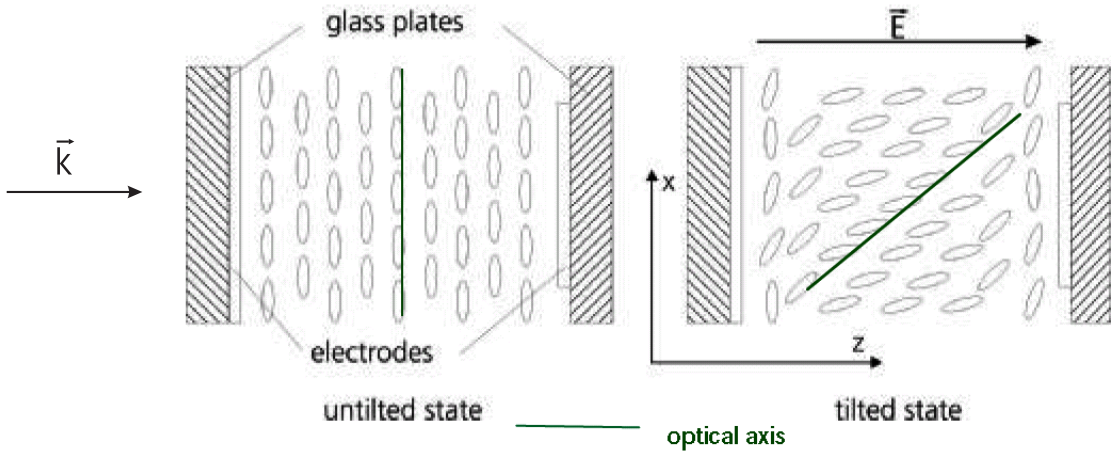

Figure 4.9: *Liquid crystal cell orientation*
The long LC molecules follow an externally applied electrical field in orientation. The anisotropy of the cell changes and the extra-ordinary index of refraction becomes larger. (Figure adapted from [Jen03].)

electrodes, which are attached from both sides of the LCD layer.

$$\Gamma_{\mathrm{SLM}}(U) = \frac{2\pi(n_e(U) - n_o)d_{LC}}{\lambda_0} \tag{4.5}$$

Before the shaper can be used, the correct relation between the voltage U and the corresponding phase shift $\Gamma_{\mathrm{SLM}}(U)$ must be measured. This is performed by measuring the degree of polarization modulation as it depends on U for a given pixel with the setup shown in fig. 4.10. An analyzer transforms the polarization modulation into a transmission modulation, which is measured by a photo-diode. The transmission T follows the Jones law:

$$T/T_0 = \sin^2\left(\frac{2 \cdot \Gamma_{\mathrm{SLM}}(U)}{2}\right) \tag{4.6}$$

The factor 2 in front of Γ_{SLM} results from the double pass through the matrix. Thus, for a double pass setup $\Gamma_{\mathrm{eff}} = 2\Gamma_{\mathrm{SLM}}$ is the effective phase shift induced by a shaper pixel induces. The measured transmission is presented in fig. 4.11.

From this transmission curve, following formula can be used to derive the effective phase shift calibration:

$$\Gamma_{\mathrm{eff}} = \frac{2\pi}{40} * U + 73 = 0.157 * U + 73 \qquad U \in [73..113] \tag{4.7}$$

4.1.5 The SLM 4f-stretcher setup

We are now ready to apply the modulator liquid crystal matrix on the spectrum of a fs-pulse. To accomplish this task, an optical system is necessary, which maps the fs-spectrum linearly on the matrix. This kind of optical system is a 4f-stretcher. A 4f-stretcher is very similar to a double grating compressor, but it consists of two additional focussing optics. The principle is demonstrated in fig. 4.12. When used in combination with a spatial light modulator the 4f-stretcher must be used without any intrinsic dispersion, thus a detailed discussion of the non-zero dispersion of a stretcher shall be excluded. More details are provided in appendix B.3.

First, the collimated fs-pulse is spectrally spread by a grating. The first focussing optic spectrally recollimates and focusses the individual frequencies spatially separated from each other on

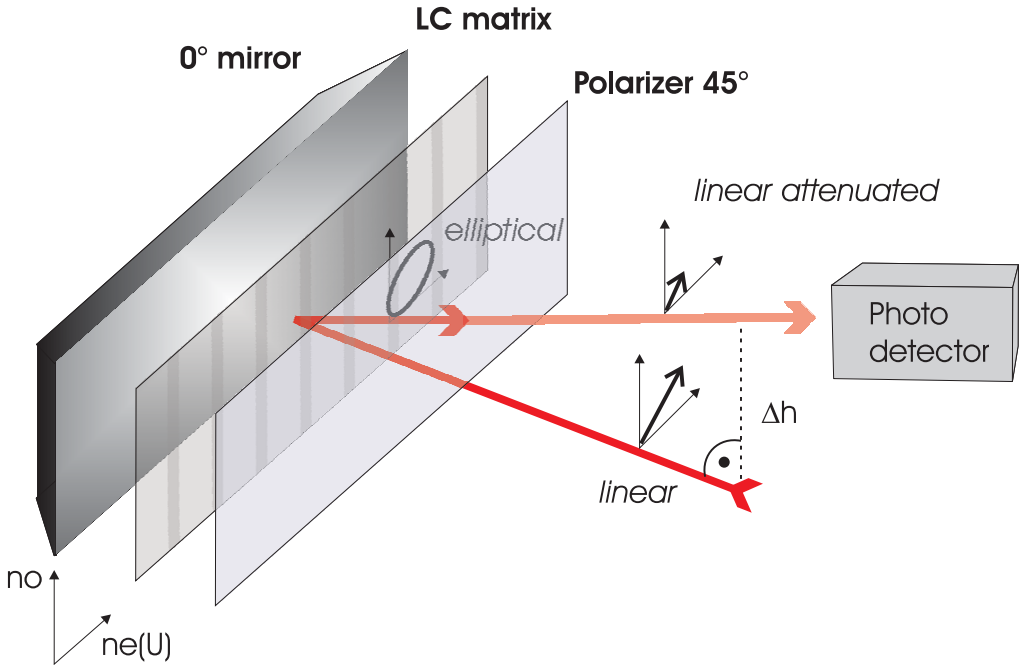

Figure 4.10: *Setup to calibrate the LC matrix.*
The setup consists of a 45°-polarizer plate, the LC matrix and a back reflector. A 45°-linear polarized laser focussed to fit into one LC cell passes the polarizer without attenuation and becomes elliptically polarized by the cell. The second polarizer pass works as an analyzer and attenuates the modified beam. The incoming and outgoing beams are separated in height, to guarantee, that both beams pass the same pixel.

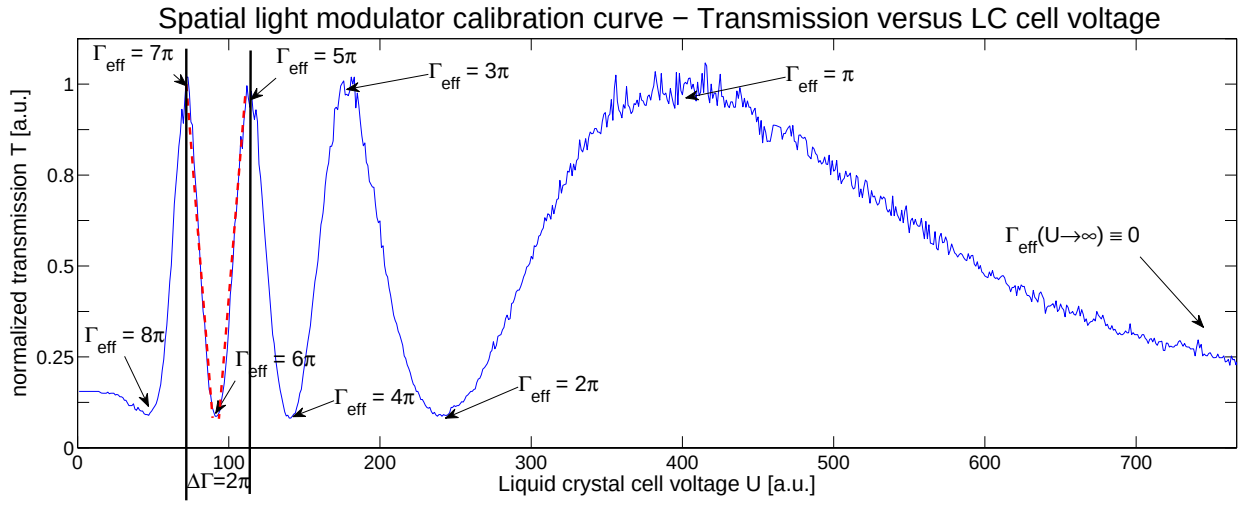

Figure 4.11: *Measured transmission calibration curve T(U) of the shaper matrix*
Within the two marks a linear dependence between Γ_{eff} and U is observed. The effective phase shift retardation varies between 0 and 2π, which is the maximal possible physically meaningful phase shift a pixel can apply ([Str03] page 52 , NYQUIST-criteria). This linear dependence allows the derivation of a calibration formula to control the shaper in double pass setup.

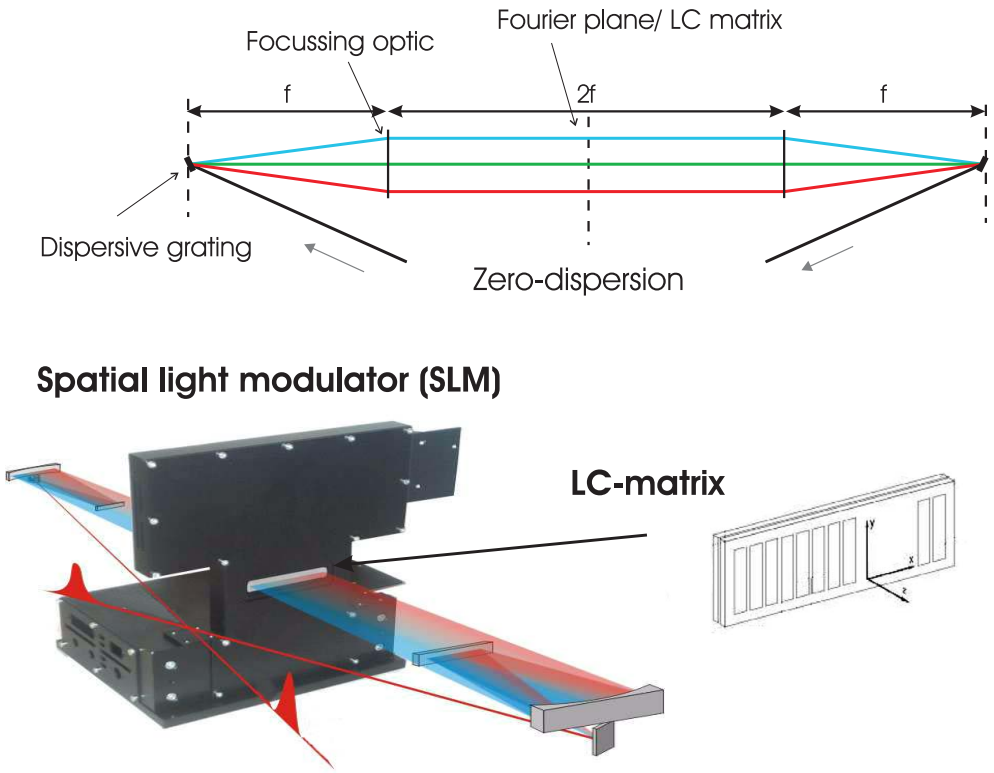

Figure 4.12: *Principle of a 4f-stretcher*
A dispersive grating disperses the spectrum of a fs-pulse. A focussing optic recollimates the dispersed spectrum and maps it into the Fourier plane, where the LC matrix is placed. The SLM controls the LC matrix cell indices of refraction. A similar second focussing optic and grating placed in a mirrored geometry reconstruct the beam again. If the setup is perfectly symmetric and the LC matrix is switched off, it is dispersion free and a spatial and temporal replica of the incident fs-pulse is created. [Figure adapted from [Jen03]]

the individual LC pixel of the shaper matrix, which is placed in the Fourier plane of the focussing optic. The matrix introduces an arbitrary spectral phase modulation $\Gamma_{\mathrm{SLM}}(\omega)$ on the pulse. With a second complementary set of focussing optics and grating, the spatial and spectral separation of the frequencies is inverted and the phase modulated fs-pulse is spatially and spectrally reconstructed.

To simplify the alignment, the 4f-stretcher is folded (fig. 4.13) and the shaper matrix is used in two-pass mode, thus $\Gamma_{\mathrm{eff}} = 2\Gamma_{\mathrm{SLM}}$. A ray tracing simulation of the folded stretcher in the TEO setup with the optics engineering software ZEMAX [SLM] is presented in fig. 4.13.

The reconstructed and phase modulated fs-pulse is obtained from an inverse Fourier transformation of the incident pulse $E(t)$. With equation (2.18) the electrical field of the modulated pulse $E_{SLM}(t)$ is

$$\begin{aligned} E_{SLM}(t) &= \mathcal{F}^{-1}\left\{\mathcal{F}(E(t)) * \exp(i \cdot \phi_{SLM}(\omega))\right\} \\ &= \mathcal{F}^{-1}\left\{\mathcal{E}(\omega) \cdot \exp\left(i \cdot (\phi_0(\omega) + \phi_{SLM}(\omega))\right)\right\} \end{aligned} \tag{4.8}$$

with the new spectral phase function $\phi(\omega) = \phi_0(\omega) + \phi_{SLM}(\omega)$.

4.1.6 Spatial mapping of the fs-pulse spectrum

To guarantee optimal control of the shaper matrix used within the 4f-stretcher setup, a wavelength to pixel calibration of the Fourier plane is required. The 4f-stretcher maps the spectrum spatially

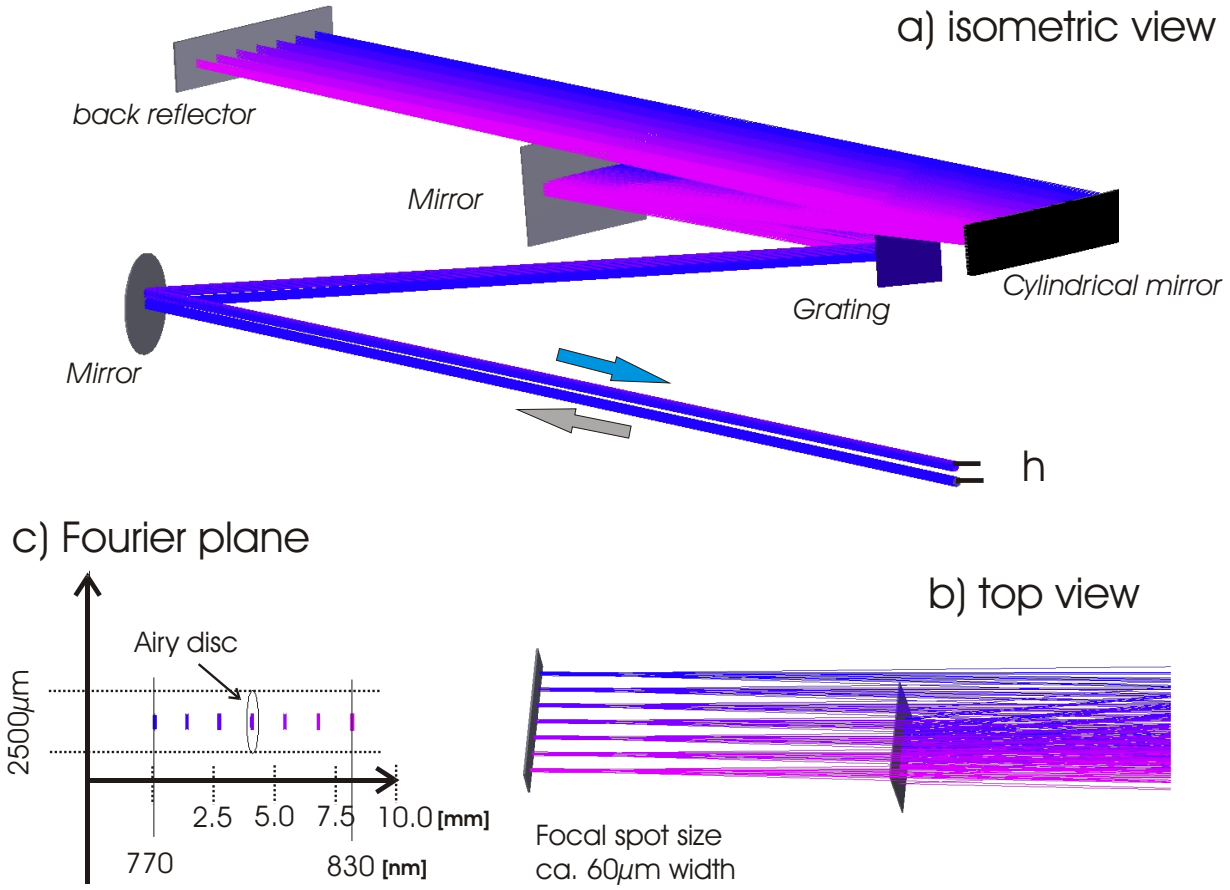

Figure 4.13: *Ray tracing simulation of a folded 4f-stretcher.*
a) *Isometric view* of a 3D ray tracing model of the TEO shaper configuration. The incident and outgoing fs-pulses are separated in height. The slight height deviation does not introduce any spectral or spatial chirp, as long as the optical path length of the central wavelength between the grating-cylindrical mirror and the back reflector equals the focal distance f of the cylindrical mirror and if the beams are orientated precisely above each other.
Longer wavelengths are diffracted stronger, i.e. the diffraction angle β enclosed by each wavelength with the grating perpendicular becomes larger for longer wavelengths (compare with fig. 4.14).
b) *Top view*: The cylindrical mirror creates a vertical line focus for each wavelength ray in the Fourier plane.
c) *Fourier plane*: Focus analysis of 6 rays of distinct wavelengths between 770 nm and 830 nm. The wavelength-to-space mapping is almost linear.
The simulation parameters are: focal length f=500 mm and grating parameter d^{-1}=2300 lines/mm.

on the shaper matrix of N=640 pixels. The angular relationship between the incident and mapped beams is displayed in fig. 4.14.

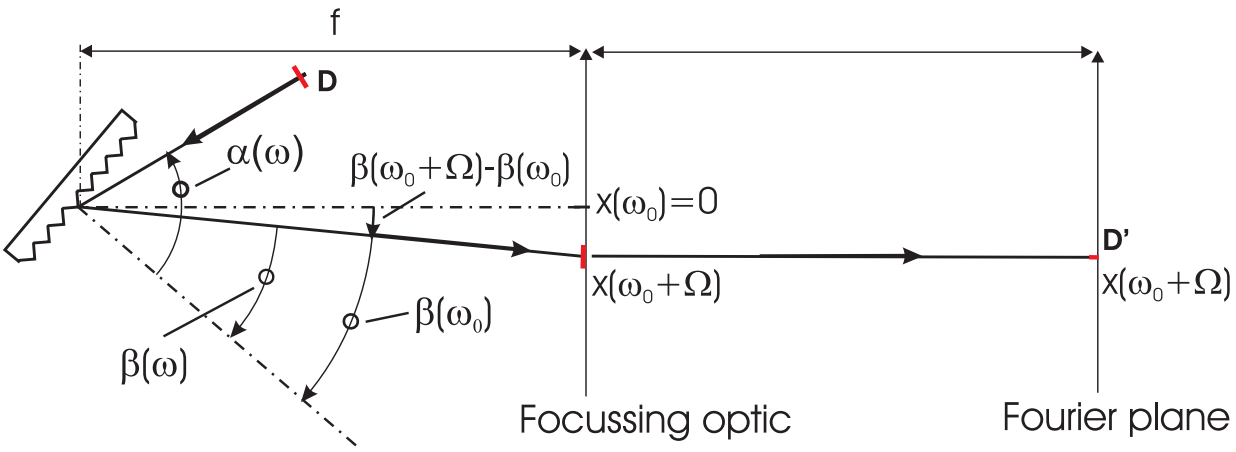

Figure 4.14: *Scheme of the spatial mapping of the fs-pulse spectrum into the plane of the shaper.* The dependence between α and β is governed by the grating equation.
The frequency variable Ω is counted with respect to the carrier frequency ω_0. The sign convention, as suggested by the arrows referenced to the grating normal, is negative for β and positive for α. For each wavelength the incident beam diameter D is focussed in horizontal direction to a much smaller line focus of width D', whereby in the Fourier plane the spectral components are separated spatially. From the spatial coordinate $x(\Omega)$ follows a dispersion- and calibration relation for the 4f-stretcher setup.

From the geometric relations of figure 4.14 one derives the dispersion calibration function

$$x(\Omega) = f \cdot \tan(\beta(\omega_0 + \Omega) - \beta(\omega_0)) \quad . \tag{4.9}$$

The spatial dispersion $x'(\Omega) \cong b(\Omega)$ follows from the first derivative of (4.9)

$$b(\Omega) = f \cdot \frac{\beta'(\omega_0 + \Omega)}{\cos\left(\beta(\omega_0 + \Omega) - \beta(\omega_0)\right)^2} \quad . \tag{4.10}$$

The first derivative $\mathrm{d}\beta(\omega_0 + \Omega)/\mathrm{d}\Omega$ is calculated from the grating equation,

$$\sin(\alpha) + \sin(\beta(\omega)) = m \cdot \frac{2\pi c}{d \cdot \omega} \quad . \tag{4.11}$$

The grating equation is applied twice on $\tilde{\omega} = \omega_0 + \Omega$ and $\tilde{\omega} = \omega_0$ and subtracted from each other to replace angle α:

$$\sin(\beta(\omega_0 + \Omega)) + \sin(\beta(\omega_0)) = m \cdot \frac{2\pi c}{d \cdot} \left(\frac{1}{\omega_0 + \Omega} - \frac{1}{\omega_0} \right) \tag{4.12}$$

Taking the first derivative $\frac{\mathrm{d}\cdot}{\mathrm{d}\Omega}$ on each side leads to an expression for $\beta'(\omega_0 + \Omega))$, which is inserted into (4.10):

$$b(\Omega) = -m \frac{f 2\pi c}{d} \cdot \frac{1}{(\omega_0 + \Omega)^2 \cos(\beta(\omega_0 + \Omega)) \cos^2\left(\beta(\omega_0 + \Omega) - \beta(\omega_0)\right)} \tag{4.13}$$

For small angular dispersions ($\Omega \approx 0 \Leftrightarrow |\beta(\omega_0 + \Omega) - \beta(\omega_0)| < 0.1\,\text{rad}$) equation (4.13) can be approximated by a constant value

$$b(0) \approx -m\frac{f2\pi c}{d} \cdot \frac{1}{\omega_0^2 \cos^2(\beta(\omega_0))} \quad . \tag{4.14}$$

In this case the calibration equation (4.9) can be linearized by

$$x(\Omega) = b(0) \cdot \Omega \quad . \tag{4.15}$$

The exact (eqn. (4.9)) and approximate (eqn. (4.15)) calibration function for the TEO setup SLM parameters are plotted in fig. 4.15. For the TEO setup one calculates $b0 = 0.72\,\text{mm/THz}$ for the calibration coefficient at a center wavelength diffraction angle $\beta(\lambda_0)$ of $-58.2°$ and incident angle α=82.0°. Another relevant calibration coefficient is b_{px}, which defines the amount of shaper pixel per dispersed THz frequency interval, as it is mapped on the shaper matrix. The used shaper has a pixel width of 0.094 mm obtaining $b_{px} = 7.2\,\text{px/THz}$.

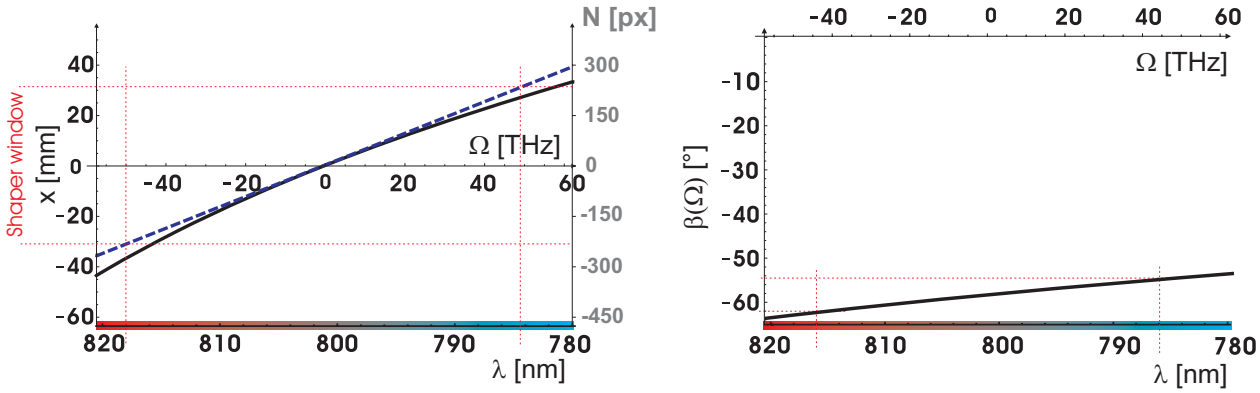

Figure 4.15: *Calibration function x(Ω)* *Angle dispersion β(Ω)*
These plots show the geometric dispersion in the Fourier plane and are calculated with the component parameters of the TEO shaper setup:
Grating parameter d^{-1}=2300/mm, focal length f=500 mm and incident angle α=82.0°.
The left ordinate of the calibration plot represents the spatial coordinate along the shaper matrix, while the right ordinate is plotted in LC matrix pixel units. The right plot shows the angular dispersion $\beta(\Omega)$ as a function of the frequency difference $\Omega = \omega - \omega_0$. Red shifted wavelength components are stronger bent away from the grating normal (larger absolute value of angle β) than blue shifted components. The size of the matrix limits the transmitted bandwidth of the shaper indicated by the shaper window markings in the plots.

4.1.7 Algorithms for pulse compression

As demonstrated before, the optical pulse traveling through the non-zero dispersive glass fiber accumulates myriad of dispersion especially higher nonlinear order of dispersion (see fig. 4.6). The amount is *a priori* unknown. It mainly depends on the particular material of the fiber core of the pulse transporting system. To compensate this additional phase a phase finding algorithm has been developed. The algorithm searches for the proper compensation phase function $\tilde{\phi}(\omega)$ for which the total phase function $\phi(\omega)$ of the pulse at the TEO cross-correlation equals a function $h(\omega) = \phi_0 + b * \omega$ with arbitrary constants ϕ_0 and b. This corresponds to a Fourier limited pulse, which is shifted in time and phase by only a constant value.

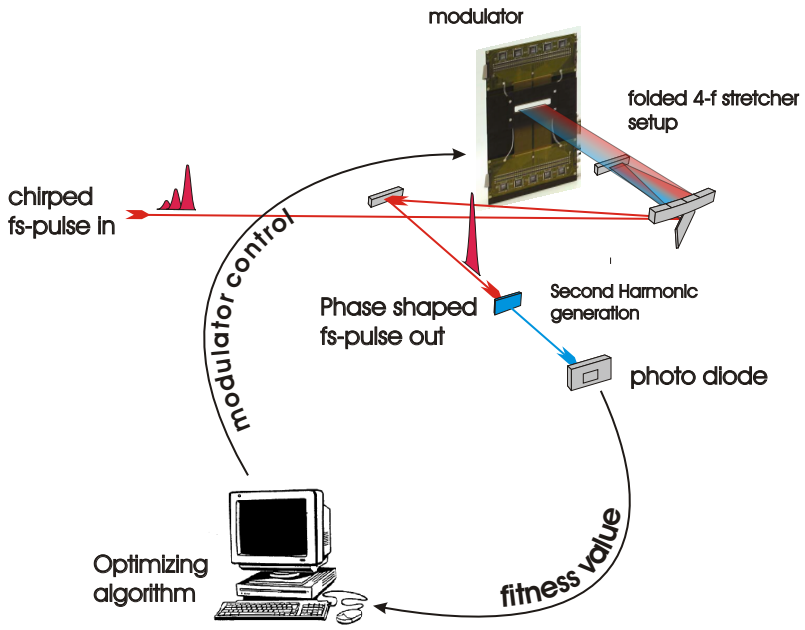

Figure 4.16: *Principle of a phase optimization setup to re-compress a dispersed pulse.* A chirped pulse modulated by an unknown spectral phase function is aligned into the 4-f stretcher phase modulator setup. The fitness value is derived from the energy of the frequency doubled pulse leaving the shaper. To decrease space and complexity the 4-f stretcher is folded once.

Generally, an optimization algorithm attempts to vary a set of parameters aiming to maximize a certain fitness parameter with an iterative approach. In the present situation the parameters, which are to be optimized, are the individual liquid crystal cell pixel values of the spatial light modulator matrix. Together with the wavelength mapping properties of the 4f-stretcher setup, each cell applies a phase retardation to a specific wavelength component of the pulse and thus applies a variable phase modulation. The optimization goal is a Fourier limited pulse after the fiber. This provides a maximized pulse intensity and a minimal pulse duration, hence maximal temporal resolution for the electro-optical sampling process of the TEO diagnostic.

Experimentally, the fitness value is realized by means of second harmonic generation (SHG) of the NIR laser pulse. The laser is focussed into a non-linear BBO-crystal and the remnant NIR light filtered by a spectral bandpass filter. The second harmonic energy is detected by a photo diode. Since the SHG-process efficiency is proportional to the square of the NIR intensity, the generated SHG energy is a sensitive indicator for the pulse shortness. The phase finding procedure for the TEO setup is explained in fig. 4.16.

The SLM matrix consists of 640 individual cells, where each can be set to a physical meaningful phase retardation value between 0 an 2π. Thus, the phase finding problem can be understood as a optimization problem in a 640 dimensional parameter space.

4.1.7.1 Taylor series based phase finding algorithm

Without any knowledge about the expected solution only algorithms like a genetic algorithm or simplex-downhill algorithms are feasible to find the correct pattern. In this work a third way to find the correct solution has been developed. It based on the fact, that the nature of the solution is not fully unknown.

Following the treatments of section 4.1.3 and 2.1.1 the spectral phase function of the pulse behind the glass fiber can be described by a Taylor expansion of the spectral phase function around the carrier frequency. With $\Phi(\omega) = \boldsymbol{k}(\omega) \cdot L$ and eqn. (2.27) follows

$$\Phi(\omega) = \phi_0 + \phi_1 \cdot (\omega - \omega_0) + 1/2!\phi_2 \cdot (\omega - \omega_0)^2 + ... + 1/n!\phi_n \cdot (\omega - \omega_0)^n + \boldsymbol{Q}(\omega) \qquad (4.16)$$

The coefficients ϕ_0 to ϕ_n are the target parameters of the optimization algorithm. The algorithm

subsequently varies the individual parameters in an iterative way and maximizes the SHG energy signal.

Two advantages of this solution method over the genetic or simplex-downhill algorithm are: First, the amount of free parameters is reduced dramatically. For the present problem only 4 to 5 non-zero Taylor coefficients are expected from theory. Compared to the 640 independent variables, which would have to be modified in case of the two other algorithms, this is a strong improvement of the optimization problem. Thus, the Taylor series based algorithm is much faster than the two other types of algorithm.

Second, once the solution of best pulse compression is found, the dispersion of the fibre is measured and known in terms of dispersion coefficients ϕ_i, which would not be the case for the two other algorithms. The genetic and simplex downhill algorithm only provide a set of phase values for the individual pixel of the shaper matrix. Once the optimal phase combination is found, the solution is applied as a 2π-wrapped phase function to the shaper matrix and a reconstruction of the dispersion coefficients would be difficult.

The solution of the introduced Taylor based phase finding algorithm is presented in fig. 4.17 and an autocorrelation of the compressed and uncompressed pulse after the fiber are presented in fig. 4.18 and fig. 4.19.

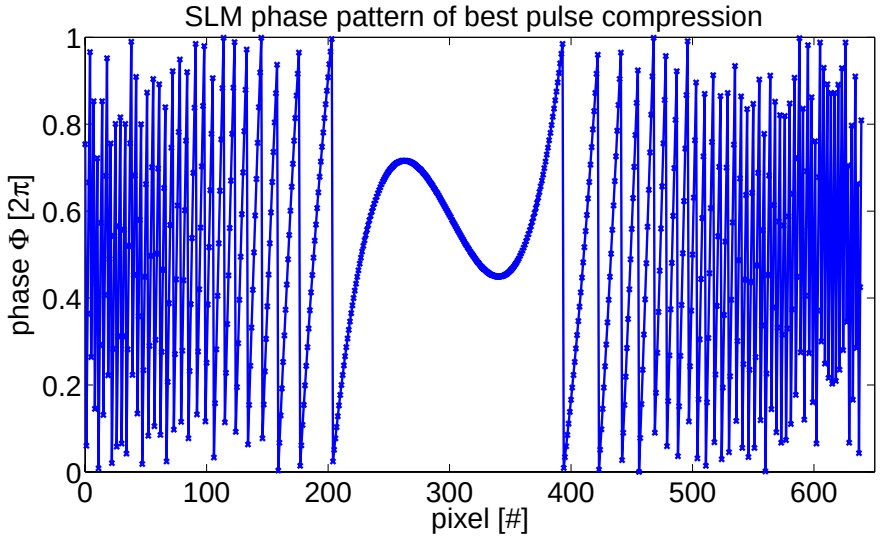

Figure 4.17: *Spatial light modulator phase pattern of best pulse compression.*
The plots shows the phase pattern of best compression/highest feedback signal, which is applied to the shaper matrix. The pattern is plotted in units of 2π and plotted versus the pixel numbers of the shaper.

4.1.7.2 Dispersion of the fiber

The applied phase pattern of fig. 4.16 shows a smooth 2π-wrapped polynomial mainly of third order. Since the abscissa is in pixel units, the coefficients of each polynomial have to be converted into spectral dispersion coefficients, before any information on the amount of dispersion can be obtained. The following conversion formula has been developed and its derivation is presented in appendix B (B.1). It connects the pixel dependent coefficients b_n with the frequency dependent Taylor coefficients ϕ_n.

$$\phi_n = \frac{b_n}{N^n} \cdot n! \cdot (b_{px})^n \cdot 10^{3n} \quad , \tag{4.17}$$

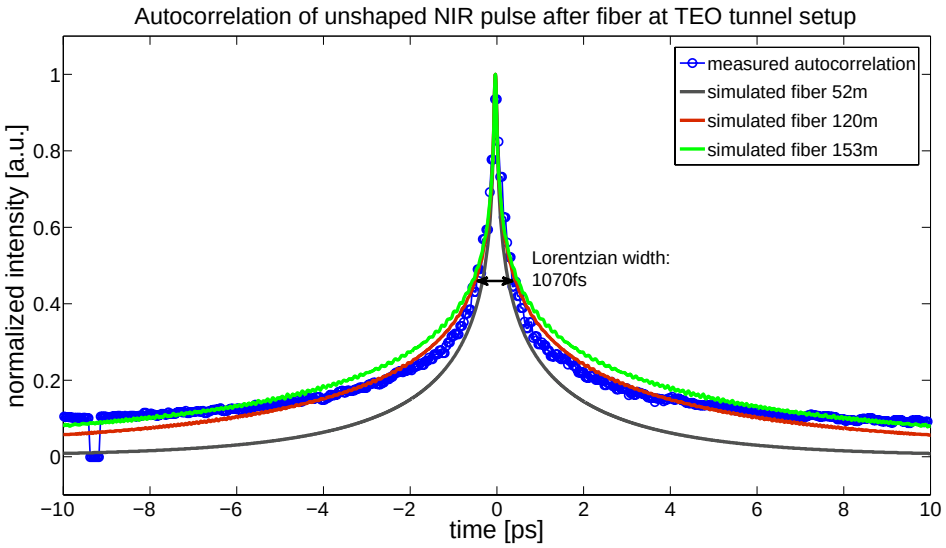

Figure 4.18: *A long range background-free autocorrelation scan of the unshaped NIR pulse after the fiber in the TEO tunnel setup.*
The plot shows an autocorrelation measurement of the unshaped pulse at the TEO setup in the tunnel (red dots). During the scan the beam was shortly blocked to identify the baseline. The second order dispersion is compensated by the double grating compressor, but the third order of dispersion is still left. Three additional simulated autocorrelations calculated by LabII [SHSF] of different fiber lengths are added to compare the measurement with the simulation. From the plot one finds, that the measured autocorrelation fits best with the simulated one, if a fibre of a length larger than 100 m is assumed. The real fiber in the experiment has been measured by an optical path length measurement to be 153 m.

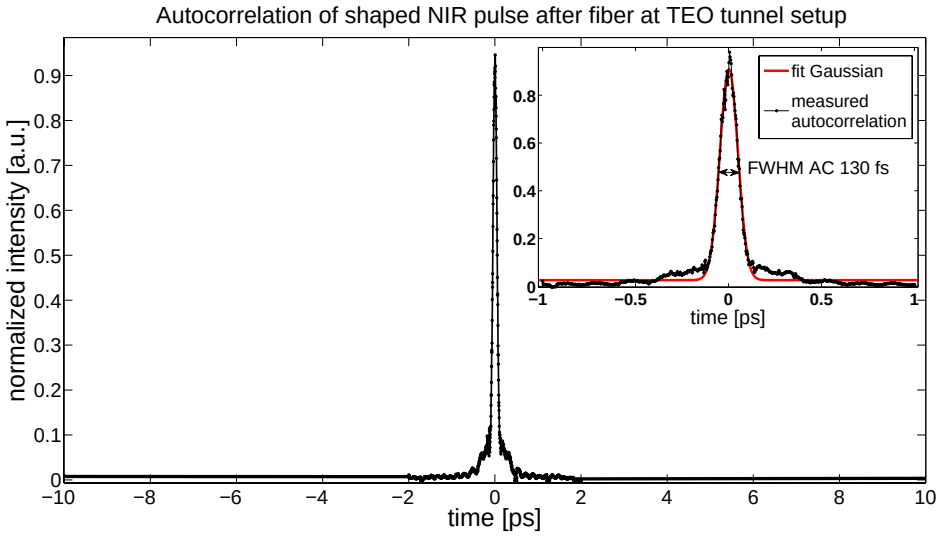

Figure 4.19: *Autocorrelation of shaped pulse after the fiber at the TEO tunnel setup.*
The plot shows an autocorrelation of the optical pulse after the fiber, while the phase pattern of fig. 4.17 was activated in the shaper matrix. The pulse is compressed to about 90-100 fs FWHM, if a Gaussian pulse shape is assumed. The measured spectral bandwidth after the fiber is 9.5 nm FWHM, which corresponds to a temporally Fourier limited pulse of 93 fs FWHM. Thus, the applied phase pattern compensates the dispersion of the pulse transport system and the shortest possible pulse at the TEO experiment can be used for the electro-optical cross-correlation with the FLASH electron bunch.

order i	b_i	ϕ_i [fs^i]	$\lvert b_{i,max}\rvert$	$\lvert\phi_{i,max}\rvert$[fs^i]	$\phi_i/\phi_{i,max}$
i=1	0	0	640	8970	0%
i=2	2.6	9460	640	$252{\cdot}10^3$	0.4%
i=3	267	$1.37{\cdot}10^7$	427	$2.20{\cdot}10^7$	62,5%
i=4	0	0	1280	$1.2{\cdot}10^9$	0%
i=5	-15	$1.90{\cdot}10^9$	1024	$1.3{\cdot}10^11$	1.4%
i=6	0	0	1707	$1.44{\cdot}10^13$	0%

Figure 4.20: *Calculated dispersion coefficients derived from the found phase pattern for optimal pulse compression* .
The table compares the calculated dispersion parameters with the calculated maximal dispersion coefficients, which the SLM is able to compensate with the used setup. The coefficients are provided in pixel b_i and frequency ϕ_i based form.

where n is the order of dispersion, b_{px} is the SLM calibration coefficient introduced in section 4.1.6 and N is the number of pixel of the shaper matrix, which is 640 in this case. Using [px/THz] as unit for b_{px}, the calculated Taylor coefficients units are [fs^n]. The calibration parameter b_{px} is 7.2 $\frac{pixel}{THz}$. With these parameters conversion table 4.20 from the pixel based polynomial coefficients to the frequency based dispersion coefficients is obtained.

The table shows the dispersion coefficients of optimal pulse compression and compares them with the maximal possible dispersion coefficients of the SLM in the used configuration. The dispersion limits for each order of dispersion of the SLM is calculated from equation eqn. (B.9) and (B.12). The table shows, that orders of dispersion higher than the third are small and thus not necessary to compress the pulse. The simulated value for ϕ_3 for optimal pulse compression assuming fused silica for the fiber glass sort is $1.4{\cdot}10^7$ fs^3 (see section 4.1.2). Thus, the measured 3rd order of dispersion of the fiber with $1.37 \cdot 10^7$ is in good agreement with the simulated value. This observation is in compliance with the autocorrelation results shown in fig. 4.18 of the uncompressed pulse.

4.1.7.3 Fiber length feedback system

Fluctuations of the fiber length would modify the effective arrival time of the optical pulse, which is used to clock the electron bunch in the linear accelerator of FLASH. This leads to a temporal uncertainty, which reduces the temporal resolution of the TEO diagnostic. To prevent this drawback, a fiber length compensation system has been developed, which compensates for fiber length variations due to the noisy environment of the fiber or temperature induced statistical phonon excitations.

As plotted in the overview scheme 4.4 the fiber feedback system measures continuously the length of the fiber and compensates the optical path length of the complete transportation beam path by a mechanical mirror delay stage. The feedback signal, which measures the relative path length modulations of the fiber, is derived from a temporal cross-correlation of an optical fs-pulse. 50 % of the pulse is back-reflected by a zero degree mirror placed in the optical beamline of the TEO diagnostic in the linear accelerator right behind the fiber exit with another fs-pulse generated by the Ti:Sa oscillator and sent back to the fiber feedback in the laser hutch.

The cross-correlation is performed using a non-linear β-BBO (beta barium borate) crystal to generate the mixed second harmonic signal from both optical pulses. The principle overview of the fiber feedback signal is shown in fig. 4.21.

An example of the signal, which is obtained by the cross-correlator is presented in figure 4.22. The signal trace shows, that the correlation peak is not perfect Gaussian. The reason is, that the nonlinear spectral phase compensation performed by the spatial light modulator is not always perfect.

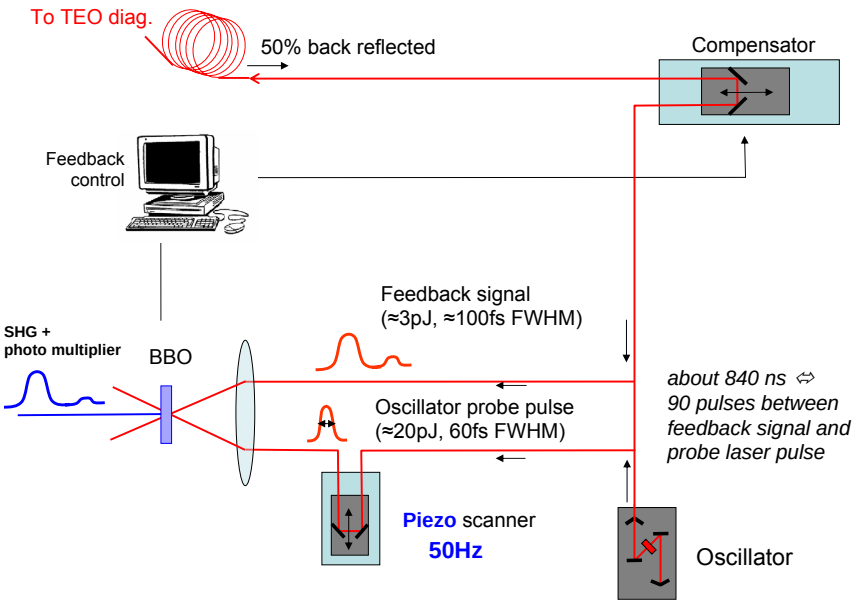

Figure 4.21: *The TEO transport fiber length stabilization feedback system.*
The back-reflected pulse from the TEO diagnostic located in the linear accelerator tunnel is cross-correlated with an oscillator pulse. The cross-correlation is background free and takes place inside an beta-BBO crystal. The back-reflected pulse is due to the losses within the dispersion control system very weak and carries only 30 fJ energy. Thus, a photo-multiplier is need to detect the cross-correlated second harmonic signal.

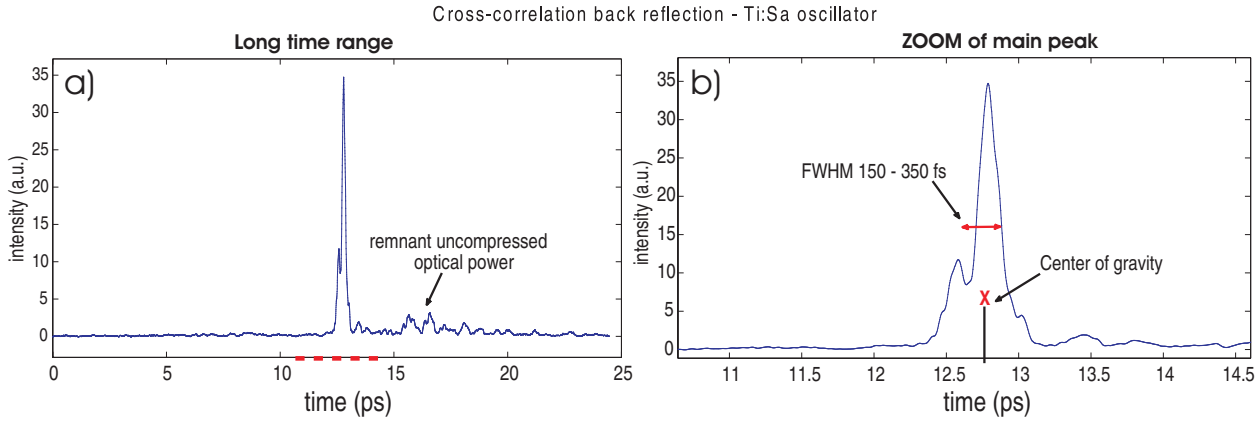

Figure 4.22: *Fiber feedback signal.*
An example of the fiber feedback signal trace. a) The long time range scan shows remnant uncompressed power at 5 ps behind the main peak. b) The short time range scan shows the main peak. Its center of gravity defines the arrival time of the back-reflected pulse.

The feedback correlation signal amplitude varies in its shape, probably because the optical alignment through the SLM is not stable and because the fiber itself slightly changes its dispersion due to environment condition changes like temperature or sound vibrations. To define the arrival time of the back-reflected pulse, for each scan, the center of gravity of the main peak is calculated. The center of gravity temporal position does not change, if the shape fluctuates due to fluctuations of the second, third or higher order of dispersion. However, because the back-reflected pulse passes the complete dispersion control system twice, it is twice times affected by imperfections of the spectral phase compensation. Because of this reason, it is not possible to use an electronically detection system for the fiber feedback stabilization like the one described in [LSC+07]. Instead the complete temporal trace must be scanned for each pulse arrival time measurement. This drawback limits the feedback repetition rate to 50 Hz.

On basis of the arrival time measurement an optical delay stage is moved to compensate for drifts on seconds timescale. A fast fiber feedback using a piezo driven delay stage, to stabilize with the same speed as the repetition rate was planned, but not yet realized.

Results of the fiber feedback measurements are presented in section 6.5.1.2.

4.1.7.4 Preventing non-linear effects in the fiber.

The power of the oscillator beam, which enters the fiber after traveling through the dispersion control system including the grating compressor and the spatial light modulator is reduced by a factor of 10 with respect to the output power of the oscillator of 450 mW. Reasons are losses on the gratings, on the shaper pixel matrix, on each of the multiple mirrors, not antireflection coated surfaces inside the optical diode (see 4.4) and the loss of spectral bandwidth of the pulse due to the narrow bandwidth acceptance window of the shaper. But in the compressed state with only 100 fs FWHM pulse duration the pulse energy would still be high enough to induce non-linear effects like self-phase modulation in the 6 µdiameter small fiber.

To prevent these effects, at the end of the fiber a 14 cm long glass rod out of highly dispersive material is placed right after the pulse exits the fiber. The idea is, that only within this glass rod the pulse is being recompressed to fs-level and not before within the fiber. This is achieved by including the dispersion of the glass rod in the phase function applied to the SLM and the grating compressor. Thus, due to the large amount of dispersion of the glass rod, inside the fiber the pulse is still 20 ps to 30 ps long and the intensity in the fiber is always small enough to prevent non-linear effects. Inside the glass rod the final recompression to fs-level is performed. The transverse beam diameter in the glass rod after outcoupling of the fiber is 1 mm diameter and thus large enough that even the fully compressed 90 fs FWHM pulse would not induce non-linear, intensity dependent effects.

In this sense the glass rod works like an intensity buffer keeping the pulse on low intensity level inside the fiber.

4.1.7.5 Conclusion

A fiber based pulse transport system has been realized, which is capable to transport a near infrared (NIR) 90 fs short Ti:Sa based oscillator pulse at 800 nm wavelength through a glass fibre over more than 150 m Fourier limited from the FLASH experimental hall into the electron bunch linear accelerator of FLASH. The fiber length can be measured with 50 Hz repetition rate and stabilized on a seconds timescale. This transport system is a prerequisite of the TEO experiment to perform the electro-optical cross-correlation of the NIR pulse and the electron bunch and to measure with high temporal accuracy the relative arrival time between the NIR pulse and the electron bunch.

4.2 The temporal bunch arrival diagnostic TEO

The electro-optical timing detector is based on the spatial decoding technique explained in section 2.4.1. Thus, the relative arrival time between the electron bunch and the NIR laser pulse can be derived from the transversal position of the EO signal within the beam profile of the NIR pulse for each bunch. Thus, a spatially resolving intensity monitor is required. The degree of temporal compression of the NIR pulse after leaving the highly dispersive glass fiber is performed with a remotely controlled autocorrelator.

Additional tools like a photo diode and an electron beam pick up are installed, to achieve the coarse and fine adjustment of the relative timing between the electron bunch and the optical laser pulse. A complete overview of the TEO setup and the used components is presented in fig. 4.23.

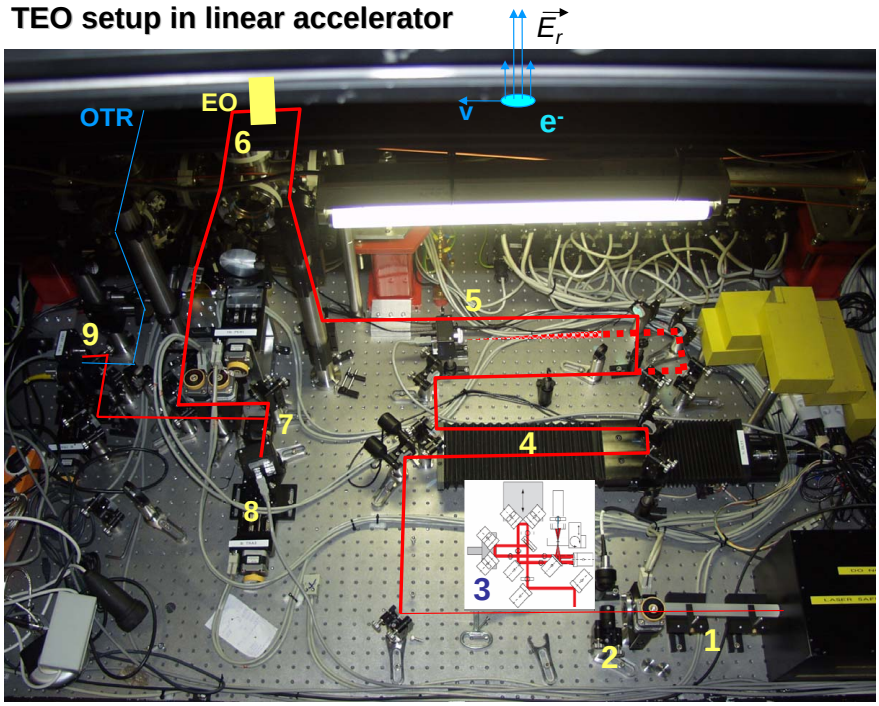

Figure 4.23: *The TEO tunnel setup.*
1: glass rod, 2: partial reflecting mirror and polarizer, 3: Autocorrelator, 4: delay line, 5: pointing monitor, 6: wedged crystal ZnTe crystal, 7: Polarizer, 8:CCD-camera, 9: Coarse timing photo diode.

4.3 Gateable intensified CCD camera

The device used as a detector of the electro-optically induced spatial intensity modulation representing the electro-optical signal of the FEL electron bunch is a commercially available gateable, intensified CCD camera. The camera includes an image intensifier, a CCD array and electronics to read out the CCD array. The camera is triggerable and temporally gateable with a minimal exposure time of 5 ns. The intensifier consists of a GaAs photo cathode, a multichannel plate and a fluorescence phosphor screen. Photons incident on the photocathode excite photo electrons, which are multiplied inside the 10^6-10^7 channels. These electrons hit a fluorescent phosphor screen, which converts the electrons back into photons. The fluorescence photons are emitted independent of the wavelength of the incident photons at a wavelength of 520 nm and are detected by the CCD array chip made of 1.3 Mio. pixels [PCO03].

Figure 4.24: *The intensified CCD camera used as detector for the electro-optical experiment.*
(fig. from [PCO03])

The photo cathode exposure time is gateable. An applied voltage decelerates or accelerates the emitted electrons preventing or allowing the electrons to pass the intensifier. Since the voltage can be switched on and off very quickly, it is possible to reduce the exposure time of the electronic gate to 5 ns. This sufficiently small time window allows to select that specific optical pulse of the Ti:Sa oscillator pulse train, which is used for the electro-optical cross-correlation and carries the EO signal information. Any unmodulated pulse, which might additionally to the modified pulse be accumulated, will cover the EO signal and thus must be excluded from detection by the fast electronic shutter gate.

4.4 Example of a spatially encoded EO signal

A typical image example of a spatial encoded EO signal is shown in figure 4.25.

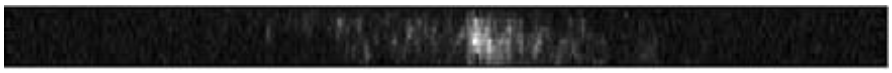

Figure 4.25: *Image of the TEO signal.*
Due to the time-to-space mapping, the horizontal dimension corresponds to a time axis.

The image shows a line focus with an intensity modulation on top of it. The reason for the use of a line focus is, that the NIR optical laser beam profile must be line focussed on the crystal to increase the signal contrast. Due to $E_r \sim \frac{1}{r}$ in equation (2.116) the strength of the EO signal scales inverse proportional with the distance from the electron bunch, i.e. the signal becomes smaller the further away the laser beam passes by the crystal. This radial dependence will be further discussed in section 4.5.3. To compensate this effect and increase the signal strength, a cylindrical lens focuses the Gaussian NIR pulse to a line focus on the crystal. In this way the total amount of energy

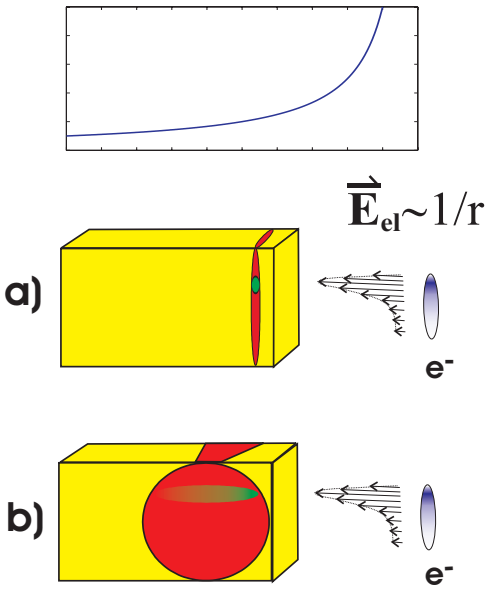

Figure 4.26: *Line focus on EO crystal.* In the unfocussed case **(b)** the total polarization rotation along the transverse beam profile is smaller than in the line focussed case **(a)**, since the electrical field strength decreases inverse proportional to the radial distance r from the electron bunch.

of the laser pulse is located closer to the electron bunch as in the unfocussed case. Thus, the 1/r-dependence of the bunch field can be neglected in case of the 100 µm width laser line focus (compare fig. 4.26).

4.5 The TEO timing signal

For the TEO diagnostic the following parameters regarding focussing, beam diameter and EO-crystal are used: The transversal size of the line focus is 1.6 mm FWHM. The optical laser pulse duration is 100 ±10 fs FWHM corresponding to a 30 μm thin disc, which is much smaller than the thickness of the electro-optical GaP crystal of 175μm.

Integrating the signal image of fig. 4.25 results in a plot of the temporal dependence of the electro-optical signal. A TEO signal traces is presented in fig. 4.27.

In the plot the trace together with a Gaussian fit of the peak area is shown. A Gaussian fit model or a Sech^2 model provides a reasonable high fit performance as measured by the coefficient of determination R^2. This coefficient is defined as the ratio between the variance of the measured data y_i and the fitted data f_i

$$R^2 = \frac{\sum_i^N \frac{1}{N}(y_i - \overline{y})^2}{\sum_i^N \frac{1}{N}(f_i - \overline{f})^2} \quad . \tag{4.18}$$

For a Gaussian fit model R^2 is larger than 0.99 compared to an optimal value of 1.00 representing perfect agreement between model and measurement. A Gaussian fit model beats other peak models like a Lorentzian peak model. Thus, in the following the Gaussian model is used to analyze the peak structure. Compared with the simulated traces of fig. 2.11 a large degree of agreement is found. The trace shows a sharp peak followed by a tail, which is up to 1 ps long. From the peak fit one derives the width, the amplitude, the center time and the time of the inflexion point of the rising edge. The inflexion point time and the peak center time are used to determine the relative arrival time between the optical pulse and the electron bunch. The calculated fit error to predict the center of the peak using a Gaussian or Sech^2 fit model is better than 5 fs RMS[‡].

[‡]Calculation performed with the MATLAB curve fitting tool box

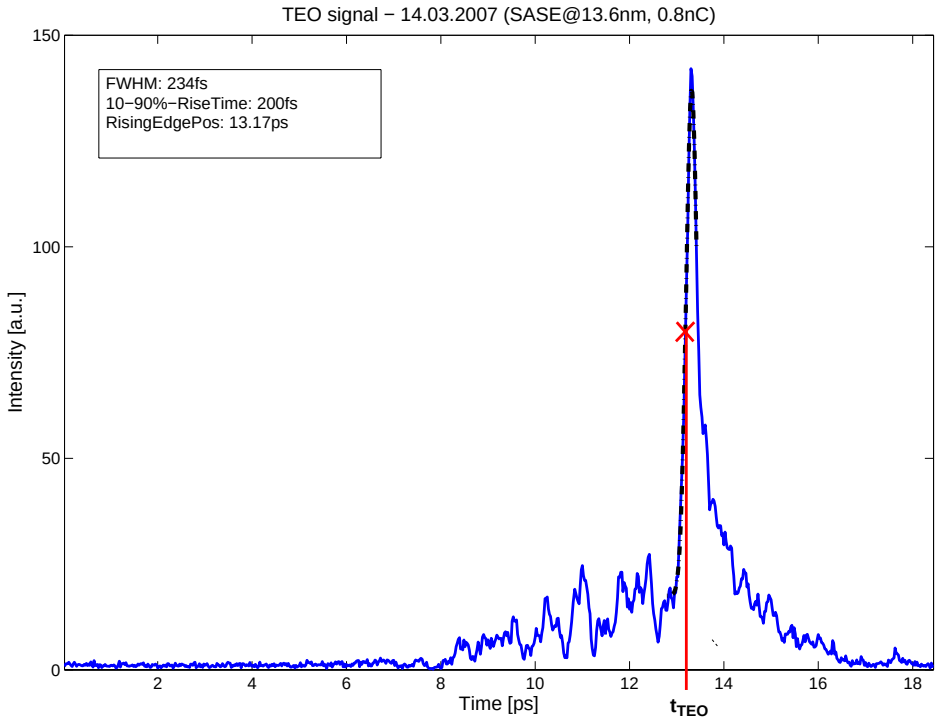

Figure 4.27: *Measured TEO signal and arrival time.*
The figure plots an electro-optical signal of the FLASH electron-bunch measured by the TEO detector. The arrival time is found from the inflexion point of the rising edge. The signal is shifted to the right, because the electron bunch is passing by the crystal 1.5 mm below the crystal center (see section 4.5.3). The area showing non-zero background defines the time window of the spatial decoding setup, because this is the area of the non-zero transversal laser beam energy profile, where it is at all possible to detect an electro-optical effect. The corresponding maximal phase retardation is calculated to 17°±3°

4.5.1 Photon count estimations of the TEO signal

Although the signal-to-noise ratio of the signal of fig. 4.24 is larger than 10:1, a lot of noise at the signal floor is still visible. The signal intensity transformation is performed by a near-crossed polarization setup. Hence, some background is unavoidable. To analyze the nature of this noise, it is compared with the detector noise. The following estimations regarding the used intensified CCD camera as intensity detector have been performed.

The beam reflected by the analyzing polarizer in front of the ICCD creates a photodiode signal (Thorlabs DET10A, see fig. 4.23, component 9). The power at this position is too small for most conventional power meters, hence the power is measured with a photo diode. To estimate the beam energy on the ICCD chip, the beam energy is calculated from the photo diode signal in the following way.

The peak amplitude is measured with a scope to be 20 mV per pulse. Terminated with a 50 Ω resistor at the scope, a peak current of 0.4 mA per pulse is induced. Each measured photo diode pulse width is 2.5 ns. The beam pulse repetition rate is 108 MHz≃9.3 ns. Hence, an average diode current of $0.4\,\text{mA} \cdot 2.5/9.3 = 0.1\,\text{mA}$ is created by the incident laser power. The photo sensitivity of the biased diode is 0.3 A/W. From this follows, that an average power of 0.4 mW from the laser beam is incident on the diode. Hence, the energy per pulse is about 4 pJ. With $E = h\nu$ one calculates an energy per photon of $2.48 \cdot 10^{-19}$ J <=> 1.55 eV for the 800 nm NIR laser photons. Thus, the number of photons per pulse in front of the polarizer is about $1.6 \cdot 10^7$. Before the crystal one measures up to 5 mW of laser beam power. Thus, about 90% of beam power is lost during the laser passes through the crystal and several optics, like the polarizer or the quarter- and half-waveplates due to scattering and reflection.

A typical retardation value for Γ achieved with the TEO crystal at FLASH is about 15°. Thus, according to $I = I_0 \cdot \sin^2(\Gamma)$ for a crossed-polarizer setup about 6.7% of EO signal beam power is transmitted through the polarizer into the ICCD. The EO effect modulates only a fraction of about 10% of the transversal beam profile. Hence, the EO signal consists of about $1.07 \cdot 10^5$ photons. The transmission efficiency of the ICCD imaging lens system amounts to 22%. The photocathode S25 shows a quantum efficiency of 2% at 800 nm. The MCP multiplies the photo electrons by $\approx 10^3$. The phosphor screen P46 has a quantum efficiency of 30% for the conversion of multiplied electrons of the MCP into photons. Each CCD pixel has a quantum efficiency of 40% to convert photons of the phosphor screen at 520 nm into photo electrons. Altogether the ICCD shows an efficiency of 50% for the conversion of a signal photon into a photo electron within the quantum wall of one CCD pixel. The CCD pixel A/D converter is specified to transform 5 photo electrons into one digital count, i.e. 0.2 counts/e^-. Thus, for the EO signal, which was assumed to be formed by 107000 photons, one expects a total of about 10000 counts for the integrated EO signal detected by the ICCD which agrees with the integrated EO signal shown in fig. 4.27.

As background noise the average statistical fluctuation $\Delta N = \sqrt{N}$ of the laser background excluding the EO signal is used, where N is the average count number before and after the EO signal derived from the signal trace. This statistical error ΔN amounts to 8 ± 1 RMS counts. The signal peak amplitude amounts to $N_{peak} = 130$ counts. Thus, the signal-to-noise ratio SNR amounts to a SNR of 16 : 1. The average dark charge rate per pixel is specified to be 0.1 e^-/pixel i.e. 0.02 counts, thus negligible to the 8±1 RMS counts large leaking background fluctuations due to the near crossed polarizer detection.

4.5.2 Signal optimization

A major improvement of the TEO signal has been achieved by a change of the EO crystal from a 450 μm Zinc-Tellurite crystal to a Gallium-Phosphite crystal of 175 μm thickness. In section 2.2.2 it has been shown that GaP supports higher maximum THz Fourier components than ZnTe. From this follows as have been shown by simulations in section 2.2.2, that GaP instead of ZnTe generates a shorter EO signal of the electron bunch of FLASH and thus is the preferred crystal material.

A direct comparison of the EO signals using either crystal materials is presented in fig. 4.28. The curves are supplemented by simulations of the detected EO signal based on the theory presented in section 2.2.2. Since it was not possible to reproduce comparable physical conditions regarding the crystal distance for the measurement with the GaP crystal as for the measurement with the ZnTe crystal, all curves including the numerical simulations, which were calculated with estimated radial distances between crystal and electron bunch, have been normalized to unity. Because the pulse width as well as the signal shape are not depending on the bunch field amplitude maximum value, but only on the remaining THz pulse and crystal properties, the normalization still allows to compare both signals with their simulations temporally. Thus, the simulations are calculated using the known crystal parameters and electron bunch properties like the crystal thickness, the bunch charge or the bunch energy and agree well with the measured data for both crystal materials. In detail the parameters of the electro-optical measurements are the following:

- waveplate settings of -4° for the quarter and 0° for the half wave plate
- the pulse duration of the optical pulse as measured at the setup and used within the simulations are 90 fs FWHM.
- bunch charge 0.8 nC,
- SASE conditions of FLASH fulfilled, thus the bunch was compressed, set SASE wavelength 13.5 nm
- Thickness of the GaP crystal is 175 µm. Thickness of the ZnTe is 400 µm.

The observed difference of the signal widths are resulting from the different crystal thickness and material.

4.5.3 Influence of the electron beam orbit

The electro-optical signal strength is dependent on the distance of the EO-crystal from the electron beam and the angle α between the horizontal $[-1, 1, 0]$-axis of the EO-crystal and the electric field vector. With equation (2.101)

$$\Gamma(\alpha) = \frac{\omega d}{c}(n_1 - n_2) = \frac{\omega d}{2c} n_0^3 r_{41} E_{THz} \sqrt{1 + 3\cos^2\alpha} \tag{4.19}$$

and fig. (4.29) and the $1/r$-proportionality of the electric field amplitude, one derives the following relation between the polarization rotation Gamma and the electron beam position relative to the location of the EO signal on the crystal

$$\Gamma(\alpha) = C \cdot \frac{1}{\sqrt{(r_\parallel - r_{\parallel,0})^2 + (\Delta h)^2}} \cdot \sqrt{1 + 3\frac{(r_\parallel - r_{\parallel,0})^2}{(r_\parallel - r_{\parallel,0})^2 + (\Delta h)^2}} \quad . \tag{4.20}$$

The angle α and the horizontal distance $r_\parallel - r_{\parallel,0}$ define the relative position of the electron bunch with respect to the laser spot on the electro-optical crystal. To define a coordinate origin, the two

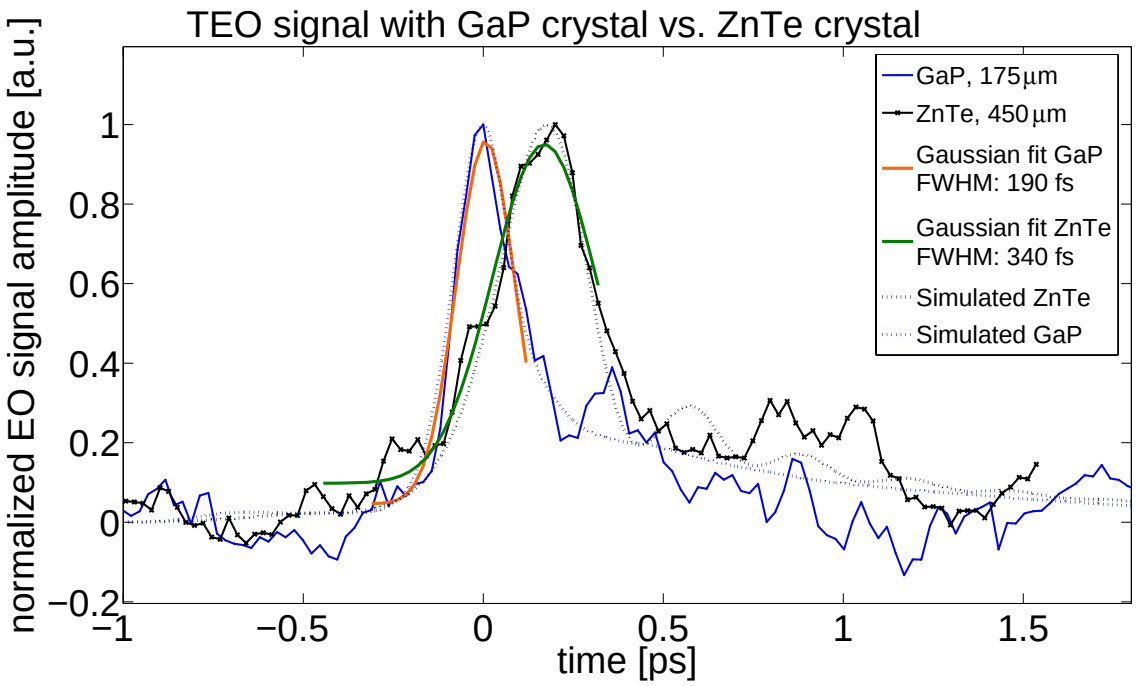

Figure 4.28: *Comparison of GaP and ZnTe crystals as electro-optical detector material of the TEO experiment.*
A direct comparison of the electro-optical signal of the TEO detector utilizing Zinc-Tellurite or Gallium-Phosphite as crystal material. The width of the GaP signal is 160 fs FWHM and thus significantly smaller than the width of 360 fs FWHM in case of using a ZnTe crystal. (Figure from [ADS+06])

offset variables $r_{\parallel,0}$ and h_0 are introduced. The vertical zero position shall be in the center of the crystal, the horizontal zero is defined by the location of the laser focus.

The generalized proportionality factor C contains all information about the electro-optical material and the electrical field strength. The unit of this proportionality factor is $[mm \cdot deg]$.

Relation (4.20) can be used to measure the relative position of the electron bunch close to the electro-optical crystal as will be shown in the next section.

4.5.3.1 Horizontal and vertical beam orbit shifts

Fig. 4.30 plots the dependence of the electro-optical phase retardation Γ of the horizontal distance of the electro-optical crystal $r_\parallel$ for various settings of the transverse displacement Δh of the electron bunch relative to the electro-optical crystal.

Plot 4.30,(b) showing the relation between Γ and $r_\parallel$ has one maximum at $r_{\parallel,max} = \frac{\Delta h}{\sqrt{2}} + 2 \cdot r_{\parallel,0}$. For distances closer than this maximum the EO-signal becomes smaller again, since only the projection of the electrical field vector $\vec{E}_\parallel$ parallel to the [-1,1,0]-axis of the crystal invokes the birefringence. The projected field vector becomes that small, that the implied EO signal decreases much and can not be compensated by counteracting inverse proportional dependence of $\Gamma(\parallel)$ anymore. A development of equation (4.20) for $r_\parallel - r_{\parallel,0} >> \Delta h$ gives rise to

$$\Gamma = \frac{2C}{r_\parallel - r_{\parallel,0}} \quad . \tag{4.21}$$

Thus, for large $r_\parallel$ the vertical displacement can be neglected leading to a complete inversion in the proportionality of Γ from $r_\parallel$.

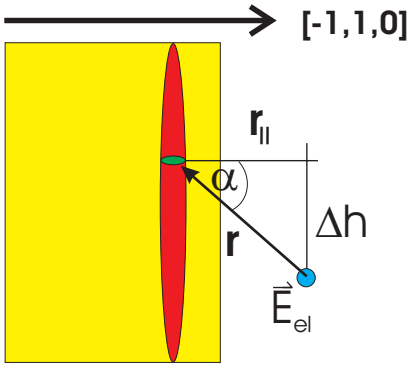

$$\cos(\alpha) = \frac{r_{\parallel}}{\sqrt{r_{\parallel}^{\,2} + \Delta h^{2}}}$$

Figure 4.29: *Geometrical relations between electron bunch and electro-optical signal.*
The [-1,1,0] direction is defined by the horizontal crystal edge. The EO signal at the coordinate $(r_{\parallel}, \Delta h)$ is depending on the angle α and the distance **r** from the electron bunch.

In the vertical case for a fixed $r_{\parallel}$ an analysis of $\Gamma(\Delta h)$ is provided in figure 4.31. Here only one fixed maximum of $\Gamma(\Delta h)$ for various $r_{\parallel}$ appears at $\Delta h = 0 \Longleftrightarrow h = h_0$.

4.5.3.2 Measuring the electron beam orbit

At the experiment neither the offset $r_{\parallel,0}$ nor the correct transverse displacement Δh is known *a priori*. Thus, it is in principle not sufficient to scan the EO signal strength Γ either in the horizontal or in the vertical directions only, since Γ depends on both parameters.

However, for the region, where $r_{\parallel} >> \Delta h$ holds true, one can use the relation of (4.21) to determine first $r_{\parallel,0}$ without knowledge of Δh. Unfortunately it was observed, that the EO signal strength drops quickly below the noise level for $r_{\parallel}$ larger than 2 mm away from the nearest possible position of the EO crystal relative to the electron bunch without clipping the electron bunch. Thus, only a few measurement points in this region are available. Thus, to increase the measurement accuracy many values of the electro optical retardation $\Gamma(r_{\parallel}, \Delta h)$ hat various distances r within an range of 2 mm and vertical displacements $\Gamma(r_{\parallel,i}, \Delta h_i)$ across the crystal are measured.

The radial distance $r_{\parallel}$ of the crystal can be modified with a vacuum linear stage motor. It moves the crystal together with the two mirrors, which are needed to align the optical line focus on the crystal. Hence, the optical line focus passes the crystal for all radial distances r at the same crystal surface position. The closest distance to which the crystal can be moved is limited by the electron bunch trajectory, which the crystal may not hit. The position at which the electron bunch hits the crystal can be measured with 0.1 mm resolution by observing the electron beam losses 5 m upstream right in front of the undulator section of FLASH.

The vertical displacement Δh can be varied by changing the optical temporal delay stage, since due to the spatial decoding setup an arrival time modulation of the optical pulse corresponds with a vertical displacement of the EO signal spot on the crystal.

For each measurement a fit with the model of eqn. (4.20) is performed to obtain the unknown parameters $C, r_{\parallel}$ and h_0. The measurements and fits are in good agreement and are presented in fig. 4.32.

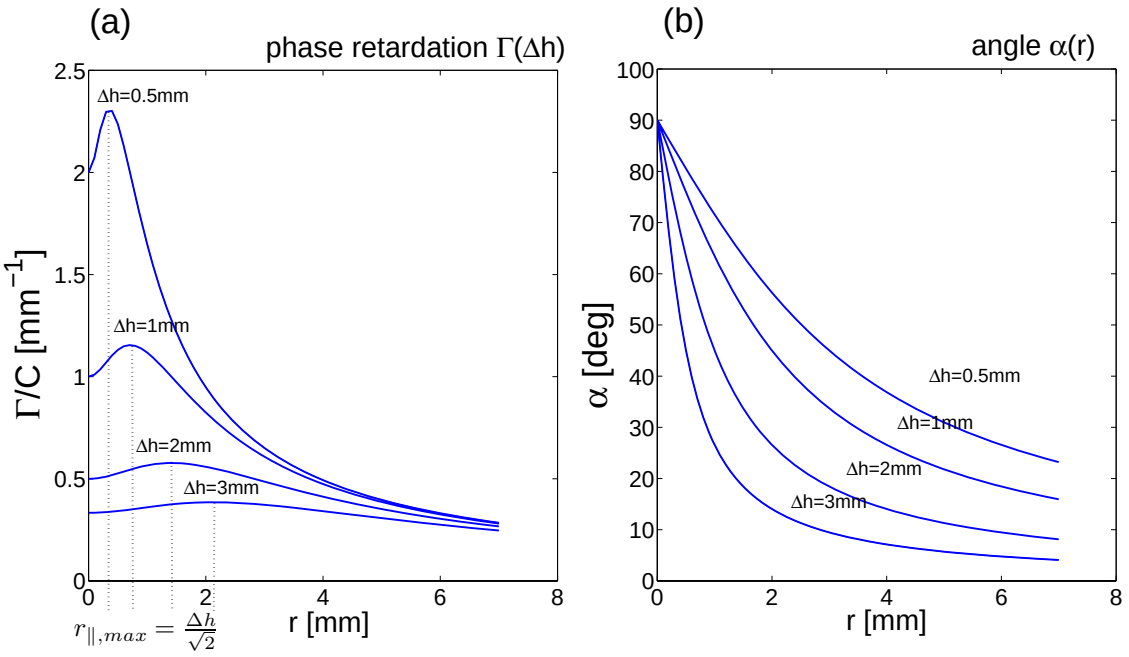

Figure 4.30: *The electro-optical signal strength* $\Gamma(r_\parallel)$ *for various settings for the transversal displacement* Δh
($r_{\parallel,0} \equiv 0$*).* (a) Calculation of Γ/C vs. radial distance r of the EO signal from the electron bunch axis for various transversal distances. (b) Calculation of angle α of corresponding $(r_\parallel, \Delta h)$-combinations.

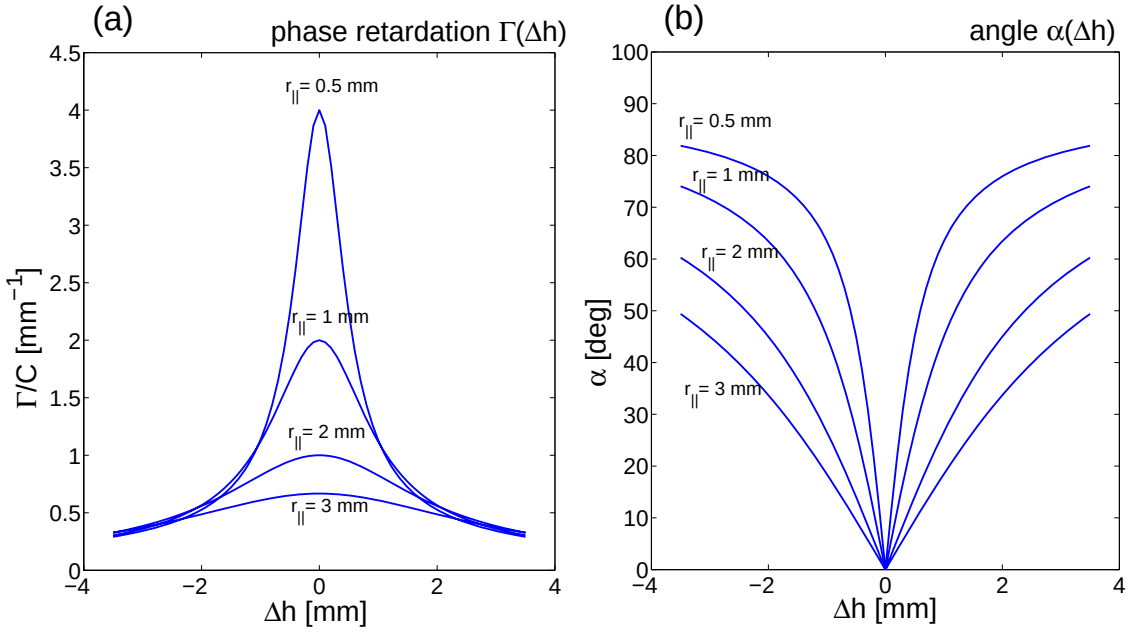

Figure 4.31: *The electro-optical signal strength* $\Gamma(\Delta h)$ *for various settings of the horizontal distance* $r_\parallel$.
(a) Calculation of Γ/C vs. horizontal displacement Δh of the EO signal from the vertical center of the crystal for various horizontal distances $r_\parallel$ of the electron bunch. (b) Calculation of angle α of corresponding $(r_\parallel, \Delta h)$-combinations. For smaller horizontal distances, $\alpha(\Delta h)$ is larger and the area of largest phase retardation along the vertical axis of the crystal is getting narrower.

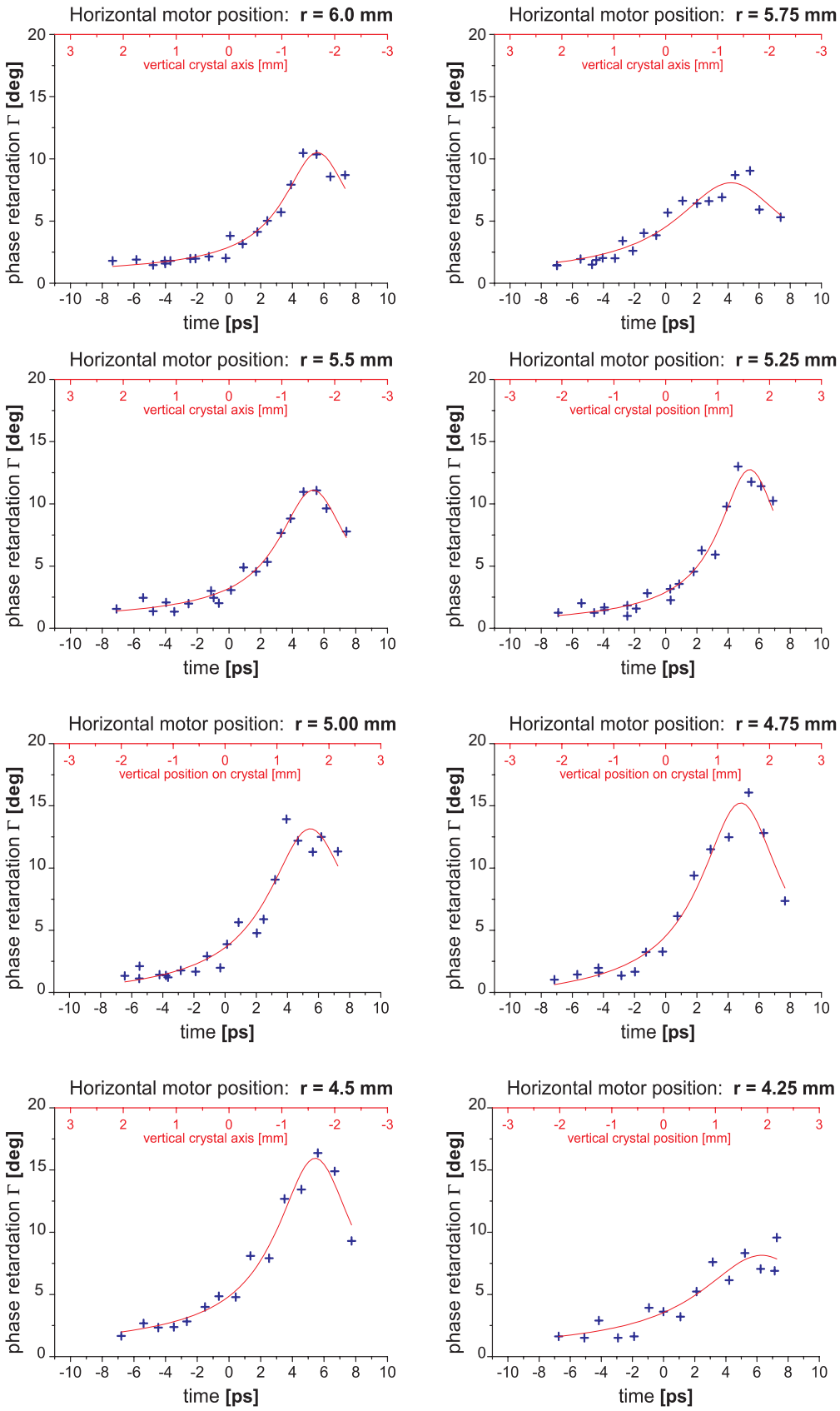

Figure 4.32: *EO signal measurements at various distances and vertical positions.*
The plot shows measurements of a scan of the phase retardation Γ by $r_{\parallel}$ and Δh. Each plot is presented with a spatial and a temporal axis, according to the space to time mapping of the spatial decoding technique. The plots shows, that the electron beam during this measurement had an offset of $1.5 \pm 0.2\,mm$ with respect the vertical center of the electro-optical crystal.

The maximum retardation Γ_{max} is observed at a transversal displacement with respect to the center of crystal of Δh =1.5 mm for each radial distance $r_{\|}$. Thus the measurement shows, that the electron beam orbit during the measurement period has been vertically displaced from the center of the electro-optical crystal by 1.5 mm. The measurement resolution corresponding with the average fit error of the peak position in vertical direction is 160 μm.

In a second step the maximal values $\Gamma_{max}(r_{\|,i})$ obtained from the fits of the scans are plotted versus the radial distance $r_{\|,i}$ of the scan in fig. 4.33. The model of eqn. (4.21) is then fitted to this plot to determine the coefficient C and the radial offset position $r_{\|,0}$.

The fitted horizontal offset $r_{\|,0}$ is (2.2 mm) and the proportionality factor C is 20.7 $mm \cdot degree$. The parameter C equals the half maximal electro-optical retardation $\Gamma_{max}/2$ at one millimeter distance from the electron bunch and zero vertical displacement $\Delta h = 0$. The distance offset $r_{\|,0}$ is used to correct the radial axis *a priori* defined by the linear stage motor positions.

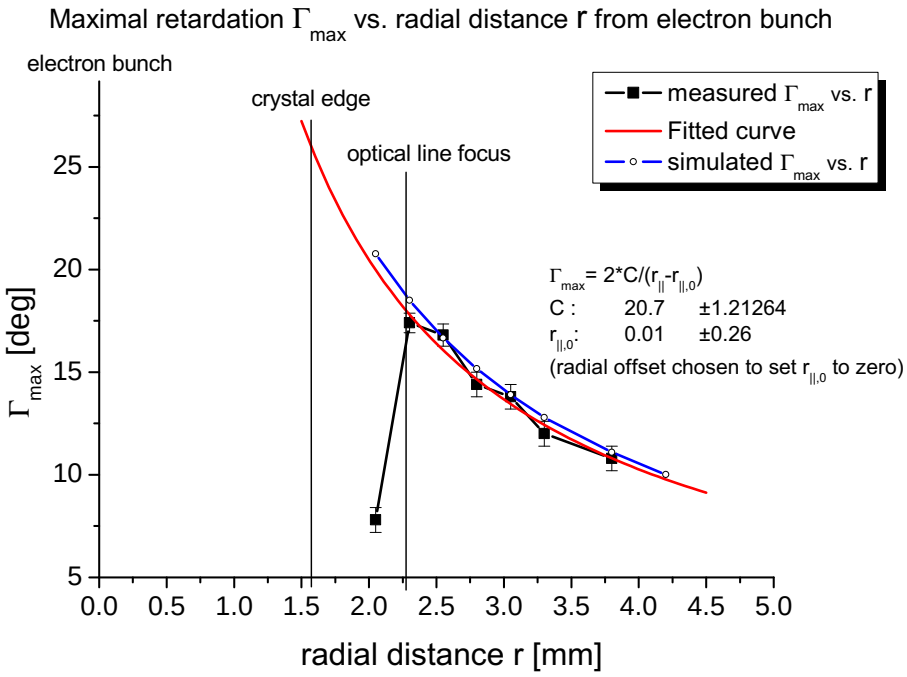

Figure 4.33: *Measuring the crystal distance from the electron bunch.*
For each plot of fig. 4.32 a maximal retardation Γ_{max} at -1.5 mm vertical displacement is observed. In this plot this maximal displacement is plotted versus the radial distance of the crystal from the electron bunch. The crystal is moved by a motor, which also moves the optical line focus to guarantee, that the sampling takes place at the same surface position on the crystal. The $1/r$ ~model of equation (4.21) is fitted to find the offset position $r_{\|,0}$, which provides the distance of the crystal for each motor position.

The location on the crystal surface, where the electro-optical sampling is performed and where the line focus is located, is not chosen to be at the very edge of the crystal but instead 0.7 mm away from the edge. The reason is, that at the edge of the crystal the electro-optical effect is reduced, since the THz wave is scattered from the edge and no longer travels parallel to the optical wave.

Hence, according to fig. 4.33 the closest position of the crystal edge from the electron bunch axis, which could be used without risking a collision of the crystal with the electron bunch is 1.5 mm of radial distance. At this position the retardation drops below the expected $1/r$-proportionality, which can be explained by dark current, which radially surrounds the electron bunch and which at this close distance already hits the crystal and reduces the electro-optical abilities of the crystal.

To find the correct parameters regarding the distance between the crystal and the electron bunch axis, this data point was excluded from the fit procedure.

The measured data are compared with simulated data. For the simulation a simulated electron bunch density distribution as shown in fig. 2.11 was assumed, since no additional electron density data have been measured parallel during the here presented electron orbit measurements. As shown in figure 4.33 a good agreement between the simulated (blue curve) and the experimental data (black curve) is found.

Chapter 5

Electro-optical measurements

5.1 Characterization of the GaP crystal

Before the electro-optical crystal has been installed inside the linear accelerator beamline, it was characterized and tested at the Terahertz to Optical Pulse Source (TOPS) at the University of Strathclyde, Glasgow, Scotland [Jar06]. The laboratory provides a user station for experiments with free-space propagating THz radiation. The sub-picosecond THz pulses are generated from photoconductive emitters (GaAs Austin switch) using a 1 kHz, 40 fs (FWHM) Ti:Sa laser. The photoconductive switch is a 2 inch GaAs wafer with two electrodes separated horizontally by ≈45 µm. The voltage applied to the electrodes was 7 kV, and the switch was illuminated with 330 μJ, 40 fs (FWHM) Ti:Sa pulses. The emitted THz pulses reach energies of ≈ 1μJ with a frequency range between 30 GHz and 2.5 THz [Ste07]. The pulses were focused on the EO crystal to be tested. The electro-optical polarization rotation was measured in a balanced detection setup. The signal was amplified by a lock-in amplifier.

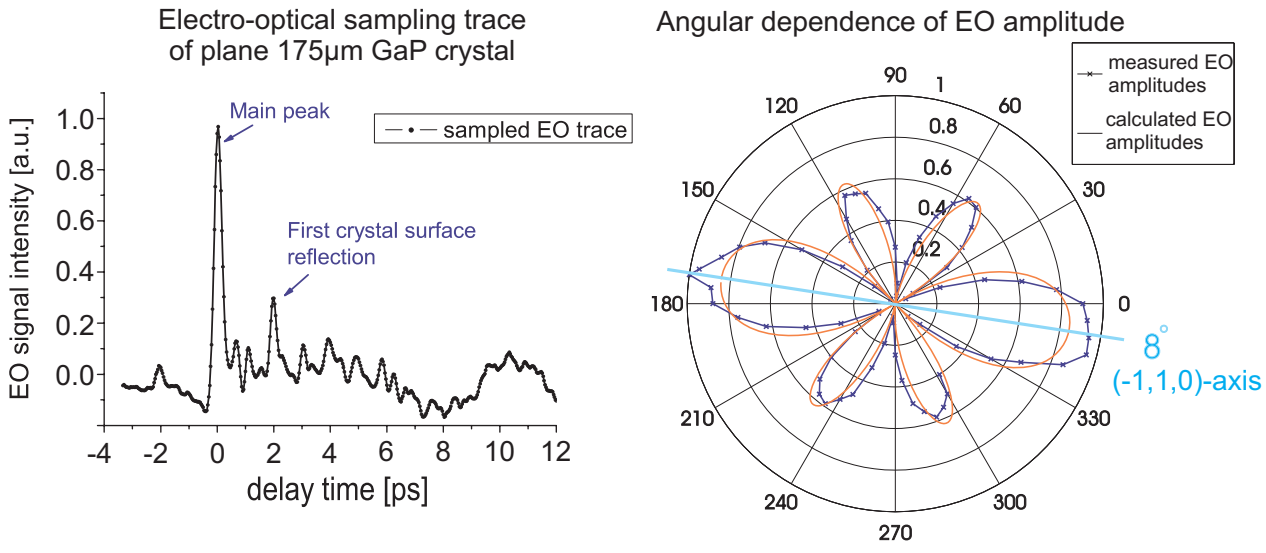

Figure 5.1: *EO crystal characterization of the Moltech GaP 175µm crystal*
Left plot: An exemplary trace of the sampled electro-optical signal. Clearly visible are the main peak and the first THz wave crystal surface reflection. **Right plot**: Polar plot of the amplitude of the main peak versus the rotation angle of the crystal. The appearance of the many lobes are a consequence of the equations (2.101) and (2.58), which rule the dependence of the retardation from the crystal rotation angle Ψ (see fig. 2.3).

The goal of the measurement was to gather information on the electro-optical efficiency and crystal orientation. To analyze the crystal axis orientation, the crystal was rotated around its surface normal. The result of the measurement is presented in fig. 5.1. The amplitude of the electro-optical signal is plotted versus its rotation angle. Using the formulas of section 2.3.2.2 the angular EO signal dependence can be reproduced. The calculated angular dependence plot fits the measured data best, if a maximum polarization rotation Γ_{max} of 210° is assumed. Using the theoretical values for the electro-optical coefficient of GaP of section 2.2, a field strength of 450 MV/m would be required to induce an rotation of that magnitude. This corresponds to the expected peak field strength estimated from the THz beam parameters, which are 1 μJ pulse energy, 650 fs and 1.5-2 mm focal THz spot size. Thus, these test measurements have confirmed the expected electro-optical efficiency of the GaP crystal.

The crystal axis (-1,1,0) to which the THz field vector should be parallel for optimal EO signal strength was found to be rotated by 8° relative to the crystal long edge, which is still acceptable.

5.2 Studies of the electron bunch profile detection

In this section the TEO detector's capability to analyze the longitudinal electron density distribution of the bunch is investigated. Although the TEO detector's purpose is to measure the relative arrival time between the electron bunch and the optical laser pulse, the detector is additionally able to take a measurement of the complete electron bunch distribution in one shot as was explained in sections 2.4.1.

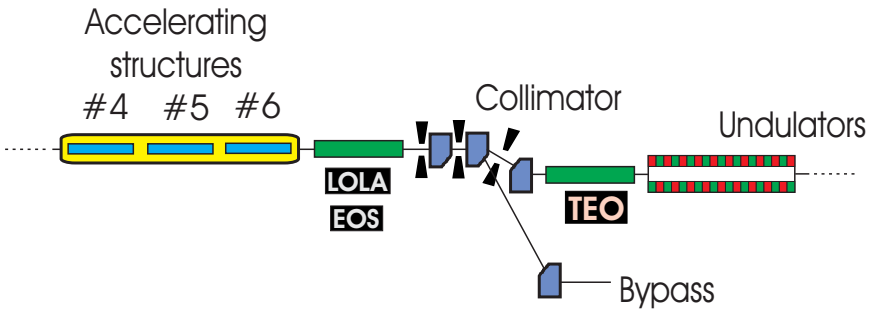

Figure 5.2: *Location of the electron bunch diagnostics, TEO, LOLA and EOS.*
In the linear accelerator of FLASH two electron bunch diagnostic section exists. One behind the last, sixth accelerating module, where the transversal deflecting cavity LOLA (see section 3.1.2.1) and another electro-optical sampling experiment named EOS [Ste07] are located.

To analyze the TEO temporal resolution, it is mandatory to compare the TEO measurement with another detector. As the electron bunch profile changes from bunch train to bunch train, this comparison must be performed ideally by a single-shot measurement of one electron bunch of the same bunch train. At FLASH another device for this purpose exists. This device bases upon a transverse deflecting RF structure and in general is known as LOLA diagnostic. Details on this diagnostic have been provided in section 3.1.2.1. LOLA is located right behind the sixth acceleration module about 50 m in front of the TEO detector (see fig. 5.2). Essentially only a free flight segment and the collimator section lies in between both detectors. The influence on the the electron bunch due to the magnetic transverse deflection to streak the electron bunch slightly modulates the longitudinal shape of the electron bunch and limits the LOLA resolution to 10-20 µm [Röh08]. However, compared to the resolution of the TEO experiment of 60 µm this effect can be neglected. Another error source results from the fact, that the electron bunch detected by LOLA is consumed and can not be

detected by TEO. Thus, only two subsequent bunches of each bunch train can be compared by both detectors. However, the differences between subsequent electron bunches are beyond the resolution of the TEO diagnostic and thus are negligible.

The diagnostic comparison measurements between LOLA and TEO have been performed on a pair of two subsequent compressed and on multiple pairs of two subsequent over-compressed electron bunches of each bunch train. The results are presented in fig. 5.3.

The measurement series demonstrates, that the longitudinal electron bunch profile changes in a systematic way, as the phase of the ACC1 accelerating field is increased relative to its phase setting for best electron bunch compression, which for this measurement series defines the zero point 0°. One finds, that a second electron peak about 1 ps after the main peak appears and increases in its amplitude as the phase is detuned further. A start to end simulation shows [Doh], that within over-compression regime in the beamline section after the first bunch compressor the amount of charge in the main peak is more than twice as large than in the compressed bunch phase regime. This high charge concentration leads to repulsive space charge effects. One part of the electron bunch will be decelerated and a second part will be accelerated thus leading to two energetically separated electron groups within the bunch. The slower part is linearly dispersed and will be compressed and time delayed in the second bunch compressor, which generates the second additional peak observed in the longitudinal electron bunch profile.

The measurement shows, that the TDS and the TEO diagnostic agree in its measured profiles even for smaller bunch structures. The shortest peak detected by TEO is 400 fs broad. This is not the highest resolution, with which TEO can detect. In measurements shown before TEO has already detected pulses of 210-230 fs width. Troubles with the optical pulse compression system led to a broader optical pulse for TEO and reduced the measurement resolution.

For further applications it would be of interest to demonstrate, that beside the main peak also the second peak is able to create SASE light inside the undulators. A way to show this would be to perform an experiment with these settings together with the infrared fs-streaking experiment developed in the group of M. Drescher, which is able to analyze the temporal structure of the FLASH XUV pulse on a few 5 fs timescale [Fru].

5.3 Studies of the bunch arrival time detection

To test the timing capabilities of the TEO diagnostic, a correlation experiment was performed. Since the temporal jitter of the electron bunch varies from shot to shot, the correlation must be performed simultaneously with another bunch arrival timing diagnostic on a single shot basis. A single-shot diagnostic with sufficient high temporal resolution just like the TEO detector is another electro-optical sampling experiment named EOS, which is located close to the position of the LOLA detector behind the 6th acceleration module (see fig. 5.2). Its measurement principle is quite similar to that of TEO. EOS encodes the electron bunch trace electro-optically inside a 800 nm fs-pulse, but unlike TEO the encoding is performed temporally or spectrally and not spatially. Furthermore, the EOS diagnostic uses a fs-pulse, which originates from a different Ti:Sa oscillator than the one used for the TEO experiment. Beside these differences EOS and TEO are able to measure the longitudinal trace of the same electron bunch on a single-shot basis, which makes both measurements comparable and correlatable. Further details on the EOS experiment are found in [CSS+08]. An example of the measured TEO and EOS electron bunch trace is provided in fig. 5.4. As a reference LOLA was measuring together with both electro-optical sampling experiments, why the corresponding LOLA trace of the bunch is also added to the plot.

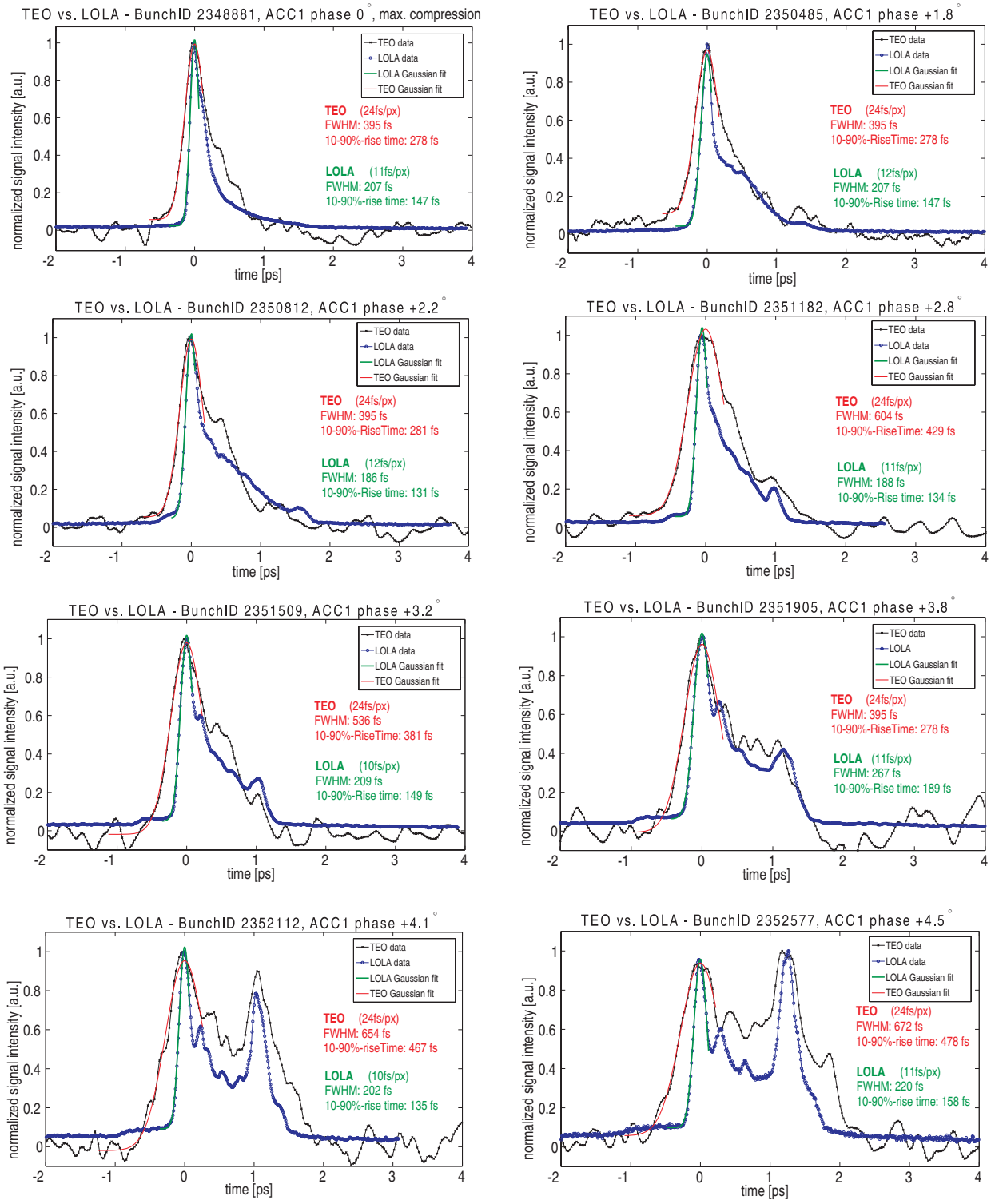

Figure 5.3: *TEO bunch profile versus LOLA bunch profile.*
Scan of ACC1 phase and comparison of TEO and LOLA bunch profiles of two subsequent bunches.

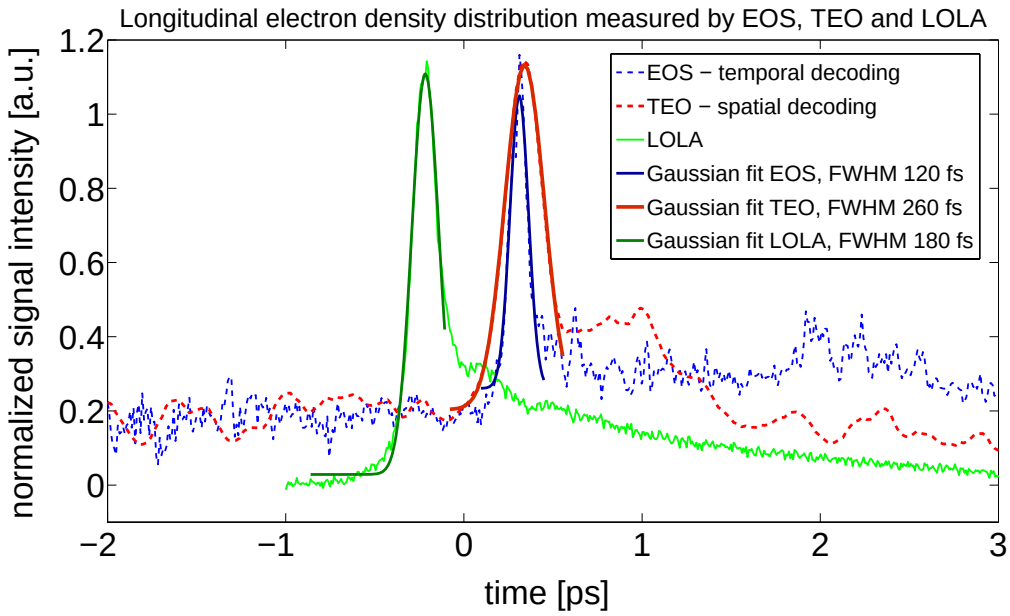

Figure 5.4: *TEO bunch profile versus EOS and LOLA bunch profile.*
Comparison of the three correlated bunch profile detectors TEO, the temporally encoded EOS diagnostic and LOLA. The width of the EOS peak is smaller than the width of the peak measured by TEO, since EOS uses a GaP crystal of only 100 µm thickness and TEO a crystal of 175 µm thickness.

5.3.1 Correlation study between TEO and an electro-optical spectral decoding experiment

For each measurement a Gaussian fit is performed to determine the arrival time and other peak parameters. The detected arrival times of many simultaneous experiments are compared in a correlation plot (fig. 5.5). From this correlation plot one can derive the relative arrival time detection error between TEO and EOS calculated by

$$\sigma(t_{EOS} - t_{TEO}) \quad , \tag{5.1}$$

, where the function $\sigma(t_i)$ is the standard deviation

$$\sigma(t_i) = \sqrt{\frac{1}{N}\sum_{i=1}^{N}\left(t_i - \bar{t}\right)^2} \quad . \tag{5.2}$$

The variable N is the number of time measurements t_i and $\bar{t}$ is the mean value of all time measurements.

The measured correlation error of 184 fs RMS is higher than one could expect from the RF synchronization error of each Ti:Sa oscillator. A typical timing jitter of a Ti:Sa oscillator synchronized to an external RF frequency by means of a phase lock loop and a cavity length tuning Piezo mirror is 100 fs RMS during a few minutes ([Men01]). For the TEO oscillator the synchronization was measured to an even better value of 70 fs RMS (see section 3.3). Hence a relative timing jitter between EOS and TEO of only 100-120 fs RMS was expected. Problems with the PLL lock of the EOS oscillator and the additional timing jitter, which results from the TEO pulse transporting 150 m glass fiber fluctuations reduce the timing correlation. However, on a 10-50 shots time base the plots show a clear correlation between both arrival timing detectors, if one compares the interpolated curves

of the upper plot in fig. 5.5. A correlation of the arrival time of TEO with the LOLA detector was omitted, since the phase instability of the RF cavity of LOLA was too high preventing a long term measurement without loosing the signal.

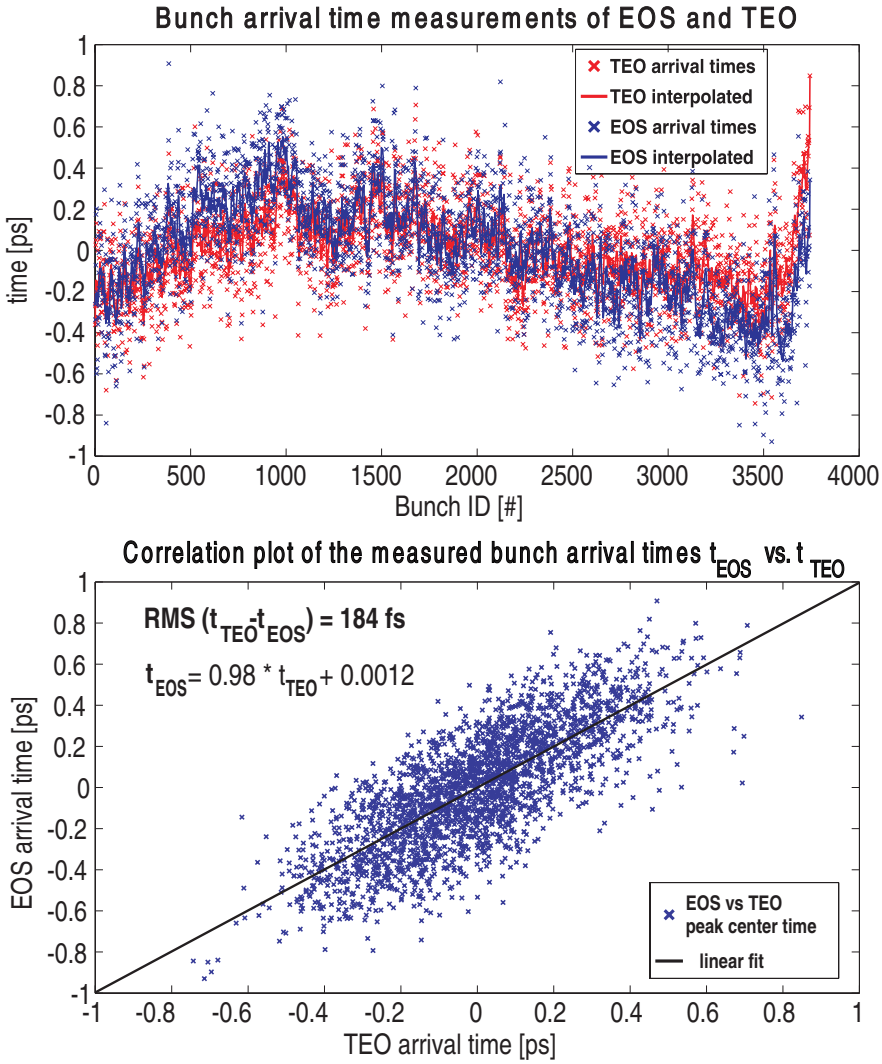

Figure 5.5: *Arrival time correlation measurement between TEO and EOS.*
Comparison of the electron bunch arrival times measured by TEO and EOS with correlation analysis. The upper plot shows the arrival time versus the bunch number and interpolations through the time jitter data, the lower plot shows the correlation plot. From the correlation plot one calculates a correlation of 184 fs RMS. The linear fit is an almost perfect zero crossing line with slope one, thus the time axis calibrations of both detectors agree. The measurement took 20 minutes.

Chapter 6

Ultra-fast pump-probe experiments at FLASH

A major goal of this work was to provide timing data for two-color pump-probe experiments. The TEO diagnostic temporal information on data recorded during pump-probe experiments is used to improve their jitter-limited temporal resolution. While the principle of all pump-probe experiments is quite similar, the observed physical properties varies strongly. The pump-probe experiments discussed in this work overlap the XUV laser pulse of the FLASH FEL in space and time with an amplified, ultra-short, near infrared (NIR) laser pulse and scan through the temporal delay between both pulses. The main differences between these pump-probe experiments is the type of target, the geometric setup, the fluence of either beam and the temporal resolution demanded. The last point is of course the most critical issue because of the temporal jitter of FLASH. It is here that the TEO diagnostic comes into play.

6.1 Principle of single event pump-probe experiments

The purpose of a pump-probe experiment is to study the temporal dynamics of a physical, chemical or biological system. The typical pump-probe experiments at FLASH cover a temporal dynamic range of interest from a few nanoseconds to a few tens femtosecond timescale.The principle is to prepare or pump the system with a short laser pulse and probe the excited system with a second short laser pulse after a variable delay time Δt. To study the full dynamic of the excited state, the measurement is repeated many times each time with a slightly different delay. This can be compared with a stroboscopic flash lamp, which periodically illuminates a moving object. The main assumption for this kind of measurements is that the system will be excited from event to event in a completely reproducible way. In particular there shouldn't exist any interaction between two consecutive pump-probe events.

Figure 6.1 illustrates the pump-probe technique in detail. To pump and probe a system, a trigger for the excitation, i.e. the pumping of the system, as well as for the probing, i.e. the interaction of the probe pulse with the excited state, must exist. Both depend on the wavelengths of the pulses. Thus, only a limited number of experiments are available with a specific wavelength pair of a pump and a probe beam.

The FLASH facility is well suited to perform two-color pump probe experiments. One pulse is generated by an amplified Ti:Sa oscillator at a wavelength of 800 nm. FLASH generates the second ultra-short pulse of high power XUV light (up to 10^9 W) in the spectral range from 6.5 nm to 45 nm [A$^+$07]. Possible experiments, which are within reach of these two-color pump-probe experiments at the FLASH facility are, for example, the probing of atomic [RDA$^+$07] and molecular

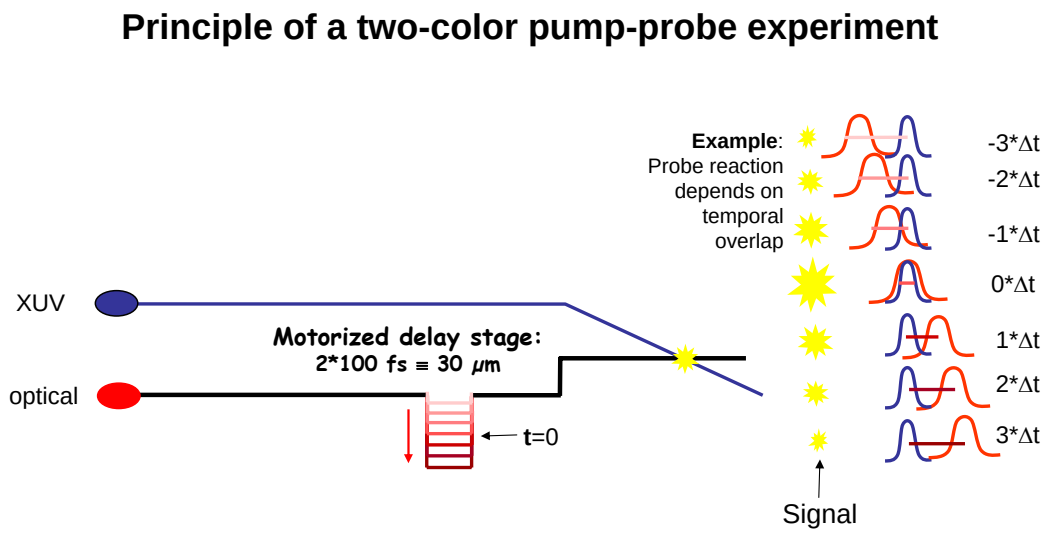

Figure 6.1: *Principle scheme of a two-color pump-probe experiment*
This scheme demonstrates the stroboscopic measurement technique to analyze the temporal dynamic of a physical system. Two laser pulses of in this case different wavelength pump and probe a reaction in a target sample 2n+1-times with varying relative arrival time t∈[-n*Δt, n*Δt]. The first pulse called *pump pulse* initiates a reaction. The second pulse referred to as the *probe pulse* analyzes the excited state and creates an additional signal, which depends on the relative delay time between both pulses. Multiple measurements with different set of delay times scan the evolution of the reaction time-resolved. The assumption is that the reaction process can be repeated without influence from a former pump-probe event.

states or the analysis of temporal electronic dynamics in solid matter [GAB+08]. An overview of the experimental environment for pump-probe experiments at the FLASH facility is provided in section 3.4. The theoretical temporal resolution limit of a pump-probe measurement depends on the temporal widths of the, typically Gaussian distributed, laser pulses and of the time duration of the triggered reactions. Let us assume a pump and probe reaction, which occurs much slower than the temporal widths of each pulse. In this case the excitation as well as the probe measure the system only when the electrical field of each laser pulse is present. Hence, a start or end time of each process can not be identified with a higher temporal precision than the temporal duration of the longer pulse.

A measured set of pump-probe data would include the temporal information of the process, if no temporal uncertainty on the arrival time of either pulse existed. However, this is not the case at FLASH. Here, a stochastic relative arrival time jitter between the XUV and the NIR pulse exists. The data measured for a set delay time does not correspond with the real delay time between both pulses. The real delay time is defined by the delay time plus an undetermined temporal offset between both pulses. Hence, a temporal uncertainty of each temporal measurement point exists, which effectively reduces the temporal resolution of the pump-probe measurement. Because the experimentalist generally must average over many measurements of a set delay time to reduce the statistical error of the measured signal, the temporal jitter contained in the data smears out the measurement of each delay time over a temporal range, which is as wide as the width of the temporal jitter distribution. A solution of the temporal jitter problematic is to measure the arrival time during the pump-probe measurement scan and correct each delay time for the measured arrival time variation. Thus, the temporal data of a pump-probe scan will be readjusted after the measurement. By means of this *a posteriori* temporal jitter correction, the actual temporal error of a pump-probe

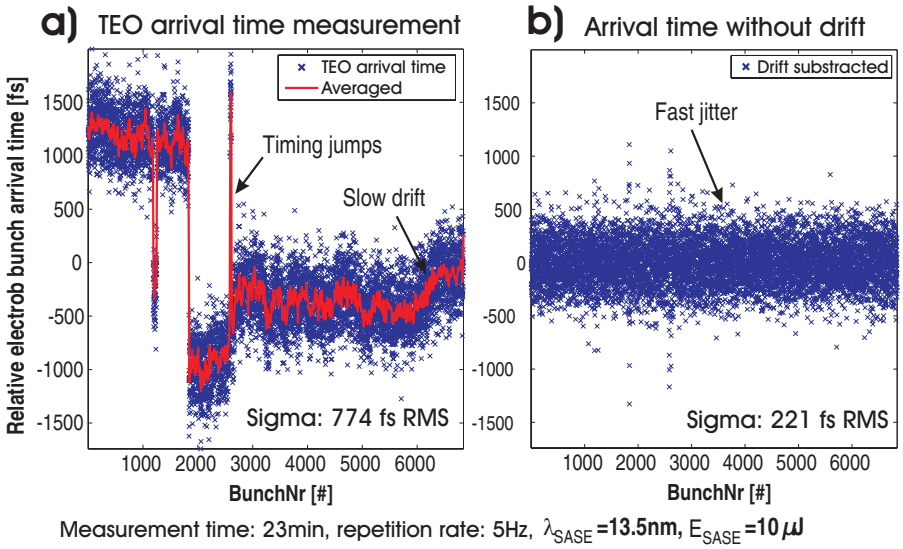

Figure 6.2: *Typical relative arrival time jitter measurement of FLASH*
These plots show the relative arrival time measurement between the electron bunch and the optical NIR Ti:Sa oscillator pulse measured by the TEO experiment. Since the temporal jitter of the NIR pulse is about 60 fs RMS [see chapter 3.3] the arrival time fluctuations mainly result from the linear accelerator. Plot **a)** shows the arrival time measurement shot-by-shot and an interpolation over 150 data points, which corresponds to the timing drift within 30 seconds. Plot **b)** shows the data of plot a) after subtraction of the interpolated curve.

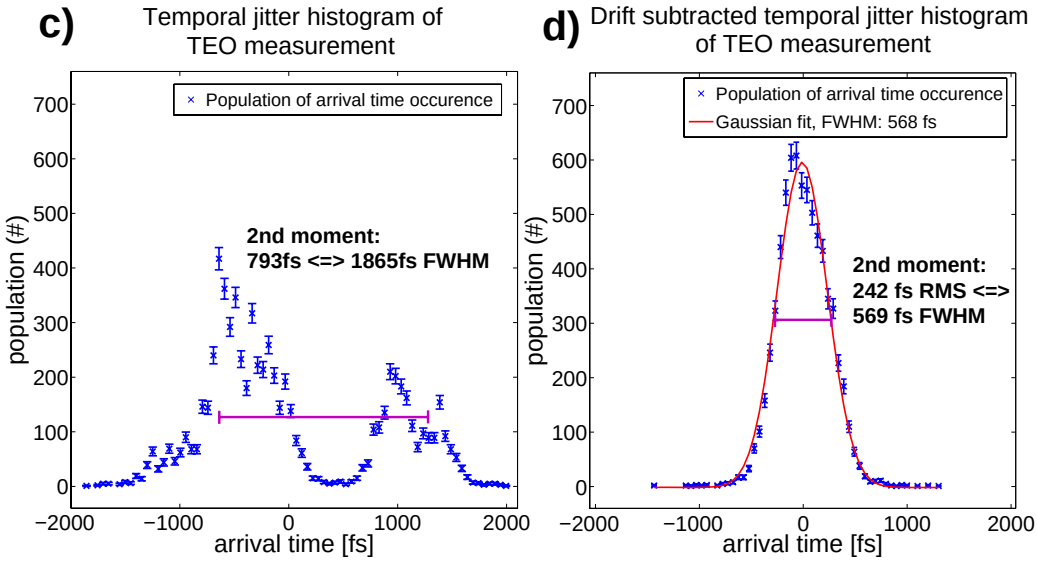

Figure 6.3: *Distribution analysis of the arrival time jitter of FLASH measured by the TEO diagnostic.*
These plots are showing distribution plots of the measured jitter of fig. 6.2. Plot **c)** shows the arrival time distribution including all types of fluctuations including long term drifts and large single shot timing jumps. Plot **d)** shows the arrival time distribution of the drift free jitter shown in plot **b)** of fig. 6.2. This distribution shows the short time scale jitter distribution.

measurement is defined by the precision of the arrival time measurement instead of the temporal arrival time fluctuations itself. Figure 6.4 demonstrates this *a posteriori* temporal jitter management technique in detail by means of a typical pump-probe signal model. The origins of the temporal jitter have been discussed in detail in chapter 3.3. As of the completion of this thesis in spring 2009, the total temporal jitter was around 150 fs - 250 fs RMS within a time range of 20-40 minutes, which is a typical measurement acquisition duration of a pump-probe measurement delay scan at FLASH. The total jitter is made up of different types of temporal fluctuations.

The single shot fluctuations are normally distributed, which is verified by the analysis shown in figure 6.3. A Gaussian provides a good fit to the short timescale distribution in plot 6.3 **d)** and the secondary moment in time of the short timescale distribution equals the σ-width (i.e. FWHM-width/2.35) of the Gaussian fit, which proves the statement.

Besides the single-shot fluctuations of 150 fs-200 fs RMS, one observes larger arrival time jumps of 1 ps-2 ps. These jumps appear randomly from one shot to the next but not more often than every 1000-2000 XUV pulses. These fast fluctuations are superimposed by slower temporal arrival time drifts, which happen on a time scale of few minutes up to hours. A typical arrival time measurement performed by the TEO experiment is presented in figure 6.2. All of these different types of temporal arrival time fluctuations reduce the temporal resolution, but can be compensated, if the delay time data of a pump-probe scan are corrected using the single-shot TEO arrival time information.

6.2 A posteriori temporal jitter correction of pump-probe experiments

In this section the process of *a posteriori* jitter correction is studied more detailed.

Once all the supplementary components of a two-color pump-probe experiment, like the target, the optical laser, etc. are prepared, a two-color pump-probe experiment at FLASH is performed in the following way. The experimentalist varies the temporal delay of the optical laser pulse with a two-mirror optical delay stage and takes a set of n measurements for each temporal delay time t. The TEO diagnostic runs parallel during the pump-probe experiment and measures the relative arrival time between the optical pump-probe fs-pulse and the XUV pulse as explained in section 4. According to this temporal information the TEO timing data is used after the pump-probe measurement is finished to subtract the temporal jitter of FLASH shot-by-shot for each set delay time. The four plots of fig. 6.4 demonstrate, how the TEO arrival time data are used to correct for the timing jitter after the pump-probe measurement is performed. Each plotted data point of delay time t_i represents a mean value of all measured pump-probe data within a certain time interval around t_i (fig. 6.4 a)). Due to the sorting procedure the time abscissa is modified to compensate for the jitter. The sorted and reaveraged data points however vary in their abscissa and ordinate (fig. 6.4 c)) compared to the unsorted data points. The TEO arrival time measurement resolution is 3-5 times smaller than the jitter width of FLASH and amounts to 60 fs RMS (see section 6.5.2). The uncertainty of TEO leads to a remnant broadening of the abscissa resorted pump-probe signal compared to the ideally jitter free pump-probe signal, but this broadening is much smaller than the broadening due to the FLASH jitter (fig. 6.4 b), d)).

Results of the pump-probe measurements typically are 2D data (e.g. velocity map (VMI) images [JRS+09]) or image data (e.g. spatially encoded reflectivity images [MCW+08]), 1D data (e.g. time-of-flight (TOF) spectra [MCO+06]) or simple numbers (e.g. reflectivity data [GAB+08]), where each data set is addressed with an individual bunch number. The bunch number identifies one measurement data set unambiguously and allows for the correlation between each single shot measurement with different simultaneous measurements throughout the linear accelerator in particular

with TEO and with the set delay time, at which the measurement was performed.

For an experimentalist it is essential to estimate, how long a pump-probe measurement will take, since the available beam time at FLASH is very limited. The duration of a pump-probe scan depends on the temporal scan range, the step size, the repetition rate of the laser pulses, which amounts to 5 Hz at FLASH and the signal to noise ratio. Especially the last point is important, since for weak signals and limited detector sensitivities the only method to increase the signal to noise ratio is to increase the data statistic. Thus, it is mandatory to quantify the data acquisition statistics of a pump-probe scan. In the following two variations to perform a pump-probe scan are discussed, which only differ in a statistical manner.

The first method **1** makes use of the delay stage and scans the temporal delay in a classical way as explained in fig. 6.1. This method shall be referred to as *multiple delay scanning* method. Assuming no temporal jitter the temporal resolution of this method is limited by the step size or the larger of both pulse durations. Assuming the presence of temporal jitter and the possibility of a single-shot temporal jitter measurement, the mechanically set delay time values of each measurement can be time jitter corrected.

The second method **2** is a special case of method **1**, which fully relies on the a-posteriori time jitter sorting ability provided by the TEO timing diagnostic. Here the temporal delay stage is not moved, instead the temporal jitter itself performs the necessary delay variations from shot-to-shot, which are measured by TEO. Thus this method shall be referred to as *single delay scanning* method.

Method two **2** is only a slight variation of the first. It differs from method **1** in the statistical distribution of the measurements.

While for method **1** a long range of time points are taken into account, for method **2** the time range is limited by the temporal jitter width but the number of measurements per time interval is larger than for method **1**. The statistical differences are a critical issue to optimize the available measurement time for best possible measurement results. It is clear, that for pump-probe signals, which are observed only at time zero of perfect overlap of both pulses, method **2** is the best choice. However, method **2** depends on stable timing conditions of FLASH, since timing drifts would change the central delay time of the measurement. In any other case the delay stage time step size must be adapted to scan a long enough time range, but keep the signal-to-noise ratio and thus the data statistics in regions of large signal amplitude changes still high enough to measure them. To choose the best settings in the following the statistic differences of both complimentary acquisition variations will be investigated. Then a measurement error analysis is performed, which leads to a set of formulas, from which an experimentalist can calculate the optimal settings for his pump-probe experiment.

6.2.1 Statistical analysis of jitter inflicted pump-probe experiments

On a short timescale disregarding single timing jumps or slow timing drifts, the probability function $P(t)$ to observe a measurement within a temporal interval [t,t+dt] is well approximated by a Gaussian distribution function as presented in the frequency analysis in fig. 6.3 of the measured arrival time jitter from figure 6.2.

Hence, the probability function $P(t)$ can be assumed to be Gaussian like distributed around a central arrival time t_0 and of width σ_J, i.e. the standard deviation of the arrival time jitter:

$$P(t, t_0) = \frac{1}{\sigma_J \sqrt{2\pi}} \exp\left(-\frac{1}{2}\left(\frac{t - t_0}{\sigma_J}\right)\right) \quad . \tag{6.1}$$

Multiplying the total number of pump-probe measurements N with eq. (6.1) results in the expected number of pump-probe measurements $n(t)$ within the time interval [t,t+dt] for the *single delay scan-*

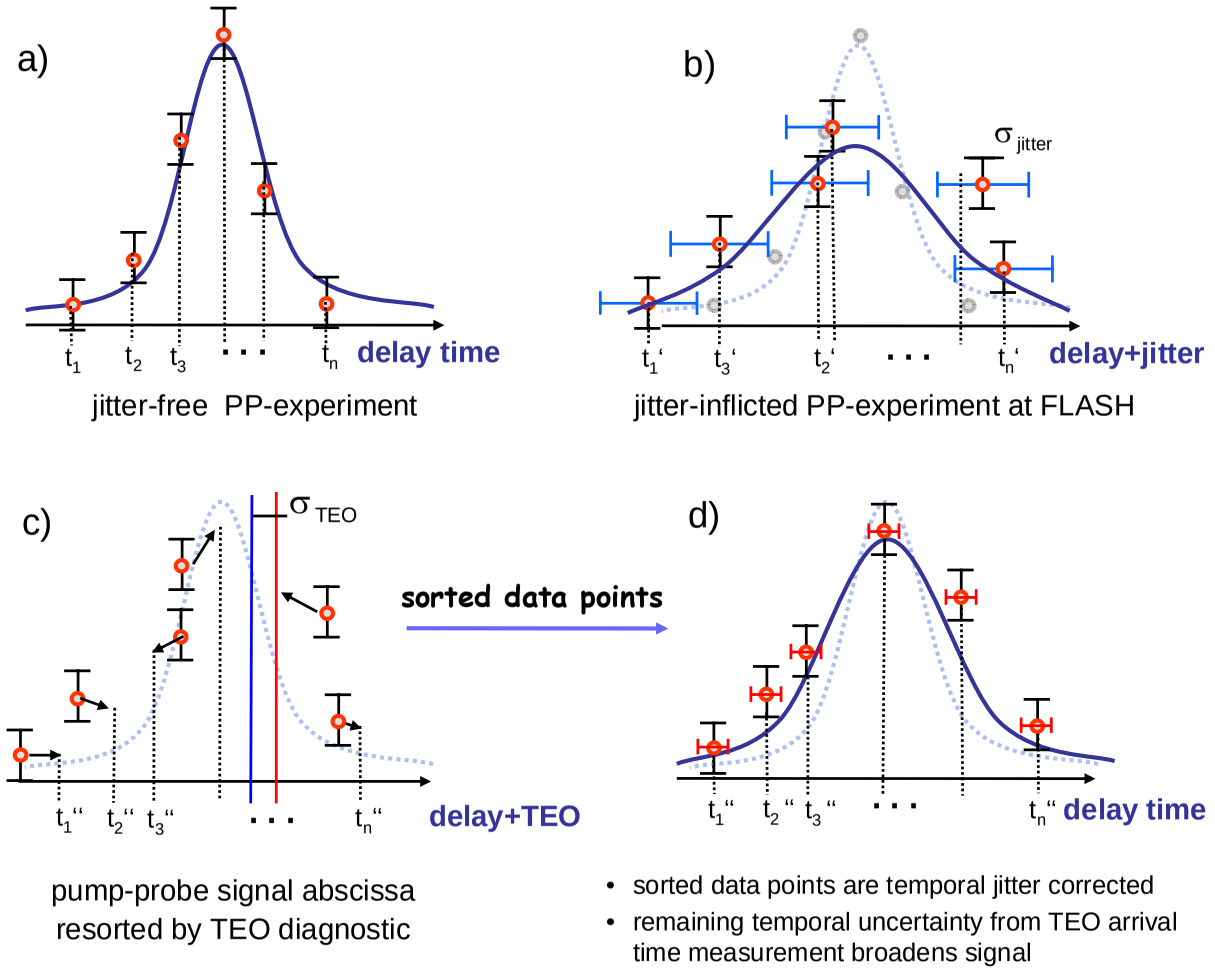

Figure 6.4: *Principle of jitter correction using TEO arrival time data.*
a) An example of a jitter-free pump-probe experiment of a pump-probe signal, which is assumed to be Gaussian like. The time independent amplitude noise is assumed to be constant. b) The FLASH jitter of up to 250 fs RMS introduces a stochastic uncertainty in the delay time of each data point indicated as horizontal error bar. As a reference the assumed jitter-free measurement points are plotted in light-gray. c) The TEO diagnostic measures the arrival time of the XUV pulse correlated with each pump-probe event. The limited resolution of TEO leaves a residual temporal uncertainty σ_{TEO}=60 fs RMS (red bar) compared to the jitter free data points (dashed bar). d) The arrival time data of TEO are used to correct for the temporal jitter data. The remnant temporal error due to the TEO measurement precision is significant smaller than the arrival jitter of the electron bunch as indicated by the horizontal error bars.

ning method

$$n(t) = N \cdot P(t, t_0) \tag{6.2}$$

The distribution function of the *multiple delays scanning* method can be approximated by the integral of eq. (6.1), since for one single arrival time t_j within the full temporal scan range, every delay time step lets the arrival time distribution shift in its center of gravity across the time t_j by a scanning time step Δt. For each scanned time step pump-probe events are summed up with a probability $P(t, t_j + i * \Delta t)$. Hence, the total number of pump-probe events with delay time t_j amounts to

$$n_j = \sum_{i=-2*m}^{2*m} N_i * P(t, t_j + i * \Delta t) \quad , \tag{6.3}$$

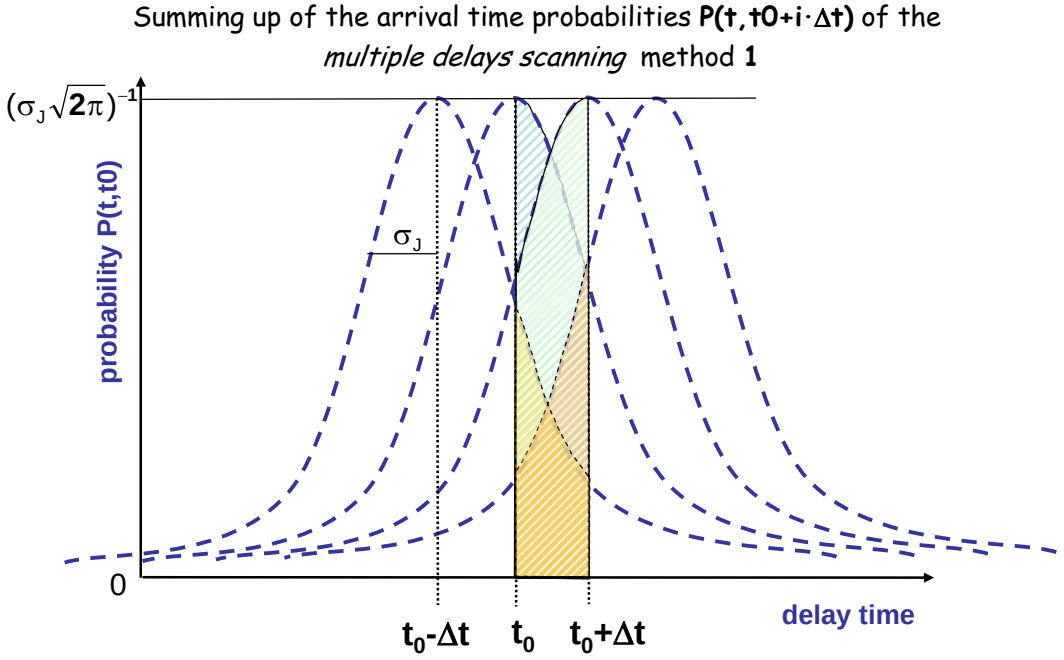

Figure 6.5: *This graphic visualizes the sum of probabilities of equation* (6.3)
The hatched area below the overlapping Gaussian peaks is a measure of the sum of the probabilities during a delay scan to perform a measurement within the time interval $[t_0, t_0 + \Delta t]$.

where N_i equals the number of pump-probe measurements per delay. Fig. 6.5 demonstrates this sum graphically. Hence, $N = \sum_{i=-2*m}^{2*m} N_i$ is the total number of measurements over the complete temporal scan range and $M = 2m + 1$ is the number of delay scans of time step Δt. For $\Delta t \to 0, n \to \infty$ eq. (6.3) transforms into the integral of eq.(6.1)

$$n(t) = N_t \cdot \int_{-\infty}^{\infty} P(\tau, t) d\tau = N_t \tag{6.4}$$

$N_t \doteq n$ is constant for all measurement times t. Thus, for a real pump-probe scan at FLASH with finite delay-time step-size Δt and n measurements per time interval $[t, t + \Delta t]$ can be approximated by the average number of pump-probe measurements per delay step

$$n = \frac{N}{M} \quad . \tag{6.5}$$

6.3 Measurement error of jitter inflicted pump-probe experiments

To investigate the influence of the temporal jitter, on a pump-probe experiment, it is necessary to estimate the amplitude measurement error for each delay time step. This measurement error decreases the signal to noise ratio of the measured pump-probe signal. Since measurement time at FLASH is expensive and very limited, it is very useful to quickly predict, how many measurements of a specific pump-probe experiment are necessary to reduce the measurement error resulting from stochastic noise sources below an acceptable limit. However, this decision depends on many parameters. In this section a formula is derived to approximate the measurement error exhibited by a specific pump-probe signal type. In the following section the derived formula is tested on a Monte-Carlo simulated pump-probe experiment.

Generally, a pump-probe measurement gives rise to the temporal dynamic of a physical quantity. Hence, the quantity to be measured can be represented by a measure variable $y(x_p, t)$. The time variable t equals the temporal delay of the probe pulse with respect to the pump pulse. Let $x_p = \{x_1, x_2, ..., x_m\}$ be the set of time independent parameters, which contribute to amplitude or form of the pump-probe signal, but do not change their value or amount of influence on the signal as the time delay t between the pump and probe pulse is varied.

Let σ_y^s and σ_t^s be the amplitude and temporal measurement error of a single pump-probe measurement. The superscript index "s" denotes a single measurement event. In the previous section the nature of the temporal jitter at FLASH was shown to have a normal distribution. Therefore one can identify the general temporal error σ_t^s with the standard deviation of the temporal jitter σ_J for now. The error variable σ_y^s denotes the stochastic amplitude error resulting from the noise of the detector or possible instabilities of the time independent parameters x_p like an externally applied magnetic or electric field or the gas pressure of a super-sonic gas jet for example. In any case the error variable σ_y^s shall be independent from the delay time t.

Several possible sources of error exist including: instrumentation error from the device detecting the signal amplitude y, systematic error originating from the modulation in the amplitudes of the pump and probe, and experimental error arising from fluctuations in the spatial overlap of the pump with the probe pulse in the target volume.

With these definitions the relative measurement error of one single pump-probe signal can be calculated from the Gaussian error propagation law.

$$\frac{\sigma_{y,t}^s}{y} = \sqrt{\left(\frac{\sigma_y^s}{y}\right)^2 + \left(\frac{y'(t)}{y} \cdot \sigma_J\right)^2} \tag{6.6}$$

This formula shows, that the effective signal amplitude error of a pump-probe measurement is influenced by the temporal jitter, which is treated as a statistical error of the time variable from which a pump-probe signal depends. A typical class of pump-probe signals can be described by the convolution function $g(t)$ of the temporal intensity distribution of each pulse. In the common case of Gaussian shaped pump and probe pulses, the pump-probe signal follows

$$\begin{aligned} y(t) \sim g(t) &= A_1 A_2 \int_{-\infty}^{\infty} \left(\exp\left[-\frac{1}{2}\left(\frac{\tau}{\sigma_1}\right)^2\right]\right)^{\alpha_1} \cdot \exp\left[-\frac{1}{2}\left(\frac{\tau + t}{\sigma_2}\right)^2\right]^{\alpha_2} d\tau \\ &= \frac{A_1 A_2 \cdot \exp\left(-\frac{1}{2} \cdot \frac{\alpha_1 \alpha_2}{\alpha_2 \sigma_1^2 + \alpha_1 \sigma_2^2} \cdot t^2\right) \sqrt{2\pi}}{\sqrt{\frac{\alpha_1}{\sigma_1^2} + \frac{\alpha_2}{\sigma_2^2}}} \end{aligned} \tag{6.7}$$

where α_1 and α_2 are general parameters that reflect the order of which a pump-probe process is dependent on the intensity of the pump- or the probe-pulse. This equation is similar to a Gaussian distribution of width

$$\sigma_{conv} = \sqrt{\frac{\alpha_2\sigma_1^2 + \alpha_1\sigma_2^2}{\alpha_1\alpha_2}} \quad . \tag{6.8}$$

In eq. (6.6) the relative first derivative $y'(t)/y(t)$ is needed to calculate the measurement error of $y(t)$. An elegant method to find the first derivative of (6.7) is to take first the natural logarithm and then the derivative on both sides. In doing so one obtains

$$\frac{y'(t)}{y(t)} = -\frac{\alpha_1\alpha_2}{\alpha_2\sigma_1^2 + \alpha_1\sigma_2^2} \cdot t \tag{6.9}$$

A Gaussian like function as in eq. (6.7) shows a maximum at time zero. However, for this case there exists no temporal influence on the amplitude error of y because $\frac{y'(0)}{y(0)} = 0$, thus this case can be neglected. The next best candidate would be a maximum of the first derivative itself, since this would provide an upper limit for the absolute instead of the relative error. (Compare to eq. (6.6) multiplied by y.) This maximum is found at the inflexion points of eq. (6.7), which are calculated to be

$$t_{\text{inflex}} = \pm\sqrt{\frac{\alpha_2\sigma_1^2 + \alpha_1\sigma_2^2}{\alpha_1\alpha_2}} = \pm\sigma_{conv} \tag{6.10}$$

At the maximum of the first derivative, i.e. at the inflexion point of a Gaussian peak a temporal jitter Δt leads to a stronger modulation of the amplitude of the signal than at the peak of the Gaussian. This principle is visualized in fig. 6.6.

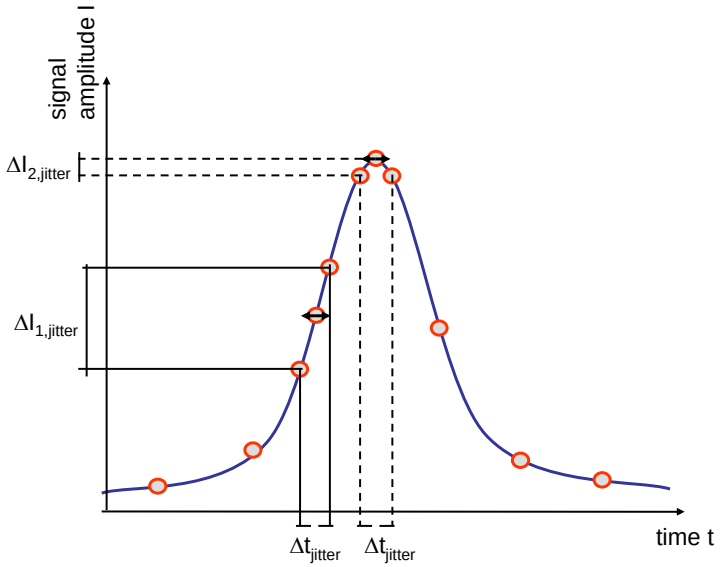

Figure 6.6: *Effect of a temporal jitter on a Gaussian type pump-probe signal*
The intensity fluctuation of a measured pump-probe signal due to a temporal jitter is larger, if the scanned time delay corresponds with the inflexion point of the signal dynamic, than if it correspond with the peak of the pump-probe signal.

Inserting (6.10) into (6.9) results in

$$\frac{y'(t_{\text{inflex}})}{y(t_{\text{inflex}})} = -\frac{\alpha_1\alpha_2\sqrt{\sigma_1^2 + \sigma_2^2}}{\alpha_2\sigma_1^2 + \alpha_1\sigma_2^2} \quad . \tag{6.11}$$

For the special case of $\alpha_1 = \alpha_2 = 1$ eq. (6.11) simplifies to

$$\left.\frac{y'(t_{\text{inflex}})}{y(t_{\text{inflex}})}\right|_{\alpha_1=\alpha_2=1} = -\frac{1}{\sigma_{conv}} \quad . \tag{6.12}$$

Inserted into (6.6) one obtains

$$\frac{\sigma^s_{y,t}}{y} = \sqrt{\left(\frac{\sigma^s_y}{y}\right)^2 + \left(\frac{\sigma_J}{\sigma_{conv}}\right)^2} \quad . \tag{6.13}$$

This formula is an upper limit of the expected error of a single pump-probe measurement at time t under the assumption, that the signal dynamic follows eq. (6.7).

The measurement error can be reduced, if the measurement of a certain delay time t is repeated n-times. Excluding systematic error sources, which can not be reduced by a higher measurement statistic, the error s_y of the mean quantity y, which is averaged over n measurements, is reduced by a factor $\sqrt{(n)}$ with respect to the single measurement error

$$s_y = \sigma^s_y / \sqrt{n} \quad . \tag{6.14}$$

Thus, in the case of n repeated measurements of $y(t)$ at time t equation (6.13) transforms into

$$\frac{s_{y,t}}{y} = \sqrt{\left(\frac{\sigma^s_y}{y \cdot \sqrt{n}}\right)^2 + \left(\frac{\sigma_J}{\sigma_{conv}\sqrt{n}}\right)^2} \quad . \tag{6.15}$$

This equation can be approximated further by distinguishing between two special cases.

In the first case the temporal jitter is small relative to the pump-probe signal width of eq. (6.8). Hence, the error is dominated by the time independent parameters, thus $s_{y,t}/y = \sigma^s_y/(y \cdot \sqrt{n})$. This case is neglected from further treatment, because the error is time independent.

In the second case the temporal jitter width σ_J is larger than the width of the convoluted Gaussian pump-probe signal and thus eq. (6.16) will be dominated by the jitter term. Therefore, the statistical relative error of $y(t)$ simplifies to

$$\frac{s_{y,t}}{y} \approx \frac{\sigma_J}{\sigma_{conv}\sqrt{n}} \quad . \tag{6.16}$$

This equation can be used to estimate the number of total measurements necessary to reduce the total pump-probe measurement error of one delay time t below an acceptable limit assuming a large temporal jitter for each of both pump-probe data acquisition methods.

For method **1** one finds (see section 6.2.1) with the definitions N for the total number of measurements over the complete temporal scan range and M for the number of delay scans of time step Δt the number of measurements n acquired within an interval $[t, t + \Delta t]$ around a delay time t according to equation (6.5) to be

$$n = \frac{N}{M} \quad . \tag{6.17}$$

Inserting (6.17) in equation (6.16) one obtains for method **1** the *multiple delay scanning* method of pump-probe data acquisition

$$\tilde{s_y} \doteq \frac{s_{y,t}}{y} \approx \frac{\sigma_J}{\sigma_{conv}\sqrt{N/M}} \qquad \Leftrightarrow \qquad \boxed{N \approx M \cdot \left(\frac{\sigma_J}{\sigma_{conv}\tilde{s_y}}\right)^2} \quad , \tag{6.18}$$

where $\tilde{s_y}$ is defined as the desired averaged relative error of a pump-probe signal $y(t)$, and $M = T/\Delta t$ is the number of time points of a pump-probe delay scan over the time range T with delay time steps Δt.

For the second pump-probe-data acquisition method **2** the temporal error σ_J originating from the relative pulse arrival time jitter in eq. (6.16) must be replaced by the measurement error of the arrival time measurement diagnostic TEO, i.e. $\sigma_J = \sigma_{TEO}$. The number of events per time n for this second method depends on the arrival time of each measurement. It varies between 0 and $\Delta t/(\sigma_J \sqrt{2\pi})$ (compare eq. (6.1)).

Sometimes the selected time step $\Delta t << \sigma_J$ is smaller than the probability distribution of the temporal jitter. For such a case a good estimate of the maximum number of pump-probe events per delay step is provided by the maximum $(\sigma_J \sqrt{2\pi})^{-1}$ of the Gaussian shaped probability function (eq. (6.1)) times the scanning time step interval Δt times the total number of pump-probe measurements N.

Hence, for the second method eq. (6.16) becomes

$$\tilde{s_y} \approx \frac{\sigma_{TEO}}{\sigma_{conv}\sqrt{\Delta t(\sigma_J\sqrt{2\pi})^{-1}\cdot N}} = 5\cdot\frac{\sigma_{TEO}}{\sigma_{conv}}\sqrt{\frac{\sigma_J}{\Delta t\cdot N}} \quad \Leftrightarrow \quad \boxed{N \approx 25\cdot\left(\frac{\sigma_{TEO}}{\sigma_{conv}}\right)^2\frac{\sigma_J}{\Delta t\tilde{s_y}}} \tag{6.19}$$

6.4 Monte-Carlo simulation of a jitter corrected pump-probe experiment

In the previous section a set of statistical equations and principles to evaluate a pump-probe experiment with the jitter afflicted femtosecond pump-and-probe pulses available at the FLASH facility have been introduced. These equations are derived from basic assumptions on the statistical distribution of the temporal relative arrival time jitter of the pump- and probe pulses. In this section these equations shall be tested on the basis of a simulation of a pump-probe experiment with pulse parameters, which match a typical situation at the FLASH pump-probe facility. Relevant for this simulation is, first of all the assumption, that pump- and probe pulses show Gaussian pulse shape.

For the optical NIR-pulse these assumption are verified with autocorrelation measurements, which are shown in the next section. For the XUV pulse a Gaussian single pulse shape is a simplification of the real situation. As explained in [YA07] the real XUV pulse might be a set of several very short fs-pulses, but the envelope of the XUV pulse is not longer than 40 fs. Thus, the pulse duration of 120 fs of the Fourier limited optical pulse is always much larger than the duration of a Fourier limited XUV pulse. One can conclude, that the Gaussian pulse shape approximation of the XUV pulse is adequately chosen for a simulation of a two-color pump-probe experiment at FLASH. The reason is that processes which are faster than the longer of the two pulses can not be resolved, since the minimal temporal resolution of a pump-probe experiment is determined by the duration of the convolution of both Gaussian pulses, i.e. the duration of the longer NIR pulse.

The pulse durations of the simulated Gaussian pulses are 120 fs FWHM for the NIR and 30 fs for the XUV pulse. To simplify the situation further, the pulse intensities are chosen to be similar and normalized to unity. The chosen simulated pump-probe signal shall be proportional to the product of both pulses and follows the model of eq. (6.7) with $\alpha_1 = \alpha_2 = 1$. The different wavelengths are not taken into account, since the model assumes that the pump-probe signal in first order shall only depend on the pulse intensities and not the electric fields. The simulation is of interest to determine the differences between the two data acquisition methods introduced in the previous section.

The simulation experiments are shown in fig. 6.7. On the left* side the results for the *multiple delays scanning* first method **1** and on the right side the results for the *single delay scanning* second method **2** are plotted. The upper row shows the simulated pump-probe data, while the lower row

*landscape oriented page

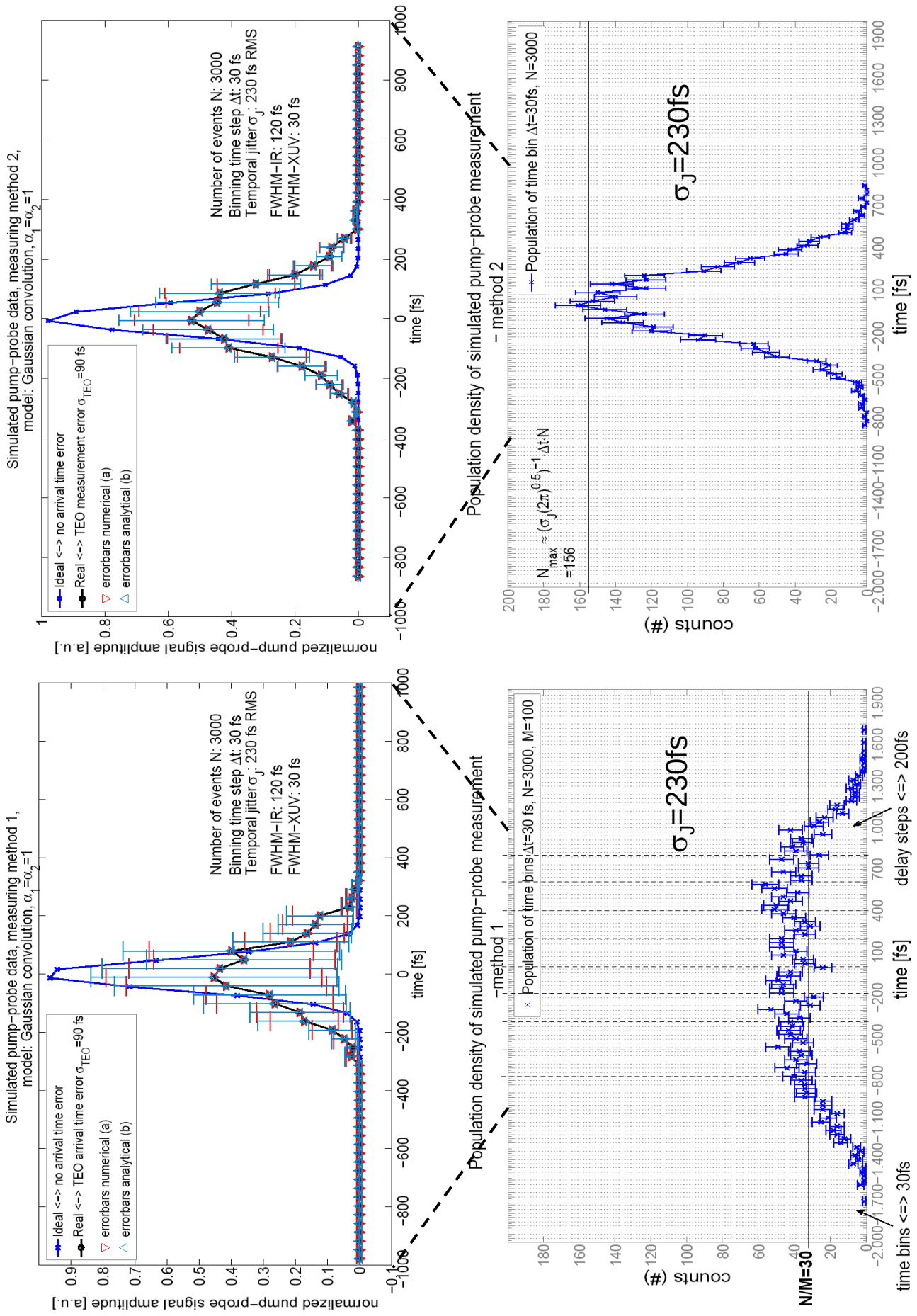

Figure 6.7: *Simulation of a fictious pump-probe experiment.* This four plots demonstrate the statistical differences between the *multiple delay scanning* method **1** on the left side and the *single delay scanning* method **2**. It turns out, that with method **1** a larger time range can be scanned, but compared with method **2** it is at the cost of a reduced statistics for the same number of measurements.

shows the population densities of pump-probe events per time step Δt. The pump-probe signals of the upper plots are showing data averaged in the following way. The simulated single shot amplitudes of a certain time interval $[t_i, t_i + \Delta t]$ also referred to as *time bin* are averaged and the resulting averaged signal amplitudes

$$y_i = \frac{\sum_{t_j \in [t_i, t_i + \Delta t]} y(t_j)}{\sum_{t_j \in [t_i, t_i + \Delta t]}} \tag{6.20}$$

are plotted versus their center time $t_{i,c} = (t_i + t_{i+1})/2$. The blue curves represent simulated, averaged pump-probe signals of temporal error free data, while the black curves are simulated assuming a certain temporal measurement error of the TEO diagnostic.

The temporal jitter distribution is chosen to be $\sigma_J = 230\,\text{fs}$ RMS, as like it is typically measured at FLASH but disregarding slow drifts or large timing jumps. Spatial jitter or additional amplitude errors of the pump-probe signal are set to zero. The simulated delay scan of method {1} is performed with a step size of 200 fs over 2 ps. The time range is chosen to match with the maximum time range of method {1}, which is defined by the temporal jitter width.

For both methods the same number of total events N=3000 are calculated and the time zero of perfect temporal overlap is set to 0 fs. The temporal resolution of the TEO diagnostic is assumed to be σ_{TEO}=90 fs, which corresponds with measurements, which will be shown in the following section. In the upper signal plots two different types of error bars are used. Error bars of type a) are calculated by eq. (6.16). In this way the simulated population of each time step is used to calculate the amplitude error for each time bin individually.

Error bars of type b) are calculated from eq. (6.18) (method **1**) or (6.19) (method **2**) respectively. The horizontal error would be constant and equal to the TEO measurement error σ_{TEO} and thus is not drawn. The error bars of the approximative equations are in good agreement with the individually calculated error bars for both methods. Furthermore, both types of error bars well estimate the actual error of each data point with respect to the temporal error free ideal pump-probe signal.

From the simulation two conclusions follow.

First, in the case of data acquisition method **2** (fig. 6.7, right plots) the error bars are smaller than in the case method **1** as expected, because the measurement density per time interval around the time of perfect temporal overlap is larger.

Second, it is shown, that the derived equations eq. (6.18) (method **1**) or (6.19) (method **2**) provide a good approximation for the statistical measurement error after binning and averaging of the single shot data. With these equations the signal amplitude error originating from the temporal jitter can be estimated from known parameters of the pump-probe scan **before** the experiment is performed. For the specifically chosen pump-probe signal model, these equations provide an estimation for the number of samples needed to decrease the maximal amplitude error below a desired threshold before the measurement actually is performed, which is important to control the quality of the acquired data. The chosen pump-probe signal model is also an approximation for other signal models, where the pump-probe signal amplitude is proportional to the product of the pump and probe pulse intensities.

6.5 Examples of jitter corrected pump-probe experiments

Once the TEO diagnostic was finished, many user groups were interested to use TEO for improving their temporal resolution. A few examples of these pump-probe experiments are herein presented. One was performed on gaseous targets and another one on a solid target.

6.5.1 Pump-probe experiment in gaseous phase

One of the first pump-probe experiments, in which the TEO diagnostic was utilized, was an experiment performed on a noble gas target. An amplified near infrared laser pulse was temporally synchronized with the XUV bunch train laser pulses from FLASH as introduced in chapter 3.1.1.2. Both pulses were focused almost collinearly into a thin gas target. The XUV pulse ionized the noble gas atoms and created unbound electrons. These electrons interacted with the electric field of the infrared pulse, which modulated the electron kinetic energy. Using a time-of-flight (ToF) spectrometer the kinetic energy distribution of the electrons was measured. The kinetic energy modulation from the dressing electric field of the NIR laser pulse led to the formation of sidebands of the main photo-emission line of a noble gas atom ground state. The analysis and detection of these sidebands was the main goal of the experiment [DR06].

In general sidebands in the frequency domain appear, if the amplitude or phase of a harmonic oscillation is modulated periodically. In the present case this simple model can not be applied directly, since electrons emitted from a noble gas atom are not real waves but particles [Kab]. A quantum-

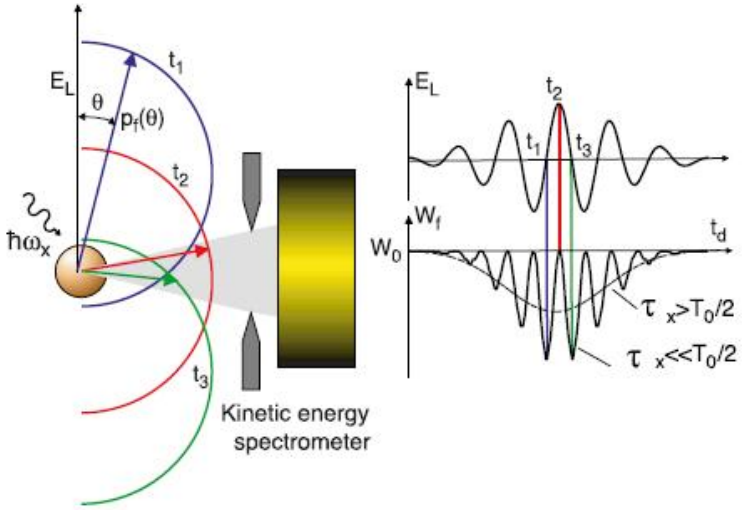

Figure 6.8: *Principle of the sideband creation*
The center of gravity motion of an ionized electron is modulated by the polarization of the IR laser ($\sim E_L$) forcing the electron to quiver. The instantaneous kinetic energy of the electron $\sim p_f(\theta)^2$ measured under an angle θ relative to the polarization of the NIR laser field and the electric field of the NIR laser pulse is shown in the right plot. Once the XUV pulse duration τ_x is longer than a period T_0 of the IR laser field, the oscillations are summed up leading to a discrete energy modulation of the interacting electrons. The oscillations do not average to zero since the oscillations of the kinetic energy W are following a $\sin^2(t)$-law as shown in formula (2) in [Dre01]. (Figure from [Dre01])

mechanical approach using the Strong Field approximation (SFA) provides a detailed model of the nature of the frequency modulation connected with energetic sidebands (see [Kit02, Scr06]). The NIR laser field modulates the quantum mechanical phase of the wave function of each electron, which is ionized during the presence of the NIR laser pulse. Sidebands appear whenever the pulse duration of the ionizing XUV pulse is larger than the period of the oscillating electro-magnetic field into which the electron is emitted [QMI05]. A schematic drawing of the full process is shown in fig. 6.8. In this case three quantum-mechanical electron wave functions having the same final kinetic energy but different ionization times, which correspond to different phases of the electric field of the NIR wave, can interfere constructively. Due to the interference the spectrum of the photo-electrons shows discrete lines at energies $W_{kin} = W_0 \pm N * \hbar\omega_{NIR}$ corresponding to an absorption or emission

of N optical photons by one photo-electron from the optical laser field. These sidebands can not appear, if free electrons are modulated by the optical pulse, since the total transported momentum from the laser field to the electron would sum up to zero. Sidebands can only appear from bound electrons, which are ionized during the presence of the NIR laser field. Classically, this restriction can be explained by the momentum conservation law, which prevents free electrons to absorb the angular momentum $\hbar$ of the NIR pulse photons. Thus, the absorption of an optical photon is only possible, if the ion absorbs the photon angular momentum, while the electron is in the field of the core potential. A detailed explanation is found in [QMI05].

The emitted photo-electrons are detected by a magnetic bottle type time-of-flight spectrometer, which is able to detect photo-electrons coming from a solid angle of 4π around the sample [RDA+07]. To achieve spatial overlap, the XUV beam and the NIR laser beam were focussed in a

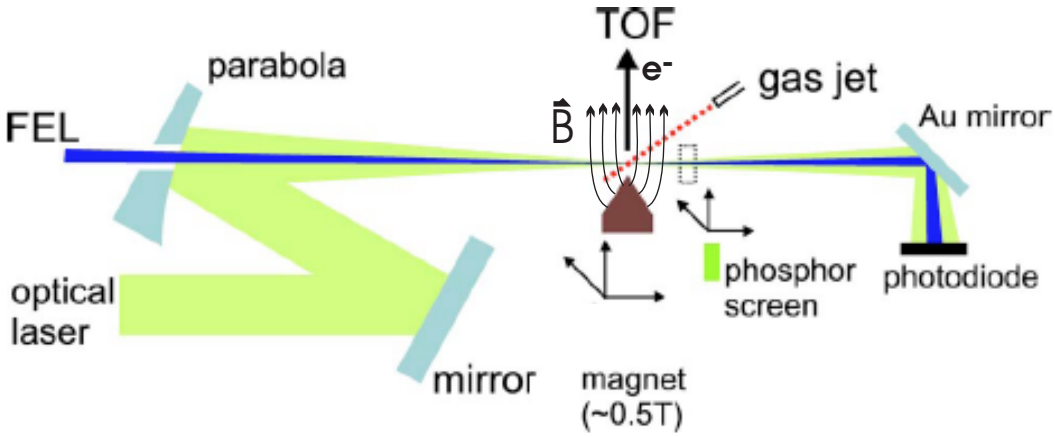

Figure 6.9: *Experimental setup of the sideband detection pump-probe experiment performed at FLASH.*
The emitted electrons are guided by a magnetic field, whose field lines form a magnetic bottle to a multi-channel plate detector, which is placed orthogonal to the direction of the XUV beam. For typical XUV photo energies in the order of 50 eV to 100 eV signals of slow electrons appear several tens of nanoseconds later than those of faster electrons, thus the kinetic energy is mapped into the time domain. Figure from [MCO+06].

collinear setup into the interaction area. An overview of the experimental setup and the geometric relationships are presented in fig. 6.9.

The experiment chamber is connected with the ultra-high vacuum of 10^{-9} mbar of the linear accelerator. Differential pumping isolates the experimental vacuum from the accelerator vacuum and makes it possible to work with a gaseous target (10^{-6}-10^{-7} mbar) utilizing a nozzle gas injection. The important properties of the experimental setup are collected in table 6.1.

In the case of a neutral Xenon atom the singly ionized atom Xe^- in ion notationhas an ionization energy of 12.13 eV [KW85] relative to the ground state. It can be ionized by the FLASH-XUV pulse of 90.5 eV wavelength. The remaining photon energy is converted into kinetic energy of the free electron. During the presence of the strong electro-magnetic, linear polarized NIR laser field, extra lines beside the main emission line are observed in the ToF-electron spectrum (see [RDM07], [MCO+06]). The transition amplitude and thus the number of energy shifted photo-electrons is proportional to the peak intensity of the optical laser pulse and the ionizing XUV pulse as derived in [QJ+03]. Thus, these sidebands can be used as an indicator of the degree of temporal overlap of both pulses since their amplitude is proportional to the degree of temporal (and spatial) overlap of both pulses and thus can be compared with the TEO arrival time measurement to benchmark the

Table 6.1: Parameters of the sideband experiment at the monochromator beamline PG2

Description	Value
Vacuum chamber pressure	10^{-8} mBar
Pressure of gas target for all species (He, Xe, Ne, Kr)	10^{-6} mBar
XUV wavelength	13.7 nm≅90.5 eV
XUV peak energy	$50\,\mu J$
XUV focus diameter	$100 \pm 10\,\mu m$
XUV intensity	10^{13} W/cm^2
IR wavelength	800 nm≅1.55 eV
IR pulse energy	$5\,\mu J$
IR focus diameter	$50 \pm 10\,\mu m$
IR peak intensity	$2*10^{12}$ W/cm^2

TEO diagnostic. For weak NIR pulses (intensity < 10^{11} W/cm^2) only one or two sidebands can appear. Since free electrons emitted by the photo effect are only created during the presence of the XUV pulse, the detected sideband amplitude is a measure of the temporal overlap of both pulses assuming a perfect spatial overlap of the two pulses at the focus [MCO+06].

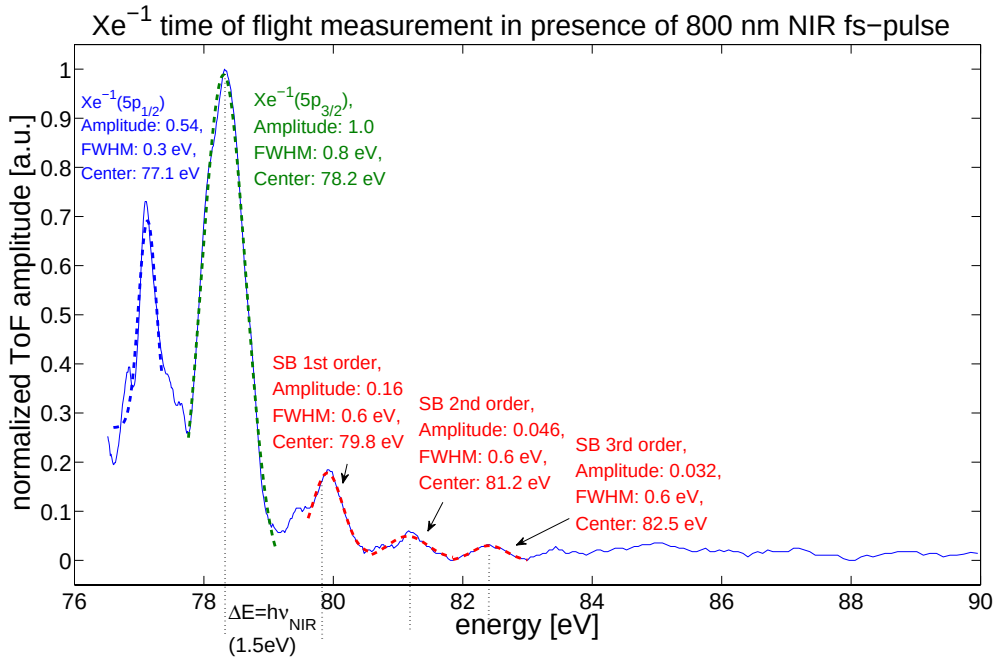

Figure 6.10: *Time of flight spectrum of Xenon with sidebands.*
This measured ToF spectrum of photo electrons emitted from Xenon atoms 5p-orbital shows sidebands up to 3rd order. The main photo emission line is split up into two spin states. The sidebands are separated by 1.5 eV corresponding to the quantum energy of the optical Ti:Sa pulse.

During this work several thousand ToF-spectra were acquired and evaluated. A typical example for a spectrum including sidebands is shown in fig. 6.10. The energy resolution of the ToF-spectrometer was 0.07 nm as measured on a synchrotron source [DR06] , which is slightly better than the FEL-XUV pulse spectral width of 0.12 nm (see fig. 6.11). Thus, the spectral width of the peaks of the sidebands as well as the width of the main photo-emission line are dominated by the width of the XUV spectral line.

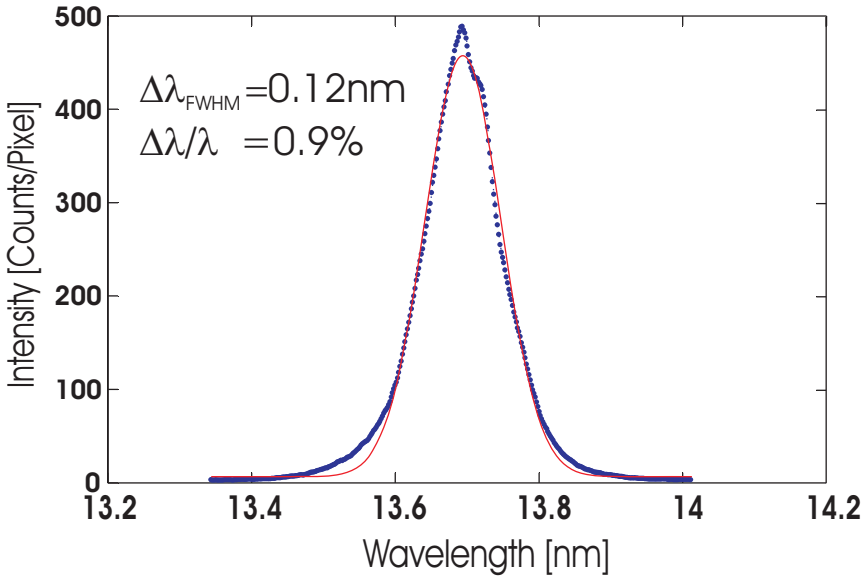

Figure 6.11: *Averaged SASE spectrum of the XUV pulse of FLASH*
SASE spectrum of the XUV pulse of FLASH during the measurement shown in fig. 6.12. The spectrum is averaged over 30 pulses (E_{SASE} = 90.5 eV ≈ 13.7 nm). The SASE line width of 0.12 nm corresponds to an energy bandwidth of 0.8 eV.

6.5.1.1 Jitter corrected sideband detection in Xenon

The sideband experiment was used to benchmark the TEO diagnostic for measure the relative arrival time of the XUV- and the NIR-pump-probe pulses. The results have been published in [ADR+09].

Once the delay stage position of temporal overlap (time zero) was found, about 2000 spectra were taken utilizing the *single delay scanning* data acquisition pump-probe measurement method. The spectra were concatenated to an array and plotted as a 2D false color matrix plot in two ways (fig. 6.12). First, the sidebands were plotted versus the sequential pulse number.

Secondly, the spectra were sorted according to the arrival time provided by TEO.

It is clearly visible that the temporal dynamics of the sideband were recovered by sorting the spectra with respect to the temporal data of the TEO experiment. In the TEO time sorted plot, two peaks become apparent at time zero, which are invisible in the pulse number sorted plot due to the reduced contrast resulting from the random arrival time jitter of FLASH.

The temporal dynamics of the sideband signal can be fit well by a Gaussian model, because the convolution of the optical NIR Gaussian pulse with the much shorter XUV pulse is a Gaussian. Theoretical models [YA07] predict a very short XUV pulse of 10-50 fs RMS pulse width. In general, the convolution of two Gaussian functions G_1 and G_2 is a Gaussian function G_{12} with a FWHM-width calculated from the following formula (6.21):

$$FWHM_{G12} = \sqrt{FWHM_{G1}{}^2 + FWHM_{G2}{}^2} \tag{6.21}$$

Inserting the values for the widths of the two pulses, one finds 125 fs± 10 fs for the expected sideband signal FWHM width.

Without the TEO timing information, the temporal evolution of the sideband signal can be observed using a classic pump-probe setup, where the position of a delay stage provides the information of the pulse delay time. To increase the signal to noise ratio of the small sideband signals, it is necessary to average spectra of several pump-probe events of the same time step Δt_{set} defined by the position of the delay stage. However, averaging under the influence of temporal jitter means,

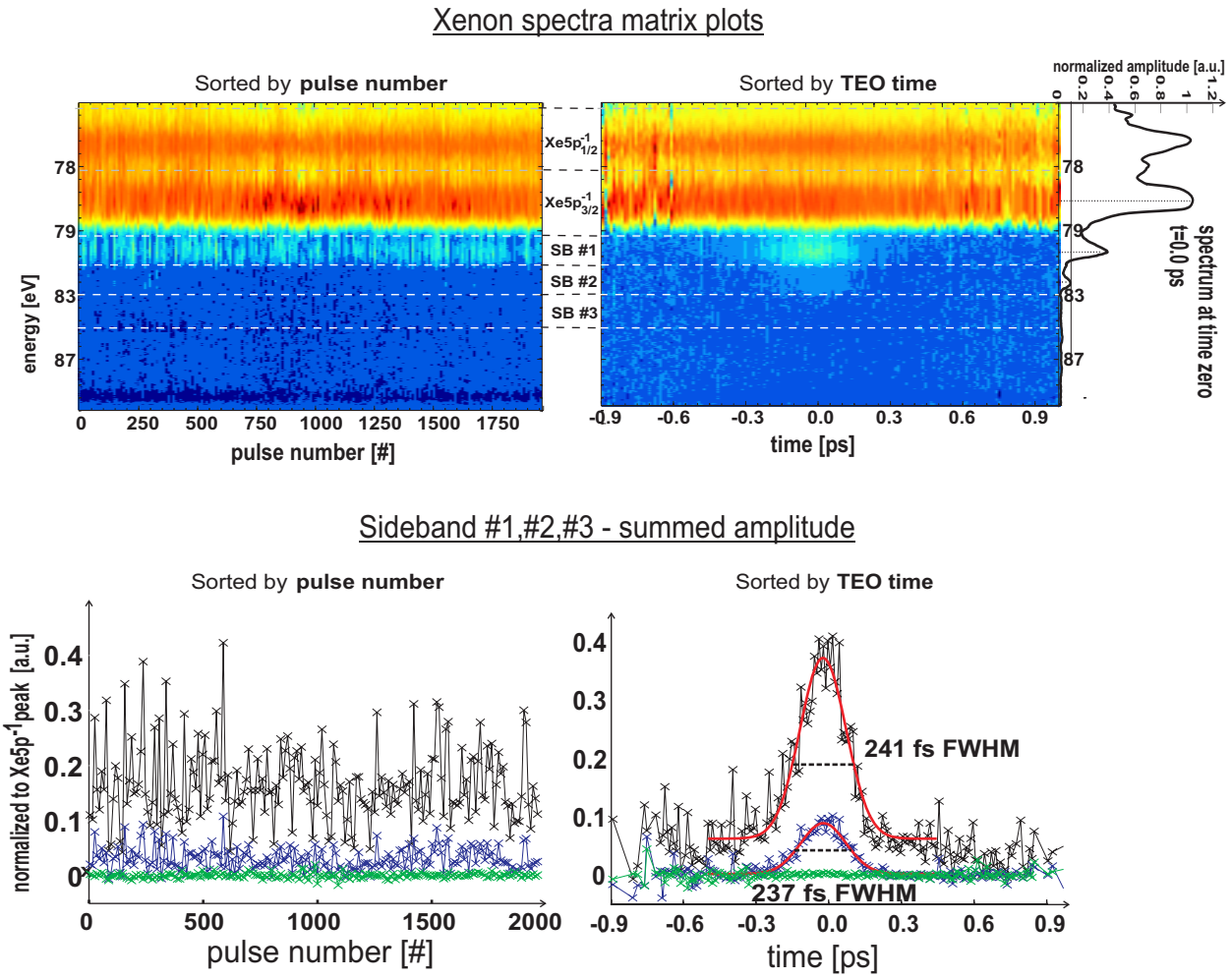

Figure 6.12: *Xe spectra matrix sorted by TEO times and pulse numbers.*
Left: sorted by pulse number, temporally unsorted. **Right**: TEO time sorted spectra. The amplitude of the spectrum is color encoded. The energetic positions of the sidebands are marked in the plot. The black blue and green curves of the lower plots respectively show the summed up sideband amplitudes as function of pulse number or delay time of the 1st, 2nd and 3rd order as marked by the horizontal dashed lines in the upper matrix plots. The attached measurement on the right side is a plot of the sorted spectrum at time zero and defines the color code.

that sideband amplitudes of delay times Δt_k different from Δt_{set} unwanted contribute to the sideband amplitude of the desired delay time Δt_{set}. Thus, the temporal resolution of the pump-probe measurement is reduced due to the spread of the temporal jitter (compare fig. 6.4). Mathematically, the signal of a jitter afflicted temporal signal $F_{pp}(t)$ measured by an averaging pump-probe scan, is described by the convolution of the ideal, jitter-free signal $F_{opt}(t)$ with the temporal jitter function $J(t)$, which can be modeled by a Gaussian for the normal distributed jitter of FLASH (compare with section 6.1).

$$F_{pp}(\tau) = \int F_{opt}(\tau) * J(t-\tau) \cdot dt \tag{6.22}$$

$$= \int F_{opt}(\tau) * \exp\left(-2\left(\frac{t-\tau}{2\sigma}\right)^2\right) \cdot dt \tag{6.23}$$

σ: RMS-radius of jitter distribution; τ: delay time between pump- and probe pulse
$F_{pp}(\tau)$: measured amplitude of the signal including the temporal jitter
$F_{opt}(\tau)$: ideal pump-probe signal

From this connection one can calculate the expected width of the scanned sideband signal provided that the distribution of the jitter is known. From (6.21) follows

$$FWHM_{PP} = \sqrt{FWHM_{opt}{}^2 + FWHM_{jitter}{}^2} \tag{6.24}$$

for the jitter afflicted width of the scanned sideband signal.

In the following paragraph the data of the sorted sideband experiment are used to derive a benchmark on how precise TEO can predict the XUV-NIR pulse arrival time at the experiment and to reproduce the temporal dynamic of the sideband creation process. To derive this number from the measured data, the reconstructed sideband signal has to be compared to the optimal sideband signal assuming zero temporal jitter. One can derive an error value for the relative photon pulse arrival time detected by TEO for the two pump-probe pulses at the focal region of interaction. Figure 6.13 shows a trace of the pump-probe signal measured by an averaging pump-probe scan as well as the TEO data based reconstructed sideband trace and the optimal trace.

Under the assumption that the TEO detection error has a normal distribution, the RMS pulse widths involved can be added quadratically according to equation (6.24):

$$\sigma_{Err} = \sqrt{\sigma_{TEO}{}^2 - \sigma_{optimal}{}^2} \tag{6.25}$$

$$= \sqrt{(102\,\text{fs})^2 - (51\,\text{fs})^2} = 88\,\text{fs RMS} \tag{6.26}$$

This assumption is justified, since the detection error of TEO manly results from statistical arrival time fluctuations induced by the NIR pulse transporting glass fiber as is discussed later on. From this sideband measurement a detection error of the TEO diagnostic of ca. 90 fs RMS was retrieved.

As shown in fig. 6.13, TEO increased the temporal resolution of this pump-probe experiment by a factor of three to four. The amount of increase of the temporal resolution by TEO depends on the jitter strength during the pump-probe scan, which usually takes 10-15 minutes. The temporal jitter consists of shot-to-shot fluctuations of $\sigma = 150\,fs - 200\,fs$, which are superimposed by slow long term temporal drifts. Typically the slowly drifting fluctuations let the temporal overlap of the NIR laser pulse and the XUV pulse drift around the original zero position of optimal temporal overlap found at the beginning of the measurement by 1-2 ps (compare figure 6.2). The reasons for the drifts are long term instabilities at the electron injector or thermally induced cable length drifts of

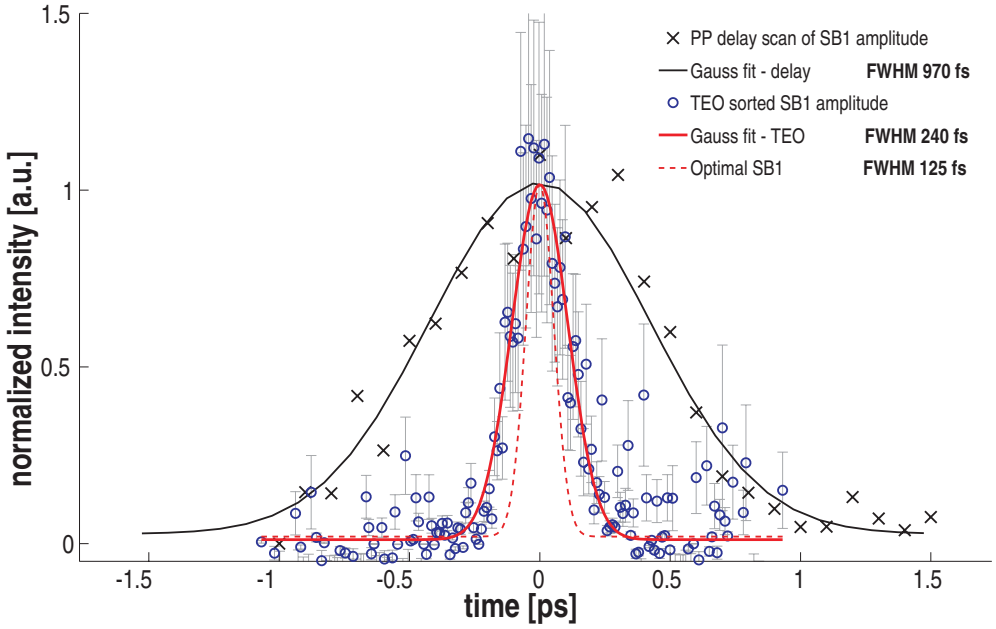

Figure 6.13: *Determining the temporal resolution of TEO.*
Comparison of the temporal sideband traces of a measured jitter-unsorted pump-probe scan (black curve), of the ideal jitter-free sideband trace calculated from the convolution of the NIR laser pulse and the XUV pulse (dashed curve) and of the sideband trace retrieved with the TEO based temporal sorting procedure (solid red curve). The error bars are calculated according to equation (6.19).

the RF cables, which transport the reference frequencies of FLASH and to which the NIR oscillator is temporally locked. The TEO diagnostic corrects the temporal pump-probe delay time for this long term drifts as well as for the shot-to-shot fluctuations.

6.5.1.2 Error sources of the TEO benchmarking experiment.

The main source, which deteriorate the temporal resolution of the TEO diagnostic, is the 150 m long fiber link, which transports the fs-pulse from the experimental area into the linear accelerator area. As has been discussed in section 4.1 temperature variations lead to pulse transit time variations on an hours to minutes time scale. Acoustic vibrations lead to fast micro-phonic excitations in the fiber, which lead to transit time variations on a ms time scale. A fiber length stabilization system has been developed and introduced in section 4.1.7.4. An example of the measured fiber length fluctuations is provided in figure 6.14. The measured fluctuations show statistically distributed deviations up to 400 $\frac{fs}{s}$.

Another error source are the pointing instabilities of the XUV beam on the used monochromator beamline PG2 (see fig. 3.11). These instabilities have been measured and are presented in fig. 6.15.

These pointing instabilities can lead to jumps of almost one XUV focus diameter (180 μm) from shot to shot. The error is statistically distributed and fluctuates with a frequency of a few 10 Hz ([Wel07]). The consequence is an additional error source of the sideband amplitude, which is statistically distributed and inflicts signal drops of the sorted sideband. This error can be reduced by averaging up sufficiently enough individual sideband amplitude measurements of the same delay time.

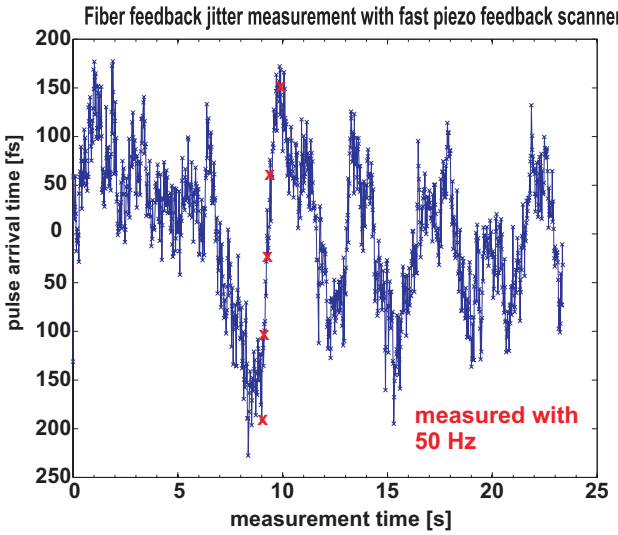

Figure 6.14: *Measured TEO fiber link transit time modulations during 25 s period.*
Fast fluctuations (50 fs RMS) are superimposed by slow drifts of up to 400 fs/s. These fluctuations strongly reduce the temporal precision of the TEO arrival time detection, since they modify the optical path length and thus the travel time of the NIR laser pulse through the fiber. The red crosses mark single pump-probe events at 5 Hz repetition rate.

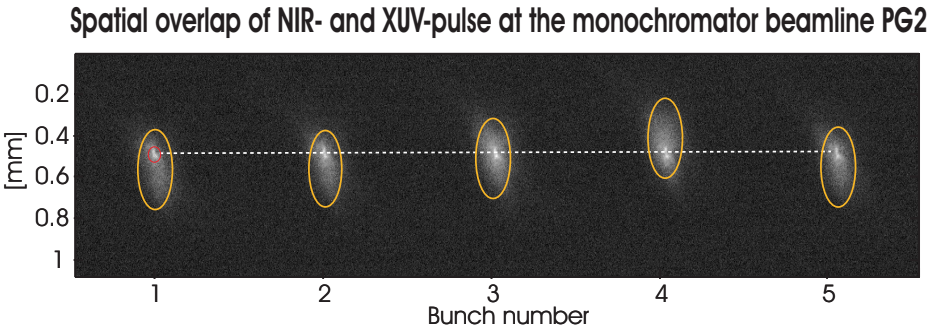

Figure 6.15: *Images of the focal spots of the XUV and NIR laser focus from the focal region measuring pointing instabilities.*
The images show fluctuations of up to 180 μm of the XUV pulse (comparing 2 with 4). While the IR laser pulse, marked in the first image by a red circle, stays stable on the same position (the dashed line), the XUV spot (large ellipse) jumps preferably up and down and changes its pulse width from shot-to-shot.

6.5.1.3 XUV pulse broadening from the monochromator grating

Inside the monochromator beamline PG2 it is possible to stretch the XUV pulse in time to a pulse duration much longer than the temporal jitter width of FLASH or the NIR pulse duration. In this section an application of the sideband experiment discussed before in section 6.5.1.1 is presented, from which the amount of temporal pulse stretching by the monochromator beamline can be measured.

The monochromator stretches the pulse in the following way. Inside the monochromator beamline a dispersive grating is installed, which can be used in combination with a slit to monochromatize the beam [WM07]. In zero order diffraction the grating works like a mirror without influencing the XUV pulse time structure. In first order diffraction the grating disperses the XUV beam and introduces a tilted wavefront, which results in a spatial chirp. The focusing optic at the end of the beamline bends the various spatial parts of the dispersed pulse on the focal axis and images in this way different transversal parts of the pulse to different longitudinal positions along the focal axis (fig. 6.16).

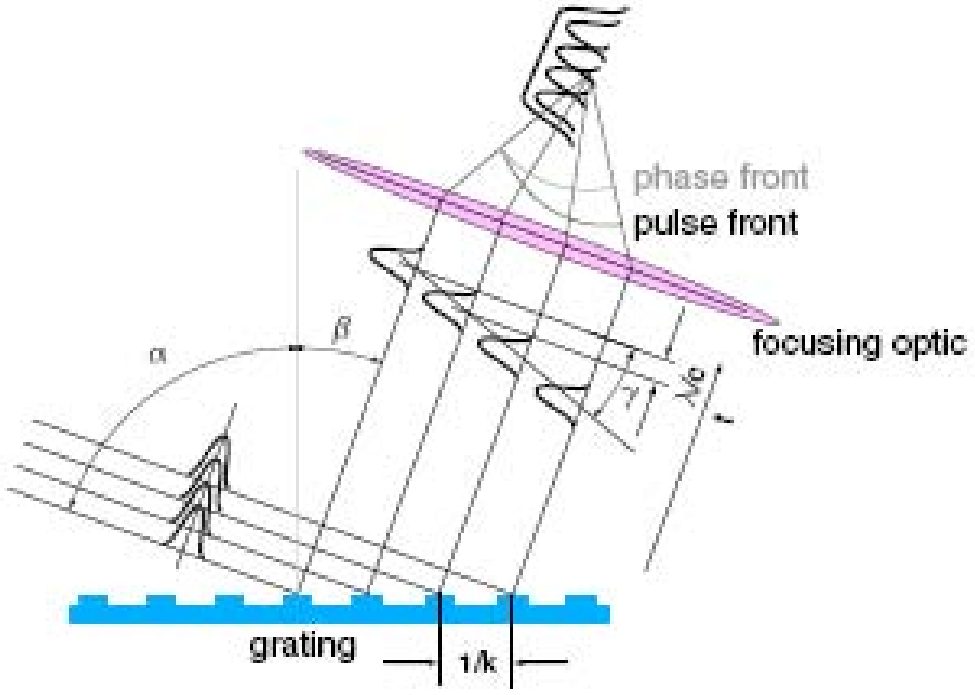

Figure 6.16: *Geometrical overview of the pulse broadening of the XUV pulse due to the spatial chirp of the monochromator grating.*
The tilted wavefront of the XUV pulse due to the monochromator grating leads to a temporal pulse broadening in the XUV focal area of the PG2 beamline. (Figure from [Wel07]).

Thus, the dispersive system effectively broadens the pulse in the focal region. The more grating grooves are illuminated, the stronger the wavefront tilt and the larger the pulse broadening. A relevant number in this context is the so called c_{ff}-value, which is defined by the ratio of the in- and outgoing angle of the XUV beam relative to the surface orthogonal of the grating. This value is proportional to the number of illuminated grooves. For the installed 200 grooves/mm grating a pulse broadening of the XUV pulse of up to 2 picoseconds is predicted [MW06].

To verify this estimation the same pump-probe sideband experiment as before on a Xenon gas target in section 6.5.1.1 is performed. This time however using the monochromator grating in first order of diffraction to temporally stretch the XUV pulse 10 to 50 times compared to the compressed

pulse. Because the XUV pulse in this case is longer than the NIR pulse, the temporal sideband dynamic is dominated by the the broadened XUV pulse. Thus, with the presented (see section 6.5.1.1) sideband based timing measurement procedure, it is possible to measure the pulse width of the broadened XUV pulse. This holds true as long as the XUV pulse is much broader than the probing NIR pulse and the temporal resolution of TEO. The pump-probe measurement is performed with different c_{ff}-values, where for each value the corresponding temporal sideband dynamics and durations are retrieved. The sideband peak durations are measured by a Gaussian fit of the measured sideband peak trace. Despite of the temporally stretched XUV pulse, it is useful to use the TEO diagnostic to correct for the temporal jitter of FLASH, because for the shorter stretched XUV pulse duration in the range of 400 fs to 600 fs seconds, the jitter would still distort the retrieved sideband widths. In fig. 6.17 the duration of the reconstructed sideband peak is plotted versus the set c_{ff}-value of the monochromator grating.

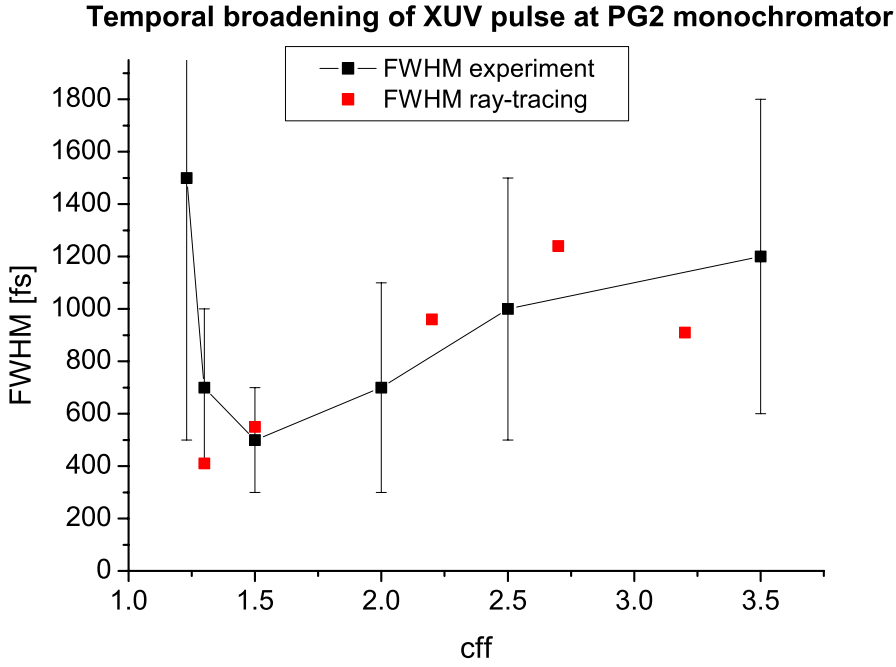

Figure 6.17: *Measured and simulated geometrical XUV pulse width elongation due to the monochromator grating of the PG-beamline*
The plot shows the retrieved temporal XUV pulse duration from the sideband amplitude sorting procedure according to the TEO timing data as function of c_{ff}-values. The large vertical error bars are mainly a result of strong pointing instabilities of the XUV beam and a resulting spatial jitter. The red dots are simulated data from a ray tracing analysis [Gue07].

This measurement suffers from the same kind of uncertainties as the discussed experiment before on Xenon with compressed XUV pulse. These are the pointing fluctuations of FLASH and the TEO temporal detection error.

Additionally the pump-probe measurements has been performed using the pump-probe scanning method **2** and thus keeping the delay stage fixed and let the temporal jitter perform the delay time variations. Thus the temporal scanning window is limited by the temporal jitter distribution width (compare fig. 6.3 b)). For all cff-values larger than 1.5 this width is smaller than the broadened XUV pulse and the retrieved temporal sideband traces are cut off at their edges.

All of these error sources contribute to the estimated error bars in the plot 6.17. A clear trend to broader XUV pulses for larger c_{ff}-values is visible. The simulated and measured pulse durations agree for c_{ff}-values larger than 1.5. For c_{ff}-values smaller than 1.5 the XUV pulse becomes broader

again, which is explained by a bug in the monochromator control system steering the grating in a wrong way for c_{ff}-values smaller than 1.5.

6.5.2 Multiple shot reflectivity measurement on GaAs surface

An example for a pump-probe experiment on a solid matter target, at which TEO was used as supporting timing tool, is presented now. In this experiment the surface of the semi-conductor GaAs is pumped by the FLASH XUV pulse. The probe pulse is a 800 nm or a frequency doubled 400 nm pulse of 120 fs FWHM. Both optical pulses originate from the optical pump-probe laser system located in the experimental hall of FLASH (see chapter 3.4). The observed property, which is the subject of this experiment, is the temporal development of the optical reflectivity of the surface under influence of the intense FLASH XUV laser pulse. Similar experiments with intense all optical femtosecond pump and probe pulses have been performed before [STBC$^+$98, STL00]. These experiments analyzed, how transient states of matter are generated in Silicone after a short laser pulse ablation and under which conditions a reflectivity change is observed. Energy fluences between 40 and 500 mJ/cm^2 around the melting fluence of 170 mJ/cm^2 for 800 nm [STBC$^+$98] and a pulse duration of 120 fs FWHM have been investigated. They suggest, that a modulation of the optical reflectivity is the result of the generation of a dense electron-hole plasma by the strong optical fs-laser pulse. So far these experiments have never been tried using an XUV source, because presently only FLASH can provide high enough XUV intensities suitable for this purpose.

The presented experiment has been performed with GaAs at the plane grating monochromator beamline PG2 in zero order as described in the following.

A clean, undoped GaAs(100) surface was prepared at a base pressure of 10^{-9} mbar by flashing off an arsenic cap layer from samples grown by molecular beam epitaxy. The preparation regarding surface quality and stoichiometry was checked by core-level photoelectron spectroscopy. As depicted schematically in fig. 6.18, XUV radiation pulses of 39.5±0.5 eV with a duration of sub 50 fs impinge on the GaAs(100) crystal at an angle of incidence of 41.5° with the electric-field vector in the surface plane. The FEL operated at a bunch train repetition rate of 5 Hz consisting with 30 bunches per bunch train and 2 µs separation (500 kHz). The XUV pulse energies reached up to 16 μJ, as measured by a gas-monitor detector [Ric03] and independently by an multi-channel based intensity monitor within the PG2 beamline. With a spot size of 400±20 μm × 280±20 μm ([DR06]) the fluence stays below the optical damage threshold of the GaAs surface (50 mJ/cm^2 for a pulse length of 30 fs at 800 nm, [C$^+$01]). The induced change of optical reflectivity was probed at an angle of incidence of 53° by delayed optical pulses at 800 nm or optionally 400 nm with a duration of 120 fs to 150 fs (FWHM) delivered from an optical parametric amplifier system with a repetition rate of 1 MHz electronically synchronized to the electron accelerator [GAB$^+$08]. The optical pulses of either 400 nm or 800 nm are reflected from the surface of a GaAs-waver and can be delayed in time relative to the XUV pulse.

To measure a reflectivity change, the optical pulse energy of the reflected pulse with and without surface modulation due to the XUV pulse is measured by a photo diode. The optical laser intensity fluctuates on a few percent scale. To get over this drawback, the optical laser is split into two pulses. One pulse is detected after being reflected by the GaAs surface, the other pulse is directly detected. The reflectivity signal normalized by the direct intensity signal is free of fluctuations of the laser source.

The 400 nm pulses operate at 1 MHz with twice the repetition rate of the FEL, such that for each pumped measurement a reference measurement of the surface reflectivity is obtained. A detailed setup of the measurement principle is shown in fig. 6.18. From the definitions made in fig. 6.18 the following formula describing the signal ΔR, which measures the reflectivity change at the GaAs

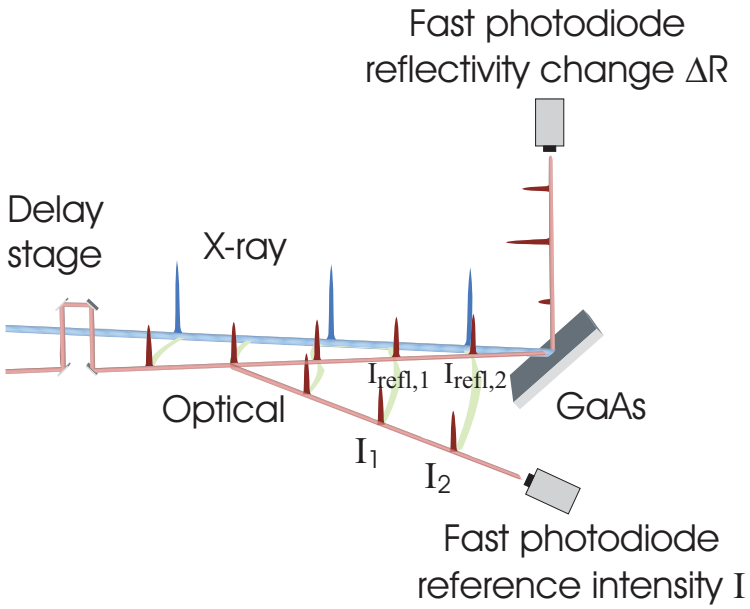

Figure 6.18: *Transient X-ray-induced optical reflectivity (ΔR/R) measurement at beamline PG2: schematic overview*
XUV FEL pulses (39.5 eV, <50 fs,<16 μJ) impinge onto a crystalline GaAs(100) surface and generate photo-excited carriers. The transient changes of the dielectric function are probed by visible laser pulses (800 nm or 400 nm, 120 fs, <10 nJ) reflected from the GaAs surface at 53° as a function of their temporal delay relative to the FEL radiation pulse (I_{refl}). As a reference measurement a part of the incident optical pulse is split and detected separately without passing the wave ($I_{1,2}$) (figure adapted from [GAB+08]).

surface, is derived:

$$\Delta R := \frac{\frac{I_{refl,1}}{I_1} - \frac{I_{refl,2}}{I_2}}{\frac{I_{refl,1}}{I_1}} \quad , \tag{6.27}$$

where $I_{refl,1/2}$ represents the reflected intensity with and without pump and $I_{1,2}$ represents the corresponding direct optical pulse intensity. For each measured reflectivity signal a pumped reflected intensity measurement with XUV pulse and without are taken in alternative order. Thus, any fluctuation slower than 2 µs, which could modify the signal, as for example drifts of the optical laser or mechanical instabilities of the transport line are filtered out of the measured signal.

For each delay time setting of the optical delay line 10 to 100 measurements were performed and summed up to optimize the signal to noise ratio. The time zero is defined as the delay time setting, where perfect temporal overlap between the NIR and the XUV pulse on the GaAs surface layer is established. The results of two temporal delay time scans, which cross time zero is presented in fig. 6.19. The intense X-ray excitation leads to an ultra-fast drop in optical reflectivity, which

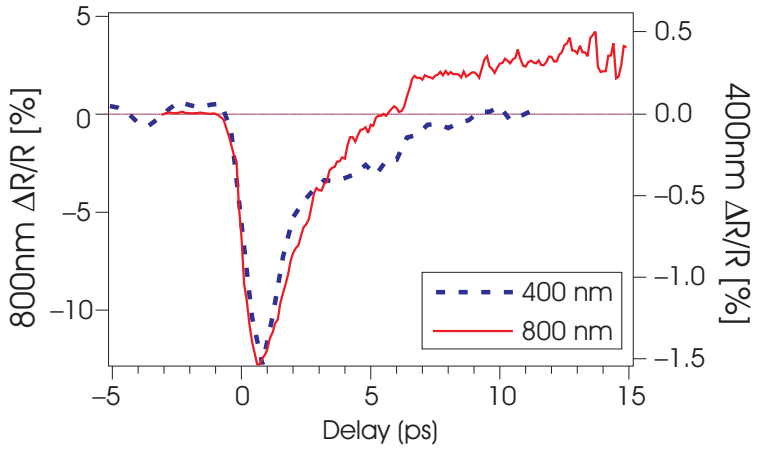

Figure 6.19: *Transient X-ray-induced optical reflectivity change on GaAs measured with a temporal delay time scan with 800 nm and 400 nm.*
Reflectivity drop after X-ray pump. The rapid drop of the relative reflectivity ΔR/R observed for 400 nm and 800 nm probe wavelengths is followed by a few 100 ps long recovery [GAB+08] (figure from [GAB+08]).

recovers within a few picoseconds. Depending on the X-ray fluence and probe wavelength, ΔR/R may even overshoot to positive values before the system approaches equilibrium on the timescale of more than 100 ps [GAB+08].

The few ten femtosecond timescale of the ΔR/R transients close to the reflectivity drop is of key relevance for cross-correlation measurements of X-ray/XUV and optical radiation fs-pulses. Figure 6.20 shows the X-ray pulse induced drop in optical reflectivity on am expanded timescale. The figure shows two scans of the transient reflectivity with and without *a posteriori* timing data correction by TEO timing. A clear increase in the steepness of the reflectivity change is observed. The interpolated curves are fit using the error function. The reason for this specific function type as fit model is, that the error function is formed from a convolution between a Gaussian peak function and a step function. The Gaussian represents the optical pulse of 120 fs pulse duration, the step function is an approximation for the physical process behind the reflectivity change. The model assumes, that the process ruling the reflectivity drop occurs as long as the XUV pulse is interacting with the semi-conductor surface, thus within a much faster time interval than the optical pulse duration and only limited by the duration of the XUV pulse. Since fig. 6.20 shows, that the width

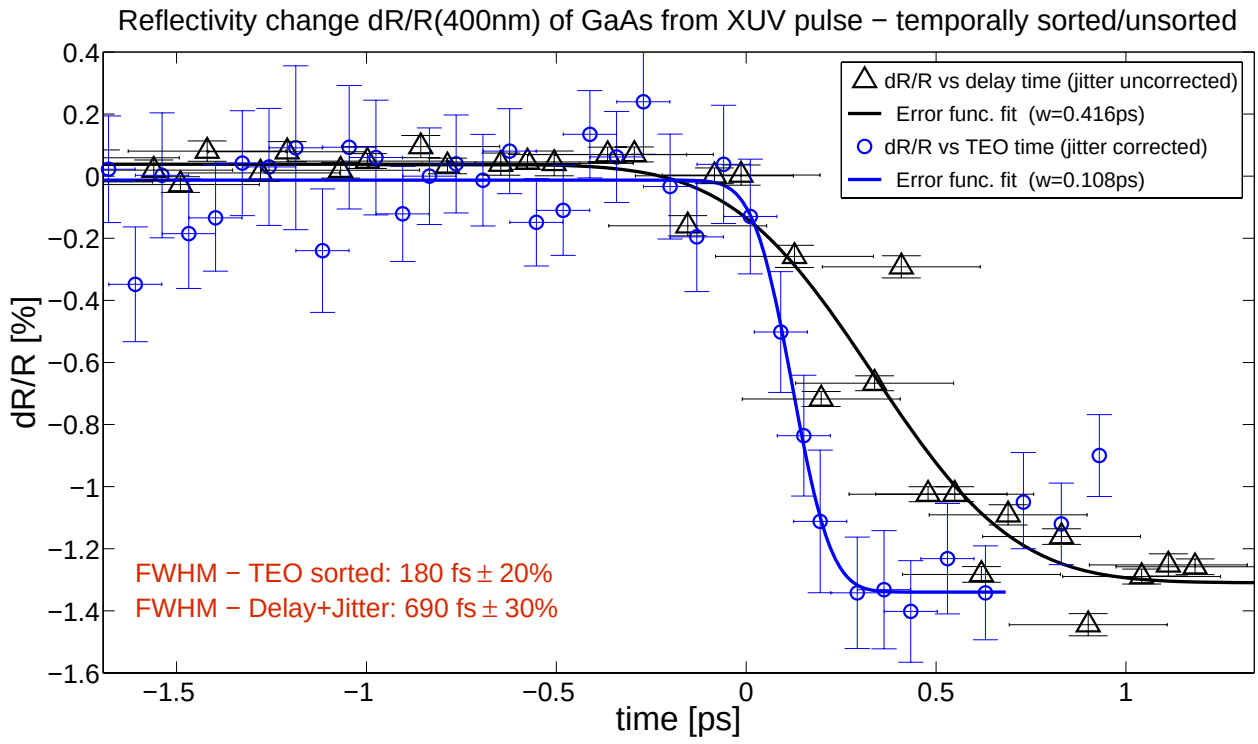

Figure 6.20: *TEO sorted/not sorted temporal measurement of the reflectivity drop with 400 nm.* The rapid drop of the relative reflectivity ΔR/R observed for 400 nm probe wavelength is analyzed using the TEO detector to correct for the temporal jitter (blue circles) and performing an error function fit including the only the fast reflectivity drop and not the slow rise. For comparison reasons a different reflectivity scan without TEO correction is plotted as well (black triangles) together with an error function fit. The horizontal error bars of the TEO sorted data measure the temporal resolution of TEO as determined in the benchmark experiment of section 6.5.1.1. In the delay stage time scan the horizontal bars are defined by the distribution width of the temporal jitter of FLASH.

of the Gaussian is getting much smaller, if the temporal jitter in the data is corrected, this model assumption is justified.

The uncorrected width of the fit error function, i.e. the width of the participating Gaussian is 690 fs, which matches with the temporal jitter of 640 fs FWHM as measured with TEO. In the temporally corrected case the width of the fit error function corresponds to a Gaussian FWHM width of 180 fs, which is slightly broader, than the width of the optical pulse. The reason is, that the temporal resolution of TEO is limited. Using the quadratic addition rule of normal distributed errors, a number for the resolution of TEO during the discussed measurement can be calculated. Let the variable $FWHMt_f = 180\,fs$ be defined as the width found from the error function fit of the corrected data, the variable Δt_{TEO} be defined as the temporal detection error of TEO measured in terms of RMS and $\Delta t_{NIR} = 120\,fs$ be the temporal duration of the optical 800 nm pulse, then one finds, that the temporal detection error of TEO is calculated by

$$\Delta t_{TEO} = \sqrt{\left(\Delta t_f\right)^2 - (\Delta t_{NIR})^2}/2.35 \quad . \tag{6.28}$$

Inserting the numbers the TEO detection error calculates to Δt_{TEO}=57 fs RMS, which is better than the value of 87 fs RMS found by the benchmark experiment in section 6.5.1.1. The reason for the difference is, that the transporting fiber applied a smaller temporal jitter during the reflectivity experiment than during the sideband experiment presented in section 6.5.1.1, because the reflectivity experiment was performed at night, while the sideband experiment was performed at day leading to a noisier fiber environment than at night.

The most important conclusion of this measurement is, that the reflectivity drop is an ultra-fast process only limited by the optical pulse duration of the near-infrared probe pulse of 120 fs FWHM width. This conclusion is an indication for the following physical explanation of the process. Due to inner core shell excitation of Gallium atoms by the XUV pulse and cascading relaxation of electrons from higher shells by Auger decays and autoionization a large amount of electron-hole pairs ($1.5{\cdot}10^2 1\ cm^2$) are created almost instantaneously by the XUV pulse, which populate the conduction and valence band. The induced electron-hole plasma in the conduction band modulates the dielectric function of GaAs and leads to the observed reflectivity drop. The intra shell electronic relaxation processes happen on a fs fs time scale [GAB+08], why the reflectivity drop with respect to the 120 fs NIR pulse is an instantaneous process, which justifies the convoluted Gaussian-Stepfunction fit model of the temporally jitter corrected signal.

As a conclusion one can summarize, that due to the support of the TEO timing detector, an interesting physical process could have been analyzed in time. Without the TEO detector the temporal jitter of FLASH would have smeared out the temporal dynamics of the process, such that a physical interpretation of the physical processes triggering the reflectivity change regarding fast inner shell electronic processes as suggested by [GAB+08] could not have been justified.

Chapter 7

Summary and Outlook

The TEO timing diagnostic has advanced from experimental state to a standard diagnostic at FLASH. From the beginning of the first pump-probe experiments in 2006 until this thesis was finished in 2009, every optical-XUV pump-probe experimental group at FLASH asked for the support of the TEO diagnostic, which underlines the importance of this diagnostic tool. Beside the here presented pump-probe experiments there exists at least three more experiments, in which TEO provided the time axis and reduces the temporal jitter hidden in the pump-probe data [JRS+09],[MCW+08] and [K+09]. However, it was decided not to show these experiments here, because they would exceed the scope of this thesis.

As a multiple purpose diagnostic tool, the spatial decoding principle is planned to be used in other relativistic electron bunch based light sources and applications either as an electron bunch density diagnostic for example for a laser accelerated electron bunch source [DS09] or as a timing tool for example at the MAXlab-short pulse facility [WTEL09] and in the single pass FEL project FERMI@Elettra [FER].

In a future upgrade the bunch arrival time of the FLASH linear accelerator will be stabilized due to a fast feedback loop, which controls the amplitude and phase of the first accelerating structure ACC1. The feedback loop will reduce the temporal jitter of FLASH down to 40-50 fs RMS [Loe09]. This will provide the needed temporal stability for the additional high-harmonics seeded XUV-FEL beamline s-FLASH, which will allow to perform future two-color pump-probe experiments at FLASH with outstanding 30 fs temporal resolution. The reason is, that no significant temporal jitter will remain between the seeded XUV-FEL pulse and the XUV seed generating NIR fs-pulse, which can thus be used in a two-color pump-probe experiment together with the seeded XUV-FEL pulse [KAB+08]. However, the system, which stabilizes the linear accelerator is very complex, that is why TEO should stay in the linear accelerator during the commissioning of this synchronization and temporal stabilization system.

Because the present temporal resolution of TEO is limited by the electro-optical crystal response of GaP and faster materials are currently not available, it is yet not predictable, if TEO will be able to increase the temporal resolution of two-color pump-probe experiments with the SASE pulse once the linear accelerator and the optical laser system is fully stabilized. But since a glass fiber network will be established in the linear accelerator to assist the timing system, which distributes 200 fs short pulses at 1550 nm throughout the accelerator, it is possible to use these pulses frequency doubled and to perform the electro-optical cross-correlation as a redundant timing system. Nevertheless, it should be pointed out, that TEO highly assisted many pump-probe experiments leading to several publications and served its purpose well.

Appendix A

A.1 Principal axis transformation of the impermeability tensor

Calculation found in [Ste07]. Assuming perpendicular incidence to the XY-plane and an angle α of the electrical field with respect to the X-axis, the components of the electric vector $\boldsymbol{E}_{\mathbf{THz}}$ of the THz radiation in the base system of the crystal lattice are

$$\boldsymbol{E}_{\mathbf{THz}} = E_{\mathrm{THz}} \begin{pmatrix} -\frac{1}{\sqrt{2}}\cos\alpha \\ \frac{1}{\sqrt{2}}\cos\alpha \\ \sin\alpha \end{pmatrix} = E_{\mathrm{THz},0} e^{-i\omega_{\mathrm{THz}}t} \begin{pmatrix} -\frac{1}{\sqrt{2}}\cos\alpha \\ \frac{1}{\sqrt{2}}\cos\alpha \\ \sin\alpha \end{pmatrix} \tag{A.1}$$

with the amplitude $E_{\mathrm{THz},0}$ and the frequency ω_{THz} of the THz wave. Inserting this into equation (2.53) yields

$$\boldsymbol{\eta}(\boldsymbol{E}_{\mathrm{THz}}) = \frac{1}{n_0^2} \begin{pmatrix} 1 & 0 & 0 \\ 0 & 1 & 0 \\ 0 & 0 & 1 \end{pmatrix} + r_{41} E_{\mathrm{THz}} \begin{pmatrix} 0 & \sin\alpha & \cos\alpha/\sqrt{2} \\ \sin\alpha & 0 & -\cos\alpha/\sqrt{2} \\ \cos\alpha/\sqrt{2} & -\cos\alpha/\sqrt{2} & 0 \end{pmatrix} \tag{A.2}$$

To find the main refractive indices and the principal axes, the eigenvalues and eigenvectors of the tensor $\boldsymbol{\eta}$ have to be calculated. The eigenvalues can be evaluated to:

$$\begin{aligned} \lambda_{1,2} &= \frac{1}{n_0^2} - \frac{r_{41} E_{\mathrm{THz}}}{2}\left(\sin\alpha \pm \sqrt{1+3\cos^2\alpha}\right) \\ \lambda_3 &= \frac{1}{n_0^2} + r_{41} E_{\mathrm{THz}} \sin\alpha \end{aligned} \tag{A.3}$$

The normalized eigenvectors are:

$$\begin{aligned} \boldsymbol{U}_1 &= \tfrac{1}{2}\sqrt{1+\tfrac{\sin\alpha}{\sqrt{1+3\cos^2\alpha}}} \begin{pmatrix} -1 \\ 1 \\ \frac{2\sqrt{2}\cos\alpha}{\sqrt{1+3\cos^2\alpha}+\sin\alpha} \end{pmatrix} \\ \boldsymbol{U}_2 &= \tfrac{1}{2}\sqrt{1+\tfrac{\sin\alpha}{\sqrt{1+3\cos^2\alpha}}} \begin{pmatrix} 1 \\ -1 \\ \frac{2\sqrt{2}\cos\alpha}{\sqrt{1+3\cos^2\alpha}-\sin\alpha} \end{pmatrix} \\ \boldsymbol{U}_3 &= \tfrac{1}{\sqrt{2}} \begin{pmatrix} -1 \\ -1 \\ 0 \end{pmatrix} \end{aligned}$$

Care has to be taken in the evaluation of the vector $\boldsymbol{U}_2$ at the limit of $\alpha \to \pi/2$ as the normalization factor vanishes and the third component tends to infinity. The result is

$$\boldsymbol{U}_2\left(\frac{\pi}{2}\right) = \begin{pmatrix} 0 \\ 0 \\ 1 \end{pmatrix} \tag{A.4}$$

So for $\alpha = \pi/2$, the vectors $\boldsymbol{U}_1, \boldsymbol{U}_2$ point in the directions of X and Y, respectively.

A.2 Analysis of the influence of a tilted object plane on the TEO signal measured by an upright detector

The question is, how strong is the influence of the mismatching imaging of the detected TEO signal and how is the timing axis in the case of a tilted or not-tilted image plane. As before the answer is found by analyzing the imaging properties of the ZEMAX model of the telescope for both cases. The imaging analysis tool of ZEMAX provides a practical ray tracing based image analysis, as it calculates the beam path of a lot amount of beam rays emitted from the object plane up to the image plane. The corresponding images of a test object are shown in fig. A.2.

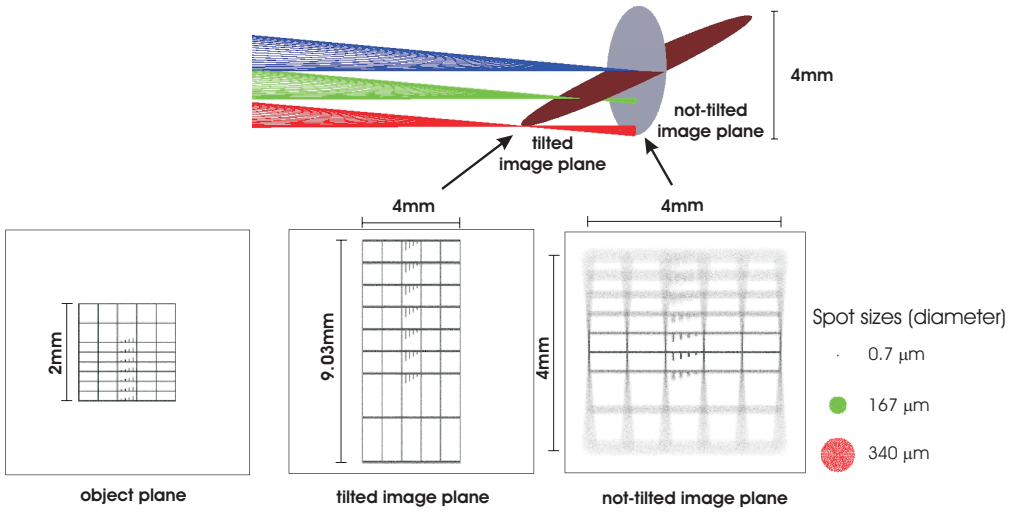

Figure A.1: *Imaging of a titled plane by a telescope.*
The dimensions are calculated by ZEMAX. Inside the tilted image plane the vertical axis is elongated by ≈ a factor 2 relative to the tilted object plane. The not-tilted image plane shows clear signs of haziness, the stronger the further away from the optical axis.

This simulation shows qualitatively, that the signal will be smeared out and become broader the further it is located away from the beam profile center. However, the simulation still does not provide a quantitative analysis for the strength of this effect. To find a value for the expected broadening, one must convolute the TEO signal with the point-spread function (PSF) of each transversal position along the y-axis of the not-tilted image plane according eqn. (A.5). ZEMAX is able to calculate the PSF numerically. The convolution is performed afterwards by MATLAB, while the TEO signal is approximated by a Gaussian of a width of 100µm on the crystal surface, which corresponds to a temporal duration of 230 fs. These values are taken from a typically detected TEO signal close to the center of the beam.

$$I(y_i') = \int (O(y) \cdot PSF_{y'}(y_i' - M_y \cdot y)dy) \tag{A.5}$$

The Point-spread function (PSF) is evaluated in the magnified coordinate system of the image plane. The coordinate system of the object plane y and the image plane y' is connected by the magnification M through $y' = M_y \cdot y$.

The convolution applied with various locations of the signal source along the vertical crystal axis y is shown in figure A.2. The ideal situation is presented in fig. A.2 a). The TEO signal is localized in the center of the object plane. The imaging is optimal and the CCD objective scales the TEO signal down by a small factor of 0.9. fig. A.2 b) and c) plot the simulated signal broadening for a signal movement away from the center of the image by 1.3 ps and 2.5 ps. The effective detected signal broadening would be 1.1 and 1.5 respectively.

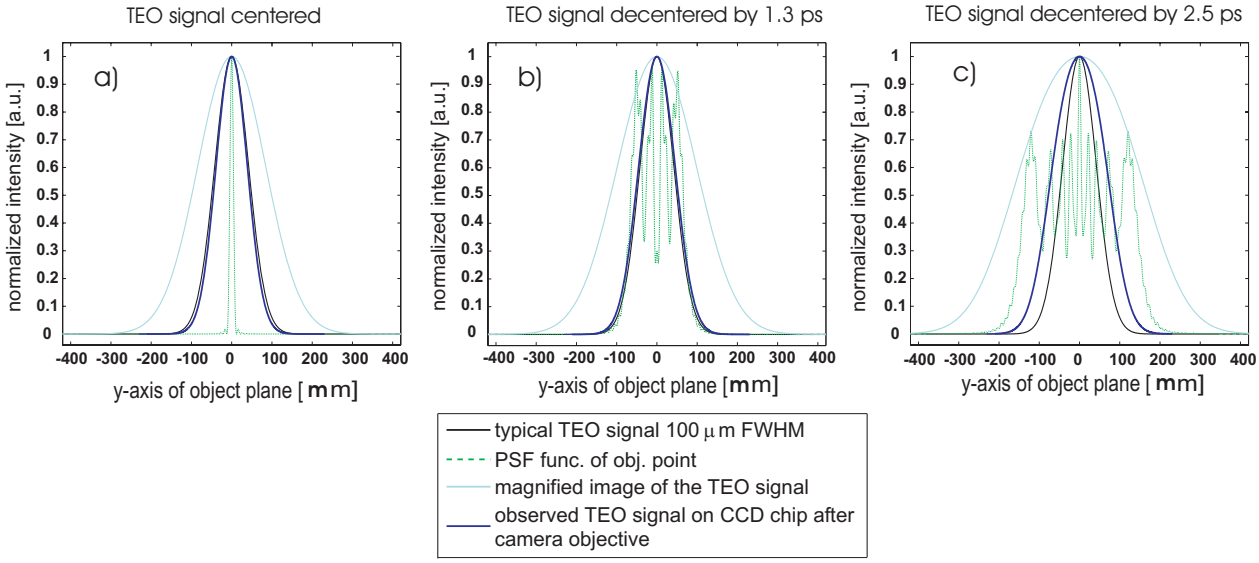

Figure A.2: *Point-spread function (PSF) of a tilted imaging system.*
The plot series shows the convolution of the numerically calculated point-spread-function for object points, which are shifted vertically along the tilted crystal plane assuming a TEO signal like spot, which is approximated by a Gaussian of a typically detected width of 100 µm. The blurring of the non-tilted image plane becomes the stronger the further away from the center. The signal broadening at 2.5 ps shifted to the center is a factor 1.5 .

The possible time range of the TEO signal is limited by the transversal width of the incoming laser beam profile, which can be variably set between 1.5 mm to 2.5 mm corresponding to a time window of 7 ps to 10 ps. From the calculation shown in fig. A.2 follows, that the broadening can not be worse than a factor of 2. Within the typical temporal jitter range of the FEL electron bunch of maximally 1-2 ps and the corresponding signal movement the broadening is even less than a factor of 1.2. Because it would be of high effort to change the geometrical proportions of the setup to be able to rotate the CCD camera, we accepted the small drawback of a not-tilted plane and the resulting small signal broadening in the edges of the time window.

Appendix B

B.1 Calibration of the SLM

The pattern of fig. 4.17 written into the SLM mathematically is generated by the following formula:

$$\Phi(x) = \sum_{i=0}^{n} \frac{b_i}{N^i}(x - x_0)^i + 0.5 \quad , \tag{B.1}$$

where variable x is the pixel number and N is the total number of shaper matrix pixel. The Taylor coefficient b_i is dimensionless, since without calibration the physical meaning of each coefficient b_i is unknown *a priori*. The directive (B.1) creates a polynomial with origin at $[x_0, 0.5]$, which physically corresponds to the frequency-phase pair $[\omega_0, \pi]$. From symmetry reasons follow that for most efficient usage of the SLM, the central pixel x_0 must be set to $N/2$ and physically the pulse spectrum should be aligned symmetrically to the SLM, such that the carrier frequency ω_0 spatially overlaps with the central pixel.

The sum is of similar structure as the Taylor series, to which the spectral phase function $\Phi(\omega)$ of a fs-pulse can be expanded (equation(4.16)). The coefficient normalization by N^i in the directive (eqn. (B.1)) makes the dispersion coefficients b_i comparable and reduces the absolute values of the coefficients. Under the assumption that the pulse spectrum is mapped linearly on the SLM matrix, a comparison of each polynomial order with the corresponding Taylor expanded dispersion order is possible:

$$\frac{b_i}{N^i}(x - x_0)^i = \frac{1}{n!}\phi_n(\omega - \omega_0)^i \tag{B.2}$$

With the dispersion relation

$$x = b_{px} \cdot \omega \tag{B.3}$$

between the pixels and frequencies, one obtains the conversion equation (4.17):

$$\phi_i = \frac{b_i}{N^i} \cdot i! \cdot (b_{px})^i \cdot 10^{3i}[\mathrm{fs}^i] \qquad (b_{px} \text{ in } [\mathrm{px/THz}]) \quad . \tag{B.4}$$

B.2 Limits of the SLM

It is of importance to know, how much spectral dispersion a spatial light modulator is able to compensate in total. In this section a formula for the maximum dispersion, which a single-pass SLM can compensate for, is derived. To calculate this limit, the dispersion maxima for each order of dispersion is calculated independently, on the same time keeping the other dispersion orders at zero. Maximum dispersion is reached, once a phase jump of 2π between two neighboring pixel in the

applied phase pattern occurs. Mathematically, each order of dispersion is described by a polynomial term of order i as shown in eqn. B.1. The difference between two pixel at a certain pixel x is approximatively calculated from the first derivative of each polynomial term

$$\frac{\partial}{\partial x}\frac{b_{i,max}}{N^i}(x-x_0)^i = 1 \tag{B.5}$$

$$i\cdot\frac{b_{i,max}}{N^i}(x-x_0)^{i-1} = 1 \quad . \tag{B.6}$$

From the monotonicity of each polynomial term follows, that the maximum phase change between two pixel is expected at the most outer pixel of the matrix pattern, for example between the pixel positions $x_{max} = N/2 + x_0$ and $x_{max} - 1$. Together with eqn. (B.6) follows the sought-after equation for the maximum amount of dispersion of a certain order i

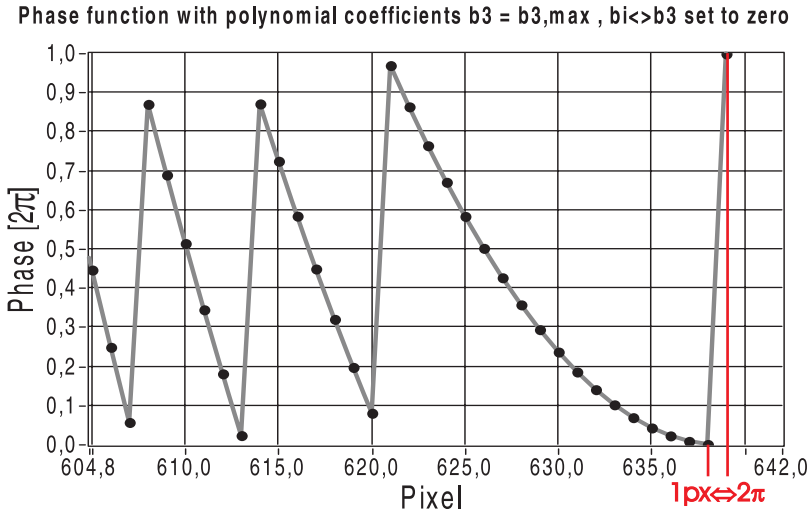

Figure B.1: *Numerically found phase pattern defining the maximal polynomial coefficient* b_3. The plot shows a phase pattern evaluated at the most outer pixel of the shaper. The phase pattern was calculated by the polynomial formula of (B.1) with b_3=$b_{3,max}$=860.3 and all other coefficients set to zero. Between the very last two pixel from 639 to 640 a 2π-jump is observed, which numerically defines the maximum possible coefficient $b_{3,max}$ of third order dispersion. The calculated value for $b_{3,max}$ from equation (B.9) is 853.3, which is in good agreement with the numerically found value.

$$i\cdot\frac{b_{i,max}}{N^i}(x-x_0)^{i-1} = 1 \tag{B.7}$$

$$i\cdot\frac{b_{i,max}}{2^{i-1}N^i}N^{i-1} = \frac{ib_{i,max}}{2^{i-1}N} = 1 \quad , \tag{B.8}$$

and thus

$$b_{i,max} = \frac{N\cdot 2^{i-1}}{i} \quad . \tag{B.9}$$

If a SLM is used in double-pass transmission setup, one must use 1/2 instead of 1 for the right side of equation (B.7). The reason is, that physically the 2π-ambiguity is already reached, if a phase difference of π between two pixel is written into the SLM matrix. Thus, for the double-pass SLM setup used in this work, the proper maximum coefficient is calculated by

$$b_{i,max} = b_{i,max,dbl} = \frac{N\cdot 2^{i-2}}{i} \quad . \tag{B.10}$$

This formula has been cross-checked numerically for exemplary dispersion orders by entering an arbitrary number for a b_i coefficient into the SLM and increase it until at the last two most outer pixel of the shaper matrix a 2π-jump, respectively π-jump appeared (see fig. B.1). The numerically and from eqn. B.9 analytically found maximum polynomial coefficients agree well. With the conversion equation (4.17) for each order of dispersion the maximum value $\phi_{i,max}$, which the double-pass SLM can apply separately, is obtained:

$$\phi_{i,max} = \phi_{i,max,dbl} = 2\pi \frac{N \cdot 2^{i-2} \cdot i! \cdot b_{px}^{i}}{i \cdot N^{i}} \cdot 10^{3i}[\mathrm{fs}^{\mathrm{i}}] \tag{B.11}$$

$$= \pi \left(\frac{2}{N}\right)^{i-1} (i-1)!\, b_{px}^{i} \cdot 10^{3i}[\mathrm{fs}^{\mathrm{i}}] \tag{B.12}$$

B.3 Principle of a of a 4f-stretcher

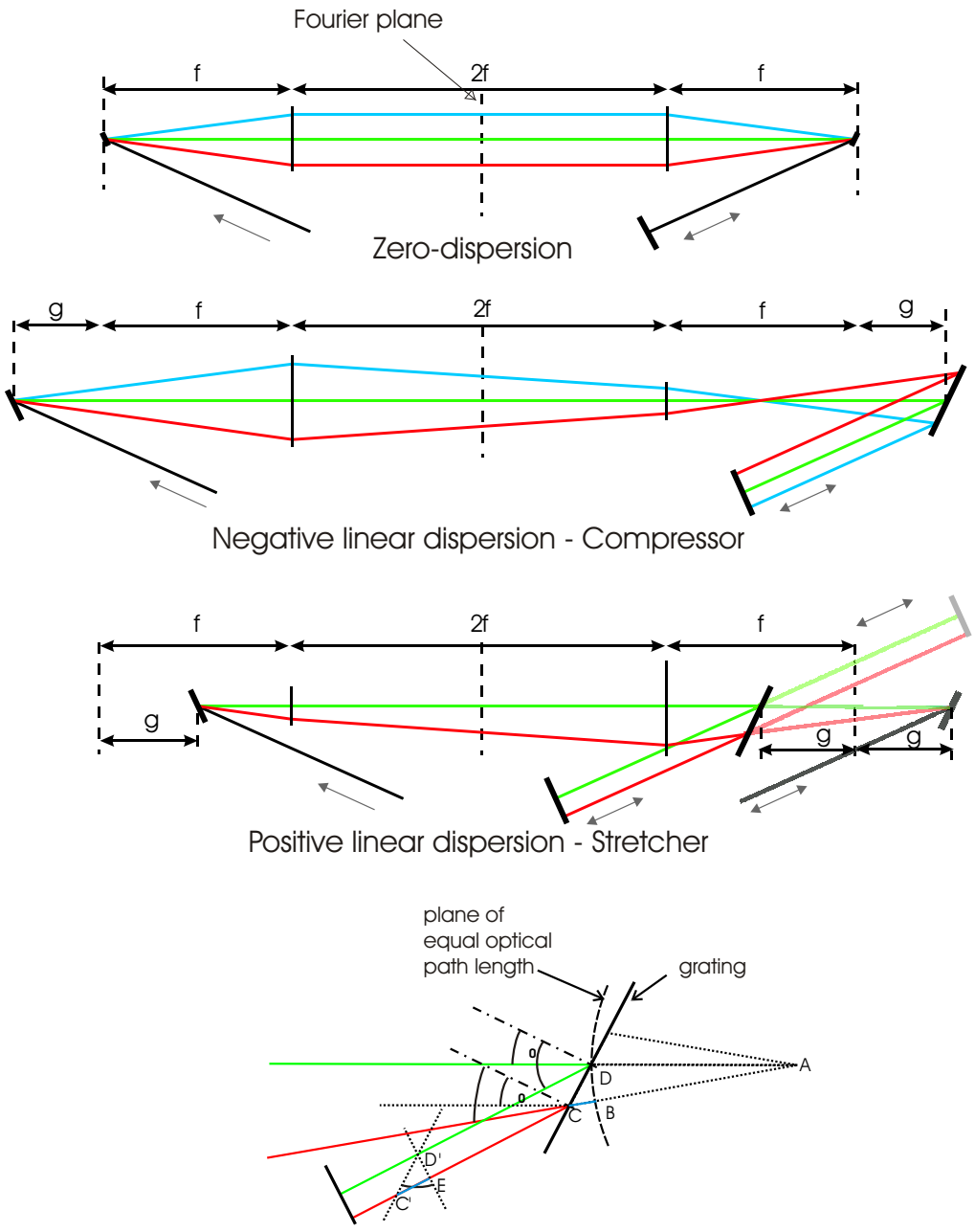

Figure B.2: *Principle of a 4f-stretcher*

A Zero-dispersion stretcher setup does not affect a fs-pulse. If the focussing optics are shifted by a variable distance g, the stretcher applies a positive chirp ⇔ normal dispersion (intermediate focus present) or negative chirp ⇔ anomalous dispersion (no intermediate focus). The bottom drawing shows the geometrical relations on the second grating in the normal dispersion case. According to the two-grating compressor, the optical path length difference $\Delta L(\omega) = \overline{C'E} - \overline{BC}$ introduces a wavelength dependent retardation of the individual frequencies, which results in a chirped pulse. [Figure adapted from [Str03]]

Bibliography

[A+02] Ayvazyan, V. et al.: A new powerful source for coherent VUV radiation: Demonstration of exponential growth and saturation at the TTF free-electron laser. In: *The European Physical Journal D - Atomic, Molecular, Optical and Plasma Physics* 20 (2002), Nr. 1. http://hal.in2p3.fr/in2p3-00011763/en/

[A+06] Ayvazyan, V. et al.: First operation of a free-electron laser generating GW power radiation at 32 nm wavelength. In: *Euro. Phys. J. D* 37 (2006), 297-303. http://dx.doi.org/10.1140/epjd/e2005-00308-1. – DOI 10.1140/epjd/e2005–00308–1

[A+07] Ackermann, W. et al.: Operation of a free-electron laser from the extreme ultraviolet to the water window. In: *Nature Photonics* 1 (2007), Juni, 336-342. http://dx.doi.org/10.1038/nphoton.2007.76. – DOI 10.1038/nphoton.2007.76

[AA+04] Abrahamyan, K. ; Ackermann, W. et al.: Characterization of the electron source at the photo injector test facility at DESY Zeuthen. In: *Nuclear Instruments and Methods in Physics Research Section A: Accelerators, Spectrometers, Detectors and Associated Equipment* 528 (2004), Nr. 1-2, 360 - 365. http://dx.doi.org/DOI:10.1016/j.nima.2004.04.068. – DOI DOI: 10.1016/j.nima.2004.04.068. – ISSN 0168–9002. – Proceedings of the 25th International Free Electron Laser Conference, and the 10th FEL Users Workshop

[ABEK02] Akre, R. ; Bentson, L. ; Emma, P. ; Krejcik, P.: Bunch length measurements using a transverse RF deflecting structure in the SLAC linac. In: *Proceedings to Eighth European Particle Accelerator Conference* (2002)

[ADR+09] Azima, A. ; Dusterer, S. ; Radcliffe, P. ; Redlin, H. ; Stojanovic, N. ; Li, W. ; Schlarb, H. ; Feldhaus, J. ; Cubaynes, D. ; Meyer, M. ; Dardis, J. ; Hayden, P. ; Hough, P. ; Richardson, V. ; Kennedy, E. T. ; Costello, J. T.: Time-resolved pump-probe experiments beyond the jitter limitations at FLASH. In: *Applied Physics Letters* 94 (2009), Nr. 14, 144102. http://dx.doi.org/10.1063/1.3111789. – DOI 10.1063/1.3111789

[ADS+06] Azima, A. ; Duesterer, S. ; Schlarb, H. ; Feldhaus, J. ; Cavalieri, A. ; Fritz, D. ; Sengstock, K.: Jitter measurement by spatial electro-optical sampling at the FLASH free electron laser, 2006 (Proceedings of EPAC06)

[Agr01a] Agrawal, Govind P.: *Applications of Nonlinear Fiber Optics, 1st Edition*. Academic Press San Diego, San Francisco, Noew York, Boston, London, Sydney, Tokyo, 2001

[Agr01b] Agrawal, Govind P.: *Nonlinear Fiber Optics, 3rd Edition*. Academic Press San Diego, San Francisco, Noew York, Boston, London, Sydney, Tokyo, 2001

[Aun00] Aune et al., B.: The superconducting TESLA cavities. In: *PRST-AB* 3 (2000), September. http://prst-ab.aps.org/pdf/PRSTAB/v3/i9/e092001

[BFR+01] Brinkmann, R. ; Flöttmann, K. ; Rossbach, J. ; Schmüser, P. ; (Editors), H. W.: TESLA Technical Design Report - Part II / DESY. Version: March 2001. http://flash.desy.de/reports_publications/. 2001. – Forschungsbericht. – DESY 2001-011

[BGG+03] Brunken, M. ; Genza, H. ; Göttlicher, P. ; Hessler, C. ; Hüning, M. ; Loos, H. ; Richter, A. ; Schlarb, H. ; Schmüser, P. ; Simrock, S. ; Suetterlin, D. ; Tonutti, M. ; Türke, D.: Electro-optic sampling at the TESLA Test Accelerator: experimental setup and first results / DESY. 2003. – Forschungsbericht. – TESLA Report 2003-11

[BGJ+07] Berden, G. ; Gillespie, W. A. ; Jamison, S. P. ; Knabbe, E.-A. ; MacLeod, A. M. ; Meer, A. F. G. d. ; Phillips, P. J. ; Schlarb, H. ; Schmidt, B. ; Schmuser, P. ; Steffen, B.: Benchmarking of Electro-Optic Monitors for Femtosecond Electron Bunches. In: *Physical Review Letters* 99 (2007), Nr. 16, 164801. http://dx.doi.org/10.1103/PhysRevLett.99.164801. – DOI 10.1103/PhysRevLett.99.164801

[BJS63] Berlincourt, D. ; Jaffe, H. ; Shiozawa, L. R.: Electroelastic Properties of the Sulfides, Selenides, and Tellurides of Zinc and Cadmium. In: *Phys. Rev.* 129 (1963), Feb, Nr. 3, S. 1009–1017. http://dx.doi.org/10.1103/PhysRev.129.1009. – DOI 10.1103/PhysRev.129.1009

[C+01] Cavalleri, A. et al.: Ultrafast x-ray measurement of laser heating in semiconductors: Parameters determining the melting threshold. In: *Phys. Rev. B* 63 (2001), 193306. http://dx.doi.org/10.1103/PhysRevB.63.1933XX. – DOI 10.1103/PhysRevB.63.1933XX

[Can] Cancellieri: *Single-Mode Optical Fiber measurement*

[CF05] Cavalieri, A. L. ; Fritz, D. M.: Clocking Femtosecond X Rays. In: *Physical Review Letters* 94 (2005), March, S. 114801. http://dx.doi.org/10.1103/PhysRevLett.94.114801. – DOI 10.1103/PhysRevLett.94.114801

[Com01] Components, 3M O.: Specifications of polarization maintaining single mode Fiber FS-PM-4611 / 3M Optical Components. 2001. – Forschungsbericht

[CSS+05a] Casalbuoni, S. ; Schlarb, H. ; Schmidt, B. ; Steffen, B. ; Schmüser, P. ; Winter, A.: Numerical studies on the Electro-Optic Sampling of Relativistic Electron Bunches / DESY. Hamburg, Germany, 2005. – Forschungsbericht. – TESLA Report 2005-01

[CSS05b] Casalbuoni, S. ; Schmidt, B. ; Schmüser, P.: Far-Infrared Transition and Diffraction Radiation, Part I: Production, Diffraction Effects and Optical Propagation / DESY. Hamburg, Germany, 2005. – Forschungsbericht. – TESLA Report 2005-15

[CSS+08] Casalbuoni, S. ; Schlarb, H. ; Schmidt, B. ; Schmüser, P. ; Steffen, B. ; Winter, A.: Numerical studies on the electro-optic detection of femtosecond electron bunches. In: *Phys. Rev. ST Accel. Beams* 11 (2008), Jul, Nr. 7, S. 072802. http://dx.doi.org/10.1103/PhysRevSTAB.11.072802. – DOI 10.1103/PhysRevSTAB.11.072802

[DES06] DESY, Deutsches Elektronen S.: *Free-electron laser FLASH*. http://zms.desy.de/research/photon_science/free_electron_laser_flash/index_eng.html. Version: 2006

[DES13] DESY, Deutsches Elektronen S.: *The European X-Ray Laser Project XFEL*. http://xfel.desy.de/. Version: 2013

[Doh] Dohlus, M.: *Simulation performed by Martin Dohlus.*

[DR95] Diels, J.-C. ; Rudolph, W.: *Ultrashort Laser Pulse Phenomena*. Academic Press, 1995

[DR06] Düsterer, S. ; Radcliffe, P.: Spectroscopic characterization of vacuum ultraviolet free electron laser pulses. In: *Optics Letters* 31 (2006), Nr. 11, 1750. http://dx.doi.org/10.1364/OL.31.001750. – DOI 10.1364/OL.31.001750

[Dre01] Drescher, M.: X-ray Pulses Approaching the Attosecond Frontier. In: *Science* 291 (2001), S. 1923. http://dx.doi.org/10.1126/science.1058561. – DOI 10.1126/science.1058561

[DS09] Debus, A. ; S., Karsch: All-optical Femtosecond Bunch Length Measurement of Laser-accelerated Electron Beams Forschungszentrum Dresden-Rossendorf e.V., 2009 (Ultra-intense Laser Interactions Science)

[Due] Duesterer, S.: *private communication*

[EO-05] *Spectral Decoding Electro-Optic Measurements For Longitudinal Bunch Diagnostics At The Desy Vuv-Fel*. Stanford, California, USA, August 2005 (FEL)

[EO-06a] *Femtosecond Resolution Bunch Profile Measurements*. 2006 (EPAC TUYPA01)

[EO-06b] *Time Resolved Single-Shot Measurements Of Transition Radiation At The Thz Beamline Of Flash Using Electro-Optic Spectral Decoding*. 2006 (EPAC TUPCH027)

[EO-07] *Single shot longitudinal bunch profile measurements by temporally resolved electro-optical detection*. 2007 (DIPAC WEO2A02). – WEO2A02 S.

[FEL05] *Observation of femtosecond bunch length using a transverse deflecting structure.* 2005 (Proceedings of the FEL 2005)

[FEL08] *OPERATION OF FLASH AT 6.5nm WAVELENGTH*. 2008 (Proceedings of EPAC08)

[FER] *FERMI@Elettra, Conceptual Design Report, ST/F-TN-07/12*. http://www.elettra.trieste.it/docs/FERMI_elettra-CDR.pdf

[FH66] Faust, W.L. ; Henry, C.H.: Mixing of visible and near-resonance infrared light in GaP. In: *Phys. Rev. Lett.* 17 (1966), 1265. http://dx.doi.org/10.1103/PhysRevLett.17.1265. – DOI 10.1103/PhysRevLett.17.1265

[FP99] Faatz, B. ; Pflüger, J.: Magnet Sorting for the TTF-FEL Undulator using Simulated Annealing / DESY. 1999. – Forschungsbericht. – TELSA-FEL 1999-01

[Fru] Fruehling, U.: A fs-streaking camera for FLASH. In: *to be published in Physical Review Letters, 2009*

[GAB+08] Gahl, C. ; Azima, A. ; Beye, M. ; Deppe, M. ; Döbrich, K. ; Hasslinger, U. ; Hennies, F. ; Melnikov, A. ; Nagasono, M. ; Pietzsch, A. ; Wolf, M. ; Wurth, W. ; Föhlisch, A.: A femtosecond X-ray/optical cross-correlator. In: *Nature Photonics* 2 (2008), 165-169. http://dx.doi.org/10.1038/nphoton.2007.298. – DOI 10.1038/nphoton.2007.298

[Gue07] Guerassimova, N.: *private communication*. 2007

[GZM+99] Gallot, G. ; Zhang, Jiangquan ; McGowan, R. W. ; Jeon, Tae-In ; Grischkowsky, D.: Measurements of the THz absorption and dispersion of ZnTe and their relevance to the electro-optic detection of THz radiation. In: *Appl. Phys. Lett.* 74 (1999), 3450-3452. http://link.aip.org/link/?APPLAB/74/3450/1

[HHMT73] Hattori, T. ; Homma, Y. ; Mitsuishi, A. ; Tacke, M.: Indeces of refraction of ZnS, ZnSe, ZnSe, CdS and CdTe in the far infrared. In: *Opt. Comm.* 7 (1973), 229-232. http://dx.doi.org/10.1016/0030-4018(73)90015-1

[HKM+02] Hergott, J.-F. ; Kovacev, M. ; Merdji, H. ; Hubert, C. ; Mairesse, Y. ; Jean, E. ; Breger, P. ; Agostini, P. ; Carré, B. ; Salières, P.: Extreme-ultraviolet high-order harmonic pulses in the microjoule range. In: *Phys. Rev. A* 66 (2002), Aug, Nr. 2, S. 021801. http://dx.doi.org/10.1103/PhysRevA.66.021801. – DOI 10.1103/PhysRevA.66.021801

[HSW+00] Heinz, Tony F. ; Shan, Jie ; Weling, Aniruddha S. ; Knoesel, Ernst ; Bartels, Ludwig ; Bonn, Mischa ; Nahata, Ajay ; Reider, Georg A. ; Heinz, Tony F.: Single-shot measurement of terahertz electromagnetic pulses by use of electro-optic sampling. In: *Optics Letters* 25 (2000), Nr. 6, 426–428. http://ol.osa.org/abstract.cfm?URI=ol-25-6-426

[Int] *Sub-Picosecond Pulse Source at SLAC*. http://www.slac.stanford.edu/~pkr/SPPS/SPPS.html

[Isc03] Ischebeck, R.: *Transverse Coherence of a VUV Free Electron Laser*, Hamburg University, Diss., 2003. – DESY-THESIS-2003-033

[Jac99] Jackson, J. D.: *Classical Electrodynamics*. 3rd. John Wiley and Sons, Inc., 1999

[Jam03] Jamison, Steven P.: High-temporal-resolution, single-shot characterization of terahertz pulses. In: *OPTICS LETTERS* 28 (2003), Nr. 18. http://silis.phys.strath.ac.uk/publications/Articles/jamison-ol2818-03.pdf

[Jar06] Jaroszynski, D.: *The Strathclyde Terahertz to Optical Pulse Source (TOPS).* http://tops.phys.strath.ac.uk/. Version: 2006

[Jen03] JenOptic: *Spatial Light modulator SLM 640/12 - Technical documentation*, 2003

[Jov02] Jovanovic, I.: Optical Parametric Chirped-Pulse Amplifier as an Alternative to Ti:Sapphire Regenerative Amplifiers. In: *Applied Optics* 41 (2002), Nr. 15, 2923-2929. http://dx.doi.org/10.1364/AO.41.002923. – DOI 10.1364/AO.41.002923

[JRS+09] Johnsson, P. ; Rouzee, A. ; Siu, W. ; Huismans, Y. ; Lepine, F. ; Marchenko, T. ; Duesterer, S. ; Tavella, F. ; Stojanovic, N. ; Azima, A. ; Treusch, R. ; Kling, M. ; Vrakking, M. J.: Field-free molecular alignment probed by the free electron laser

in Hamburg (FLASH). In: *ArXiv e-prints* (2009), Februar. http://dx.doi.org/arXiv:0902.0171v1. – DOI arXiv:0902.0171v1

[K+09] Krikunova, M. et al.: Auger decay probing using FLASH XUV pulses, to be published. In: *New Journal Of Appl. Phys.* (2009)

[Kab] Kabachnik, N.: *private communication*. – Lomonosov Moscow State University

[KAB+08] Khan, S. ; Azima, A. ; Bödewadt, J. ; Delsim-Hashemi, H. ; Drescher, M. ; Maltezopoulos, T. ; Miltchev, V. ; Mittenzwey, M. ; Rossbach, J. ; Tarkeshian, R. ; Wieland, M. ; Düsterer, S. ; Feldhaus, J. ; Laarmann, T. ; Schlarb, H. ; Meseck, A.: sFLASH: An Experiment for Seeding VUV Radiation at FLASH. In: *DESY publication database* (2008). http://pubdb.desy.de/anonymous/search.php?lid=8619

[Kit02] Kitzler: Quantum Theory of Attosecond XUV Pulse Measurement by Laser Dressed Photoionization. In: *Physics Review Letters* 88 (2002), S. 173904. http://dx.doi.org/10.1103/PhysRevLett.88.173904. – DOI 10.1103/PhysRevLett.88.173904

[KS60] Kleinman, D. A. ; Spitzer, W.G.: Infrared lattice absorption of GaP. In: *Phys. Rev.* 118 (1960), 110. http://link.aps.org/doi/10.1103/PhysRev.118.110

[KW73] Kroll, N. ; Watson, K.: Charged-Particle Scattering in the Presence of a Strong Electromagnetic Wave. In: *Physical Review A* 8 (1973), August, Nr. 2. http://link.aps.org/doi/10.1103/PhysRevA.8.804

[KW85] Knight, R. D. ; Wang, Liang guo: One-photon laser spectroscopy of the np and nf Rydberg series in xenon. In: *J. Opt. Soc. Am. B* 2 (1985), Nr. 7, 1084–1087. http://josab.osa.org/abstract.cfm?URI=josab-2-7-1084

[KY87] Krinski, S. ; Yu, L. H.: Output power in guided modes for ampli

ed spontaneous emission in a single-pass free-electron laser. In: *Phys. Rev.A* 35 (1987), 3406. http://link.aps.org/doi/10.1103/PhysRevA.35.3406

[LHS+99a] Leitenstorfer, A. ; Hunsche, S. ; Shah, J. ; Nuss, M. C. ; Knox, W. H.: Detectors and sources for ultrabroadband electro-optic sampling: Experiment and theory. In: *Appl. Phys. Lett.* 74 (1999), 1516. http://link.aip.org/link/?APPLAB/74/1516/1

[LHS+99b] Leitenstorfer, A. ; Hunsche, S. ; Shah, J. ; Nuss, M. C. ; Knox, W. H.: Femtosecond Charge Transport in Polar Semiconductors. In: *Phys. Rev. Lett.* 82 (1999), Jun, Nr. 25, 5140–5143. http://dx.doi.org/10.1103/PhysRevLett.82.5140. – DOI 10.1103/PhysRevLett.82.5140

[Loe] Loehl, F.: *private communication*

[Loe09] Loehl, F.: *Arrival time stabilization of a XUV SASE free electron laser*, University Hamburg, Diss., 2009

[LSC+07] Loehl, F. ; Schlarb, H. ; Chen, J. ; Kärtner, F. X. ; Kim, J.-W.: First prototype of an optical cross-correlation based fiber-link stabilization for the FLASH synchronization system. In: *Proceedings of the DIPAC 2007 Conference, Venice, Italy*, 2007

[Lud] Ludwig, F.: *private communication*

[Mad71] Madey, J. M.: Stimulated Emission of Bremsstrahlung in a Periodic Magnetic Field. In: *J. Appl. Phys.* 42 (1971), 1906. http://link.aip.org/link/?JAPIAU/42/1906/1

[Mar64] Marple, D. T. F.: Refractive index of ZnSe, ZnTe and CdTe. In: *Journal Of Appl. Phys.* 35 (1964), Nr. 3. http://dx.doi.org/10.1063/1.1713411. – DOI 10.1063/1.1713411

[Mat] *Calculations performed with MATHEMATICA 6.0, Wolfram research inc. 2007*

[MCO+06] Meyer, M. ; Cubaynes, D. ; OKeeffe, P. ; Luna, H. ; Yeates, P. ; Kennedy, E. T. ; Costello, J. T. ; Orr, P. ; Taïeb, R. ; Maquet, A. ; Düsterer, S. ; Radcliffe, P. ; Redlin, H. ; Azima, A. ; Plönjes, E. ; Feldhaus, J.: Two-color photoionization in xuv free-electron and visible laser fields. In: *Physical Review A* 74 (2006), S. 011401. http://dx.doi.org/10.1103/PhysRevA.74.011401. – DOI 10.1103/PhysRevA.74.011401

[MCW+08] Maltezopoulos, T. ; Cunovic, S. ; Wieland, M. ; Beye, M. ; Azima, A. ; Redlin, H. ; Krikunova, M. ; Kalms, R. ; Frühling, U. ; Budzyn, F. ; Wurth, W. ; Föhlisch, A ; Drescher, M.: Single-shot timing measurement of extreme-ultraviolet free-electron laser pulses. In: *New Journal of Physics* 10 (2008), Nr. 3. http://dx.doi.org/10.1088/1367-2630/10/3/033026

[Men01] Menzel, R.: *Photonics*. Springer, 2001

[MKT+00] Miura, Taisuke ; Kobayashi, Katsuyuki ; Takasago, Kazuya ; Zhang, Zhigang ; Torizuka, Kenji ; Kannari, Fumihiko: Timing jitter in a kilohertz regenerative amplifier of a femtosecond-pulse Ti:Al2O3 laser. In: *Opt. Lett.* 25 (2000), Nr. 24, 1795–1797. http://ol.osa.org/abstract.cfm?URI=ol-25-24-1795

[Moo07] Moore, Ken: *ZEMAX, Optical Design Program*. www.zemax.com. Version: 2007

[MW06] Martins, M. ; Wellhoefer, M.: Monochromator beamline for FLASH. In: *Review Of Scientific Instruments* 77 (2006), September, 115108. http://link.aip.org/link/?RSINAK/77/115108/1

[PCO03] PCO imaging (Hrsg.): *DiCAM-PRO manual*. PCO imaging, 2003

[PET] *The new PETRA synchrotron radiation light source*. http://petra3.desy.de/

[PPY76] Pikhtin, A. N. ; Prokopenko, V. T. ; Yas'kov, A. D.: Dispersion of the refractive index of light and permittivity of gallium phosphide. In: *Soviet Physics - Semiconductors* 10 (1976), Nr. 11, S. 1224–1226

[QJ+03] Quéré, F. ; J., Itatani et al.: Attosecond Spectral Shearin Interferometry. In: *Physical Review Letters* 90 (2003), Feb, Nr. 7. http://dx.doi.org/10.1103/PhysRevLett.90.073902. – DOI 10.1103/PhysRevLett.90.073902

[QMI05] Quéré, F. ; Mairesse, Y. ; Itatani, J.: Temporal characterization of attosecond XUV fields. In: *Journal of Modern Optic* 52 (2005), February, Nr. 2-3, 339-360. http://www.informaworld.com/smpp/783223069-3603525/content~db=all~content=a713694480~tab=linking

[RDA+07] Radcliffe, P. ; Düsterer, S. ; Azima, A. ; Li, W.B. ; Plönjes, E. ; Redlin, H. ; Feldhaus, J. ; Nicolosi, P. ; Poletto, L. ; Dardis, J. ; Gutierrez, J.P. ; Hough, P. ; Kavanagh, K.D. ; Kennedy, E.T. ; Luna, H. ; Yeates, P. ; Costello, J.T. ; Delyseries, A. ; Lewis, C.L.S. ; Glijer, D. ; Cubaynes, D. ; Meyer, M.: An experiment for two-color photoionization using high intensity extreme-UV free electron and near-IR laser pulses. In: *Nuclear Instruments and Methods in Physics Research Section A: Accelerators, Spectrometers, Detectors and Associated Equipment* 583 (2007), Nr. 2-3, 516 - 525. http://dx.doi.org/DOI:10.1016/j.nima.2007.09.014. – DOI DOI: 10.1016/j.nima.2007.09.014. – ISSN 0168–9002

[RDM07] Radcliffe, P. ; Düsterer, S. ; Meyer, M.: Single-shot characterization of independent femtosecond extreme ultraviolet free electron and infrared laser pulses. In: *Applied Physics Letters* 90 (2007), S. 131108. http://dx.doi.org/10.1063/1.2716360. – DOI 10.1063/1.2716360

[REF+07] Rudenko, A ; Ergler, Th ; Feuerstein, B ; Zrost, K ; Schroter, C D. ; Moshammer, R ; Ullrich, J: Time-resolved measurements with intense ultrashort laser pulses: a 'molecular movie' in real time. In: *Journal of Physics: Conference Series* 88 (2007), 012050 (8pp). http://stacks.iop.org/1742-6596/88/012050

[Rei04] Reider, Georg A.: *Photonik*. 2. Springer WienNewYork, 2004

[Röh08] Röhrs, M.: *Investigation of the Phase Space Distribution of Electron Bunches at the FLASH-Linac Using a Transverse Deflecting Structure*, University Hamburg, Diss., 2008

[Ric03] Richter, M.: Measurement of gigawatt radiation pulses from a vacuum and extreme ultraviolet free-electron laser. In: *APPLIED PHYSICS LETTERS* 83 (2003), Nr. 14. http://dx.doi.org/DOI:10.1063/1.1614417. – DOI DOI:10.1063/1.1614417

[Rou01] Rousse, A.: Non-thermalmelting in semiconductors measured at femtosecond resolution. In: *NATURE* 410 (2001), March. http://dx.doi.org/10.1038/35065045. – DOI 10.1038/35065045

[RSTE01] Richard, F. ; Schneider, J. R. ; Trines, D. ; (Editors), A. W.: TESLA Technical Design Report / DESY. Version: March 2001. http://tesla.desy.de/new_pages/TDR_CD/start.html. 2001. – Forschungsbericht. – DESY 2001-011

[SA09] Schott AG, Germany: *Coefficient tables of various glass sorts*. http://www.schott.com/advanced_optics/english/our_products/materials/data_tools/index.html. Version: 2009

[SAL+05] Schlarb, H. ; Ayvazyan, V. ; Ludwig, F. ; Noelle, D. ; Schmidt, B. ; Simrock, S. ; Winter, A. ; Kärtner, F. X.: Next Generation Synchronisation System for the VUV-FEL at DESY. In: *27th FEL Conference, Stanford, USA*, 2005

[SCH+00] Schnürer, M. ; Cheng, Z. ; Hentschel, M. ; Krausz, F. ; Wilhein, T. ; Hambach, D. ; Schmahl, G. ; Drescher, M. ; Lim, Y. ; Heinzmann, U.: Few-cycle-driven XUV laser harmonics: generation and focusing. In: *Applied Physics B: Lasers and Optics* 70 (2000), 227-232. http://www.springerlink.com/content/y7bafh6b6vu7pg5e/?p=0959ef839ba849eeb8058c12b3608eaa&pi=0

[Scr06] Scrinzi: Attosecond physics. In: *Journal Physics B* 39 (2006), S. R1. http://dx.doi.org/doi:10.1088/0953-4075/39/1/R01. – DOI doi:10.1088/0953–4075/39/1/R01

[SHSF] Schmidt, B. ; Hacker, M. ; Stobrawa, G. ; Feurer, T.: *LAB2 - A virtual femtosecond laser lab*. http://www.lab2.de

[SJ66] Sliker, T. R. ; Jost, J. M.: Linear Electro-Optic Effect and Refractive Indices of Cubic ZnTe∗. In: *J. Opt. Soc. Am.* 56 (1966), Nr. 1, 130–131. http://www.opticsinfobase.org/abstract.cfm?URI=josa-56-1-130

[SLA09] SLAC, Stanford Linear Accelerator C.: *The Linac Coherent Light Source (LCLS) i*. http://ssrl.slac.stanford.edu/lcls/science.html. Version: 2009

[SLM] *ZEMAX Development Corp.* http://www.zemax.com

[STBC+98] Sokolowski-Tinten, K. ; Bialkowski, J. ; Cavalleri, A. ; Linde, D. von d. ; Oparin, A. ; Vehn, J. Meyer-ter ; Anisimov, S. I.: Transient States of Matter during Short Pulse Laser Ablation. In: *Phys. Rev. Lett.* 81 (1998), Jul, Nr. 1, S. 224–227. http://dx.doi.org/10.1103/PhysRevLett.81.224. – DOI 10.1103/PhysRevLett.81.224

[Ste07] Steffen, B.: *Electro-Optic Methods for Longitudinal Bunch Diagnostics at FLASH*, Department of physics, university of Hamburg, Diss., 2007

[STL00] Sokolowski-Tinten, K. ; Linde, D. von d.: Generation of dense electron-hole plasmas in silicon. In: *Phys. Rev. B* 61 (2000), Jan, Nr. 4, S. 2643–2650. http://dx.doi.org/10.1103/PhysRevB.61.2643. – DOI 10.1103/PhysRevB.61.2643

[Str03] Strobawa, G.: *Aufbau und Anwendungen eines hochaufloesenden Impulsformers zur Kontrolle ultrakurzer Laserimpulse*, Friedrich-Schiller-Universitaet Jena, Diss., 2003

[SWJ01] Schall, M. ; Walther, M. ; Jepsen, P. U.: Fundamental and second-order phonon processes in CdTe and ZnTe. In: *Phys. Rev. B* 64 (2001), 094301. http://link.aps.org/doi/10.1103/PhysRevB.64.094301

[Syn] *Measured using the TEO fiber feedback cross-correlator with F. Tavella*

[TA71] Tada, Kunio ; Aoki, Masaharu: Linear Electrooptic Properties of ZnTe at 10.6 Microns. In: *Japanese Journal of Applied Physics* 10 (1971), Nr. 8, 998-1001. http://dx.doi.org/10.1143/JJAP.10.998. – DOI 10.1143/JJAP.10.998

[TAB+09] Tiedtke, K ; Azima, A ; Bargen, N von ; Bittner, L ; Bonfigt, S ; Dusterer, S ; Faatz, B ; Fruhling, U ; Gensch, M ; Gerth, Ch ; Guerassimova, N ; Hahn, U ; Hans, T ; Hesse, M ; Honkavaar, K ; Jastrow, U ; Juranic, P ; Kapitzki, S ; Keitel, B ; Kracht, T ; Kuhlmann, M ; Li, W B. ; Martins, M ; Nunez, T ; Plonjes, E ; Redlin, H ; Saldin, E L. ; Schneidmiller, E A. ; Schneider, J R. ; Schreiber, S ; Stojanovic, N ; Tavella, F ; Toleikis, S ; Treusch, R ; Weigelt, H ; Wellhofer, M ; Wabnitz, H ; Yurkov, M V. ; Feldhaus, J: The soft x-ray free-electron laser FLASH at DESY: beamlines, diagnostics and end-stations. In: *New Journal of Physics* 11 (2009), Nr. 2, 023029 (16pp). http://stacks.iop.org/1367-2630/11/023029

[Tre] Trebino, R.: *FROG - Frequency resolved optical gating*

[Tre69] Treacy, E. B.: Optical pulse compression with diffraction gratings. In: *IEEE Journal of Quantum Electronics* 5 (1969), S. 454–460

[W+02] Wilke, I. et al.: Single-Shot Electron-Beam Bunch Length Measurements. In: *Phys. Rev. Lett.* 88 (2002), 124801-1. http://link.aps.org/doi/10.1103/PhysRevLett.88.124801

[War91] *Kapitel* Zinc Selenide (ZnSe) Zinc Telluride (ZnTe). In: Ward, L.: *Handbook of Optical Constants of Solids II*. Boston : Academic Press, 1991 (Handbook of Optical Constants of Solids II), S. 737

[Wel07] Wellhoefer, M.: *The Monochromator Beamline at the Free-Electron Laser in Hamburg (FLASH) Assembly, Characterization, and First Experiments*, University Hamburg, Diss., 2007

[Win04] Winter, A.: *Bunch length measurements using electro-optical sampling at the SLS linac*, RTWH Aachen, Diplomarbeit, 2004. – DESY-THESIS-2004-027

[Win08] Winter, A.: *Fiber Laser Master Oscillator for Optical Synchronization Systems*, University of Hamburg, Diss., 2008

[WKT05] Will, I. ; Koss, G. ; Templin, I.: The upgraded photocathode laser of the TESLA Test Facility. In: *Nuclear Instruments and Methods in Physics Research Section A: Accelerators, Spectrometers, Detectors and Associated Equipment* 541 (2005), Nr. 3, 467 - 477. http://dx.doi.org/DOI:10.1016/j.nima.2004.12.007. – DOI DOI: 10.1016/j.nima.2004.12.007. – ISSN 0168–9002

[WLP+93] Wahlström, C.-G. ; Larsson, J. ; Persson, A. ; Starczewski, T. ; Svanberg, S. ; Salières, P. ; Balcou, Ph. ; L'Huillier, Anne: High-order harmonic generation in rare gases with an intense short-pulse laser. In: *Phys. Rev. A* 48 (1993), Dec, Nr. 6, S. 4709–4720. http://dx.doi.org/10.1103/PhysRevA.48.4709. – DOI 10.1103/PhysRevA.48.4709

[WM07] Wellhoefer, M. ; Martins, M.: Performance of the monochromator beamline at FLASH. In: *Journal Of Optics A* 9 (2007), June, S. 749,756. http://dx.doi.org/doi:10.1088/1464-4258/9/7/030. – DOI doi:10.1088/1464–4258/9/7/030

[WRD93] Warren, S. ; Rabitz, Herschel ; Dahleh, Mohammed: Coherent Control of Quantum Dynamics The Dream Is Alive. In: *Science* 259 (1993), Nr. 5101, 1581-1589. http://dx.doi.org/10.1126/science.259.5101.1581. – DOI 10.1126/science.259.5101.1581

[WTEL09] Werin, Sverker ; Thorin, Sara ; Eriksson, Mikael ; Larsson, Jörgen: Short pulse facility for MAX-lab. In: *Nuclear Instruments and Methods in Physics Research Section A: Accelerators, Spectrometers, Detectors and Associated Equipment* 601 (2009), Nr. 1-2, 98 - 107. http://dx.doi.org/DOI:10.1016/j.nima.2008.12.106. – DOI DOI: 10.1016/j.nima.2008.12.106. – ISSN 0168–9002. – Special issue in honour of Prof. Kai Siegbahn

[WZ95] Wu, Q. ; Zhang, X.-C.: Free-space electro-optic sampling of terahertz beams. In: *Appl. Phys. Lett.* 67 (1995), 3523. http://link.aip.org/link/?APPLAB/67/3523/1

[WZ97] Wu, Q. ; Zhang, X.-C.: 7 terahertz broadband GaP electro-optic sensor. In: *Appl. Phys. Lett.* 70 (1997), 14. http://link.aip.org/link/?APPLAB/70/1784/1

[YA07] Yurkov, M.V. ; Ayvazyan, V.: Operation of a free electron laser from the extreme ultraviolet to the water window. In: *Nature Photonics 1* 6 (2007), Jun, 336-342. http://dx.doi.org/10.1038/nphoton.2007.76. – DOI 10.1038/nphoton.2007.76

[YY84] Yariv, A. ; Yeh, P.: *Optical Waves in Crystals - Propagation and Control of Laser Radiation*. New York : John Wiley & Sons, 1984

Acknowledgement

I would like to thank all my colleagues at DESY, the University of Hamburg, the Daresbury Lab, the University of Strathclyde, the Stanford University, and elsewhere, who contributed to the electro-optical and the two-color pump-probe experiments at FLASH. This work would not have been possible without their willingness to share their time and experience with me.

First of all I would like to thank my two advisors *Dr. Stefan Düsterer and Dr. Holger Schlarb* for their immense support throughout the last years, for giving me hints to perform successful pump-probe experiments and teaching me the basics of electro-optic detection and machine physics. Without the many fruitful discussions and constructive ideas the timing tool would not have been as successful in the process as a timing diagnostic for pump-probe experiments as it was.

I owe very special thanks to *Dr. Harald Redlin* from DESY, *Dr. David Fritz* and *Dr. Adrian Cavalieri* from SLAC/ Stanford University for helping me to discuss and understand the non-linear optic issues regarding the fs-pulse transporting glass fiber. The time the people from SLAC spent at DESY was indispensable for the success of the project especially for the compression of the fiber pulse.

Especially i would like to thank my fellow PhD student *Dr. Bernd Steffen*, who introduced the FLASH accelerator to me, when I first came to DESY and who worked tightly with me in many aspects regarding electro-optical sampling issues and finally allowed me to use many parts of his simulation code to simulate our EO signals. I am grateful to *Prof. Dr. Dino Jaroszynski* for his support during the crystal characterization at the Strathclyde Terahertz to Optical Pulse Source (TOPS).

Thanks to *Dr. William Schlotter*, *Dr. Franz Tavella* and *Dr. Michael Gensch* for the numerous discussions on THz- and femtosecond science.

Thanks to *Dr. Nicola Stojanovic* for carefully taking over the TEO experiment as scientist in charge, as i moved to my new position.

Many thanks to *Prof. Dr. Peter Schmüser* for the helpful theoretical seminars and discussions on FEL concepts and electro-optical bunch diagnostics.,

I owe many thanks to *Dr. Michael Meyer* and *Dr. Alexander Foehlisch* and *Dr. Cornelius Gahl* and *Prof. Dr. John Costello* and especially their group members, who allowed me to participate them during their pump-probe experiment user times at FLASH. Only from the fruitful teamwork with these user groups, the presented experimental pump-probe data were realized.

I have spent a wonderful time in the Photon Diagnostic group of HASYLAB and want to thank my former group leader *Dr. Josef Feldhaus* for the possibility to perform this very inspiring and many-topics including thesis position. Thanks to my colleagues *Dr. Sven Toleikis, Dr. Kai Tiedtke* for the always friendly and inspiring atmosphere in the group. Many thanks to *Dr. Elke Ploenjes*, who invited me to this PhD position and introduced me to HASYLAB.

Special thanks go to *Dr. Ingo Will* from the Max-Born institute in Berlin, who designed and built the laser synchronization of the pump-probe laser system and thus provided the basic electronic hardware for the TEO timing and signal finding.

I'm very grateful to *Prof. Dr. Jörg Roßbach*, *Dr. Siggi Schreiber*, all FLASH operators, and the

whole FLASH team, who made the successful operation of the accelerator and the FEL possible and gave me the opportunity to perform these measurements. Special thanks to *Gerhard Grygiel*, *Dr. Vitali Kocharyan*, and *Dr. Vladimir Rybnikov* for the ICCD camera server and the numerous discussions on the data acquisition system; to *Jörg Thomas* for the motor control server; to *Helmut Remde*, *Dirk Ahrent*, and the MVP vacuum team for fitting last minute crystal changes into the time schedule. Many thanks to *Dr. Martin Dohlus* I owe thanks for providing me with simulation data of the longitudinal electron bunch profile.

Many thanks to *Prof. Dr. Klaus Sengstock* for guiding and supervising me through the time this thesis meant.

A very special thanks to my new working group led by *Prof. Dr. Markus Drescher* for supporting me, while i finished this thesis.

Finally, i want to thank my friends and my family for their tremendous support during the last years and apologize for the negligence you had to experience lately. Last but not least, I thank my wife *Olja* for reminding me once in a while that life is more than electrons and lasers alone and for keeping patience during all times.

Selbständigkeitserklärung

Hiermit versichere ich, diese Arbeit selbständig ausgeführt und nur die angegebenen Quellen verwendet zu haben.

Hamburg, im Juni 2009

_____